8-2019

Synthesis, Characterizations, and Study of the Antioxidant Activity of Novel Ruthenium-Thione and -Selone Complexes

Mohammed Abdulali Abbas
Clemson University, mabbas@g.clemson.edu

SYNTHESIS, CHARACTERIZATIONS, AND STUDY OF THE ANTIOXIDANT ACTIVITY OF NOVEL RUTHENIUM-THIONE AND -SELONE COMPLEXES

A Dissertation
Presented to
the Graduate School of
Clemson University

In Partial Fulfillment
of the Requirements for the Degree
Doctor of Philosophy
Chemistry

---

by
Mohammed Abdulali Abbas
August 2019

Accepted by:
Julia L. Brumaghim, Committee Chair
William T. Pennington
Joseph S. Thrasher
Daniel C. Whitehead

ABSTRACT

Coordination chemistry of imidazole thione and selone compounds with 2nd and 3rd row *d*-block metals are of considerable interest due to their wide-ranging applications of reducing heavy metal toxicity, catalysis, and antimicrobial and antitumor activity. Antioxidant behavior of some imidazole thiones and selones is attributed to their ability to scavenge hydrogen peroxide or other reactive oxygen species as well as their coordination of redox-active iron and copper to prevent hydroxyl-radical-mediated DNA damage. Chapter 1 of this dissertation provides an overview of 2nd and 3rd row *d*-block metal complexes with imidazole thione and selone ligands and their applications.

Ruthenium complexes with labile solvato ligands represent versatile synthons for entry into Ru(II) coordination chemistry. Thus, homoleptic and heteroleptic solvato Ru(II) complexes were synthesized from readily available $RuCl_3 \cdot xH_2O$ (Chapter 2). An improved synthesis of $[Ru(NCCH_3)_6][BF_4]_2$ affords higher yields with fewer reaction steps, and the $[Ru(NCCH_3)_2(DMSO)_3Cl][BF_4]_{1.5}[Cl]_{0.5}[Na]$, $[Ru(NCCH_3)_4(DMSO)_2][BF_4]_2$, and $[Ru(NCCH_3)_5(DMSO)][BF_4]_2$, (DMSO = dimethylsulfoxide) mixed-solvato complexes could be useful for synthesizing heteroleptic Ru(II) complexes.

Sulfur and selenium compounds can scavenge reactive oxygen species to prevent oxidative damage, and metal coordination can improve this activity. Therefore, novel homoleptic Ru(III) and Ru(II) complexes with methimazole (MMI), *N*,*N'*-dimethylimdiazole thione (dmit) and selone (dmise) ligands of the formula $[RuL_6]Cl_3$ and $[RuL_6][BF_4]_2$ were synthesized (Chapter 3). Heteroleptic complexes RuL_4Cl_2 were also

synthesized with the same three ligands. The $[RuL_6]Cl_3$ complexes quickly react with hydrogen peroxide, with the MMI and dmise complexes reacting significantly faster than the dmit complex. $[Ru(MMI)_6]Cl_3$ also prevents iron-mediated DNA damage at very low micromolar concentrations.

Ruthenium nitrosyl complexes are some of the most investigated compounds for biological NO delivery. Therefore, Ru(II)-nitrosyl complexes $[Ru(NO)(L)_4Cl][BF_4]_2$ (L = dmit dmise) were synthesized from $RuCl_3 \cdot xH_2O$ with silver nitrate as a simple and convenient nitrosyl source (Chapter 4). This novel method considerably simplifies synthesis of Ru-nitrosyl complexes with good yields and avoids the use of unstable or toxic starting materials to generate nitrosyl complexes. This work develops Ru(II) and Ru(III) chemistry as starting materials and with thione, selone, and nitrosyl ligands that have promising biological applications as antitumor, antimicrobial, and photodynamic therapy agents as well as catalytic applications.

DEDICATION

I dedicate this dissertation to my beloved mother for her love, prayer, encouragements, and all her efforts to be, soul of my beloved father, my brother, and sisters for their love and encouragements.

I would like to dedicate this work to my first and last love, my life partner, my lovely wife for her love, patience, encouragements, sacrifice and support, and my lovely children, Mustafa, Mariam, and Mayar.

ACKNOWLEDGMENTS

First, with gratitude and appreciation, I would like to thank my advisor Dr. Julia L. Brumaghim for accepting me to join to her group, scientific guidance, generous cooperation, suggestions, encouragement, patience, support and inspiration during the research work. Everything is possible and there is a solution for each problem, I really have learned bioinorganic chemistry filed and air sensitives synthesis and enjoyed in the research work with her.

I would like to thank the higher committee for education development in Iraq (HCED) for the financial support as well as giving me this great opportunity to get the PhD degree in chemistry from Clemson University.

I am very grateful to Dr. Colin McMillan for X-ray crystal structures collections and analysis. He is always ready to help with smile face. Also, I would like to thank my group members, past and present for their help, I have spent great time with them.

I would like to express my greatest gratitude to my mother, brother and sisters for their love and prayers.

All the beautiful words in the words dictionary will not be enough to express my feeling and gratitude to thank my lovely wife, she has helped, scarified, encouraged, supported, and loved, she does not wait anything except seeing me a successful person, I would say she has my heart.

TABLE OF CONTENTS

Page

TITLE PAGE i

ABSTRACT ii

DEDICATION iv

ACKNOWLEDGMENTS v

LIST OF TABLES viii

LIST OF FIGURES x

LIST OF SCHEMES xx

LIST OF ABREVIATION xxi

CHAPTER

I. COORDINATION CHEMISTRY, BIOLOGICAL ACTIVITY, AND CATALYIC APPLICATIONS OF IMIDAZOLE THIONE AND SELONE COMPLEXES WITH SECOND- AND THIRD-ROW TRANSITION METAL IONS 1

1.1. Biological roles of thione and selone compounds 1
1.2. Coordination chemistry of imidazole thione and selone compounds 4
1.3. Applications of imidazole thione and selone complexes 17
1.4. Conclusions and Outlook 23
1.5. Using Ruthenium Solvato Complexes as an Entry into Ruthenium Thione and Selone Complexes 24
1.6. References 25

II. SYNTHESIS, CHARACTERIZATION, AND STRUCTURES OF RUTHENIUM(II) COMPLEXES WITH MULTIPLE SOLVATO LIGANDS 34

2.1. Introduction 34
2.2. Results and Discussion..... 35
2.3. Conclusions 45
2.4. Experimental Methods 46
2.5. Supplemental Material 53
2.6. References 63

III. SYNTHESIS, CHARACTERIZATION, AND STUDY OF THE ANTIOXIDANT ACTIVITY OF NOVEL RUTHENIUM IMIDAZOLE-2-THIONE AND -SELONE COMPLEXES.....68

2.7. Introduction 68
2.8. Results and Discussion..... 70
2.9. Conclusions 82
2.10. Experimental Methods 82
2.11. Supplemental Material 92
2.12. References 112

IV. SYNTHESIS OF NOVEL RUTHENIUM NITROSYL THIONE AND SELONE COMPLEXES USING A NITRATE SALT.....118

2.13. Introduction 118
2.14. Results and Discussion.....119
2.15. Conclusions 128
2.16. Experimental Methods 129
2.17. Supplemental Material 133
2.18. References 138

LIST OF TABLES

Table		Page
1.1	C=S/Se infrared stretching bands for thione and selone ligands; ligand structures are shown in Figure 1.2	13
1.2	EC_{50} values for cisplatin, carboplatin, and Pt-thione and -selone complexes in human cancer cell lines	19
2.1	IR stretching bands for C≡N and S-O in complexes **1-5**	38
2.2	^{1}H NMR chemical shifts (δ) in D2O of the solvato ligands in complexes **1-5**	39
2.3	Selected interatomic distances (Å) and angles (°) for hexakis(acetonitrile) complexes **1a** and **1bb**	41
2.4	Selected interatomic distances (Å) and angles (°) for complexes **2**, **3**, **4**, and **5**. The structure of complex **3** contains four unique Ru centers, and the Ru1 center is tabulated here as a representative example.	43
2.5	Crystallographic data for complexes **1a** and **1b**	51
2.6	Crystallographic data for complexes **2** and **3**	51
2.7	Crystallographic data for complexes **4** and	52
2.8	Selected interatomic distances (Å) and angles (°) for $[Ru(NCCH_3)_5(DMSO)][BF_4]_2 \cdot 2CH_3CN$ (**5** with additional lattice acetonitrile)	54
2.9	Crystallographic data for $[Ru(NCCH_3)_5(DMSO)][BF_4]_2 \cdot 2CH_3CN$ (**5** with additional lattice acetonitrile)	54
3.1	Selected bond lengths (Å) and angles (°) for $[Ru(MMI)_6]Cl_3$ (**1a**) and $[Ru(dmit)_6](BF_4)2$ (**5**) and unbound thione ligands	74
3.2	C=S/Se IR stretches and ^{1}H NMR resonances (in D2O)	75

List of Tables (Continued)

Table Page

3.3 Initial rates for reaction of complexes **1a**, **2**, and **3** with H_2O_2 79

3.4 Crystallographic data for complexes 1 and 5 88

3.5 Selected interatomic distances (Å) and angles (°) for $[Ru(MMI)_6][BF_4]_2[NO_3]$ (**1b**) 92

3.6 Crystallographic data for $[Ru(MMI)_6][BF_4]_2[NO_3]$ (**1b**). 93

3.7 Gel electrophoresis results for DNA damage prevention assays with $[Ru(MMI)_6]Cl_3$ (**1**) 111

4.1 Selected bond lengths (Å) and angles (deg) for $[Ru(NO)(dmit)_4Cl][BF_4]_2$ (**1**) and $[Ru(NO)(dmise)_4Cl][BF_4]_2$ (**2**; E = S, dmit; E = Se, dmise) 122

4.2 Selected IR stretches and NMR resonances (in D_2O) for compounds **1** and **2** 124

4.3 Electrochemical data for thione and selone ligands and ruthenium complexes **1** and **2** vs. NHE 127

4.4 Crystallographic data for $[RuCl(NO)(dmit)_4][BF_4]_2$ (**1**) and $[RuCl(NO)(dmise)_4][BF_4]_2$ (**2**) 132

4.5 Selected interatomic distances and angles for $[Ru(NO)(dmit)_4Cl][BF_4]_2$ (**1**) 135

4.6 Selected interatomic distances (Å) and angles (°) for $[Ru(NO)(dmise)_4Cl][BF_4]_2$ (**2**) 135

LIST OF FIGURES

Figure		Page
1.1	Sulfur and selenium compounds discussed in this work	1
1.2	Imidazole -thione and selone ligands discussed in this work	3
1.3	Resonance structures of imidazole thione (E = S) and selone (E = Se) compounds (R, R' = aryl, alkyl, or H)	3
1.4	A) Monodentate and B) bidentate binding modes of thione (E = S) and selone (E = Se) ligands, where M = metal and R = H, alkyl, or aryl group.	5
1.5	Crystal structure diagrams of A) $Cp(Tm^{Me})ZrCl_2$ and B) $Tm^{Bu}Hf(CH_2Ph)_3$. Hydrogen atoms are omitted for clarity	7
1.6	Crystal structure diagrams of A) $Tm^{Me}Nb(=NR)Cl_2$ and B) $Tm^{Me}Ta(=NR)Cl_2$. Hydrogen atoms are omitted for clarity	7
1.7	Crystal structure diagrams of A) $[\kappa^3\text{-}(N\text{-MeImid})Tm^{Me}]_2$ Ru, B) $[\kappa^3\text{-}(N\text{-MeImid})Tm^{Me}]_2Rh$. Hydrogen atoms, solvent, and counterions are omitted for clarity	8
1.8	Crystal structure diagram of $[\kappa^2\text{-}((N\equiv C)Tm^{Me})]_2Pd$. Hydrogen atoms are omitted for clarity	8
1.8	Crystal structure diagrams of A) *fac*-$Tc(k^2Tm^{Me})(CO)_3$ and B) *fac*-$Re(Tm^{Me})(CO)_2(ImzH)$. Hydrogen atoms are omitted for clarity	9
1.10	Crystal structure diagrams of A) $\kappa^2\text{-}Bm^{Me}Ru(CO)(PPh_3)H$, and B) $\kappa^2\text{-}Bm^{Me}Os(CO)(PPh_3)H$	9
1.11	Crystal structure diagram of $(\kappa^2\text{-}S,N\text{-bimt})_3Y(THF)_2$. Hydrogen atoms are omitted for clarity	10

List of Figures (Continued)

Figure Page

1.12 Crystal structure diagrams of A) [Mo(tmeimt)$(CO)_5$ and B) W(tmeimt)$(CO)_5$. Hydrogen atoms are omitted for clarity 11

1.13 Crystal structure diagram of *cis*-Ru$(imt^{MePh})_2(PPh_3)_2Cl_2$. Hydrogen atoms are omitted for clarity 11

1.14 Crystal structure diagrams of A) [CpRh(bmtp)]Cl_2 and B)[CpIr(bmtp)]Cl_2 Hydrogen atoms and counterions are omitted for clarity 12

1.15 Crystal structure diagram of [Au(bptp)Cl_2]Cl. Hydrogen atoms and counterions are omitted for clarity 13

1.16 Crystal structure diagrams of *trans*-[Pt$(NH_3)_2(Hims)_2$][NO_3] and [Ag_2(μ-imdt)$_2(imdt)_2(PPh_3)_2$][NO_3]$_2$. Hydrogen atoms and counterions are omitted for clarity 14

1.17 Crystal structure diagrams of Hg(Me, Et-OH-Bimt)Cl_2. Hydrogen atoms are omitted for clarity 15

1.18 Crystal structure diagrams of A) [Cp*Rh(mbis)Cl]Cl, B) [Cp*Ir(mbis)Cl]Cl, C) $Au_2(mbis)(C_6F_5)_6$ and D) $Au_2(ebis)(C_6F_5)_2$ Hydrogen atoms and counterions are omitted for clarity 15

1.19 Crystal structure diagrams of A) $(bmimise)_2Pd_2Cl_4$ and B) $(bbmimise)_2Pt_2Cl_4$. Hydrogen atoms are omitted for clarity 16

1.20 Crystal structure diagram of [Cd$(dmise)_4$][PF_6]$_2$. Hydrogen atoms and counterions are omitted for clarity 17

2.1 Coordination geometries about the Ru(II) centers for hexakis(acetonitrile) polymorphs **1a** and **1b**, respectively. Atoms are shown with 50% probability ellipsoids, with hydrogen atoms, counterions, and solvent molecules omitted for clarity 40

List of Figures (Continued)

Figure Page

2.2 X-ray diffraction structures for complexes **2**, **3**, **4**, and **5**, with mixed acetonitrile and DMSO coordination. Atoms are shown as 50% probability ellipsoids, with hydrogen atoms, counterions, and solvent molecules omitted for clarity 42

2.3 Packing diagrams for $[Ru(NCCH_3)_6][BF_4]_2$ polymorphs **1a** and **1b** as viewed along the *c*-axis. Hydrogen atoms are omitted for clarity 53

2.4 X-ray diffraction structure for $[Ru(NCCH_3)_5(DMSO)][BF_4]_2 \cdot 2CH_3CN$ (**5**) with additional lattice acetonitrile) with mixed acetonitrile and DMSO coordination. Atoms are shown as 50% probability ellipsoids, and hydrogen atoms, counterions, and solvent molecules are omitted for clarity 53

2.5 ^1H NMR spectrum of $[Ru(NCCH_3)_6][BF_4]_2$ (**1**) in D_2O. The resonance at δ 2.12 is from unbound CH_3CN. 55

2.6 ^1H NMR spectrum of $[RuCl(NCCH_3)_2(DMSO)_3][BF_4]_{1.5}[Cl]_{0.5}[Na]$ (**2**) in D_2O. The resonance at δ 2.05 is from unbound acetonitrile, and the resonance at δ 2.71 is from unbound DMSO 55

2.7 ^1H NMR spectrum of $[Ru(NCCH_3)_4(DMSO)_2][BF_4]_2$ (**3**) in D_2O. The resonance at δ 2.10 is from unbound acetonitrile, and the resonance at δ 2.52 is $[Ru(NCCH_3)_6][BF_4]_2$ 56

2.8 ^1H NMR spectrum of $[Ru(NCCH_3)_5(DMSO)][NO_3]_2$ (**4**) in D_2O. The resonance at δ 2.04 is from unbound acetonitrile, and the resonance at δ 3.71 is from unbound DMSO 56

List of Figures (Continued)

Figure Page

2.9 ^{1}H NMR spectrum of $[Ru(NCCH_3)_5(DMSO)][BF_4]_2$ (**5**) in D_2O. The resonance at δ 2.04 is from unbound acetonitrile, and the resonance at δ 3.71 is from unbound DMSO..... 57

2.10 Transmittance IR spectrum of $[Ru(NCCH_3)_6][BF_4]_2$ (**1**) acquired as a Nujol mull 57

2.11 Transmittance IR spectrum of $[Ru\ Cl(NCCH_3)_2(DMSO)_3][BF_4]_{1.5}[Cl]_{0.5}[Na]$ (**2**) acquired as a Nujol mull. 58

2.12 Transmittance IR spectrum of $[Ru(NCCH_3)_4(DMSO)_2][BF_4]_2$ (**3**) acquired as a Nujol mull..... 58

2.13 Transmittance IR spectrum of $[Ru(NCCH_3)_5(DMSO)][NO_3]_2$ (**4**) acquired as a Nujol mull 59

2.14 Transmittance IR spectrum of $[Ru(NCCH_3)_5(DMSO)][BF_4]_2$ (**5**) acquired as a Nujol mull 59

2.15 MALDI mass spectrum with insets of experimental (left) and simulated (right) envelope intensities for $[RuCl(NCCH_3)_2(DMSO)_3]\ [BF_4]_{1.5}[Cl]_{0.5}[Na]$ (**2**)..... 60

2.16 MALDI mass spectrum with insets of experimental (left) and simulated (right) envelope intensities for $[Ru(NCCH_3)_4(DMSO)_2]\ [BF_4]_2$ (**3**)..... 61

2.17 MALDI mass spectrum with insets of experimental (left) and simulated (right) peak envelope intensities for $[Ru(NCCH_3)_5(DMSO)][NO_3]_2$ (**4**).....62

2.18 MALDI mass spectrum with insets of experimental (left) and simulated (right) peak envelope intensities for $[Ru(NCCH_3)_5(DMSO)][BF_4]_2$ (**5**).....63

3.1 Imidazole thione and selone compounds, derivatives, and their biological forms 69

List of Figures (Continued)

Figure Page

3.2 Reported Ru(II) complexes with imidazole-2-thione and -selone ligands (R = alkyl or aryl; E = S or Se) 69

3.3 Crystal structure diagrams of A) $[Ru(MMI)_6]Cl_3$ (**1a**) and B) $[Ru(dmit)_6](BF_4)_2$ (**5**) with 50% probability density ellipsoids. Hydrogen atoms and counterions are omitted for clarity 73

3.4 UV-vis spectra of $[Ru(MMI)_6]Cl_3$ (100 μM) in acetonitrile before and after addition of 2 and 12 equiv H_2O_2 78

3.5 Kinetics of $[Ru(MMI)_6]Cl_3$ with A) 2 equiv and 12 equiv H_2O_2, (0-8000 s) B) The best-fit line fit to the initial linear portion of the kinetic curves for 2 equiv and 12 equiv H_2O_2 (0-100 sec, $R^2 = 0.991$ and $R^2 = 0.99$, respectively) 78

3.6 Gel electrophoresis image of iron-mediated DNA damage prevention by $[Ru(MMI)_6]Cl_3$. Lanes are MW: 1 kb molecular weight marker; lane 1: plasmid DNA (p); lane 2: p + H_2O_2 (50 μM); lane 3: p + 1000 μM $[Ru(MMI)_6]Cl_3$ + H_2O_2; lane 4: p + Fe^{2+} (2 μM) + H_2O_2; lanes 5-14: p + Fe^{2+} + H_2O_2 + 0.001, 0.01, 0.1, 1, 10, 50, 100, 500, and 1000 μM $[Ru(MMI)_6]Cl_3$, respectively 81

3.7 Graph of oxidative DNA damage prevention by $[Ru(MMI)_6]Cl_3$ showing the best-fit dose response curve with a calculated IC_{50} value of 1.76 ± 0.01 μM 81

3.8 X-ray diffraction structure for $[Ru(MMI)_6][BF_4]_2[NO_3]$ (**1b**) with 50% probability density ellipsoids; hydrogen atoms, counterions, and solvent molecules omitted for clarity 92

3.9 ^1H NMR spectrum of unbound methimazole (MMI) in D_2O (δ 4.79) 93

3.10 ^1H NMR spectrum of unbound *N*,*N*'-dimethylimidazole-2-thione (dmit) in D_2O (δ 4.79) 94

List of Figures (Continued)

Figure Page

3.11 ^{1}H NMR spectrum of unbound *N*,*N*'-dimethylimidazole-2-selone (dmise) in D_2O (δ 4.79) 94

3.12 ^{1}H NMR spectrum of $[Ru(MMI)_6][BF_4]_2$(**4**) in D_2O (δ 4.79) 94

3.13 ^{1}H NMR spectrum of $[Ru(dmit)_6][BF_4]_2$ (**5**) in D_2O (δ 4.79) 95

3.14 ^{1}H NMR spectrum of $[Ru(dmise)_6][BF_4]_2$ (**6**) in D_2O (δ 4.79) 95

3.15 ^{1}H NMR spectrum of $Ru(MMI)_4Cl_2$ (**7**) in D_2O (δ 4.79) 95

3.16 ^{1}H NMR spectrum of $Ru\ Cl_2(dmit)_4$ (**8**) in D_2O (δ 4.79) 96

3.17 ^{1}H NMR spectrum of $RuCl_2(dmise)_4$ (**9**) in D_2O (δ 4.79) 96

3.18 Transmittance IR spectrum of $[Ru(MMI)_6]Cl_3$ (**1a**) acquired as a Nujol mull 97

3.19 Transmittance IR spectrum of $[Ru(MMI)_6][BF_4]_2\ [NO_3]$ (**1b**) acquired as a Nujol mull. 97

3.20 Transmittance IR spectrum of $[Ru(dmit)_6]Cl_3$ (**2**) acquired as a Nujol mull. 98

3.21 Transmittance IR spectrum of $[Ru(dmise)_6]Cl_3$ (**3**) acquired as a Nujol mull. 98

3.21 Transmittance IR spectrum of $[Ru(MMI)_6][BF_4]_2$ (**4**) acquired as a Nujol mull 99

List of Figures (Continued)

Figure Page

3.23 Transmittance IR spectrum of $[Ru(dmit)_6][BF_4]_2$ (**5**) acquired as a Nujol mull 99

3.24 Transmittance IR spectrum of $[Ru(dmise)_6][BF_4]_2$ (**6**) acquired as a Nujol mull 100

3.25 Transmittance IR spectrum of $RuCl_2(MMI)_4$ (**7**) acquired as a Nujol mull 100

3.26 Transmittance IR spectrum of $RuCl_2(dmit)_4$ (**8**) acquired as a Nujol mull 101

3.27 Transmittance IR spectrum of $RuCl_2(dmise)_4$ (**9**) acquired as a Nujol mul 101

3.28 MALDI mass spectrum with insets of experimental (left) and simulated (right) envelope intensities for $[Ru(MMI)_6]Cl_3$ (**1a**).....102

3.29 MALDI mass spectrum with insets of experimental (left) and simulated (right) envelope intensities for $[Ru(MMI)_6](BF_4)_2(NO_3)$ (**1b**) 102

3.30 MALDI mass spectrum with insets of experimental (left) and simulated (right) envelope intensities for $[Ru(dmit)_6]Cl_3$ (**2**).....103

3.31 MALDI mass spectrum with insets of experimental (left) and simulated (right) envelope intensities for [Ru(dmise)6]Cl3 **(3)** 103

3.32 MALDI mass spectrum with insets of experimental (left) and simulated (right) envelope intensities for [Ru(MMI)6][BF4]2 **(4)**.....104

3.33 MALDI mass spectrum with insets of experimental (left) and simulated (right) envelope intensities for [Ru(dmit)6][BF4]2 **(5)**.....104

List of Figures (Continued)

Figure Page

3.34 MALDI mass spectrum with insets of experimental (left) and simulated (right) envelope intensities for $[Ru(dmise)_6][BF_4]_2$ (**6**) 105

3.35 MALDI mass spectrum with insets of experimental (left) and simulated (right) envelope intensities for $RuCl_2(MMI)_4$ (**7**) 105

3.36 MALDI mass spectrum with insets of experimental (left) and simulated (right) envelope intensities for $Ru(dmit)_4Cl_2$ (**8**) 106

3.37 MALDI mass spectrum with insets of experimental (left) and simulated (right) envelope intensities for Ru $(dmise)_4Cl_2$ (**9**) 107

3.38 Positive-ion MALDI mass spectrum with insets of experimental (left) and simulated (right) envelope intensities for $[Ru(MMI)_6]Cl_3$ (**1a**) after H_2O_2 addition 107

3.39 Negative-ion MALDI mass spectrum with insets of experimental envelope intensities for $[Ru(MMI)_6]Cl_3$ (**1a**) after H_2O_2 addition. 108

3.40 Positive-ion MALDI mass spectrum with insets of experimental (left) and simulated (right) envelope Intensities for $[Ru(dmit)_6]Cl_3$ (**2**) after H_2O_2 addition 108

3.41 Negative-ion MALDI mass spectrum with insets of experimental envelope intensities for $[Ru(dmit)_6]Cl_3$ (**2**) after H_2O_2 addition. 109

3.42 Positive-ion MALDI mass spectrum with insets of experimental (left) and simulated (right) envelope intensities for $[Ru(dmise)_6]Cl_3$ (**3**) after H_2O_2 addition 109

3.43 Negative-ion MALDI mass spectrum with insets of experimental envelope intensities for $[Ru(dmise)_6]Cl_3$ (**3**) after H_2O_2 addition 110

List of Figures (Continued)

Figure Page

3.44 UV-vis spectra of A) $[Ru(dmit)_6]Cl_3$ and B)$[Ru(dmise)_6]Cl_3$ (100 μM) in acetonitrile before and after addition of 2 and 12equiv H_2O_2 110

3.45 Kinetics curves for [Ru(dmit)6]Cl3 upon treatment with 2 equiv and 12 equiv H2O2, (0-8000 s) and B) the best-fit line fit to the initial linear portion of the kinetic curves with 2 equiv and 12 equiv H2O2 (0-2000 s; R2 = 0.996 and 0.999, respectively) 111

3.46 Kinetics curves for $[Ru(dmise)_6]Cl_3$ upon treatment with A) 2 equiv and 12 equiv H_2O_2, (0-8000 s) and B) the best-fit line fit to the initial linear portion of the kinetic curves with 2 equiv and 12 equiv H_2O_2 (0-100 s; R_2 = 0.994 and 0.995, respectively) 111

4.1 Crystal structure diagrams of $[Ru(NO)(dmit)_4Cl][BF_4]_2$ (**1**) and $Ru(NO)(dmise)_4Cl][BF_4]_2$ (**2**) showing 50% ellipsoids; hydrogen atoms and counterions are omitted for clarity..... 122

4.2 A) Cyclic voltammogram (CV) for $[Ru(dmit)_4Cl(NO)]$ $[BF_4]_2$ (**1**), B) CV for $[Ru(dmise)_4Cl(NO)][BF_4]_2$ (**2**). Samples were prepared with 0.1 mM complex in acetonitrile with tetra-*n*-butyl ammonium phosphate (0.1 M) as the supporting electrolyte..... 126

4.3 MALDI mass spectrum with insets of experimental (left) and simulated (right) envelope intensities for $[Ru(NO)(dmit)_4Cl][BF_4]_2$ (**1**) 133

4.4 MALDI mass spectrum with insets of experimental (left) and simulated (right) envelope intensities for $[Ru(NO)(dmise)_4Cl][BF_4]_2$ (**2**) 134

4.5 MALDI mass spectrum with insets of experimental (left) and simulated (right) envelope intensities for the reaction mixture prior to addition of dmit or dmise..... 134

4.6 Transmittance IR spectrum of $[Ru(NO)(dmit)_4Cl][BF_4]_2$ (**1**) acquired as a Nujol mull..... 136

List of Figures (Continued)

Figure Page

4.7 Transmittance IR spectrum of [Ru (NO)(dmise)$_4$Cl][BF_4]$_2$ (**2**) acquired as a Nujol mull.....136

4.8 ^{1}H NMR spectrum of [Ru(NO)(dmit)$_4$Cl][BF_4]$_2$ (**1**) in D_2O (δ 4.79).....137

4.9 ^{1}H NMR spectrum of [Ru(NO)(dmise)$_4$Cl][BF_4]$_2$ (**2**) in D_2O (δ 4.79).....137

4.10 IR spectrum of reaction mixture prior to dmit or dmise addition acquired as a Nujol mull.....137

LIST OF SCHEMES

Scheme Page

1.1 Organomercury removal from glutathione (GSH) and conversion to HgS nanoparticles (NPs) upon treatment with imidazole thione or selone ligands (bimt or bimse) 21

1.2 Hydrogen transfer by $[(\eta^6\text{-}C_6H_6)RuLCl][PF_6]$ (L= benzoimithione (1) or benzoimiselone (2) in the presence of a hydrogen source (R_1, R_2 = alkyl or aryl) 23

2.1 Syntheses of ruthenium complexes with multiple solvato ligands 34

3.1 Synthesis of Ru-thione and -selone complexes **1**-**9**. All reactions were carried out in a 2:1 ratio of acetonitrile to CH_2Cl_2 71

3.2 Reactivity of $[RuL_6]Cl_3$ with H_2O_2; E = S, L= MMI or dmit; E = Se, L = dmise 80

4.1 Method for forming Ru(II) complexes **1** and **2** in acetonitrile 120

ABREVIATION LIST

ROS = reactive oxygen species

DPPH = 2,2-diphenyl-1-picrylhydrazyl

dmit = N,N'-dimethylimidazole thione

dmise = N,N'-dimethylimidazole selone

mbit = 1,1'-methylenebis(1,3-dihydro-3-methyl-2H-imidazole-2-thione)

mbis = 1,1'-methylenebis(1,3-dihydro-3-methyl-2H-imidazole-2-selone)

ebit = 1,1'-(1,2-ethanediyl)bis(3-methyl-imidazole-2-thione)

ebis = 1,1'-(1,2-ethanediyl)bis(3-methyl-imidazole-2-selone)

Tm^R = tris(1-alkyl-2-mercaptoimidazolyl)hydroborate

bimt = benzimidazole-2-thiolate

Imt = *N*-aryl-imidazole-2-thione

Bmtp = 2,6-bis(1-methylimidazole-2-thione)pyridine

Bbtp = 2,6-bis(1-isopropylimidazole-2-thione)pyridine

Bptp = 2,6-bis(1-tert-butylimidazole-2-thione)pyridine

tmeimt = 2,3-(hydro-l,3,4,5-tetramethyl-2-thíoimidazole)

Rims = 1-R-imidazolidine-2-thione

imdt = 1,3-imidazolidine-2-thione

MeIms = 1-methylimidazolidine-2-thione

bbmimise = meta-phenylene-bis(1-methyl-1H-imidazole-2(3H)-selone

bbmimis = meta-phenylene-bis(1-methyl-1H-imidazole-2(3H)-selone

DNA = deoxyribonucleic acid

CHAPTER ONE

COORDINATION CHEMISTRY, BIOLOGICAL ACTIVITY, AND CATALYIC APPLICATIONS OF IMIDAZOLE THIONE AND SELONE COMPLEXES WITH SECOND- AND THIRD-ROW TRANSITION METAL IONS

1.1. Biological roles of thione and selone compounds

Cysteine, selenocysteine, ergothioneine, and selenoneine are biological sulfur and selenium compounds (Figure 1.1) studied for their antioxidant properties. Cysteine and selenocysteine amino acids play significant roles in protein structure and enzymatic activity.[1-3] The main role of ergothioneine is protection against oxidative damage,[4-11] and *in vitro* studies of selenoneine show it is a potent radical scavenger.[12] Cysteine and selenocysteine contain thiol/selenol functional groups (C-SH/C-SeH), whereas ergothioneine and selenoneine contain thione/selone functional groups (C=S/C=Se). Thiol and selenol compounds have the ability to form disulfide[13] and diselenide[14] bonds that help to control cellular redox balance and play a significant role in enzymatic function. Similar to thiols, imidazole thiones can also form disulfide bonds upon oxidation.[15]

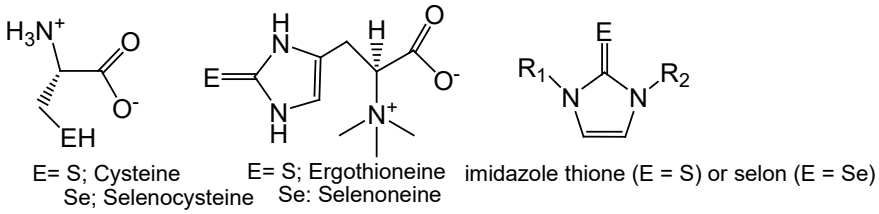

Figure 1.1. Sulfur and selenium compounds discussed in this work (R = alkyl, aryl or H).

Ergothioneine and selenoneine are very effective radical scavengers, and their metal coordination abilities may also contribute to their biological functions. Ergothioneine scavenges reactive oxygen species (ROS), prevents copper-mediated

oxidative deoxyribose damage,[16] and is proposed to bind iron to prevent iron-mediated oxidative damage.[16] Selenoneine has not been studied for prevention of metal-mediated oxidative damage, but it effectively scavenges the 2,2-diphenyl-1-picrylhydroazyl (DPPH) radical, a radical commonly used to mimic biological radical species.[12] Antioxidant activities of imidazole thione and selone compounds are attributed to binding redox-active iron and copper that represent essential biological elements[17-19] to prevent hydroxyl radical generation and metal-mediated DNA damage, hydrogen peroxide scavenging, or scavenging other ROS.[17-24] Brumaghim, *et al.*[24] have examined the antioxidant activities of imidazole thiones and selones as antioxidants to prevent metal-mediated DNA damage *in vitro*.

The discovery of the antioxidant properties of ergothioneine[4-11,16] and selenoneine[12] has prompted significant interest in the analogous thione and selone compounds for antithyroid,[25-27] antioxidant,[20,28] antimicrobial,[29] and antifungal[29] activities. In particular, methimazole (MMI; 2-mercapto-1-methylimidazole) is a widely prescribed antithyroid drug (Figure 1.2; $R_1 = CH_3$, $R_2 = H$)[25-26,30] that prevents oxidative DNA damage as a hydrogen peroxide scavenger.[25-26] Similar imidazole thione and selone compounds have been synthesized with a wide variety of alkyl and aryl substituents (R_1 and R_2; Figure 1.2).[25-29] Many imidazole thione and selone compounds, including methimazole, also have been studied for their ability to coordinate a wide variety of metal ions.[25-30]

Imidazole thione and selone compounds have two resonance forms, neutral and zwitterionic, and the presence of a zwitterionic resonance structure increases their ability to bind metal ions by increasing the negative charge at the S or Se atom (Figure 1.3).[20,31-32]

The energetic contribution of this zwitterionic resonance structure for some imidazole chalcogenides has been examined by X-ray structural analysis of the C=E bond length (E= O, S, Se, Te), and the results of these studies show that the zwitterionic contribution

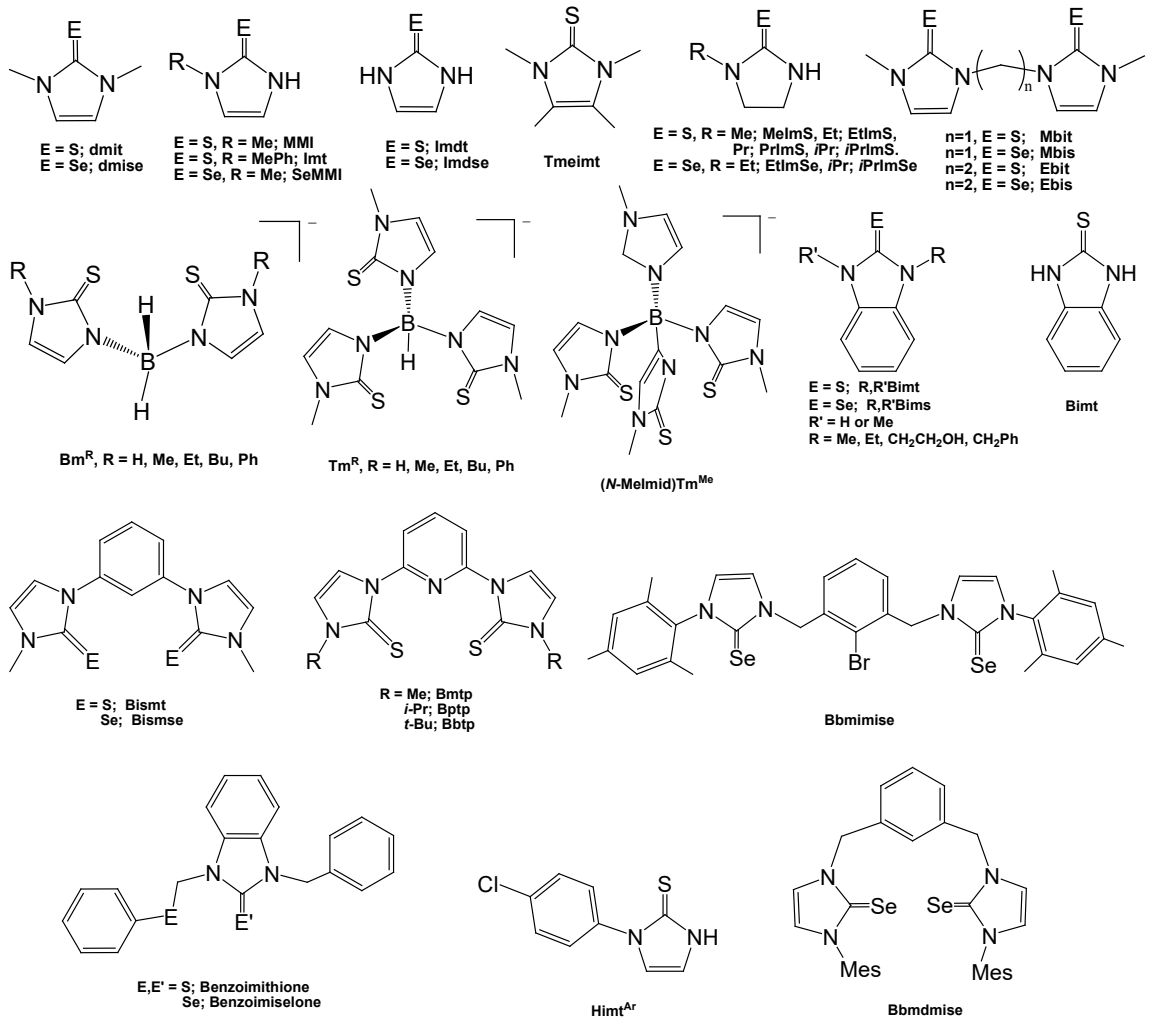

Figure 1.2. Imidazole -thione and selone ligands discussed in this work.

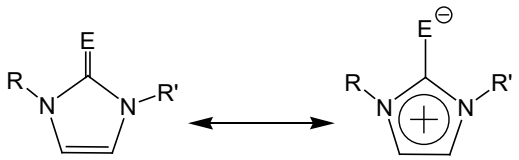

Figure 1.3. Resonance structures of imidazole thione (E = S) and selone (E = Se) compounds (R, R' = aryl, alkyl, or H).

increases with increasing atomic number of the chalcogenide.[31] The C=O bond length is shorter than the thione and selone bond lengths, corresponding to a full double bond, thione and selone compounds have intermediate bond lengths, and the C-Te bond is nearly a single-bond length, indicating dominance of the zwitterionic resonance structure for the tellurium species.[31]

Imidazole thione and selone complexes of late first-row *d*-block metal ions have been extensively studied as described in a review by Stadelman, *et al*.[20] Thione and selone coordination to second- and third-row *d*-block metal ions is also of significant interest, with applications for reducing toxicity of heavy metals,[33-37] catalysis,[38-42] and as antimicrobial[43-45] and antitumor[46-51] complexes. These wide ranging applications invite further exploration of the rich coordination chemistry of these systems; therefore, 2nd and 3rd row *d*-block metal ion complexes with imidazole thione and selone ligands is the focus of this review.

1.2. Coordination chemistry of imidazole thione and selone compounds

Imidazole thione and selone compounds coordinate a variety of metal ions, primarily through the S or Se atoms in monodentate fashion[20] although in some cases, they can also bind as bidentate ligands through an unsubstituted N atom of the imidazole ring (Figure 1.4).[52] The C=S/C=Se moiety of imidazole thione and selone compounds is electron rich as a result of the localization of negative charge on the S/Se atom due to resonance (Figure 1.).[31,53] This, coupled with the large size and polarizable nature of the S/Se atom, gives these ligands soft Lewis basic properties. Since many of the 2nd and 3rd

row *d*-block metal ions are also soft Lewis acids, they form stable complexes with imidazole thione and selone ligands.[54-59]

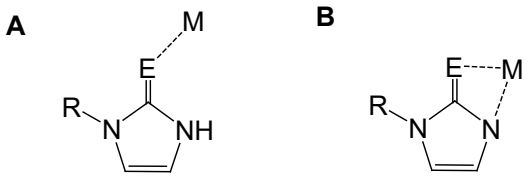

Figure 1.4. A) Monodentate and B) bidentate binding modes of thione (E = S) and selone (E = Se) ligands, where M = metal and R = H, alkyl, or aryl group.

Imidazole thione complexes. Imidazole thione complexes are reported for all of the 2nd row *d*-block metals in a variety of oxidation states: Y(III),[57] Zr(IV),[60-61] Nb(II),[62] Mo(0),[63] Tc(V),[64] Ru(II)/(III),[38,65-66] Rh(II)/(III),[65,69-70] Pd(II),[53,65] and Ag(I),[67] and Cd(II)[77]. Similarly, imidazole thione complexes of the 3rd row *d*-block metals include Hf(IV),[60] Ta(II),[62] W(0),[63] Re(IV),[64] Os(II),[66] Ir(III),[69-70] Pt(II)/(III),[50,53] Au(I/III),[71-72] and Hg(II).[55] Complexes with imidazole selone ligands are less common, and are reported for late 2nd row *d*-block metal ions, including Ru(II)/(III),[31] Rh(II)/(III),[31,69] Pd(II),[53,60] Ag(I),[31] and Cd(II).[68] Similar to 2nd row *d*-block complexes, imidazole selone complexes are only reported for the late 3rd row *d*-block metal ions Re(II),[31] Os(II),[31] Ir(0),[31] Pt(II),[48-49,53] Au(III),[53] and Hg(II).[55]

A wide variety of imidazole thione- and selone-containing ligands have been synthesized, but only a selection of the imidazole thione and selone ligands found in 2nd and 3rd row *d*-block metal complexes (Figure 1.2) are discussed in this review. The majority of these types of ligands are monodentate thiones or selones that bind through the sulfur or selenium atom. Bidentate ligands are typically synthesized by linking imidazole thione or selone moieties through alkyl, aryl, or borohydride groups. Bidentate

benzoimithione/benzoimiselone ligands combine a thione/selone moiety with a thio- or selenoether group in a mixed functionality ligand (Figure 1.2).

Tridentate ligands can be mixed donor, such as the N,S,S-donor ligands bmtp, bptp, and bbtp (Figure 1.2), where two *N*-substituted thione groups are linked through a pyridine bridge.[69] In addition, three thione or selone groups can be linked through a borohydride moiety to yield ligands such as hydrotris(methimazolyl)borate (Tm^{Me}).[65] These ligands are similar to the widely used hydrotris(pyrazolyl)borate (Tp) ligands, but replace the harder nitrogen atom donors with soft sulfur donors. In this review, complexes with similar imidazole thione and selone ligands are discussed based on the order of the metal ions in the periodic table. The complexes discussed do not represent all of the reported imidazole thione and selone complexes, but rather have been selected to highlight the variety of imidazole thione and selone complexes with 2nd and 3rd row *d*-block metal ions. For the selected complexes, M-S/Se and C=S/C=Se bond lengths are presented and mostly compared to those of the unbound ligands, since these bond lengths are most diagnostic of the degree of electronic delocalization on the imidazole ring upon coordination (Figure 1.3).

Hydrotris(imidazole thione)borate ligands such as Tm^{Me} and its derivatives (Tm^{Et}, Tm^{Bu}, and Tm^{Ph}; Figure 1.2) have been used to synthesize complexes with the majority of the 2nd and 3rd row *d*-block metal ions.[60] The Zr(IV) and Hf(IV) complexes $Cp(Tm^{Me})ZrCl_2$ (Cp = cyclopentadienyl) and $Tm^{Bu}Hf(CH_2Ph)_3$ have been structurally characterized (Figure 1.5),[61] and have Zr-S bond lengths in the range 2.66(11)-2.76(11) Å, in the middle of the range for most Cp-Zr-S complexes (2.46(11)-2.83(11) Å[69]). The Hf-

S bond length is 2.631(3) Å. The range of C=S bond lengths in these Zr complexes is 1.71(4)- 1.73(4) Å, and for the Hf complex, the C=S bond length is 1.728(11) Å. These values are approximately the same as the C=S bond length in unbound Tm^{Me} (1.69(4) Å).[60] The Nb(V)

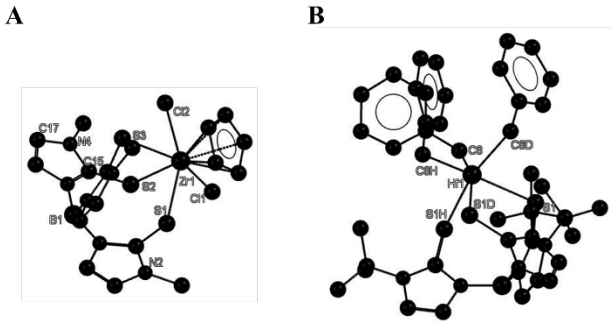

Figure 1.5. Molecular drawing from crystallographic data of A) $Cp(Tm^{Me})ZrCl_2$ and B) $Tm^{Bu}Hf(CH_2Ph)_3$.[61] Hydrogen atoms are omitted for clarity.

and Ta(V) complexes $Tm^{Me}M(=NR)Cl_2$ (R = 2,6-^{i}Pr$_2$C$_6$H$_3$; Figure 1.6)[62] have Nb-S and Ta-S bond lengths of 2.5446(14) and 2.725(3) Å, respectively. Similar to the Tm^{Me} complexes of Zr(IV) and Hf(IV), C=S bond lengths for these Nb and Ta complexes are 1.75(3) and 1.76(3) Å, respectively, relatively unchanged compared to unbound Tm^{Me}.[62]

Several homoleptic sandwich complexes of Ru(III), Rh(III), Pd(II) and Cd(II) with the tridentate (*N*-MeImid)Tm^{Me} (*N*-MeImid = *N*-methylimidazolium; Figure 1.2) thione ligand have been synthesized (Figure 1.7). The sandwich complexes $[\{\kappa^3\text{-}(N\text{-MeImid})Tm^{Me}\}_2Ru]^{3+}$ and $[\{\kappa^3\text{-}(N\text{-MeImid})Tm^{Me}\}_2Rh]^{3+}$ have M-S bond lengths of 2.374(4) and 2.453(10) Å, respectively, with C=S bond lengths of 1.720(4) and 1.731(19)Å, respectively.[65] Similarly, the structure of $[\kappa^2\text{-}(N{\equiv}C)Tm^{Me}]_2Pd$[65] (Figure 1.8) has a range of 2.333(11)-2.338(11) Å for the Pd-S bond lengths, with C=S bonds ranging from 1.721(4) to 1.725(5)Å.[65] No significant differences in C=S bond lengths are observed

for the Ru(III) and Rh(III) complexes of κ^3-(*N*-MeImid)Tm^{Me} and the Pd(II) complex of κ^2-(N≡C)Tm^{Me} compared to their respective unbound ligands.

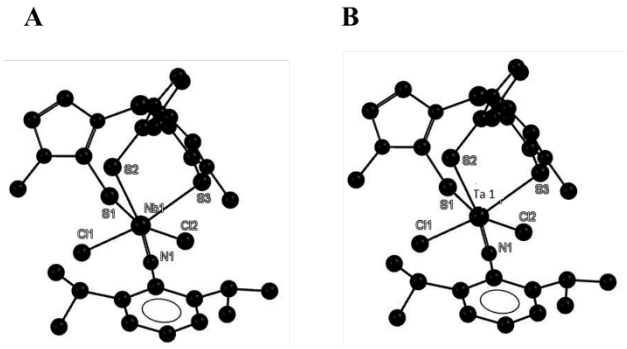

Figure 1.6. Molecular drawing from crystallographic data of A) $Tm^{Me}Nb(=NR)Cl_2$ and B) $Tm^{Me}Ta(=NR)Cl_2$.[62] Hydrogen atoms are omitted for clarity.

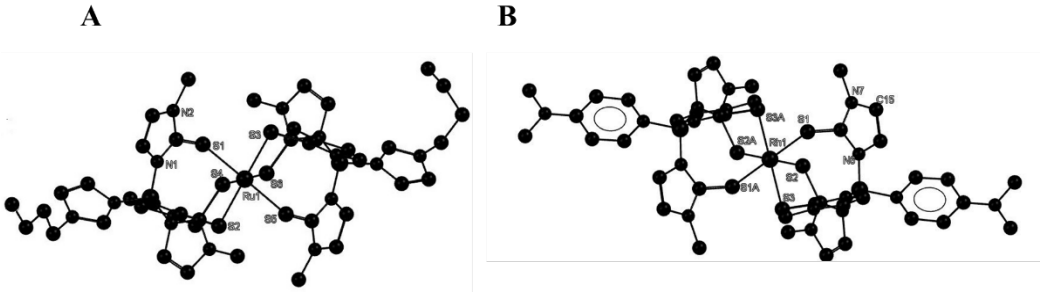

Figure 1.7. Molecular drawing from crystallographic data of A) [κ^3-(*N*-MeImid)Tm^{Me}]$_2$Ru and B) [κ^3-(*N*-MeImid)Tm^{Me}]$_2$Rh.[65] Hydrogen atoms, solvent, and counterions are omitted for clarity.

In general, ruthenium complexes are investigated for a wide range applications, especially in biology and catalysis, due to favorable ligand exchange rates, the range of accessible oxidation states (+2, +3, and +4), and ability of ruthenium ions to mimic iron,[73] In addition, ruthenium complexes are widely used as catalysts to catalyze very important reactions such as hydrogen transfer reaction, and organic polymerization.[38]

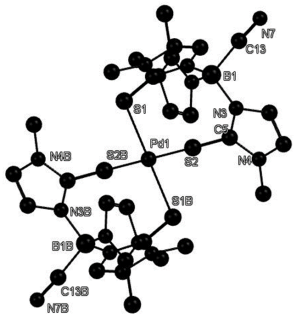

Figure 1.8. Molecular drawing from crystallographic data of $[\kappa^2\text{-}(N{\equiv}C)Tm^{Me}]_2Pd$.[65] Hydrogen atoms are omitted for clarity.

The Bm^{Me} ligand, with a borohydride linking two imidazole thione groups (Figure 1.2), was used to synthesize *fac*-$Tm^{Me}Tc(CO)_3$ and *fac*-$Tm^{Me}Re(CO)_2(ImzH)$ (ImzH = imidazole; Figure 1.9).[64] Similar Ru(II) and Os(II) complexes κ^2-$Bm^{Me}Ru(CO)(PPh_3)H$ and κ^2-$Bm^{Me}Os(CO)(PPh_3)H$ also have been reported (Figure 1.10).[66] In these complexes, Tc-S and Re-S bond lengths are 2.51(11) and 2.53(4) Å, respectively[64] longer than the Ru-S and Os-S bond lengths of 2.401(5) and 2.461(11) Å, respectively.[66] In all of these complexes, there are no significant differences in the C=S bond lengths (1.70(2)-1.73(4) Å).[64,66]

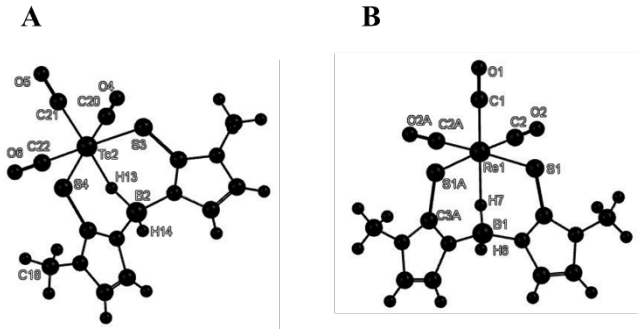

Figure 1.9. Molecular drawing from crystallographic data of A) *fac*-Tc(k^2Tm^{Me})$(CO)_3$ and B) *fac*-Re(Tm^{Me})$(CO)_3$.[64]

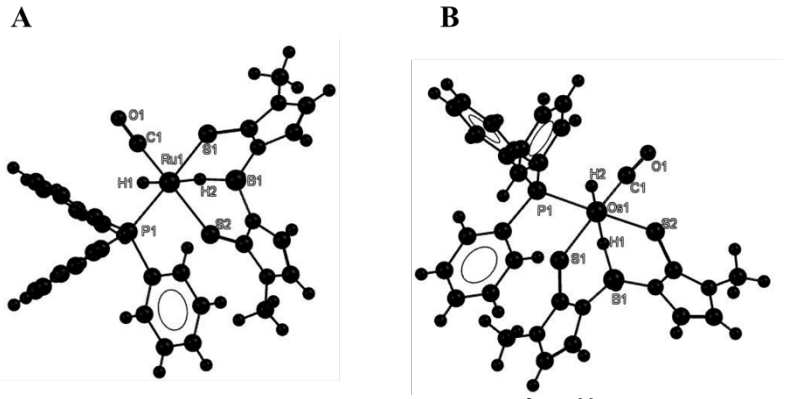

Figure 1.10. Molecular drawing from crystallographic data of A) κ^2-$Bm^{Me}Ru(CO)(PPh_3)H$, and B) κ^2-$Bm^{Me}Os(CO)(PPh_3)H$.[66]

Many complexes with monodentate imidazole thione ligands such as MMI, dmit, imdt, bimt, and $himt^{Ar}$ and bidentate imidazole thione ligands such as tmeimt, mbit, ebit, and bismt (Figure 1.2) have been synthesized with most of the 2nd and 3rd row *d*-block metal ions. In an interesting ligand exchange reaction, treating Cp_3Y with benzimidazole-2-thiolate (bimt) forms the Y(III) complex (κ^2-*S*,*N*-bimt)$_3$Y(THF)$_2$ (THF = tetrahydrofuran; Figure 1.11), where bmit protons are lost to the Cp ligands and deprotonated bimt binds as a bidentate ligand. In this complex, the Y-S bond length is 2.996(6) Å, the longest of all the imidazole thione M-S bonds with 2nd row *d*-block metal ions. The Y-N bond length is 2.361(6) Å, and the C=S bond length is 1.706(5) Å, with C1-S1-Y1, C8-S2-Y1, and C15-S3-Y1 angles of (κ^2-*S*,*N*-bimt)$_3$Y(THF)$_2$ and 73.88(18), 77.0(2), and 76.53(16)°, respectively, and N1-Y1-S2 and N5-Y1-S2 angles of 91.5(2) and 162.20(9)°, respectively.[57]

The tetramethylated imidazole thione, tmiemt (Figure 1.2), coordinates Mo(0) and W(0) to yield M(tmeimt)$(CO)_5$ complexes (Figure 1.12). Mo-S and W-S bonds lengths are very similar at 2.610(11) and 2.614(14) Å, respectively, but the C=S bond lengths are

somewhat different at 1.719(2) and 1.731(5) Å, respectively.[65] Both C=S bonds are longer than the C=S bond of unbound tmiemt (1.69(2) Å),[65] and the longer C=S bonds in these low-valent Mo and W complexes suggest backbonding into the π* orbital of the C=S bond.

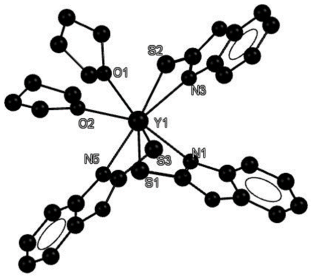

Figure 1.11. Molecular drawing from crystallographic data of (κ^2-*S*,*N*-bimt)$_3$Y(THF)$_2$.[57] Hydrogen atoms are omitted for clarity.

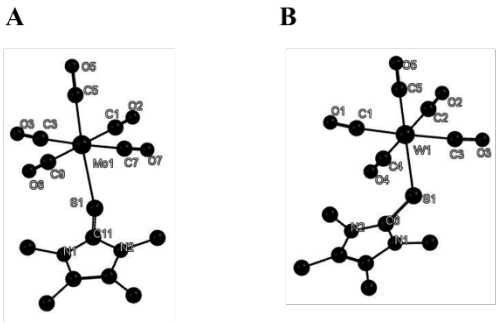

Figure 1.12. Molecular drawing from crystallographic data of A) [Mo(tmeimt)(CO)$_5$ and B) W(tmeimt)(CO)$_5$.[63] Hydrogen atoms are omitted for clarity.

As can be inferred from the structures in Figure 1.2, thione ligands with aryl substituents are less common than those with alkyl substituents. An example of a Ru(II) complex bound to an *N*-aryl-imidazole-2-thione is *cis*-Ru(imt)$_2$(PPh$_3$)$_2$Cl$_2$ (Figure 1.13).[57] The structure of this complex has a Ru-S bond length of 2.478(1) Å,[57] somewhat longer than the Ru-S bond length in κ^2-Bm^{Me}Ru(CO)(PPh$_3$)H (2.401(5) Å).[66]

A series of half-sandwich Rh(III) and Ir(III) complexes with bmtp, bbtp, and bptp ligands were synthesized by Jia, *et al.*,[69] with representative structures of the

[CpM(bmtp)]Cl_2 complexes shown in Figure 1.14. The range of Rh-S bond lengths is 2.3829(12) to 2.3866(14) Å, not significantly different from Ir-S bond lengths that range from 2.3850(19) to 2.3870(16) Å. The C=S bond lengths are little varied among different thione ligands and metal ions, with a range of 1.684(4)-1.687(4) Å for the Rh complexes and 1.696(5)-1.707(4) Å for the Ir complexes.[69]

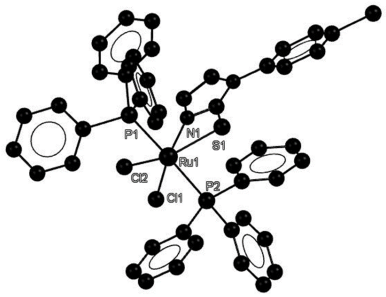

Figure 1.13. Molecular drawing from crystallographic data of *cis*-Ru(imt^{Ph})$_2$(PPh_3)$_2$$Cl_2$.[57] Hydrogen atoms are omitted for clarity.

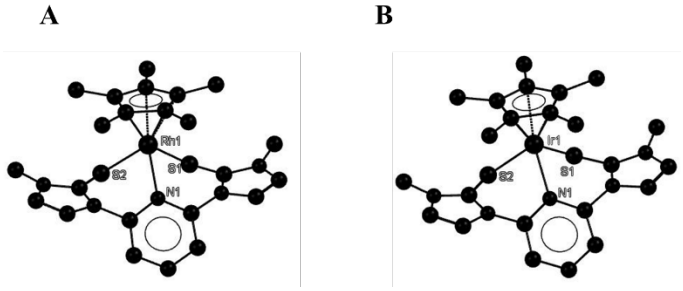

Figure 1.14. Molecular drawing from crystallographic data of A) [CpRh(bmtp)]Cl_2[69] and B) [CpIr(bmtp)]Cl_2.[69] Hydrogen atoms and counterions are omitted for clarity.

IR studies of imidazole thione complexes are not common, but thione bonding in the $[CpM(bmtp)]^{2+}$ complexes was also investigated to determine the effects of metal binding on the C=S stretch. These IR data show a 15-17 cm^{-1} shift to higher energy for the C=S bonds in Rh- or Ir-bound bmtp and bbtp ligands compared to the unbound ligands, but the C=S stretching bands for analogous bptp complexes show no significant shifts

compared to that of free ligand (Table 1.1).[69] The IR data indicate that these imidazole thione ligands are primarily σ and π donors, and that backbonding is minimal. Similar trends were observed for the C=S stretches of the $[Cp^*MLCl]^+$ (L = mbit and ebit) complexes with shifts in the 10-16 cm^{-1} range compared to unbound ligands.[70]

The same bmtp, bbtp, and bptp ligands were also used to synthesize the Au(III) complexes $[AuLCl_2]Cl$ (Figure 1.15).[71] Only $[Au(bptp)Cl_2]Cl$ was structurally characterized, with Au-S bond lengths ranging from 2.340(5) - 2.332(4) Å and C=S bonds lengths ranging from 1.68 (2)-1.726(17) Å,[71] compared to the C-S bond length for unbound bptp (1.6836(10)) Å.[69] The differences in C=S bond lengths for $[Au(bptp)Cl_2]Cl$ (0.046 Å) is greater than for analogous Rh(III) and Ir(III) complexes (0.003 and 0.009 Å, respectively).

Table 1.1. C=S/C=Se infrared stretching bands for thione and selone ligands; ligand structures are shown in Figure 1.2.

Metal complex	C=S/C=Se Band (cm^{-1})	Change from Unbound Ligand (cm^{-1})	Ref.
$[CpRh(bmtp)]Cl_2$	1158	15	69
$[CpIr(bmtp)]Cl_2$	1158	15	69
$[CpRh(bptp)]Cl_2$	1157	4	69
$[CpIr(bptp)]Cl_2$	1155	2	69
$[CpRh(bbtp)]Cl_2$	1153	16	69
$[CpIr(bbtp)]Cl_2$	1154	17	69
$[Cp^*Ir(mbit)Cl]Cl$	1171	10	70
$[Cp^*Ir(mbis)Cl]Cl$	1150	22	70
$[Cp^*Ir(ebit)Cl]Cl$	1150	14	70
$[Cp^*Ir(ebis)Cl]Cl$	1146	20	70
$[Cp^*Rh(mbit)Cl]Cl$	1177	16	70
$[Cp^*Rh(mbis)Cl][Cp^*RhCl_3]$	1152	24	70
$[Cp^*Rh(ebit)Cl]Cl$	1149	13	70
$[Cp^*Rh(ebis)Cl]Cl$	1145	19	70

Trans-$[Pt(NH_3)_2(dmit)_2](NO_3)_2$ was synthesized by Jomaa, *et al*. (Figure 1.16).[50] The bond length of Pt-S is 2.313(4) Å and the C-S bond length is 1.731(5) Å (Figure 1.16).[50]

The Pt-S bond length in *trans*-$[Pt(NH_3)_2(Hims)_2][NO_3]_2$ (Hims = imidazolidine-2-thione) is 2.3260(9) Å, that is in the average of Pt-S bond length values for the similar platinum complexes.[74]

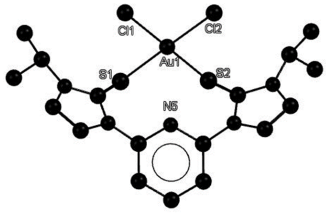

Figure 1.15. Molecular drawing from crystallographic data of $[Au(bptp)Cl_2]Cl$.[71] Hydrogen atoms and counterions are omitted for clarity.

Platinum complexes have been extremely well-investigated due to the antitumor activity of cisplatin and its clinical use in treating cancer. Platinum complexes with imidazole thione and selone ligands have been specifically examined for their antitumor and antimicrobial activity, as discussed later in the applications sections of this review. Similar to cisplatin (*cis*-$Pt(NH_3)_2Cl_2$), *trans*-$[Pt(NH_3)_2(Hims)_2][NO_3]_2$ has been investigated for its anticancer properties, with two Hims ligands replacing the Cl^- leaving group ligands on cisplatin.[50]

Silver(I) is the most well-studied 2nd row *d*-block metal with imidazole thione ligands.[67,75-76] For example, the structure of dinuclear $[Ag_2(\mu\text{-imdt})_2(imdt)_2(PPh_3)_2][NO_3]_2$ (imdt = 1,3-imidazolidine-2-thione; Figure 1.16) has Ag-S bond lengths for the bridging imdt ligands of 2.5674(5) and 2.8120(5) Å, 0.04 and 0.29 Å longer, respectively, than the Ag-S bond length for the monodentate imdt ligand (2.5276(5) Å).[67] There is no significant change in the C=S bond length for bridging and non-bridging imdt ligands (1.711(2) and 1.712(2) Å, respectively).[67]

$[Cd(MeIms)_4][BPh_4]_2$ is an example of a Cd(II) complex with imidazole thione ligands that was reported by Dean *et al.* (Figure 1.16).[77] Its structure shows Cd-S bond lengths ranging from 2.516(1)-2.563(1) Å, similar to the Ag-S bond lengths of 2.5674(5) and 2.5120(5) Å in $[Ag_2(\mu\text{-imdt})_2(imdt)_2(PPh_3)_2][NO_3]_2$[67] and longer than the Pt-S bond length in *trans*-$[Pt(NH_3)_2(dmit)_2](NO_3)_2$ 2.313(4) Å[74]. The structure of the Hg(II) complex $Hg(Me,CH_2CH_2OH\text{-bimt})Cl_2$ has a Hg-S bond length of 2.511(4) Å (Figure 1.17).[36] The

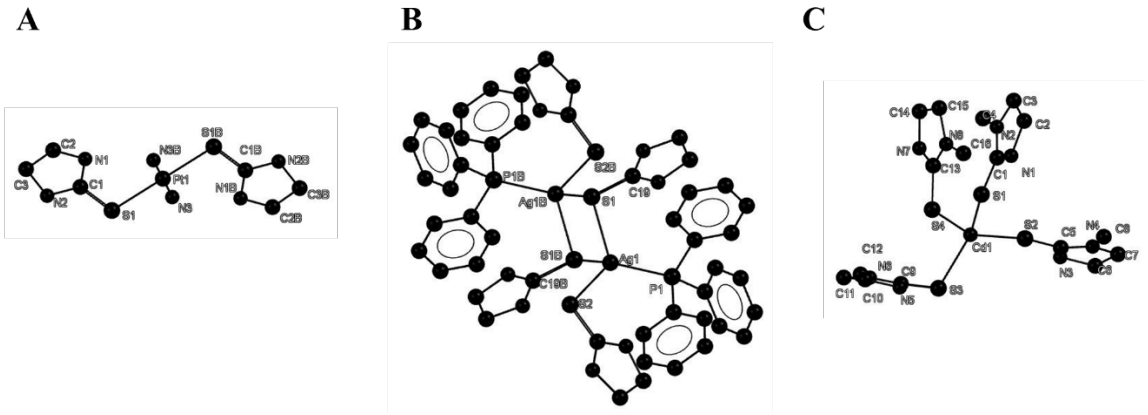

Figure 1.16. Molecular drawing from crystallographic data of A) *trans*-$[Pt(NH_3)_2(Hims)_2][NO_3]$,[50] B) $[Ag_2(\mu\text{-imdt})_2(imdt)_2(PPh_3)_2][NO_3]_2$[67] and C) $[Cd(MeIms)_4][BPh_4]_2$.[77] Hydrogen atoms and counterions are omitted for clarity.

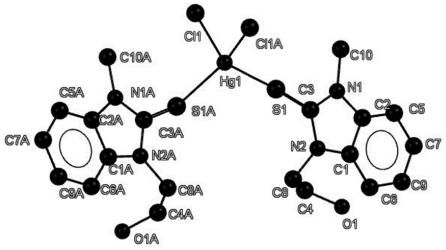

Figure 1.17. Molecular drawing from crystallographic data of $Hg(Me,CH_2CH_2OH\text{-bimt})Cl_2$.[36] Hydrogen atoms are omitted for clarity.

ability of this bimt-derivative ligand (Figure 1.2) to detoxify organomercurial compounds through ligand exchange reactions is discussed in the *heavy metal detoxification* section of this review.

Imidazole selone complexes. Imidazole selone complexes with 2nd and 3rd row *d*-block metal ions are much less studied than their thione counterparts, and only a few publications describe these types of complexes.[38,53,68,70,72,78,81-83] For example, [Cp*Rh(mbis)Cl]Cl,[69] [Cp*Ir(mbis)Cl]Cl,[69] $Au_2(C_6F_5)_2$(mbis),[71] and $Au_2(C_6F_5)_6$(ebis)[72] have been synthesized and structurally characterized (Figure 1.18). The Rh-Se bond in [Cp*Rh(mbis)Cl]Cl[70] (2.528(1) Å) is slightly longer than the Ir-Se bond in [Cp*Ir(mbis)Cl]Cl[70] (2.505(1) Å), and the Au(I)-Se bond in $Au_2(C_6F_5)_2$(mbis)[72] length is shorter than 2.4263(5) Å and Au(III)-Se are and 2.4607(6) Å, respectively. In addition, the range of the C=Se bonds lengths in these four complexes above are 1.867(6)-1.894(4) Å.[70,72]

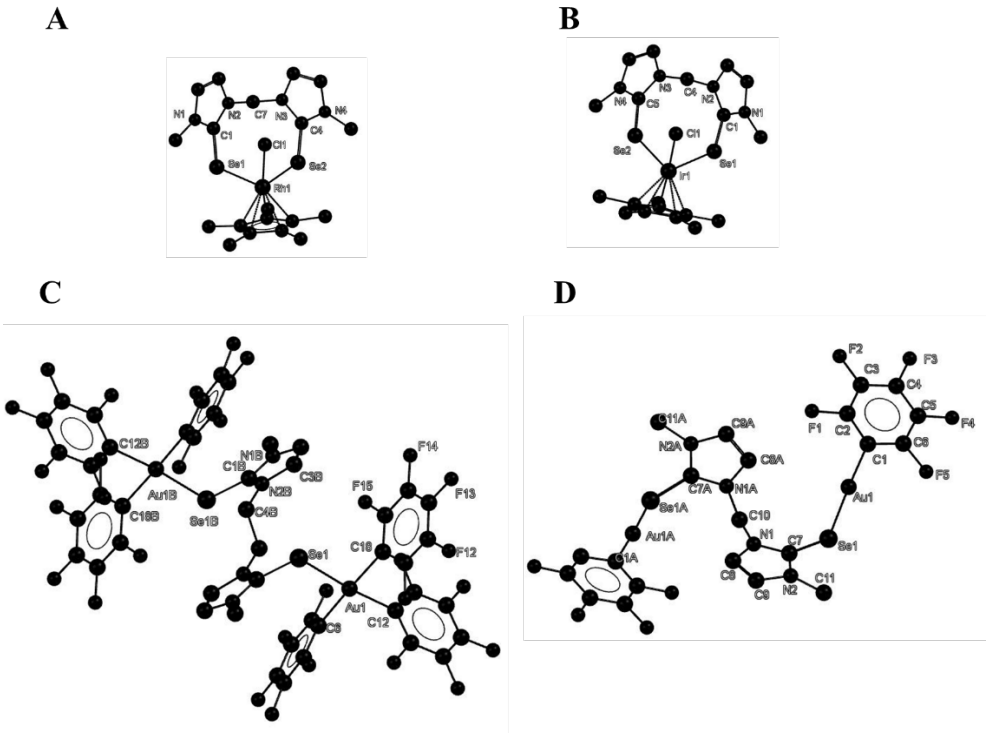

Figure 1.18. Molecular drawing from crystallographic data of A) [Cp*Rh(mbis)Cl]Cl,[70] B) [Cp*Ir(mbis)Cl]Cl,[70] C) Au_2(mbis)$(C_6F_5)_6$,[72] and D) Au_2(ebis)$(C_6F_5)_2$.[72] Hydrogen atoms and counterions are omitted for clarity.

Dinuclear Pd(II) and Pt(II) complexes $(bbmimise)_2Pd_2Cl_4$ and $(bbmimise)_2Pt_2Cl_4$ complexes (Figure 1.19) are analogous dinuclear complexes where the metal ions are bridged by two bidentate bbmimise ligands. In $(bbmimise)_2Pd_2Cl_4$, Pd-Se bond lengths range from 2.4329(8)-2.4414(8)Å and C-Se bond lengths range from 1.870(7)-1.882(6) Å).[53] In the analogous $(bbmimise)_2Pt_2Cl_4$, the Pt-Se bond lengths range from 2.415(3)-2.431(3)Å and C-Se bond lengths range from 1.870(2)-1.890(2) Å.[53] The Pt-Se bonds are slightly shorter than the Pd-Se bonds, whereas the C-Se bond length similar for both complexes.[53]

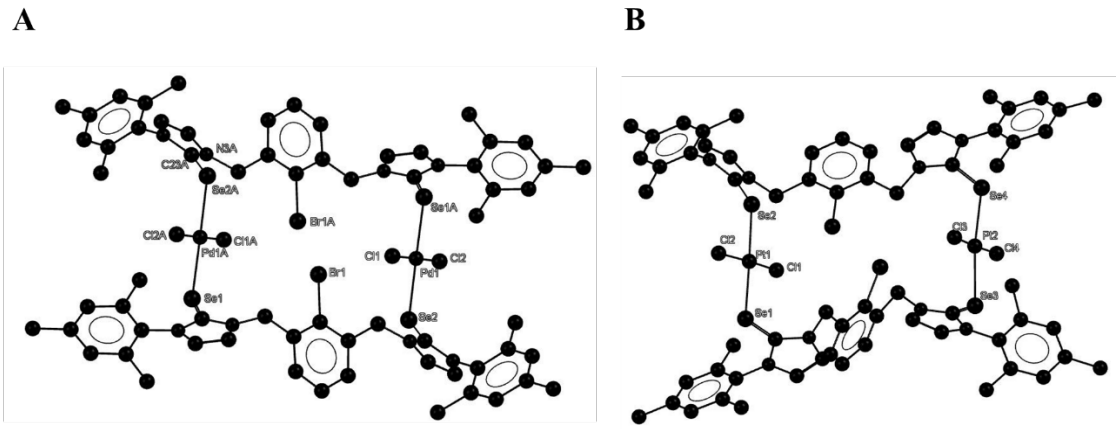

Figure 1.19. Molecular drawing from crystallographic data of A) $(bmimise)_2Pd_2Cl_4$ and B) $(bbmimise)_2Pt_2Cl_4$.[53] Hydrogen atoms are omitted for clarity.

In addition, the dmise ligand has been used to synthesize Cd(II) complex.[68] The structure of $[Cd(dmise)_4][PF_6]_2$ (Figure 1.20) shows a Cd-Se bond length of 2.609(2) Å and a C-Se bond length of 1.852(10) Å.[68] Due to the high affinity of selenium ligands for Cd(II), understanding the bonding in this complex allows researchers to explore the possibility of using imidazole selone ligands to reduce cadmium toxicity.[68]

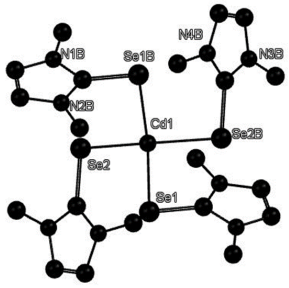

Figure 1.20. Molecular drawing from crystallographic data of $[Cd(dmise)_4][PF_6]_2$.[68] Hydrogen atoms and counterions are omitted for clarity.

All the thione and selone complexes with 2nd and 3rd row *d*-block metals that have been discussed in this Chapter gave fairly consistent M-S or M-Se bond lengths based on the identity of the metal ion. In addition, the C=S and C=Se bond length values of the bound imidazole thione or selone ligands are generally the same as for the unbound ligands. Notable exceptions to this trend are the very low-valent $M(tmeimt)(CO)_5$ (Mo and W) complexes with C=S bond lengths slightly longer than that of the tmeimt ligand.[65] The infrared spectroscopy of these metal complexes with imidazole thione and selone ligands has not been investigated deeply, except for the complexes shown in Table 1.1. Given the differences in C=S or C=Se stretches between complexes, this remains an interesting area for investigation. In addition, studies reporting the coordination chemistry of imidazole selone ligands are sparse, with much room for additional work in this area.

1.3. Applications of imidazole thione and selone complexes

Imidazole thione complexes with 2nd and 3rd row *d*-block metal ions have a wide range of applications in both biological and materials directions. Although imidazole selone complexes of these metals have received less attention than their thione

counterparts, their biological activity and ability to prevent metal toxicity also have been explored.[34-36,42,86] This review focuses on the four major applications for these complexes: as antitumor agents, as antimicrobial agents, as complexes that ameliorate heavy-metal toxicity, and as catalysts.

Antitumor activity. Since the discovery of cisplatin, *cis*-$Pt(NH_3)_2Cl_2$, in the 1960s[85] and its current clinical use in chemotherapy,[86] developing cisplatin analogs with 2nd and 3rd row *d*-block metal complexes has been a major focus of bioinorganic chemical research.[87-88] Cisplatin's toxicity and narrow effective concentration range for antitumor activity significantly limit use of this chemotherapeutic drug.[87-88] Thus, researchers are developing cisplatin analogs with lower toxicity and higher efficacy for killing various cancer cell lines.[87-88] Several cisplatin analogs with M-S[63,69,71,75] and M-Se[49-50,89] bonds have been synthesized and investigated for their antitumor activities, including complexes that contain imidazole thione[47,50,74,90] and selone[48-49] ligands.

The antitumor activity of cisplatin and analogous complexes depends on dissociation of the chloride or other, non-amine ligands and their replacement by water molecules that facilitates metal binding to the aromatic N7 position of guanine and adenine bases in DNA.[91] Because of this tendency for ligand exchange, one disadvantage of cisplatin and analog complexes is binding to proteins in the blood through the sulfur atoms of cysteine residues.[87-88,91] Including imidazole thione and selone ligands in the coordination sphere of the Pt complexes may reduce undesirable binding due to thione and selone similarity to and competition with biological sulfur and selenium ligands such as cysteine, ergothioneine, and selenoneine.[92]

Most cisplatin analogs with imidazole thione[47,50,74,90] and selone[48-49] ligands effectively kill cancer cells based as measured by the concentration of complex required to kill 50% of cells (EC_{50} value). For example, *cis*-$[Pt(PEt_3)_2L_2]Cl_2$ (L = imt, imt^{Me}, imt^{Me2}, imt^{Et2}) complexes have been tested for their *in vitro* cytotoxic effects against human cervical (HeLa), breast (MCF-7), lung (A549), and colon (HTC15) cancer cell lines. All of these Pt(II)-thione complexes show enhanced cytotoxicity (EC_{50} values of 1.4-16 μM) compared to the currently used drugs cisplatin (EC_{50} values of 19-42 μM) and carboplatin (EC_{50} values of 56-71 μM), Table 1.2.[74]

Table 1.2. EC_{50} values for cisplatin, carboplatin, and Pt-thione[74] and -selone[48] complexes in human cancer cell lines.

Compound	EC_{50} values (μM)				
	HeLa	**A549**	**MCF7**	**HCT15**	**MDA-231**
Cisplatin, $Pt(NH_3)_2Cl_2$	19 ± 2	42 ± 1	22 ± 1	30 ± 2	–
Carboplatin	56 ± 2	71 ± 3	56 ± 3	64 ± 2	–
cis-$[Pt(PEt_3)_2(imt)_2]Cl_2$	1.4 ± 0.3	3.5 ± 0.7	5 ± 1	7 ± 1	–
cis-$[Pt(PEt_3)_2(imt^{Me})_2]Cl_2$	1.8 ± 0.3	3.9 ± 0.5	2.6 ± 0.9	8.6 ± 0.9	–
cis-$[Pt(PEt_3)_2(imt^{Me2})_2]Cl_2$	1.5 ± 0.2	2.4 ± 0.3	3.8 ± 0.6	4.2 ± 0.7	–
cis-$[Pt(PEt_3)_2(imt^{Et2})_2]Cl_2$	10 ± 2	13 ± 1	14 ± 1	16 ± 1	–
Cisplatin	3.6 ± 0.3	–	–	–	6.3 ± 0.1
trans-$[Pt(NH_3)_2(ims^{Et})_2][NO_3]_2$	2.1 ± 0.2	–	–	–	4.4 ± 0.2
trans-$[Pt(NH_3)_2(ims^{iPr})_2][NO_3]_2$	3.1 ± 0.3	–	–	–	5.7 ± 0.2

Pt(II) complexes with imidazole selone ligands also have been studied as antitumor agents by Alhoshani *et al*.[48] Cytotoxicity of *trans*-$[Pt(NH_3)_2L_2][NO_3]_2$ (L = EtImse and *i*PrImse) complexes were studied in cervical (HeLa) and breast cancer (MDA-231) cell lines, and both Pt-selone complexes are more effective than cisplatin (Table 1.2).[48] Thus, in these two studies, the Pt(II) complexes with imidazole thione and selone ligands show between 5-18 times greater activity for killing cancer cells than cisplatin. The high activity

of these Pt(II)-imidazole thione complexes is promising, and the next step will be testing these complexes *in vivo* to assess toxicity and to compare these results to cisplatin.

Antimicrobial activity. Emerging new infectious diseases and the increasing number of multi-drug resistant microbial pathogens are challenging problems,[93] and developing new antimicrobial agents is of critical importance. Although only a few complexes have been investigated for their antimicrobial properties, imidazole thione and selone complexes of Pd(II), Ag(I) and Cd(II) show promising antimicrobial activities.[37,43-44,67,84,93] For example, the activity of $[Pd(imt)_4]I_2$ was tested against two gram positive (*S. aureus*, and *B. subtilis*) and two gram negative (*E. coli*, and *P. aeruginosa)* strains and compared to the activity of Imipenem.[93] The synthesized complex $[Pd(HIms)_4]I_2$ exhibit fair activity compared to antibiotic control, the authors used Petra/Osiris/Molinspiration (POM) analysis to predict the biological activities of these complexes by determining the relationships between their steric/electrostatic properties and observed biological activity with pharmacophore groups.[93] These relationships help model potential ligand-receptor interactions and indicate that ligands with C=S groups have potential antimicrobial behavior.[93]

Heavy metal detoxification. Organomercury compounds, including methylmercury ($MeHg^+$), are very highly toxic[34-36,84] and have negative environmental effects.[34-36] Toxicity of organomercurials is an ongoing problem, since anthropological activities such as industrial processes have increased environmental mercury levels.[35] Methylmercury ($MeHg^+$) toxicity is due to its lipophilic properties and its high affinity for coordinating biological sulfur- and selenium-containing ligands, such as cystine, selenocysteine, and

methionine in proteins.[36] Synthesis and characterization of mercury imidazole thione and selone complexes and examination of their reactivity is vital to understanding the biological effects of mercury and to developing new methods to detoxify methylmercury and other organomercury species.[34]

A few heterocyclic thione and selone mercury complexes have been synthesized and their reactivities examined to provide insight into mercury detoxification in biological systems.[34-36,84] Ligand exchange reactions with mercury or its complexes can be a promising solution to remove mercury from biomolecules. Since imidazole thione and selone compounds have high affinity for mercury coordination, they have been used to explore these ligand exchange reactions with organomercurials.[36] In one example reported by Roy, *et al.*,[36] benzimidazole thione and selone ligands (R,R'-bimt and R,R'-bimse, respectively, with R = Me, R' = CH_2CH_2OH) preferentially coordinate glutathione-bound $MeHg^+$ in a 1:1 ratio. Bimt/bimse-Hg binding generates a partial positive charge on the carbon atom of the C=S/C=Se group, leading to loss of S/Se from the imidazole ring and conversion of $MeHg^+$ to less toxic and water-soluble HgS nanoparticles (Scheme 1.1).[36]

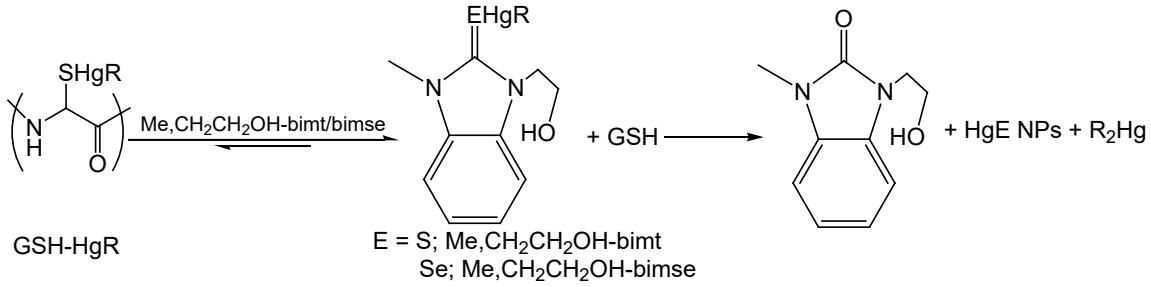

Scheme 1.1. Organomercury removal from glutathione (GSH) and conversion to HgS nanoparticles (NPs) upon treatment with imidazole thione or selone ligands (bimt or bimse).

Separately, the products of this type of ligand exchange reaction were studied by treating ArHgCys-GSH (Ar = 2-vinyl, 2-phenylpyridine) with Me, CH_2CH_2OH-bimt or Me,CH_2CH_2OH-bimse (Figure 1.2) in a 1:2 molar ratio at pH 9. An ArHg(Me,CH_2CH_2OH bmit/bmise) complex forms that is in equilibrium with the ArHgCys-GSH complex, as identified by high-pressure liquid chromatography (Scheme 1.1).[36] This Me,CH_2CH_2OH-bimt/bmise-HgAr complex gradually decomposes to form HgE nanoparticles, Ar_2Hg, and GSH (Scheme 1.1).[36] The ArHg-selone complex is highly unstable in solution, resulting in much faster degradation to HgSe nanoparticles than the analogous thione.[36] Understanding the ligand exchange reactions that can remove mercury from biomolecules may contribute to development of effective drugs to reduce heavy metal toxicity.

Catalytic applications. The electronic properties, ease and versatility of nitrogen substitution, and stability of the C=S and C=Se bonds make imidazole thiones and selones excellent ligands for heavy metal catalysts.[94] Imidazole thione and selone complexes have been designed as promising catalysts for activation for transfer hydrogenation,[38] Suzuki−Miyaura and Sonogashira coupling reactions,[94] and norbornene polymerization.[69] For example, the ability of (η^6-C_6H_6)RuLCl[PF_6] (L = benzoimithione (**1**) or benzoimiselone (**2**); Figure 1.2) complexes to catalyze hydrogen transfer reactions (Scheme 1.2).[38] In this work, catalyst complexes **1** and **2** (0.1-0.5 mol %) were used to transform eight substrates including benzaldehyde, 4-methylacetophenone, or cyclopentanone to the corresponding alcohols at 80 ºC using 2-propanol, glycerol, citric acid, ascorbic acid, and formic acid as hydrogen sources. Using 4-methylacetophenone, acetophenone, or cyclopentanone as the ketone and 2-propanol as the hydrogen source

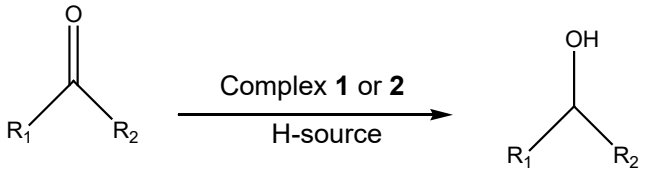

Scheme 1.2. Hydrogen transfer by [(η^6-C_6H_6)RuLCl][PF_6] (L= benzoimithione (**1**) or benzoimiselone (**2**) in the presence of a hydrogen source (R_1, R_2 = alkyl or aryl).

results in 90-95% conversion, while using glycerol as the hydrogen source gives 83-90% product conversion. The benzoimiselone-Ru complex **2** is more efficient at hydrogen transfer compared to the thione analog **1**.[38] Development of novel hydrogen transfer catalysts such as these Ru-imidazole thione and selone complexes has the potential for great impact, since hydrogen transfer is a very important reaction in the production of pharmaceuticals.[38]

1.4 Conclusions and Outlook

Due to the variety of applications of imidazole thione and selone of 2nd and 3rd row *d*-block metal ions complexes, synthesis of new thione and selone complexes will continue to improve their biological, catalytic, and heavy metal detoxifying activities. In addition, fully understanding their versatile coordination chemistry will require the synthesis of unexplored types of thione and selone ligands and coordination to unexamined metal oxidation states. Overall, such imidazole thione and selone complexes are promising for new applications in medicine and industry. Synthesis of Pt-thione and -selone antitumor agents with higher activity and less toxicity compared to cisplatin opens the door for clinical applications of these complexes in the future. In addition, in the development of new antimicrobials, imidazole thione complexes may contribute strongly in this field due

to identification of the bioactivity of the C=S moiety. There are still major gaps in understanding heavy metal toxicity, and exploring the coordination chemistry of mercury-imidazole thione and selone complexes is helping to elucidate mechanisms for treating this toxicity. In the future, such compounds may be developed as heavy metal detoxifying drugs.

1.5 Using Ruthenium Solvato Complexes as an Entry into Ruthenium Thione and Selone Complexes

The variety of imidazole thione and selone complexes with 2nd and 3rd row *d*-block metals, as well as their applications in catalysis and medicine was the focus of the review in Chapter 1. This overview of 2nd and 3rd row *d*-block metal ion complexes with imidazole thione and selone ligands provides a foundation for understanding the novelty of synthesizing homoleptic and hetroleptic ruthenium-thione and -selone complexes.

To synthesize homoleptic thione and selone ruthenium complexes requires suitable ruthenium starting materials. The lability of acetonitrile and DMSO ligands makes these ruthenium complexes valuable synthons for a variety of ruthenium complexes. The homoleptic $[Ru(NCCH_3)][BF_4]_2$ and heteroleptic $[Ru(NCCH_3)_5(DMSO)][BF_4]_2$, $[Ru(NCCH_3)_4(DMSO)_2][BF_4]_2$, and $[Ru(NCCH_3)_2(DMSO)_3Cl][BF_4]_{1.5}[Cl]_{0.5}[Na]$ solvato Ru(II) complexes were synthesized and fully characterized for use as novel ruthenium starting materials (Chapter 2). The ease of synthesis for these complexes will allow greater entry into the synthesis of a variety of Ru(II) complexes, including potential anticancer ruthenium species.

Novel Ru(III) complexes with imidazole thione and selone ligands of the formula $[RuL_6]Cl_3$ and Ru(II) complexes with formulae $[RuL_6][BF_4]_2$ and $RuCl_2L_4$ (L = MMI, dmit, dmise) were synthesized and characterized (Chapter 3). In addition, the kinetics of the reactivity of the air-stable $[RuL_6]^{3+}$ with H_2O_2 are also reported. The ability of $[RuMMI_6]Cl_3$ to prevent oxidative DNA damage was significantly higher than for MMI alone, indicating that these complexes have substantial antioxidant activity.

Chapter 4 describes the synthesis and characterization of novel Ru(II) nitrosyl complexes with imidazole thione or selone ligands of the formula $[Ru(NO)L_4Cl][BF_4]_2$ (L = dmit or dmise). These complexes were synthesized with $AgNO_3$ as the NO source, a much simpler reagent to work with compared typical NO addition reagents. This important contribution will open the door widely to synthesize nitrosyl ruthenium complexes with possible biological activities.

1.6. References

(1) Lu, J.; Holmgren, A. *J. Biol. Chem.* **2009**, *284*, 723-727.

(2) Turanov, A. A.; Xu, X.-M.; Carlson, B. A.; Yoo, M.-H.; Gladyshev, V. N.; Hatfield, D. L. *Adv. Nutr.* **2011**, *2*, 122–128.

(3) Gonzalez-Flores, J.; Shetty, S. P.; Dubey, A.; Copeland, P. R. *Biomol. Concepts* **2013**, *4*, 349–365.

(4) Franzoni, F.; Colognato, R.; Galetta, F.; Laurenza, I.; Barsotti, M.; Di Stefano, R.; Bocchetti, R.; Regoli, F.; Carpi, A.; Balbarini, A.; Migliore, L.; Santoro, G. *Biomed. Biopharmcother.* **2006**, *60*, 453-457.

(5) Short, R. D. J.; Baskin, S. I. In *Oxidants, Antioxidants and Free Radicals*; Baskin, S. I., Salem, H., Eds.; Taylor&Friends: Washington, D.C., 1997, pp 203-206.

(6) Aruoma, O. I.; Spencer, J. P. E.; Mahmood, N. *Food Chem. Toxicol.* **1999**, *37*, 1043-1053.

(7) Deiana, M.; Rosa, A.; Casu, V.; Piga, R.; Assunta, D. M.; Aruoma, O. I. *Clin. Nutr.* **2004**, *23*, 183-193.

(8) Jang, J.-H.; Aruoma, O. I.; Jen, L.-S.; Chung, H. Y.; Surh, Y.-J. *Free Radical Biol. Med.* **2004**, *36*, 288-299.

(9) Colognato, R.; Laurenza, I.; Fontana, I.; Coppede, F.; Siciliano, G.; Coecke, S.; Aruoma, O. I.; Benzi, L.; Migliore, L. *Clin. Nutr.* **2006**, *25*, 135-145.

(10) Markova, N. G.; Karaman-Jurukovska, N.; Dong, K. K.; Damaghi, N.; Smiles, K. A.; Yarosh, D. B. *Free Radical Biol. Med.* **2009**, *46*, 1168-1176.

(11) Paul, B. D.; Snyder, S. H. *Cell Death Differ.* **2010**, *17*, 1134-1140.

(12) Yamashita, Y.; Yamashita, M. *J. Biol. Chem.* **2010**, *285*, 18134-18138.

(13) Thornton, J. M. *J. Mol. Biol.* **1981**, *151*, 261-287.

(14) Metanis, N.; Hilvert, D. *Angew. Chem. Int. Ed. Engl.* **2012**, *51*, 5585-5588

(15) Kimani, M. M.; Watts, D.; Graham, L. A.; Rabinovich, D.; Yap, G. P.; Brumaghim, J. L. *Dalton Trans.* **2016**, *44*, 16313-16324.

(16) Cheah, I. K.; Halliwell, B. *Biochim. Biophys. Acta.* **2012**, *1822*, 784–793.

(17) Linder, M. C., Ed. *Biochemistry of Copper*, Plenum Press, New York 1991.

(18) Barceloux, D. G. *J. Toxicol. Clin. Toxicol.* **1999**, *37*, 217– 230.

(19) Chevion, M. *Free Radical Biol. Med.* **1988**, *5*, 27–37.

(20) Stadelman, B. PhD. Dissertation, Clemson University, Clemson, SC **2016**.

(21) Battin, E. E.; Zimmerman, M. T.; Ramoutar, R. R.; Quarles, C. E.; Brumaghim, J. L. *Metallomics* **2010**, *3*, 503-512.

(22) Battin, E. E.; Perron, N. R.; Brumaghim, J. L. *Inorg. Chem.* **2006**, *45*, 499-501.

(23) Ramoutar, R. R.; Brumaghim, J. L. *Cell Biochem. Biophys.* **2010**, *58*, 1-23.

(24) Zimmerman, M. T.; Bayse, C. A.; Ramoutar, R. R.; Brumaghim, J. L. *J. Inorg. Biochem.* **2015**, *145*, 30–40.

(25) Roy, G.; Das, D.; Mugesh, G. *Inorg. Chim. Acta* **2007**, *360*, 303–316.

(26) Roy, G.; Mugesh, G. *Bioinorg. Chem. Appl.* **2006**, *23214,* 1-9.

(27) Gaetke, L. M., Chow, C. K. *Toxicology* **2003**,*189*, 147–163.

(28) Reich, H. J.; Hondal, R. J. *ACS Chem. Biol.* **2016**, *11*, 821–841.

(29) Savjani, J. K.; Gajjar, A. K. *Pak. J. Biol. Sci.* **2011**, *14*, 1076–1089.

(30) Cooper, D. S. *N. Engl. J. Med.* **2005**, *352*, 905-917.

(31) Rong, Y.; Al-Harbi, A.; Kriegel, B.; Parkin, G. *Inorg. Chem.* **2013**, *52*, 7172–7182.

(32) Kimani, M. M.; Brumaghim, J. L.; VanDerveer, D. *Inorg. Chem.* **2010**, *49*, 9200-9211.

(33) Vallee, B. L.; Auld, D. S. *Acc. Chem. Res.* **1993**, *26*, 543–551.

(34) Banerjee, M.; Karri, R.; Rawat, K. S.; Muthuvel, K.; Pathak, B.; Roy, G. *Angew. Chem. Int. Ed.* **2015**, *54*, 9323–9327.

(35) Rahaman, S. A.; Roy, B.; Mandal, S.; Bandyopadhyay, S. *Inorg. Chem.* **2016**, *55*, 1069–1075.

(36) Banerjee, M.; Karri, R.; Chalana, A.; Das, R.; Rai, R. K.; Rawat, K. S.; Pathak, B.; Roy, G. *Chem. Eur. J.* **2017**, *23*, 5696–5707.

(37) Al-Maythalony, B. A.; Wazeer, M. I. M.; Isab, A. A.; Nael, M. T.; Ahmad, S. *Spectroscopy* **2008**, *22*, 361–370.

(38) Sharma, A. K.; Joshi, H.; Sharma, K. N.; Gupta, P. L.; Singh, A. K. *Organometallic* **2014**, *33*, 3629–3639.

(39) Saleem, F.; Rao, G. K.; Kumar, A.; Mukherjee, G.; Singh, A. K. *Organometallic* **2013**, *32*, 3595–3603.

(40) Prakash, O.; Sharma, K. N.; Joshi, H.; Gupta, P. L.; Singh, A. K. *Dalton Trans.* **2013**, *42*, 8736–8747.

(41) Zhang, Q.-F.; Cheung, F. K. M.; Wong, W.-Y.; Williams, I. D.; Leung, W.-H. *Organomet.* **2001**, *20*, 3777–3781.

(42) Akrivos, P. D. *Coord. Chem. Rev.* **2001**, *213*, 181–210.

(43) Beheshti, A.; Babadi, S. S.; Nozarian, K.; Heidarizadeh, F.; Ghamari, N.; Mayer, P.; Motamedi, H. *Polyhedron* **2016**, *110*, 261–273.

(44) Ahmad, S.; Rüffer, T.; Lang, H.; Nadeem, S.; Tirmizi, S. A.; Saleem, M.; Anwar, A. *Russ. J. Coord. Chem.* **2010**, *36*, 520–524.

(45) Sharman, W. M.; Allen, C. M.; van Lier, J. E., *Drug Discov. Today* **1999**, *4,* 507-517.

(46) Santana, M. D.; García-Bueno, R.; García, G.; Sánchez, G.; García, J.; Pérez, J.; García, L.; Serrano, J. L. *Dalton Trans.* **2011**, *40*, 3537–3546.

(47) Feng, C.; Wang, L.; Yan, Y.; Liu, J.; Li, S. *Med. Chem. Res.* **2012**, *21*, 315–320.

(48) Alhoshani, A.; Seliman, A. A. A.; Altoum, A. O.; Abuelizz, H. A.; Ahmad, S.; Altaf, M.; Omer, K. H.; Sohail, M.; Isab, A. A. *Polyhedron* **2019**, *158*, 234–240.

(49) Ahmad, S.; Altoum, A. O. S.; Vančo, J.; Křikavová, R.; Trávníček, Z.; Dvořák, Z.; Altaf, M.; Sohail, M.; Isab, A. A. *J. Mol. Struct.* **2018**, *1152*, 232–236.

(50) Jomaa, M. Y.; Altaf, M.; Ahmad, S.; Alhoshani, A.; Baig, N.; Kawde, A.-N.; Bhatia, G.; Singh, J.; Isab, A. A. *Polyhedron* **2018**, *141*, 360–368.

(51) Mustafa, A. Z. A.; Altaf, M.; Monim-ul-Mehboob, M.; Fettouhi, M.; Wazeer, M. I. M.; Isab, A. A.; Dhuna, V.; Bhatia, G.; Dhuna, K. *Inorg. Chem. Commun.* **2014**, *44*, 159–163.

(52) Osman S. Altoum, A.; Vančo, J.; Křikavová, R.; Trávníček, Z.; Dvořák, Z.; Altaf, M.; Ahmad, S.; Sulaiman, A. A. A.; Isab, A. A. *Polyhedron* **2017**, *128*, 2–8.

(53) Rani, V.; Singh, H. B.; Butcher, R. J. *Eur. J. Inorg. Chem.* **2017**, *2017*, 3720–3728.

(54) Akrivos, P. D. *Coord. Chem. Rev.* **2001***, 213,* 181-210.

(55) Yadav, S.; Singh, H. B.; Butcher, R. J. *Eur. J. Inorg. Chem.* **2017**, *1*, 2968–2979.

(56) Dewhurst, R.; Hansen, A.; Hill, A.; Smith, M. *Organometallics* **2006** *25*, 5843-5846.

(57) Liu, R.; Li, X.; Zhang, H.; Weng, L.; Zhou, X. *Dalton Trans.* **2010**, *39*, 11053–11059.

(58) Qin, Y.; Ma, Q.; Jia, A.-Q.; Chen, Q.; Zhang, Q.-F. J. Coord. Chem. 2013, 66, 1405–1415.

(59) Zhu, H.; Ma, Q.; Jia, A.-Q.; Chen, Q.; Leung, W.-H.; Zhang, Q.-F. *Inorg. Chim. Acta* **2013**, *405*, 427–436.

(60) Buccella, D.; Shultz, A.; Melnick, J. G.; Konopka, F.; Parkin, G. *Organometallics* **2006**, *25*, 5496–5499.

(61) Rong, Y.; Sambade, D.; Parkin, G. *Acta Crystallogr.* **2016**, *C72*, 806–812.

(62) Hill, A. F.; Rae, A. D.; Smith, M. K. *Inorg. Chem.* **2005**, *44*, 7316–7318.

(63) Saito, K.; Kawano, Y.; Shimoi, M. *Eur. J. Inorg. Chem.* **2007**, *2007*, 3195–3200.

(64) Garcia, R.; Paulo, A.; Domingos, Â.; Santos, I.; Ortner, K.; Alberto, R. *J. Am. Chem. Soc.* **2000**, *122*, 11240–11241.

(65) Bailey, P. J.; Bell, N. L.; Nichol, G. S. *Dalton Trans.* **2013**, *42*, 11281–11294.

(66) Foreman, M. R. S.-J.; Ma, C.; Hill, A. F.; Otten, N. E.; Sharma, M.; Tshabang, N.; Ward, J. S. *Dalton Trans.* **2017**, *46*, 14957–14972.

(67) Lobana, T. S.; Sultana, R.; Butcher, R. J.; Jasinski, J. P.; Akitsu, T. *Z. Anorg. Allg. Chem.* **2014**, *640*, 1688–1695.

(68) Williams, D. J.; McKinney, B. J. *J. Chem. Crystallogr.* **2007**, *37*, 691–694.

(69) Jia, W. -G.; Huang, Y.-B.; Jin, G.X. S. *J. Organomet. Chem.* **2009**, *694*, 4008–4013.

(70) Jia, W.-G.; Huang, Y.-B.; Lin, Y.-J.; Jin, G.X. S. *Dalton Trans.* **2008**, 5612–5620.

(71) Jia, W. G.; Dai, Y. C.; Zhang, H. N.; Lu, X.; Sheng, E.H. *RSC Adv.* **2015**, *5*, 29491–29496.

(72) Aroz, M. T.; Gimeno, M. C.; Kulcsar, M.; Laguna, A.; Lippolis, V. *Eur. J. Inorg. Chem.* **2011**, *2011*, 2884–2894.

(73) Allardyce, C. S.; Dyson, P. J. *Platinum Metals Rev.* **2001**, *45*, 62–69.

(74) Jomaa, M. Y.; Altaf, M.; Ahmad, S.; Bhatia, G.; Singh, J.; Altuwaijri, S.; Isab, A. A. *BioMetals* **2017**, *30*, 787–795.

(75) Bowmaker, G.; Pakawatchai, C.; W. Skelton, B.; Wattanakanjana, Y.; H. White, A. *Z. Anorg. Allg. Chem.* **2008**, *634*, 2583–2588.

(76) García-Vázquez, J. A.; Sousa-Pedrares, A.; Carabel, M.; Romero, J.; Sousa, A. *Polyhedron* **2005**, *24*, 2043–2054.

(77) Dean, P. A. W.; Jennings, M.; Rajalingam, U.; Craig, D. C.; Scudder, M. L.; Dance, I. G. *Cryst. Eng. Comm.* **2002**, *4*, 46–50.

(78) Williams, D. J.; Gulla, D.; Arrowood, K. A.; Bloodworth, L. M.; Carmack, A. L.; Evers, T. J.; Wilson, M. S.; Concepcion, J. J.; Brevett, C. A. S.; Huck, B. E.; VanDerveer, D. *J. Chem. Crystallogr.* **2009**, *39*, 581–584.

(79) Williams, D. J.; McKinney, B. J. *J. Chem. Crystallogr.* **2007**, *37*, 691–694.

(80) Jia, W.-G.; Huang, Y.-B.; Lin, Y.-J.; Jin, G.-X. S. *Dalton Trans.* **2008**, 5612–5620.

(81) Ghavale, N.; Manjare, S. T.; Singh, H. B.; Butcher, R. J. *Dalton Trans.* **2015**, *44*, 11893–11900.

(82) Wang, C.; Tong, Y.; Huang, Y.; Zhang, H.; Yang, Y. S. *RSC Adv.* **2015**, *5*, 63087–63094.

(83) Perras, J. H.; Mezibroski, S. M. J.; Wiebe, M. A.; Ritch, J. S. *Dalton Trans.* **2018**, *47*, 1471–1478.

(84) Karri, R.; Banerjee, M.; Chalana, A.; Jha, K. K.; Roy, G. *Inorg. Chem.* **2017**, *56*, 12102–12115.

(85) Rosenberg, B., Van Camp, L., Krigas, T. *Nature*, **1965**, *205*, 698–699.

(86) Rosenberg, B., Van Camp, L., Trosko, J.E., Mansour, V.H. *Nature,* **1969**, *222*, 385–386.

(87) Deo, K. M.; Pages, B. J.; Ang, D. L.; Gordon, C. P.; Aldrich-Wright, J. R. *Int. J. Mol. Sci.* **2016**, *17*, 1818-1835

(88) Brabec, V.; Nováková, O.*, Drug Resist Updat.* **2006**, *9*, 111–122.

(89) Collery, P.; Veena, V.; Harikrishnan, A.; Desmaele, D. *New Drugs* **2019**, 1-11.

(90) de Moura, T. R.; Cavalcanti, S. L.; de Godoy, P. R. D. V.; Sakamoto-Hojo, E. T.; Rocha, F. V.; de Almeida, E. T.; Deflon, V. M.; Mauro, A. E.; Netto, A. V. G. *Transition Metal Chem.* **2017**, *42*, 565–574.

(91) Dasari, S.; Tchounwou, P. B., *Eur. J. Pharmacol.* **2014**, *0*, 364–378.

(92) Zimmerman, M. T.; Bayse, C. A.; Ramoutar, R. R.; Brumaghim, J. L. *J. Inorg. Biochem.* **2015**, *145*, 30–40.

(93) Nadeem, S.; Sirajuddin, M.; Ahmad, S.; Tirmizi, S. A.; Ali, M. I.; Hameed, A., Alex. *J. Med.* **2016**, *52*, 279–288.

(94) Zhang, L.-M.; Li, H.-Y.; Li, H.-X.; Young, D. J.; Wang, Y.; Lang, J.-P. *Inorg. Chem.* **2017**, 56, 11230−11243.

CHAPTER TWO

SYNTHESIS, CHARACTERIZATION, AND STRUCTURES OF RUTHENIUM(II) COMPLEXES WITH MULTIPLE SOLVATO LIGANDS

2.1 Introduction

Ruthenium complexes with monodentate, photolabile ligands such as *cis*-[Ru(phpy)(phen)($NCCH_3$)$_2$][PF_6] (phpy = 2-phenylpyridine; phen = 1,10-phenanthroline) and *cis*-[Ru(phpy)(bpy)($NCCH_3$)$_2$][PF_6] (bpy = 2,2-bipyridine)[1] as well as *cis*- and *trans*-$RuCl_2(DMSO)_4$ (DMSO = dimethyl sulfoxide) have been investigated as potential photodynamic therapy (PDT) agents to treat cancer.[1-2] Dimethyl sulfoxide and acetonitrile are monodentate, labile ligands, so homoleptic and heteroleptic ruthenium complexes of these ligands also provide excellent starting materials for entry into synthetic ruthenium chemistry.[3-9] As befits their synthetic utility, many Ru(II) complexes with multiple acetonitrile ligands are reported, including [$CpRu(NCCH_3)_3$][PF_6] (Cp = cyclopentadienyl),[6,10] *cis*-[Ru(nbd)(η^2-C_3H_5)($NCCH_3$)$_2$][BF_4] (nbd = norbornadiene),[7] and [Ru(phpy)(phen)($NCCH_3$)$_2$][PF_6].[2]

Although the lability of the Ru-coordinated acetonitrile ligands gives rise to several advantages,[1,3,5-9] including synthesis of complexes with less labile ligands using acetonitrile complexes as starting materials,[3-4,9,11-12] synthesis of Ru(II) complexes with exclusively acetonitrile ligands is challenging when $RuCl_3 \cdot 3H_2O$, $RuCl_2(DMSO)_4$, and $RuCl_2(PPh_3)_3$ are used as starting materials because most of the resulting ruthenium complexes retain chloride, DMSO, or PPh_3 ligands, respectively.[3,13-15] Alternatively, the $[Ru(H_2O)_6]^{2+}$ complex can be used as a synthon, but this complex has solubility issues in

organic solvents, and the presence of the aqua ligands can hinder further water-sensitive synthetic steps.[4,9,11] Aqua ligand basicity can also exclude further synthesis with ligand classes such as amines,[9] and aqua ligands can promote complex decomposition through deprotonation reactions, limiting their use in starting materials.[9,14] Instead, $[Ru(H_2O)_6]^{2+}$ has itself been used to synthesize $[Ru(NCCH_3)_6][OTs]_2$ and $[Ru(NCCH_3)_6][OTf]_2$ complexes (OTs = *p*-toluene sulfonate; OTf = trifluoromethane sulfonate),[16] but purification of $[Ru(H_2O)_6]^{2+}$ requires many steps.[17-18]

$[Ru(NCCH_3)_6][ZnCl_4]$ and $[Ru(NCCH_3)_6][BF_4]_2$ (**1**) have been synthesized using various methods,[3,9] but several difficulties accompany the reported synthesis and uses of these complexes as starting materials. The $[ZnCl_4]^{2-}$ counterion in the former complex can interact with metal-binding species instead of, or in addition to, the ruthenium-containing cation. The reported preparation and purification of complex **1** takes several days and requires several synthetic steps.[9] In this work, we have synthesized complex **1** in higher yield and in shorter times compared to previously reported methods.[3,9] In addition, the previously reported $RuCl_2(DMSO)_4$ complex[19-21] was used to synthesize mixed Ru(II) acetonitrile/DMSO complexes with varying numbers of acetonitrile and DMSO ligands (**2-5**). The work presented in this Chapter is published in *Inorganica Chimica Acta* (Abbas, M. A.; McMillen, C. D.; Brumaghim, J. L *Inorg. Chim. Acta* **2017**, *468*, 308-315), and reproduction in this dissertation is allowed by the publisher.

2.2 Results and Discussion

The reported method for synthesis of $[Ru(NCCH_3)_6][BF_4]_2$ (**1**)[9] does not always

reduce Ru(III) in $RuCl_3 \cdot 3H_2O$, depending on the source of the ruthenium chloride hydrate starting material. Therefore, a more robust synthesis was developed by modifying methods reported for synthesis of **1** and $[Ru(NCCH_3)_6][ZnCl_4]$.[3] Instead of directly isolating $[Ru(NCCH_3)_6][ZnCl_4]$ in low yield as reported by Anzellotti and Briceño,[3] excess $AgNO_3$ was added to the reaction mixture to remove the $[ZnCl_4]^{2-}$ counterion and Cl^- ligands as $ZnCl_2$ and AgCl precipitates, respectively (Scheme 2.1). Addition of $NaBF_4$ to exchange the resulting nitrate counterion for tetrafluoroborate yields complex **1**. This modified synthetic procedure reduces the reaction time to form complex **1** from 13 h[9] to 8 h and improves the yield from 60% for $[Ru(NCCH_3)_6][BF_4]_2$ (**1**) and 36% for $[Ru(NCCH_3)_6][ZnCl_4]$ in the reported syntheses[3,9] to 75%.

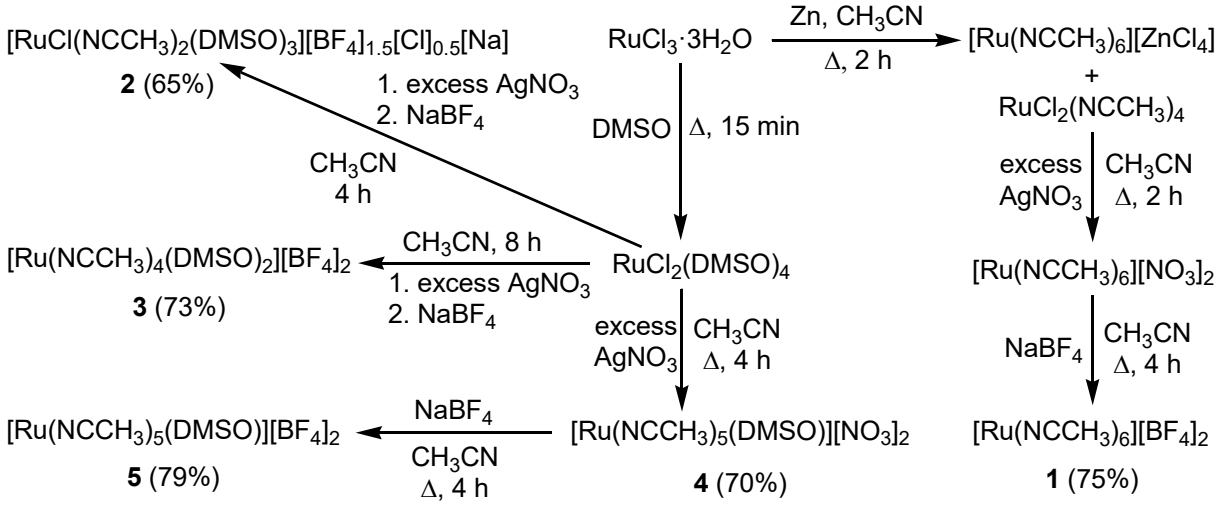

Scheme 2.1. Syntheses of ruthenium complexes with multiple solvato ligands.

Synthesis and characterization of Ru(II)-acetonitrile/DMSO complexes. The reported $RuCl_2(DMSO)_4$ complex[19-21] was used as a starting material to synthesize novel mixed-solvato Ru(II) complexes **2**, **3**, **4**, and **5**. In $RuCl_2(DMSO)_4$, three of the four DMSO ligands coordinate Ru(II) through the sulfur atom, whereas the remaining DMSO

ligand binds through the oxygen atom, indicated as [$RuCl_2$(DMSO-*S*)$_3$(DMSO-*O*)].[20-24] The weaker O-bound DMSO is replaced first;[21] therefore, only this bound DMSO and one chloride are replaced by acetonitrile to form the *bis*-acetonitrile complex **2** (Scheme 2.1) when the reaction is stirred for 4 h without heating. Upon stirring for 8 h, both chloride ligands and two DMSO ligands are replaced by acetonitrile ligands to afford complex **3**.

Upon heating $RuCl_2(DMSO)_4$ to reflux in acetonitrile with excess $AgNO_3$, the two chlorides and three of the four DMSO ligands are replaced with acetonitrile to form complex **4** (Scheme 2.1). $[Ru(NCCH_3)_5(DMSO)][BF_4]_2$ (**5**) was synthesized by treating complex **4** with $NaBF_4$ in acetonitrile to replace the nitrate counterion (Scheme 2.1). Complexes **1**-**5** are stable as solids, but readily lose solvato ligands under vacuum. The facile synthetic methods and high yields of these mixed solvato complexes make them valuable as potential synthons for a variety of heteroleptic ruthenium complexes.

Spectroscopic characterization of Ru-solvato complexes. In infrared (IR) spectroscopic measurements, the two bands for the C≡N stretches of the acetonitrile ligands in Ru(II) complexes **1**-**5** were observed between 2296 and 2332 cm^{-1} (Table 2.1), higher in energy than for unbound acetonitrile (2283 cm^{-1} [25]) and typical of Ru(II) binding.[9,25-26] For complex **1**, these bands are observed at 2296 and 2332 cm^{-1}, matching literature reports.[3,9]

The IR spectrum of the *cis*-$RuCl_2(DMSO)_4$ complex used as a starting material shows two bands for the S-O stretches at 1120 and 1090 cm^{-1}, arising from the non-equivalent DMSO-*S* ligands, shifted higher in energy than the S-O stretch of unbound

Table 2.1. IR stretching bands for C≡N and S-O in complexes **1-5**.

Complex	C≡N (cm^{-1})	S-O (cm^{-1})	Reference
$[Ru(NCCH_3)_6][BF_4]_2$ (**1**)	2296, 2332	-	9
$[RuCl(NCCH_3)_2(DMSO)_3][BF_4]_{1.5}[Cl]_{0.5}[Na]$ (**2**)	2300, 2332	1121, 1067	This work
$[Ru(NCCH_3)_4(DMSO)_2][BF_4]_2$ (**3**)	2296, 2325	1122, 1070	This work
$[Ru(NCCH_3)_5(DMSO)][NO_3]_2$ (**4**)	2300, 2324	1127, 1035	This work
$[Ru(NCCH_3)_5(DMSO)][BF_4]_2$ (**5**)	2303, 2324	1123, 1029	This work

DMSO (1055 cm^{-1}) due to Ru(II) coordination. In contrast, the S-O stretch of the DMSO-*O* ligand in *cis*-$RuCl_2(DMSO)_4$ shifts to significantly lower energy (928 cm^{-1}) due to a decrease in the S-O bond order upon Ru(II)-O binding.[20] In the IR spectrum of complex **2**, with three bound DMSO ligands, S-O stretches are observed at 1121 and 1067 cm^{-1}, consistent with only sulfur-bound DMSO ligands, and indicating that acetonitrile has replaced the DMSO-*O* ligand.[20] Similarly for complex **3** with two bound DMSO ligands, these S-O stretches occur at similar energies and indicate DMSO-*S* binding. In the IR spectrum of complexes **4** and **5**, the second S-O stretch shifts ~30 cm^{-1} lower in energy when only one DMSO ligand is coordinated.

The single resonance from the bound acetonitrile at δ 2.53 in D_2O in the ^1H NMR spectra for Ru(II) complex **1** matches previous reports[9] and is shifted downfield compared to that of unbound acetonitrile (δ 2.06 in D_2O[27]). Complexes **2-5** also have similar acetonitrile ligand resonances in their ^1H NMR spectra, consistent with Ru(II)-acetonitrile complex **1** (Table 2.2). The three DMSO ligands in **2** give rise to two resonances with a 2:1 integration ratio, corresponding to DMSO ligands *trans* to DMSO and chloride, respectively, similar to ^1H NMR shifts observed previously for Ru complexes with multiple DMSO ligands.[20,26] Similarly, the acetonitrile ligands in **3** give rise to two singlet resonances with a 1:1 integration ratio, corresponding to acetonitrile

Table 2.2. ^{1}H NMR chemical shifts (δ) in D_2O of the solvato ligands in complexes **1-5**.

Complex	$NCCH_3$	DMSO-*S*	Reference
$[Ru(NCCH_3)_6][BF_4]_2$ (**1**)	2.53	-	3,9
$[RuCl(NCCH_3)_2(DMSO)_3][BF_4]_{1.5}[Cl]_{0.5}[Na]$ (**2**)	2.59	3.49, 3.46	This work
$[Ru(NCCH_3)_4(DMSO)_2][BF_4]_2$ (**3**)	2.61, 2.59	3.46	This work
$[Ru(NCCH_3)_5(DMSO)][NO_3]_2$ (**4**)	2.55, 2.53	3.44, 3.43	This work
$[Ru(NCCH_3)_5(DMSO)][BF_4]_2$ (**5**)	2.56, 2.53	3.43, 3.42	This work

ligands *trans* to acetonitrile or DMSO. In **3**, the DMSO ligand resonance is a singlet, indicating that the $[Ru(NCCH_3)_4(DMSO)_2]^{2+}$ adopts a *cis* geometry in solution with both DMSO ligands *trans* to acetonitrile. In all cases, the Ru-bound DMSO ligands are shifted downfield from unbound acetonitrile (δ 2.71 in D_2O[27]), similar to resonance shifting observed for bound acetonitrile.

Complexes **4** and **5** show two sets of singlet resonances for the DMSO and acetonitrile ligands in approximately 2:3 ratios for **4** and 1:3 ratios for **5** that together have the expected integrations of 6H for the DMSO resonances and 15H for the acetonitrile resonances. This doubling of each resonance may result from outer-sphere interactions or ligand dissociation in solution. Removing all unbound solvent before acquiring NMR spectra was not possible, since the solvato ligands are labile and readily lost under vacuum and complexes **2**, **3**, and **4** crystalized with unbound acetonitrile in the lattice. In addition, ^{1}H NMR spectra in D_2O for these mixed-solvato complexes change over hours to days, particularly for complex **3**, indicating isomerization and/or decomposition in solution.

X-ray structural analysis. For the *hexakis*(acetonitrile) complex **1**, two polymorphs were observed in this study, denoted **1a** and **1b**. The polymorphs were

distinguishable based on the physical morphology of the crystals, and often were found to crystallize concurrently with one another. Complex **1a** crystallizes as block-like crystals, and its structure is consistent with that previously reported for $[Ru(NCCH_3)_6][BF_4]_2$ in space group $P2_1/c$, though an improved refinement is presented in the present study from data collected at 100 K. Complex **1b** crystallizes as columnar crystals, with the same chemical formula $[Ru(NCCH_3)_6][BF_4]_2$, but crystallizing in space group $C2/m$. In both polymorphs, the Ru(II) ions are bound to six acetonitrile ligands in a distorted octahedral geometry (Figure 2.1), and the Ru atom sits on a center of symmetry, rigorously enforcing 180° *trans*-N-Ru-N angles. A small amount of distortion is observed about the *cis*-N-Ru-N angles, ranging from 88.06(4) to 91.94(4)° in **1a** and 87.63(8) to 92.37(8)° in **1b** (Table 2.3). The observed average Ru-N bond distances in **1a** (Ru-N = 2.022(1) Å) and **1b** (Ru-N = 2.023(3) Å) are consistent with those previously reported for ruthenium centers having six acetonitrile ligands coordinated to Ru(II) (2.030(6) Å),[3] as well as with other acetonitrile-rich Ru(II) complexes such as $[Ru(NCCH_3)_5I]$,[28] $[Ru(NCCH_3)_5(PPh_3)]$,[29] and $[Ru(NCCH_3)Cl]$,[30] all having Ru-N interatomic distances

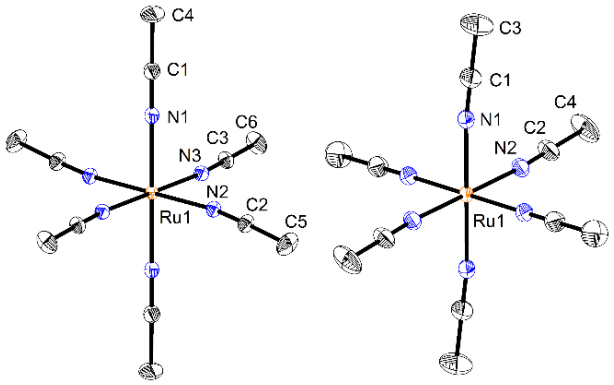

1a **1b**

Figure 2.1. Coordination geometries about the Ru(II) centers for *hexakis*(acetonitrile) polymorphs **1a** and **1b**, respectively. Atoms are shown with 50% probability ellipsoids, with hydrogen atoms, counterions, and solvent molecules omitted for clarity.

around 2.00-2.04 Å for ligands not experiencing elongation from *trans* effects.

Polymorphs **1a** and **1b** do exhibit certain subtle local structural differences. For example, there is a slight elongation of the axial Ru-N1 bonds relative to the equatorial Ru-N2 bonds in **1b** that is not observed in **1a**. Primarily, the polymorphs differ in their packing arrangements of the $[Ru(NCCH_3)_6]^{2+}$ and $[BF_4]^-$ ions (Figure 2.3). The packing of **1b** is likely affected by disorder of two of the fluorine sites (half-occupied general positions) of the tetrafluoroborate anion, whereas in **1a** the tetrafluoroborate anion is fully-ordered at all the fluorine sites.

Table 2.3. Selected interatomic distances (Å) and angles (°) for *hexakis*(acetonitrile) complexes **1a** and **1b**.

1a $[Ru(NCCH_3)_6](BF_4)_2$		**1b** $[Ru(NCCH_3)_6](BF_4)_2$	
Ru1−N1 (×2)	2.0218(11)	Ru1−N1 (×2)	2.032(3)
Ru1−N2 (×2)	2.0218(10)	Ru1−N2 (×4)	2.019(2)
Ru1−N3 (×2)	2.0217(10)		
N1−Ru1−N1	180	N1−Ru1−N1	180
N1−Ru1−N2	89.07(4)	N1−Ru1−N2	87.63(8)
	90.93(4)		92.37(8)
N1−Ru1−N3	89.78(4)	N2−Ru1−N2 (*trans*)	180
	90.22(4))		
N2−Ru1−N2	180	N2−Ru1−N2 (*cis*)	88.41(13)
			91.59(13)
N2−Ru1−N3	88.06(4)		
	91.94(4)		
N3−Ru1−N3	180		

The coordination geometries of Ru(II) complexes **2**, **3**, **4**, and **5** with mixed acetonitrile and DMSO coordination are shown in Figure 2.2, with selected interatomic distances and angles in Table 2.4. These complexes display a range of ratios of the coordinated ligands. Complex **2** exhibits acetonitrile:DMSO of 2:3 with an additional non-solvato Cl ligand, complex **3** is comprised of 4:2 acetonitrile:DMSO, and complexes **4** and **5** have acetonitrile:DMSO in a 5:1 ratio. Complex **5** was crystallized from

acetonitrile in two different forms: without crystallized solvent molecules as $[Ru(NCCH_3)_5(DMSO)][BF_4]_2$ (Figure 2.2 and Table 2.4) in space group $P2_1/c$, and as an acetonitrile solvate $[Ru(NCCH_3)_5(DMSO)][BF_4]_2 \cdot 2CH_3CN$ (Figure 2.4 and Tables 2.8-2.9) in space group *P*-1. Data for six-coordinate Ru(II) complexes involving mixed acetonitrile and DMSO ligands are somewhat lacking in the structural literature. Previously reported crystal structures with mixed acetonitrile and DMSO coordination to Ru(II) also have non-solvato ligands bound to the Ru center, including [Ru(phen-NH-phen)$(NCCH_3)$(DMSO)] (*N*,*N*-bis(1,10-phenanthroline-2-yl)amine),[31] $[RuCl_2(NCCH_3)(DMSO)_3]$,[32] and [Ru(cyclen)$(NCCH_3)$(DMSO)] (cyclen = 1,4,7,10-tetraazacyclododecane).[32-34] Complex **2**, resulting from acetonitrile treatment of

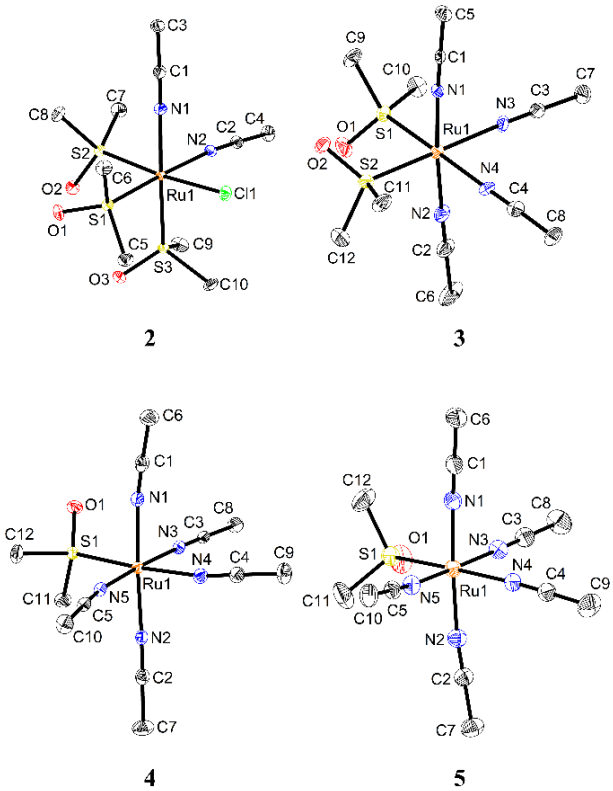

Figure 2.2. X-ray diffraction structures for complexes **2**, **3**, **4**, and **5**, with mixed acetonitrile and DMSO coordination. Atoms are shown as 50% probability ellipsoids, with hydrogen atoms, counterions, and solvent molecules omitted for clarity.

Table 2.4. Selected interatomic distances (Å) and angles (°) for complexes **2**, **3**, **4**, and **5**. The structure of complex **3** contains four unique Ru centers, and the Ru1 center is tabulated here as a representative example.

2 $[RuCl(NCCH_3)_2(DMSO)_3][BF_4]_{1.5}[Cl]_{0.5}[Na]\cdot xCH_3CN$		**3** $[Ru(NCCH_3)_4(DMSO)_2][BF_4]_2\cdot 0.5CH_3CN$		**4** $[Ru(NCCH_3)_5(DMSO)][NO_3]_2\cdot 2CH_3CN$		**5** $[Ru(NCCH_3)_5(DMSO)][BF_4]_2$	
Ru1−N1	2.073(3)	Ru1−N1	2.020(9)	Ru1−N1	2.031(2)	Ru1−N1	2.042(5)
Ru1−N2	2.085(3)	Ru1−N2	2.015(10)	Ru1−N2	2.0240(19)	Ru1−N2	2.023(5)
Ru1−S1	2.2902(8)	Ru1−N3	2.101(9)	Ru1−N3	2.0233(19)	Ru1−N3	2.012(5)
Ru1−S2	2.2832(8)	Ru1−N4	2.073(9)	Ru1−N4	2.0765(19)	Ru1−N4	2.101(5)
Ru1−S3	2.2896(8)	Ru1−S1	2.268(3)	Ru1−N5	2.0299(19)	Ru1−N5	2.029(5)
Ru1−Cl1	2.4253(8)	Ru1−S2	2.275(3)	Ru1−S1	2.2621(6)	Ru1−S1	2.2580(14)
N1−Ru1−N2	89.32(11)	N1−Ru1−N2	175.6(4)	N1−Ru1−N2	174.94(7)	N1−Ru1−N2	175.06(18)
N1−Ru1−S1	92.20(8)	N1−Ru1−N3	90.6(3)	N1−Ru1−N3	91.21(7)	N1−Ru1−N3	87.77(18)
N1−Ru1−S2	88.64(8)	N1−Ru1−N4	88.3(3)	N1−Ru1−N4	85.37(7)	N1−Ru1−N4	89.14(18)
N1−Ru1−S3	178.16(8)	N1−Ru1−S1	93.9(2)	N1−Ru1−N5	89.50(7)	N1−Ru1−N5	93.39(18)
N1−Ru1−Cl1	85.56(8)	N1−Ru1−S2	89.0(2)	N1−Ru1−S1	92.33(5)	N1−Ru1−S1	91.23(13)
N2−Ru1−S1	177.79(9)	N2−Ru1−N3	86.8(4)	N2−Ru1−N3	90.36(7)	N2−Ru1−N3	88.55(18)
N2−Ru1−S2	91.18(8)	N2−Ru1−N4	88.0(4)	N2−Ru1−N4	89.88(7)	N2−Ru1−N4	87.59(18)
N2−Ru1−S3	88.92(8)	N2−Ru1−S1	89.7(3)	N2−Ru1−N5	88.63(7)	N2−Ru1−N5	90.19(19)
N2−Ru1−Cl1	88.58(8)	N2−Ru1−S2	93.6(3)	N2−Ru1−S1	92.54(5)	N2−Ru1−S1	92.05(13)
S1−Ru1−S2	90.46(3)	N3−Ru1−N4	86.6(4)	N3−Ru1−N4	88.05(7)	N3−Ru1−N4	90.23(18)
S1−Ru1−S3	89.55(3)	N3−Ru1−S1	92.4(3)	N3−Ru1−N5	176.18(7)	N3−Ru1−N5	177.81(17)
S1−Ru1−Cl1	89.94(3)	N3−Ru1−S2	179.6(3)	N3−Ru1−S1	87.39(5)	N3−Ru1−S1	89.83(13)
S2−Ru1−S3	91.93(3)	N4−Ru1−S1	177.6(2)	N4−Ru1−N5	88.26(7)	N4−Ru1−N5	87.92(18)
S2−Ru1−Cl1	174.20(3)	N4−Ru1−S2	93.4(3)	N4−Ru1−S1	174.85(5)	N4−Ru1−S1	179.63(13)
S3−Ru1−Cl1	93.86(3)	S1−Ru1−S2	87.66(10)	N5−Ru1−S1	96.34(5)	N5−Ru1−S1	92.00(14)

$RuCl_2(DMSO)_4$ without reflux is similar in this regard. The three DMSO ligands are in a *fac*- arrangement and bound through the sulfur atoms, indicating that the oxygen-bound DMSO of the $RuCl_2(DMSO)_4$ is the first to depart during synthesis. Extending the same reaction from 4 h to 8 h resulted in the formation of complex **3**, having a 4:2 acetonitrile:DMSO coordination. This suggests that the remaining chloride ligand on the Ru center is the next ligand to depart, along with one of the sulfur-bound DMSO ligands. This leaves two DMSO ligands on the Ru center of **3** in a *cis* arrangement. Complexes **4** and **5** show more extensive, though still incomplete acetonitrile substitution, and present a unique 5:1 acetonitrile:DMSO coordination that, to our knowledge, has not yet been structurally characterized for a transition metal center.

In complexes **2**, **3**, **4**, and **5**, the angular distortion of the Ru octahedron arises from the unsymmetrical ligand coordination (Table 2.4). In **2**, Ru-L angles range from 85.56(8)°-93.86(3)°, and in **3**, Ru-L angles range from 83.5(4)° to 96.0(3)°. Sterics of the single bulkier DMSO ligand result in acute *cis*-N-Ru-N angles (85.37(7)°-90.23(18)°) involving the N4 nitrogen (*trans* to DMSO) in **4** and **5**. The *trans* influence of the DMSO ligand also imparts measurable differences in the Ru-N bond distances for the acetonitrile ligands (Table 2.4). This occurs in the Ru-N1 and Ru-N2 interactions of **2** (2.073(3) and 2.085(3) Å), the Ru-N3 and Ru-N4 interactions (and the equivalent Ru-N bonds on the three other unique Ru sites) of **3** (2.101(9) and 2.073(9) Å), and the Ru-N4 interactions of **4** (2.0765(19) Å) and **5** (2.094(5) Å). Similar *trans* effects are observed in other ruthenium complexes with acetonitrile and mixed ligands, notably in [Ru(phen-NH-phen)($NCCH_3$)(DMSO)] (Ru-N = 2.064 Å) compared to [Ru(phen-NH-phen)($NCCH_3$)$_2$] (Ru-N = 2.026 Å).[30] Acetonitrile ligands coordinated to Ru opposite another acetonitrile ligand exhibit Ru-N distances similar to those in the *hexakis*(acetonitrile) complexes **1a** and **1b** where no *trans* effect is imparted. Typical Ru-Cl (2.4253(8) Å) and Ru-S (ranging from 2.2580(14) to 2.2902(8) Å) distances are observed in the complexes in the present study. We do note that the Ru-S bond lengths are all slightly longer in complex **2**, with three DMSO ligands (ranging from 2.2832(8) to 2.2902(8) Å) compared to those in complex **3** having a *cis* arrangement of two DMSO ligands (2.260(3) to 2.277(3) Å), as well as to the single DMSO ligands present in **4** and **5** (2.2580(14) to 2.2621(6) Å). This likely arises due to the steric effects of three DMSO ligands in the *fac* arrangement in **2**, as these distances are nearly identical to those in [$RuCl_2$($NCCH_3$)$(DMSO)_3$],[32] also

having a *fac* arrangement of DMSO ligands.

Based on the crystals obtained, several broad observations can be made regarding the synthetic approach and the resulting coordination. Following Scheme 2.1, we observe there is a definite sensitivity of complex formation toward the reaction conditions. When treated under mild conditions in acetonitrile, the $RuCl_2(DMSO)_4$ complex reacts to form a Ru complex that retains the three sulfur-bound DMSO ligands as well as one of the chloride ligands (**2**). The crystallized material of complex **2** proved to be a somewhat complicated mixture of the reaction components, but nevertheless the reaction is promising for developing a greater variety of targeted coordination patterns about Ru(II). Maintaining the mild conditions (no reflux), but increasing the reaction time affords acetonitrile substitution for the remaining chloride ligand and one of the DMSO ligands of **2**, resulting in **3**, the 4:2 acetonitrile:DMSO complex. When reflux in acetonitrile is employed with the $RuCl_2(DMSO)_4$ precursor, then the 5:1 acetonitrile:DMSO complexes were obtained (**4** and **5**). Once DMSO has coordinated the Ru center of $RuCl_2(DMSO)_4$, complete substitution by acetonitrile proves challenging, since even after reflux for up to 4 h and crystal growth in acetonitrile, one DMSO ligand remains.

2.3 Conclusions

The lability of acetonitrile and DMSO ligands makes these ruthenium complexes valuable synthons for a variety of ruthenium complexes. $[Ru(NCCH_3)_6][BF_4]$ (**1**) is an excellent starting material to synthesize homoleptic ruthenium complexes. In contrast,

complexes **2-5** could be used to synthesize heteroleptic ruthenium complexes, and complexes **4** and **5** are the first 5:1 acetonitrile: DMSO Ru(II) complexes. The ease of synthesis for these complexes will allow greater entry into the synthesis a variety of Ru(II) complexes, including potential anticancer ruthenium species.

2.4 Experimental Methods

General methods. Synthesis of all complexes was performed under argon using standard Schlenk techniques except where indicated. Ruthenium(III) chloride hydrate (Oakwood), silver nitrate, sodium tetrafluoroborate, hydrochloric acid (20%), and zinc powder were used without purification. Acetonitrile, acetone, and ethanol were purified by distillation under an argon atmosphere; dimethyl sulfoxide and anhydrous diethyl ether were used without further purification. DMSO was dried over 4 Å molecular sieves prior to use. $RuCl_2(DMSO)_4$ was synthesized as reported by Evans *et al.* [20]. ^1H NMR spectra were recorded using a 300 MHz Bruker-AVANCE NMR spectrometer and ^1H NMR chemical shifts are reported in δ relative to tetramethylsilane (δ 0) and referenced to solvent (Figures 2.5-2.9). IR spectra were obtained from Nujol mulls on KBr salt plates with a Magna 550 IR spectrometer (Figures 2.10-2.14). MALDI mass spectra were obtained using a Bruker Microflex MALDI-TOF mass spectrometer with trans-2-[3-(4-tert-butylphenyl)-2-methyl-2-propenyldiene]malonitrile (*m*/*z* 251.3 for cation with H^+) as the matrix. All observed peak envelopes match theoretical calculations for their ions (2.15-2.18).

*Synthesis of $[Ru(NCCH_3)_6][BF_4]_2$ (**1**).* Synthesis of $[Ru(NCCH_3)_6][BF_4]_2$ was

accomplished by modifying the methods reported for the previous syntheses of $[Ru(NCCH_3)_6][BF_4]_2$ (**1**) and $Ru(NCCH_3)_6][ZnCl_4]$ [3,9]. $RuCl_3 \cdot 3H_2O$ (261 mg, 1 mmol) was dissolved in freshly distilled acetonitrile (25 mL), and zinc powder (65 mg, 1 mmol) was added. The reaction mixture was heated to reflux with stirring for 2 h, and the color changed from black to yellow during this time. The reaction mixture was then cooled and filtered to remove excess zinc. $AgNO_3$ (340 mg, 2 mmol) was added to the filtrate, and this mixture was again heated to reflux with stirring for 2 h. A white precipitate formed, and the reaction mixture was cooled and filtered. The counterion was exchanged by adding $NaBF_4$ (220 mg, 2 mmol) to the filtrate and heating the reaction mixture to reflux with stirring for 4 h, resulting in formation of a white precipitate. Again the reaction mixture was cooled and filtered; the filtrate was cooled to -20˚C for 15 h and filtered a second time to remove any precipitate before the solvent volume was reduced to 10 mL *in vacuo*. Diethyl ether (40 mL) was then added, yielding a white precipitate that was recrystallized in acetonitrile to afford the product. Yield: 390 mg (75%). Crystals for X-ray analysis were grown from vapor diffusion of diethyl ether into a solution of **1** in acetonitrile. NMR and IR spectra match previous characterization of **1** [3,9]. Analysis of $C_{12}H_{18}B_2F_8N_6Ru$, Calcd. (Exp.): C, 27.66 (27.70); H, 3.48 (3.49); N, 16.13 (15.94).

Synthesis of $[RuCl(NCCH_3)_2(DMSO)_3][BF_4]_{1.5}[Cl]_{0.5}[Na]$ (***2***). $AgNO_3$ (340 mg, 2 mmol) was added to a solution of $RuCl_2(DMSO)_4$ (484 mg, 1 mmol) in acetonitrile (20 mL) and stirred for 4 h at room temperature. During this time, a white precipitate formed, and the reaction color turned from yellow to colorless. The reaction mixture was filtered, and the filtrate was treated with $NaBF_4$ (220 mg, 2 mmol) and stirred for an additional 4

h. The reaction mixture was filtered again, and the filtrate solvent was removed in vacuo. The resulting white powder was washed with diethyl ether (20 mL) and dried. Vapor diffusion of diethyl ether into an acetonitrile solution of **3** was used to grow crystals suitable for X-ray analysis. Yield: 400 mg (65%). ^{1}H NMR (D_2O): δ 2.62 (s, 6H, CH_3CN), 3.49 (s, 12H, DMSO *trans* to CH_3CN), and 3.46 (s, 6H, DMSO *trans* to Cl). IR (Nujol, cm^{-1}): 2300 (w, C≡N), 2332 (w, C≡N), 1121 (S-O), 1067 (S-O). Analysis of $[Ru(NCCH_3)_4(DMSO)_2][BF_4]_2$ ($C_{12}H_{24}B_2ClF_8N_4O_2RuS_2$), Calcd. (Exp.): C, 24.22 (23.60); H, 4.06 (3.87); N, 9.41 (9.21). MALDI-MS (m/z) = 369 $[RuCl(NCCH_3)(DMSO)_2+Cl+H]^+$, 448 $[RuCl(NCCH_3)(DMSO)_3]+Cl+H]^+$.

*Synthesis of $[Ru(NCCH_3)_4(DMSO)_2][BF_4]_2$ (**3**)*. A similar procedure that was used to synthesize **2** was used to synthesize **3** except the reaction time was increased to 8 h at room temperature. During this time, a white precipitate formed, and the solution turned from yellow to colorless. The reaction mixture was filtered, and the filtrate was treated with $NaBF_4$ (220 mg, 2 mmol) and stirred for an additional 12 h. The reaction mixture was filtered again, and the filtrate solvent was removed *in vacuo*. The resulting white powder was washed with diethyl ether (20 mL) and dried. Vapor diffusion of diethyl ether into an acetonitrile solution of **3** was used to grow crystals suitable for X-ray analysis. Yield: 434 mg (73%). ^{1}H NMR (D_2O): δ 2.59 (s, 6H, CH_3CN), 2.61 (s, 6H, CH_3CN), 3.46 (s, 12H, DMSO). IR (Nujol, cm^{-1}): 2296 (w, C≡N), 2325 (w, C≡N), 1122 (S-O), 1070 (S-O). Analysis of $[RuCl(NCCH_3)_2(DMSO)_3][BF_4]_{1.5}[Cl]_{0.5}[Na]\cdot CH_3CN$ ($C_{12}H_{27}B_{1.5}Cl_{1.5}F_6N_3NaO_3RuS_3$), Calcd. (Exp.): C, 24.22 (23.60); H, 4.06 (3.87); N, 9.41 (9.21). MALDI-MS (*m*/*z*) = 386 $[Ru(NCCH_3)(DMSO)_2+BF_4]^+$, 431

$[Ru(NCCH_3)_4(DMSO)+BF_4]^+$.

*Synthesis of $[Ru(NCCH_3)_5(DMSO)][NO_3]_2$ (**4**)*. $RuCl_2(DMSO)_4$ (484 mg, 1 mmol) was treated with (340 mg, 2 mmol) $AgNO_3$ in acetonitrile (30 mL), and the mixture was heated to reflux and stirred for 4 h. A white precipitate formed, and the reaction mixture turned from yellow to colorless. The reaction mixture was then filtered, the solvent was removed *in vacuo*, and the resulting white powder was washed with diethyl ether (20 mL) and dried. Crystals of **4** suitable for X-ray analysis were grown by slow vapor diffusion of diethyl ether into acetonitrile. Yield: 410 mg (70%). ^{1}H NMR (D_2O): δ 2.53 and 2.55 (both s, 15H, CH_3CN); 3.43 and 3.44 (both s, 6H, DMSO). IR (Nujol, cm^{-1}): 2300 (w, C≡N) 2324 (w, C≡N), 1127 (S-O), 1035 (S-O). Analysis of $[Ru(NCCH_3)_5(DMSO)][NO_3]_2 \cdot H_2O$ ($C_{12}H_{23}N_7O_8RuS$), Calcd. (Exp.): C, 27.38 (27.04); H, 4.40 (4.27); N, 18.62 (18.27). MALDI-MS (*m*/*z*): 364 $[Ru(NCCH_3)_3(DMSO)+NO_3]^+$, 408 $[Ru(NCCH_3)_4(DMSO)+NO_3]^+$.

*Synthesis of $[Ru(NCCH_3)_5(DMSO)][BF_4]_2$ (**5**)*. Complex **4** (590 mg, 1 mmol) was treated with $NaBF_4$ (220 mg, 2 mmol) in acetonitrile (30 mL), the reaction mixture was heated to reflux with stirring for 4 h, and a white precipitate formed. The reaction mixture was filtered, and the solvent was removed *in vacuo*. The resulting white powder was washed with diethyl ether (20 mL) and dried to afford **5**. Vapor diffusion of diethyl ether into an acetonitrile solution **5** was used to grow crystals suitable for X-ray analysis. Yield: 440 mg (79%). Elemental analysis showed a 6% $NaBF_4$ impurity from the counterion exchange, so the complex was recrystallized in acetonitrile before performing additional characterization. ^{1}H NMR (D_2O): δ 2.53 and 2.56 (both s, 15H, CH_3CN), 3.42

and 3.42 (both s, 6H, DMSO). IR spectra (Nujol, cm^{-1}): 2303 (w, C ≡ N), 2324 (w, C ≡ N), 1123 (S-O), 1029 (S-O). Analysis of $[Ru(NCCH_3)_5(DMSO)][BF_4]_2 \cdot NCCH_3 \cdot NaBF_4$ ($C_{14}H_{24}B_3F_{12}N_6NaORuS$), Calcd.(Exp.): C, 23.72 (23.30); H, 3.41 (3.34); N, 11.85 (11.56). MALDI-MS (*m*/*z*): 281 $[Ru(NCCH_3)_2(DMSO)]+F]^+$, 321 $[Ru(NCCH_3)_3(DMSO)]+F]^+$, 471 $[Ru(NCCH_3)_5(DMSO)+BF_4]^+$.

X-ray crystallography. Single crystal X-ray diffraction measurements were acquired using two different diffractometers, both equipped with Mo Kα (λ = 0.71073 Å) radiation. Diffraction data at 100 K were measured using a Bruker D8 Venture with an Incoatec microfocus source and a Photon 100 CMOS detector. Room temperature data were obtained using a Rigaku AFC8S diffractometer with a sealed glass X-ray tube and a Mercury CCD detector. Instrument control, data processing, and scaling corrections were performed using the Apex3 software suite in the case of the Bruker instrument, and the CrystalClear software package in the case of the Rigaku instrument [35-36]. Space group assignments were unambiguously made based on systematic absences. All structures were solved by direct methods and refined to convergence by full-matrix least squares using the SHELXTL software suite [37]. All non-hydrogen atoms were refined anisotropically. Hydrogen atoms attached to carbon atoms were placed geometrically and treated using appropriate riding models.

Data from the structure refinements of the resulting ruthenium complexes are shown in Tables 2.5-2.7. Ruthenium atoms were always six-coordinate, but coordinated by varying ratios of the ligands. In several instances the presence of solvent molecules in the crystals was deduced from the X-ray data, presumably assisting in the long-range

Table 2.5. Crystallographic data for complexes **1a** and **1b**.

	1a $[Ru(NCCH_3)_6][BF_4]_2$	**1b** $[Ru(NCCH_3)_6][BF_4]_2$
empirical formula	$C_{12}H_{18}B_2F_8N_6Ru$	$C_{12}H_{18}B_2F_8N_6Ru$
formula weight (g/mol)	521.01	521.01
temperature (K)	100	100
crystal system	Monoclinic	Monoclinic
space group	$P2_1/c$	$C2/m$
unit cell dimensions (Å, ^{0})	a = 8.0927(8) b = 8.1321(8) c = 15.7736(17) β = 93.119(3)	a = 11.8512(10) b = 17.1331(14) c = 5.5973(4) β = 103.799(2)
volume (Å^3)	1036.53	1103.72
Z, calcd density (mg/m^3)	2, 1.669	2, 1.568
absorption coefficient (mm^{-1})	0.836	0.785
F(000)	516	516
crystal size (mm)	0.48 x 0.41 x 0.28	0.10 x 0.09 x 0.09
T_{max}, T_{min}	1.0000, 0.8819	1.0000, 0.9012
Θ range for data	2.52-36.37	2.13-25.98
reflns collected/unique/obs.	28908/5024/4289	10432/1125/1124
data/restraints/parameters	5024/0/136	1125/9/85
goodness-of-fit on F^2	1.180	1.074
R1, wR2 ($I \geq 2\sigma(I)$)	0.0230, 0.0686	0.0296, 0.0809
R1, wR2 (all data)	0.0302, 0.0794	0.0296, 0.0810
largest diff. peak, hole (e/Å^3)	0.726, -1.259	0.988, -0.558

Table 2.6. Crystallographic data for complexes **2** and **3**.

	2 $[RuCl(NCCH_3)_2(DMSO)_3][BF_4]_{1.5}[Cl]_{0.5}[Na]\cdot xNCCH_3$	**3** $[Ru(NCCH_3)_4(DMSO)_2][BF_4]_2\cdot 0.5NCCH_3$
empirical formula	$C_{10}H_{24}B_{1.5}Cl_{1.5}F_6N_2NaO_3RuS_3$	$C_{13}H_{25.5}B_2F_8N_{4.5}O_2RuS_2$
formula weight (g/mol)	623.94	615.69
temperature (K)	100	100
crystal system	Orthorhombic	Triclinic
space group	$Fdd2$	P-1
unit cell dimensions (Å, ^{0})	a = 15.7199(9) b = 40.665(2) c = 14.8332(8)	a = 12.8875(10) b = 15.1344(12) c = 27.244(2) α = 101.191(3) β = 102.226(3) γ = 90.229(4)
volume (Å^3)	9482.1(9)	5088.9(7)
Z, calcd density (mg/m^3)	16, 1.748	8, 1.607
absorption coefficient (mm^{-1})	1.174	0.856
F(000)	4992	2472
crystal size (mm)	0.39 x 0.16 x 0.08	0.20 x 0.17 x 0.08
T_{max}, T_{min}	1.0000, 0.9078	1.0000, 0.8920
Θ range for data	1.95-33.13	1.94-25.25
reflns collected/unique/obs.	26136/8037/7643	114946/18357/16257
data/ restraints/parameters	8037/1/276	18357/0/1206
goodness-of-fit on F^2	1.206	1.153
R1, wR2 ($I \geq 2\sigma(I)$)	0.0245, 0.0628	0.0938, 0.2135
R1, wR2 (all data)	0.0284, 0.0736	0.1041, 0.2198
largest diff. peak, hole (e/Å^3)	0.910, -1.131	2.959, -1.455

Table 2.7. Crystallographic data for complexes **4** and **5**.

	4 $[Ru(NCCH_3)_5(DMSO][NO_3]_2 \cdot 2NCCH_3$	**5** $[Ru(NCCH_3)_5(DMSO)][BF_4]_2$
empirical formula	$C_{16}H_{27}N_9O_7RuS$	$C_{12}H_{21}B_2F_8N_5ORuS$
formula weight (g/mol)	590.59	558.09
temperature (K)	100	293
crystal system	Monoclinic	Monoclinic
space group	$P2_1/c$	$P2_1/c$
unit cell dimensions (Å,^{0})	a = 16.3743(9) b = 7.6068(4) c = 20.9641(13) β = 98.822(2)	a = 12.8983(14) b = 12.4288(13) c = 15.5070(18) β = 106.081(3)
volume (Å^3)	2580.3(3)	2388.7(5)
Z, calcd density (mg/m^3)	4, 1.520	4, 1.552
absorption coefficient (mm^{-1})	0.740	0.817
F(000)	1208	1112
crystal size (mm)	0.27 x 0.22 x 0.03	0.47 x 0.35 x 0.29
T_{max}, T_{min}	1.0000, 0.9232	1.0000, 0.8900
Θ range for data	2.49-26.52	2.13-25.25
reflns collected/unique/obs.	43231/5344/4746	20203/4333/3717
data/ restraints/parameters	5344/12/316	4333/0/278
goodness-of-fit on F^2	1.040	1.096
R1, wR2 ($I \geq 2\sigma(I)$)	0.0291, 0.0605	0.0681, 0.1896
R1, wR2 (all data)	0.0352, 0.0630	0.0766, 0.2110
largest diff. peak, hole (e/Å^3)	1.145, -0.195	1.926, -1.020

packing of the target molecules. These atoms were modeled and refined in the same way as the rest of the atoms in the structure, except in the case of complex **2**. Complex **2** crystallized with highly disordered acetonitrile solvent molecules that were modeled using the SQUEEZE algorithm of PLATON (corresponding to approximately 0.66 C_2H_3N molecules per formula unit) [38]. These crystals also possessed a more complex mixture of counterions derived from the reaction mixture including Na^+ and Cl^- in addition to the expected $[BF_4]^-$ anions. Crystals of **3** contained 0.5 acetonitrile molecules per formula unit. Crystals of complex **4** contained two molecules of acetonitrile per formula unit. The crystals of complex **3** were always found to be non-merohedrally twinned over multiple domains, which ultimately limited the intensities contributed by the primary domain and the quality of those refinements. However, the structural model

of **3** is reasonable and consistent with the supporting characterization. Finally, we note that the structure of complex **1a** was already reported at 168 K,[9] but an improved refinement from data collected at 100 K in the course of this study is included for completeness and comparative purposes to polymorph **1b**.

2.5 Supplemental Material

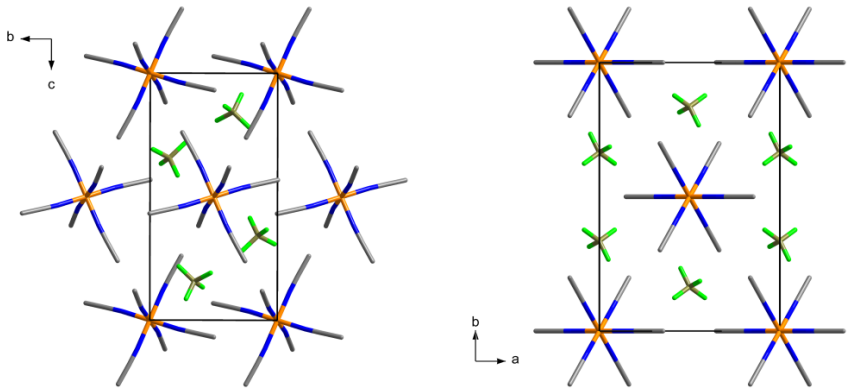

1a **1b**

Figure 2.3. Packing diagrams for $[Ru(NCCH_3)_6][BF_4]_2$ polymorphs **1a** and **1b** as viewed along the *c*-axis. Hydrogen atoms are omitted for clarity.

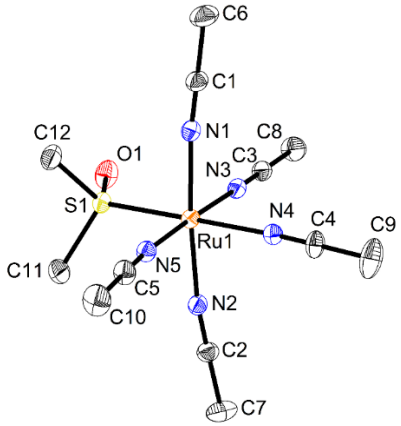

Figure 2.4. X-ray diffraction structure for $[Ru(NCCH_3)_5(DMSO)][BF_4]_2 \cdot 2CH_3CN$ (**5** with additional lattice acetonitrile) with mixed acetonitrile and DMSO coordination. Atoms are shown as 50% probability ellipsoids, and hydrogen atoms, counterions, and solvent molecules are omitted for clarity.

Table 2.8. Selected interatomic distances (Å) and angles (°) for $[Ru(NCCH_3)_5(DMSO)][BF_4]_2 \cdot 2CH_3CN$ (**5** with additional lattice acetonitrile).

$[Ru(NCCH_3)_5(DMSO)][BF_4]_2 \cdot 2CH_3CN$	
Ru1−N1	2.042(5)
Ru1−N2	2.023(5)
Ru1−N3	2.012(5)
Ru1−N4	2.101(5)
Ru1−N5	2.029(5)
Ru1−S1	2.2580(14)
N1−Ru1−N2	175.06(18)
N1−Ru1−N3	87.77(18)
N1−Ru1−N4	89.14(18)
N1−Ru1−N5	93.39(18)
N1−Ru1−S1	91.23(13)
N2−Ru1−N3	88.55(18)
N2−Ru1−N4	87.59(18)
N2−Ru1−N5	90.19(19)
N2−Ru1−S1	92.05(13)
N3−Ru1−N4	90.23(18)
N3−Ru1−N5	177.81(17)
N3−Ru1−S1	89.83(13)
N4−Ru1−N5	87.92(18)
N4−Ru1−S1	179.63(13)
N5−Ru1−S1	92.00(14)

Table 2.9. Crystallographic data for $[Ru(NCCH_3)_5(DMSO)][BF_4]_2 \cdot 2CH_3CN$ (**5** with additional lattice acetonitrile).

	$[Ru(NCCH_3)_5(DMSO)][BF_4]_2 \cdot 2NCCH_3$
empirical formula	$C_{16}H_{27}B_2F_8N_7ORuS$
formula weight (g/mol)	640.19
temperature (K)	293
crystal system	Triclinic
space group	*P*-1
unit cell dimensions (Å, ^{0})	*a* = 10.779(2) *b* = 10.878(2) *c* = 13.416(3) α = 101.783(4) β = 90.281(5) γ = 111.654(3)
volume (Å^3)	1425.7(5)
Z, calcd density (mg/m^3)	2, 1.491
absorption coefficient (mm^{-1})	0.697
F(000)	644
crystal size (mm)	0.56 x 0.40 x 0.14
T_{max}, T_{min}	1.0000, 0.5985
Θ range for data	2.61-25.15
reflections collected/unique/observed	9215/4853/4126/
data/ restraints/ parameters	4853/0/334
goodness-of-fit on F^2	1.066
R1, wR2 (I≥ 2σ(I))	0.0605, 0.1558
R1, wR2 (all data)	0.0723, 0.1714
largest diff. peak, hole (e/Å^3)	1.388, -0.880

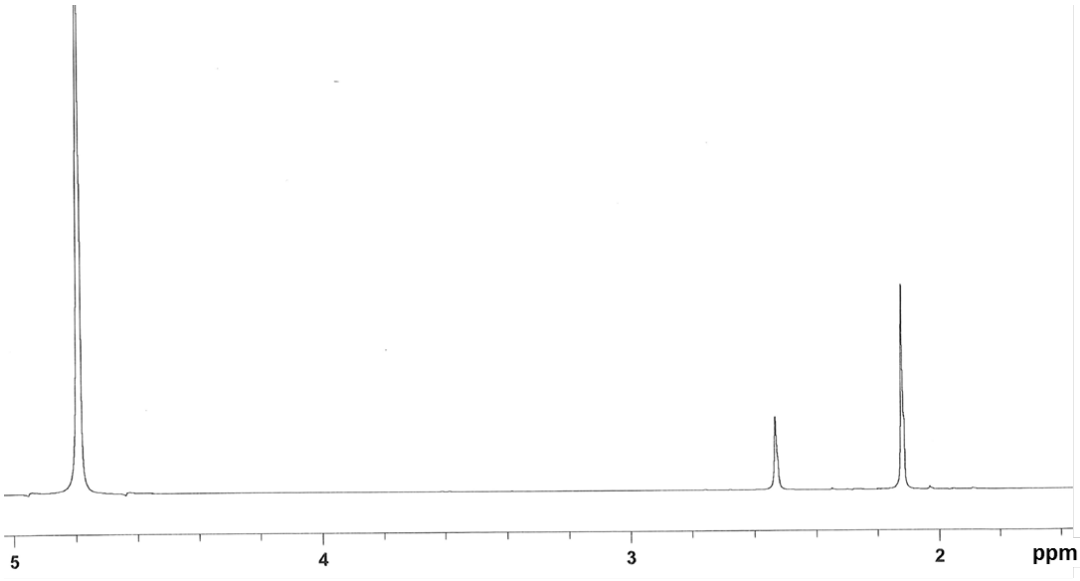

Figure 2.5. ^{1}H NMR spectrum of $[Ru(NCCH_3)_6][BF_4]_2$ (**1**) in D_2O. The resonance at δ 2.12 is from unbound CH_3CN.

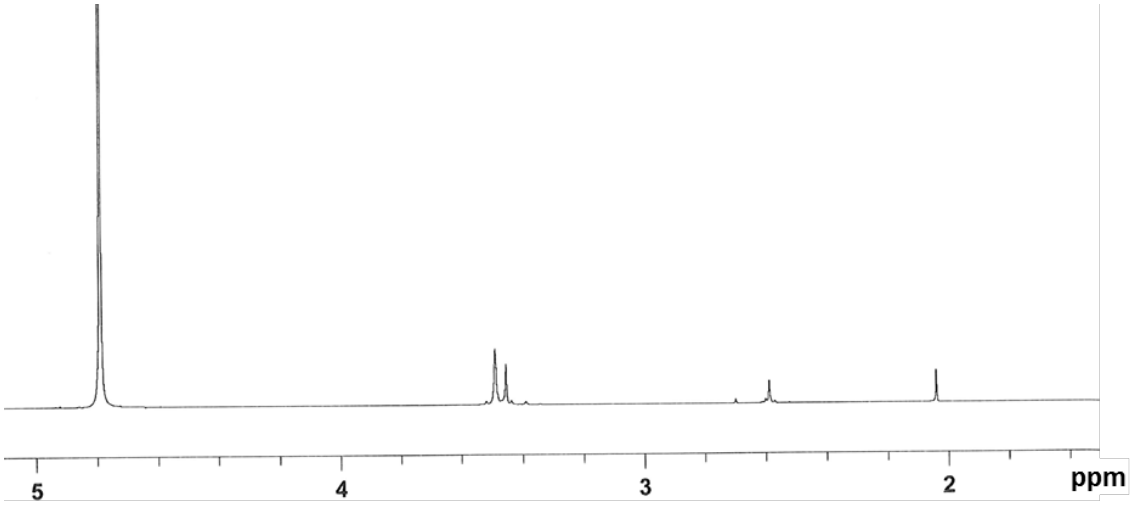

Figure 2.6. ^{1}H NMR spectrum of $[RuCl(NCCH_3)_2(DMSO)_3][BF_4]_{1.5}[Cl]_{0.5}[Na]$ (**2**) in D_2O. The resonance at δ 2.05 is from unbound acetonitrile, and the resonance at δ 2.71 is from unbound DMSO.

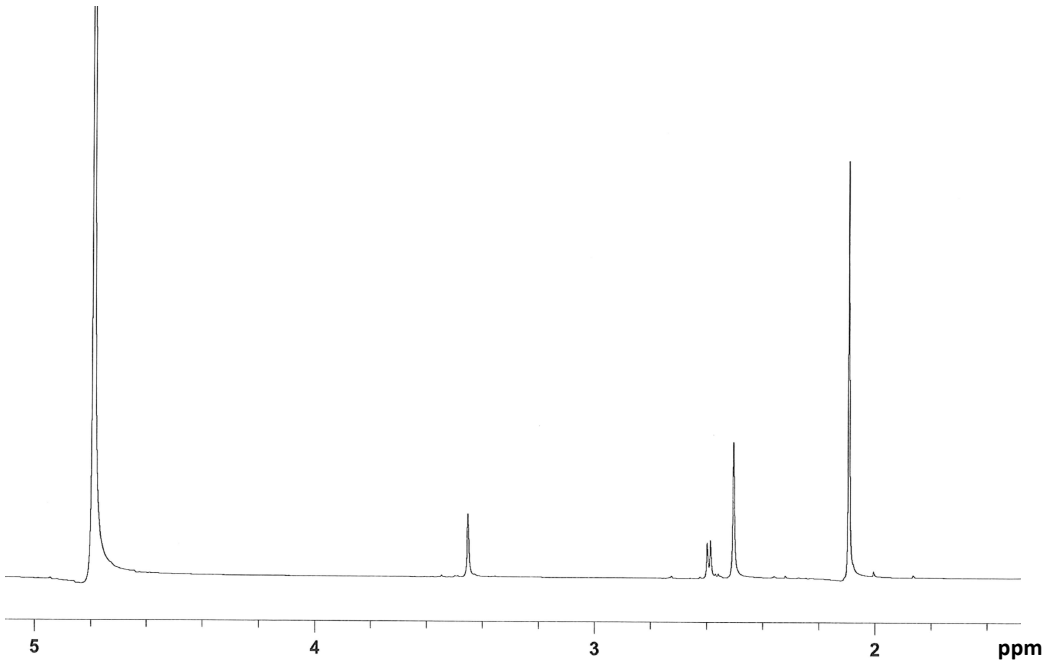

Figure 2.7. ^{1}H NMR spectrum of $[Ru(NCCH_3)_4(DMSO)_2][BF_4]_2$ (**3**) in D_2O. The resonance at δ 2.10 is from unbound acetonitrile, and the resonance at δ 2.52 is $[Ru(NCCH_3)_6][BF_4]_2$.

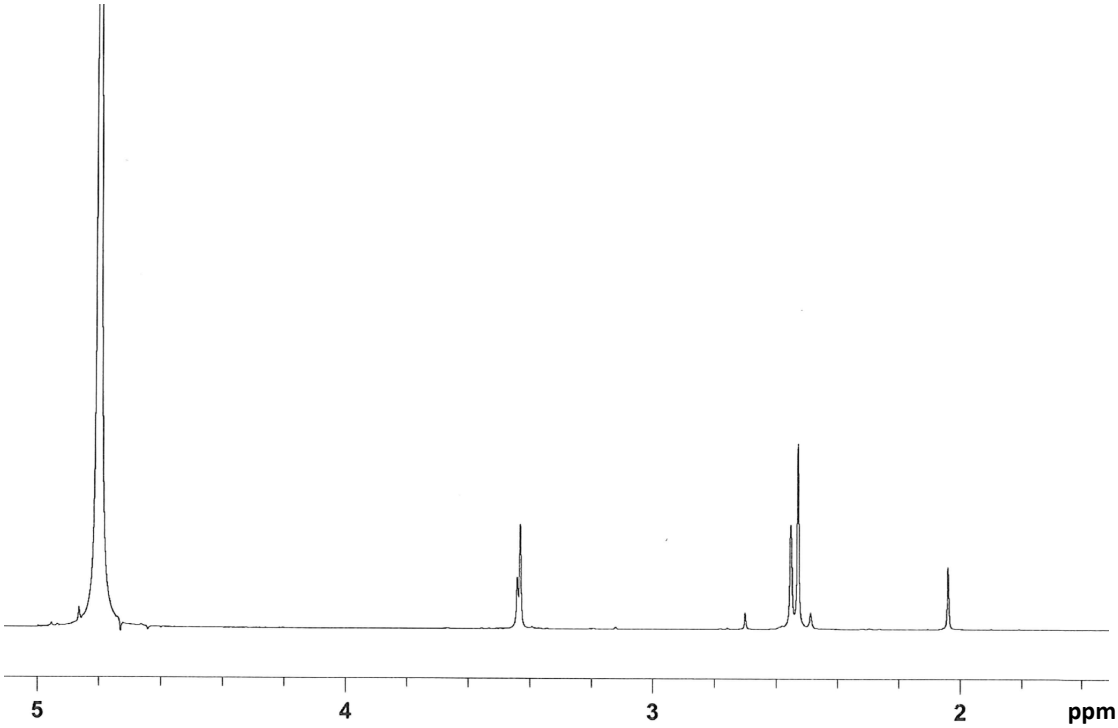

Figure 2.8. ^{1}H NMR spectrum of $[Ru(NCCH_3)_5(DMSO)][NO_3]_2$ (**4**) in D_2O. The resonance at δ 2.04 is from unbound acetonitrile, and the resonance at δ 3.71 is from unbound DMSO.

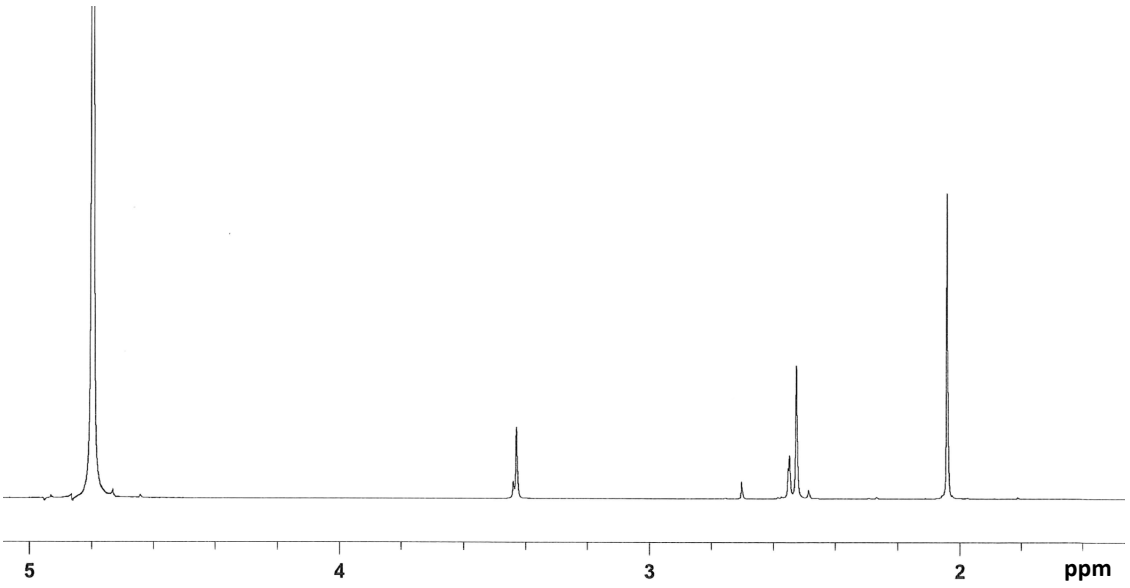

Figure 2.9. ^{1}H NMR spectrum of $[Ru(NCCH_3)_5(DMSO)][BF_4]_2$ (**5**) in D_2O. The resonance at δ 2.04 is from unbound acetonitrile, and the resonance at δ 3.71 is from unbound DMSO.

Figure 2.10. Transmittance IR spectrum of $[Ru(NCCH_3)_6][BF_4]_2$ (**1**) acquired as a Nujol mull.

Figure 2.11. Transmittance IR spectrum of [Ru $Cl(NCCH_3)_2(DMSO)_3][BF_4]_{1.5}[Cl]_{0.5}[Na]$ (**2**) acquired as a Nujol mull.

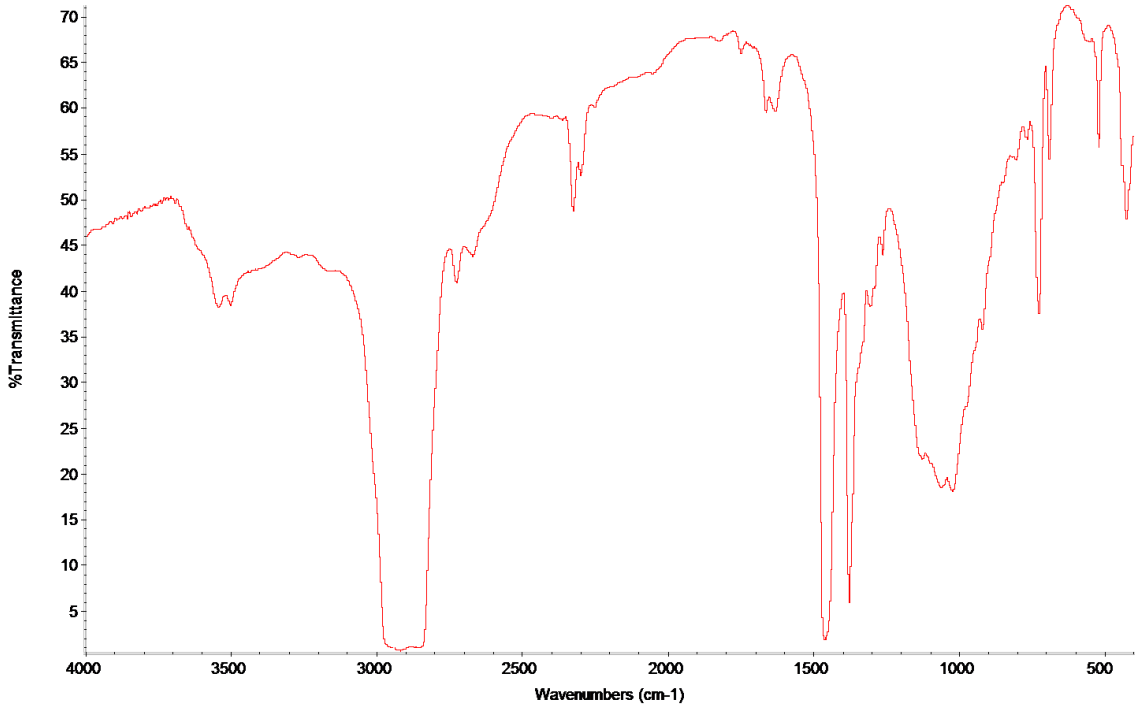

Figure 2.12. Transmittance IR spectrum of $[Ru(NCCH_3)_4(DMSO)_2][BF_4]_2$ (**3**) acquired as a Nujol mull.

Figure 2.13. Transmittance IR spectrum of $[Ru(NCCH_3)_5(DMSO)][NO_3]_2$ (**4**) acquired as a Nujol mull.

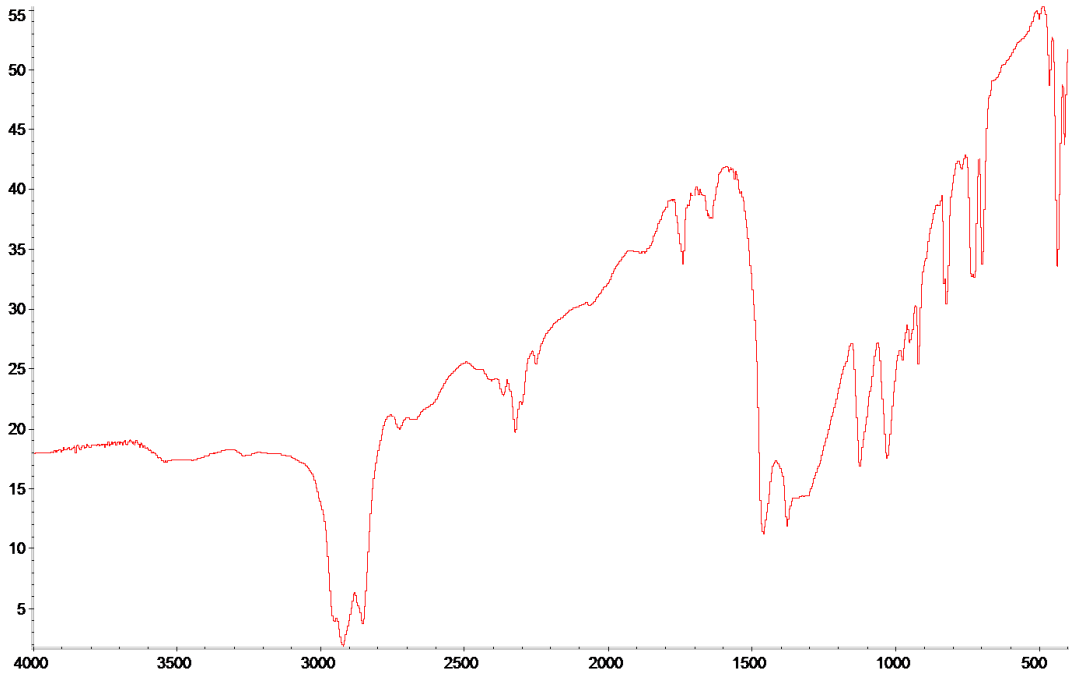

Figure 2.14. Transmittance IR spectrum of $[Ru(NCCH_3)_5(DMSO)][BF_4]_2$ (**5**) acquired as a Nujol mull.

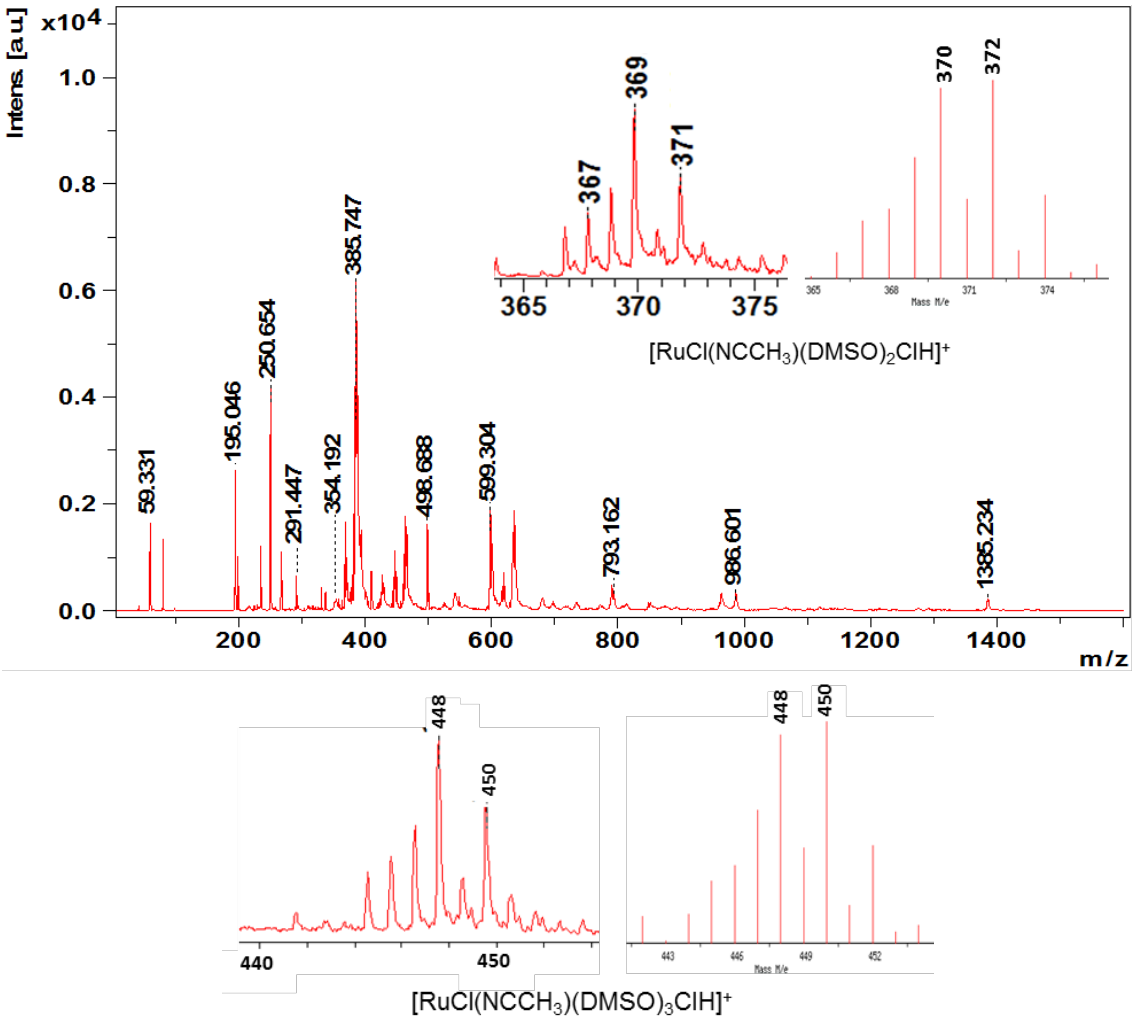

Figure 2.15. MALDI mass spectrum with insets of experimental (left) and simulated (right) envelope intensities for $[RuCl(NCCH_3)_2(DMSO)_3]\ [BF_4]_{1.5}[Cl]_{0.5}[Na]$ (**2**).

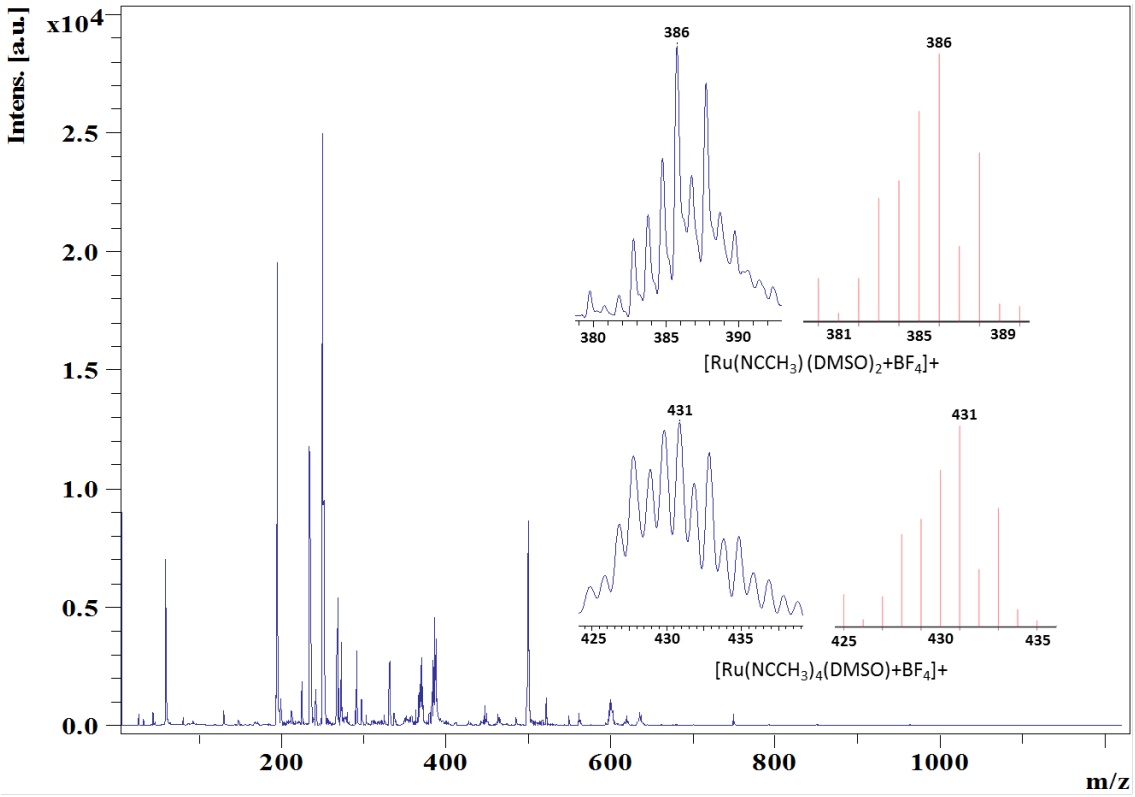

Figure 2.16. MALDI mass spectrum with insets of experimental (left) and simulated (right) envelope intensities for $[Ru(NCCH_3)_4(DMSO)_2]\,[BF_4]_2$ (**3**).

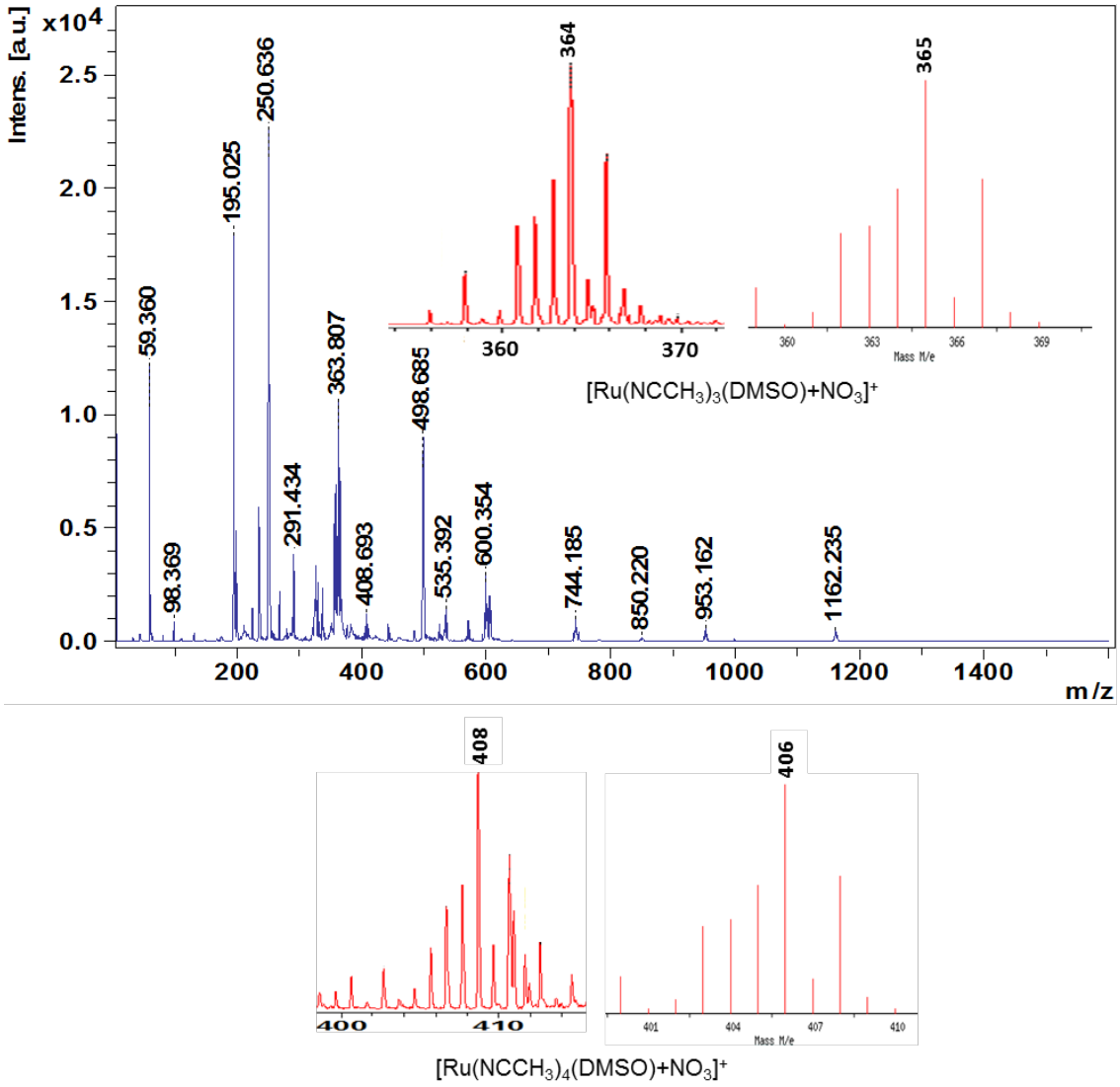

Figure 2.17. MALDI mass spectrum with insets of experimental (left) and simulated (right) peak envelope intensities for $[Ru(NCCH_3)_5(DMSO)][NO_3]_2$ (**4**).

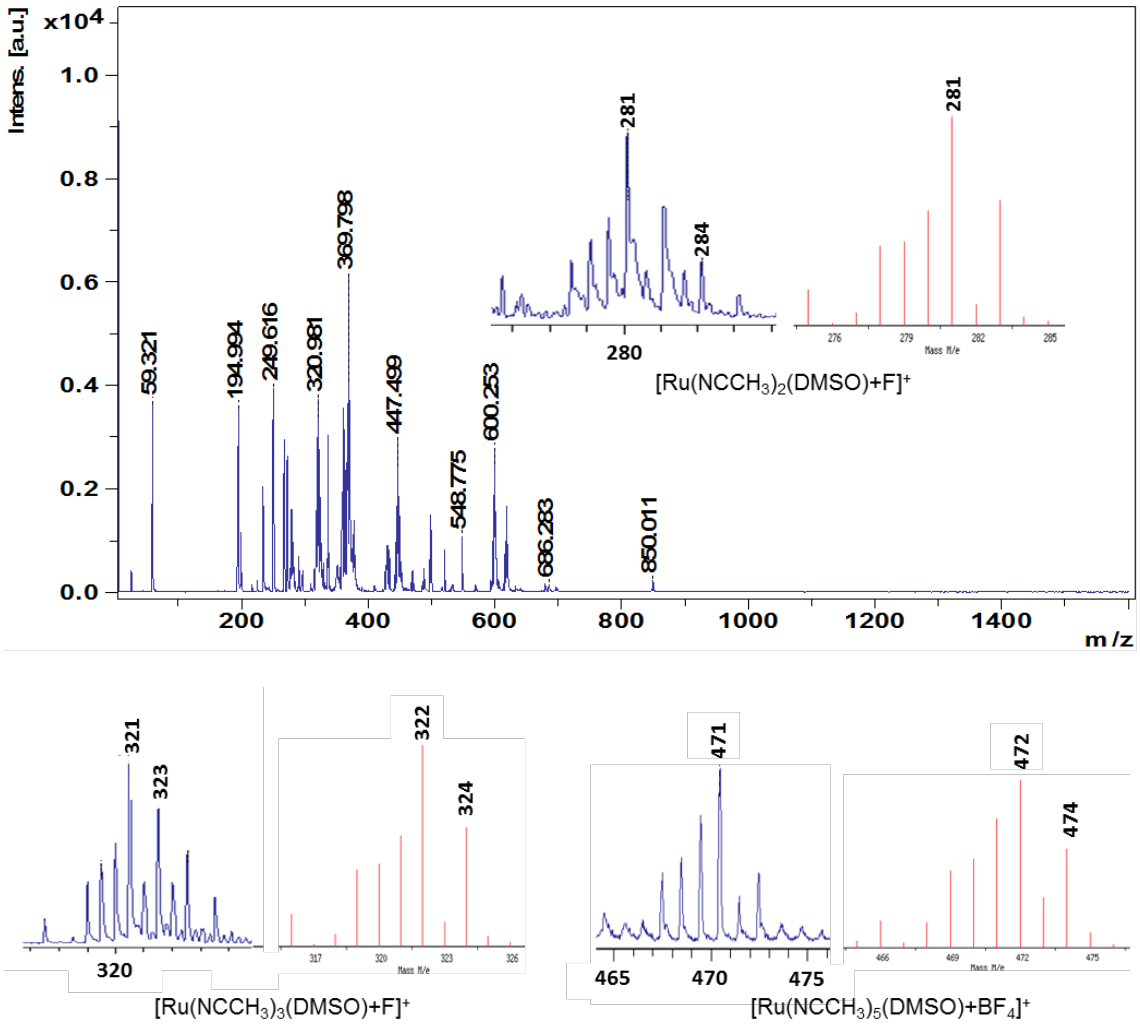

Figure 2.18. MALDI mass spectrum with insets of experimental (left) and simulated (right) peak envelope intensities for $[Ru(NCCH_3)_5(DMSO)][BF_4]_2$ (**5**).

2.6 References

(1) Brindell, M.; Kuliś, E.; Elmroth, S. K. C.; Urbańska, K.; Stochel, G., *J. Med. Chem.* **2005**, *48*, 7298-7304.

(2) Palmer, A. M.; Pena, B.; Sears, R. B.; Chen, O.; El Ojaimi, M.; Thummel, R. P.; Dunbar, K. R.; Turro, C., *Phil. Trans. R. Soc. A* **2013**, *371*, 20120135 (DOI: org/10.1098/rsta.2012.0135).

(3) Anzellotti, A.; Briceño, A., *Acta Crystallogr.* **2001**, *E57*, 538-540.

(4) Chen, C.; Lu, C.; Zheng, Q.; Ni, S.; Zhang, M.; Chen, W., *Beilstein J. Org. Chem.* **2015**, *11*, 1786-1795.

(5) Derrah, E. J.; Giesbrecht, K. E.; McDonald, R.; Rosenberg, L., *Organometallics* **2008**, *27*, 5025-5032.

(6) Monnier, F.; Peter Kundig, E., *Adv. Synth. Catal.* **2004**, *346*, 901-904.

(7) Schrock, R. R.; Johnson, B. F. G.; Lewis, J. *J. Chem. Soc., Dalton Trans.* **1974**, 951-959.

(8) Tu, Y.-J.; Mazumder, S.; Endicott, J. F.; Turro, C.; Kodanko, J. J.; Schlegel, H. B., *Inorg. Chem.* **2015**, *54*, 8003-8011.

(9) Underwood, C. C.; Stadelman, B. S.; Sleeper, M. L.; Brumaghim, J. L., *Inorg. Chim. Acta* **2013**, *405*, 470-476.

(10) Gill, T. P.; Mann, K. R. *Organometallics* **1982**, *1*, 485-488.

(11) Sharma, R.; Knoll, J. D.; Ancona, N.; Martin, P. D.; Turro, C.; Kodanko, J. J., *Inorg. Chem.* **2015**, *54*, 1901-1911.

(12) Stadelman, B. S.; Kimani, M. M.; Bayse, C. A.; McMillen, C. D.; Brumaghim, J. L., *Dalton Trans.* **2016**, *45*, 4697-4711.

(13) Dewhurst, R.; Hansen, A.; Hill, A.; Smith, M., *Organometallics* **2006**, *25*, 5843-5846.

(14) Judd, R. J.; Cao, R.; Biner, M.; Armbruster, T.; Buergi, H.-B.; Merbach, A. E.; Ludi, A., *Inorg. Chem.* **1995**, *34*, 5080-5083.

(15) Qin, Y.; Ma, Q.; Jia, A.-Q.; Chen, Q.; Zhang, Q.-F., *J. Coord. Chem.* **2013**, *66*, 1405-1415.

(16) Rapaport, I.; Helm, L.; Merbach, A. E.; Bernhard, P.; Ludi, A., *Inorg. Chem.* **1988**, *27* 873-879.

(17) Bernhard, P.; Buergi, H.-B.; Hauser, J.; Lehmann, H.; Ludi, A., *Inorg. Chem.* **1982**, *21*, 3936-3941.

(18) Bernhard, P.; Helm, L.; Ludi, A.; Merbach, A. E., *J. Am. Chem. Soc.* **1985**, *107* 312-317.

(19) Alessio, E.; Mestroni, G.; Nardin, G.; Attia, W. M.; Calligaris, M.; Sava, G.; Zorzet, S., *Inorg. Chem.* **1988**, *27*, 4099-4106.

(20) Evans, I. P.; Spencer, A.; Wilkinson, G. J., *Chem. Soc., Dalton Trans.* **1973**, *2*, 204-209.

(21) Tarighi, S.; Abbasi, A., *J. Sci. Univ. Tehran* **2007**, *33*, 19-21.

(22) Anagnostopoulou, A.; Moldrheim, E.; Katsaros, N.; Sletten, E., *J. Biol. Inorg. Chem.* **1999**, *4*, 199-208.

(23) Bratsos, I.; Serli, B.; Zangrando, E.; Katsaros, N.; Alessio, E., *Inorg. Chem.* **2007**, *46*, 975-992.

(24) Shukla, S. N.; Gaur, P.; Kaur, H.; Prasad, M., *J. Coord. Chem.* **2007**, *60*, 1047-1055.

(25) Rüba, E.; Simanko, W.; Mereiter, K.; Schmid, R.; Kirchner, K., *Inorg. Chem.* **2000**, *39*, 382-384.

(26) Ferrer, Í.; Rich, J.; Fontrodona, X.; Rodríguez, M.; Romero, I., *Dalton Trans.* **2013**, *42*, 13461-13469.

(27) Gottlieb, H. E.; Kotlyar, V.; Nudelman, A. *J. Org. Chem.* **1997**, *62*, 7512-7515.

(28) Leigh, G. J.; Sanders, J. R.; Hitchcock, P. B.; Fernandes, J. S.; Togrou, M., *Inorg. Chim. Acta* **2002**, *330*, 197-212.

(29) Lackner, W.; Standfest-Hauser, C. M.; Mereiter, K.; Schmid, R.; Kirchner, K., *Inorg. Chim. Acta* **2004**, *357*, 2721-2727.

(30) Jansen, A.; Goerls, H.; Pitter, S., *Organometallics* **2000**, *19*, 135-138.

(31) Concepción, J.; Just, O.; Leiva, A. M.; Loeb, B.; Rees, W. S., *Inorg. Chem.* **2002**, *41*, 5937-5939.

(32) Piggot, P. M. T.; Hall, L. A.; White, A. J. P.; Williams, D. J., *Inorg. Chim. Acta* **2004**, *357*, 250-258.

(33) Berben, L. A.; Faia, M. C.; Crawford, N. R. M.; Long, J. R., *Inorg. Chem.* **2006**, *45*, 6378-6386.

(34) Lee, C.-C.; Liu, Y.-H.; Peng, S.-M.; Chou, P.-T.; Chen, J.-T.; Liu, S.-T., *Polyhedron* **2012**, *35*, 23-30.

(35) Apex 3, Bruker AXS, Inc., Madison, WI, 2015.

(36) CrystalClear, Rigaku and Molecular Structure Corporation, The Woodlands, TX, 2006.

(37) Sheldrick, G., A short history of SHELX. *Acta Crystallogr.* **2008**, *A64*, 112-122.

(38) Spek, A. L., *J. Appl. Crystallogr.* **2003,** *36*, 7-13.

CHAPTER THREE

SYNTHESIS, CHARACTERIZATION, AND STUDY OF THE ANTIOXIDANT ACTIVITY OF NOVEL RUTHENIUM IMIDAZOLE-2-THIONE AND SELONE COMPLEXES

3.1 Introduction

Recently, ruthenium complexes with sulfur- and selenium-containing ligands have attracted attention for their catalytic[1-3] and biological[3-10] applications. Ruthenium can mimic iron in biological systems because it is redox active and can bind to sulfur in biomolecules.[11-13] In cells, Fe(II) can generate damaging hydroxyl radical in the presence of hydrogen peroxide (Reaction 3.1) that cause oxidative damage and cell death that can lead to cancer, cardiovascular diseases, and neurodegenerative diseases.[14-18] Ru(II) also may generate damaging hydroxyl radical, similar to Fe(II) (Reaction 3.1).[19] Some sulfur- and selenium-containing compounds can scavenge hydroxyl radical to prevent oxidative damage,[20-21] and metal coordination can improve this activity.[22-26]

$$Ru(II)/Fe(II) + H_2O_2 \rightarrow Ru(III)/Fe(III) + {}^{\bullet}OH + {}^{-}OH \quad (3.1)$$

Cysteine, selenocysteine, ergothioneine, and selenoneine are common biological sulfur and selenium compounds (Figure 3.1) that can bind metal ions. These compounds prevent metal-mediated DNA damage by hydroxyl radical, and are widely investigated for their roles as antioxidants to prevent diseases caused by oxidative stress.[15,18,27-28] In particular, imidazole thiones (C=S) and selones (C=Se) are versatile metal-binding ligands that have established or emerging biological roles. Ergothioneine prevents copper-mediated oxidative DNA damage through metal binding[29] and also scavenges reactive

oxygen species (ROS; Figure 3.1).[30-32] Selenoneine is also a potent radical scavenger,[33] and may help detoxify heavy metals[34-37] In addition, imidazole thione and selone compounds have pharmaceutical importance as anti-thyroid,[38-39] antioxidant[26,39 -40] antifungal[41] and antimicrobial,[42] and compounds. Similar to ergothioneine, the anti-thyroid drug methimazole (MMI) as well as the dimethylated dmit and dmise scavenge ROS and prevent metal-mediated DNA damage (Figure 3.1).[23, 42-46]

Figure 3.1. Imidazole thione and selone compounds, derivatives, and their biological forms.

Although imidazole thione and selone ligands are well known to bind iron and other late first-row transition metals,[26] only a few ruthenium complexes with imidazole thione and selone ligands are known (Figure 3.2).[1,47-50] Methimazole binds Ru(II) as a monodentate ligand coordinated through the S atom, and when this complex is treated with[1,47-50] to deprotonate the imidazole nitrogen, methimazole binds as a bidentate ligand through the S and aromatic N atoms.[47,50] Ru(II) coordination of bidentate thione and selone ligands with appended thioether or selenoether groups are also reported (Figure3.2).[1,47-50]

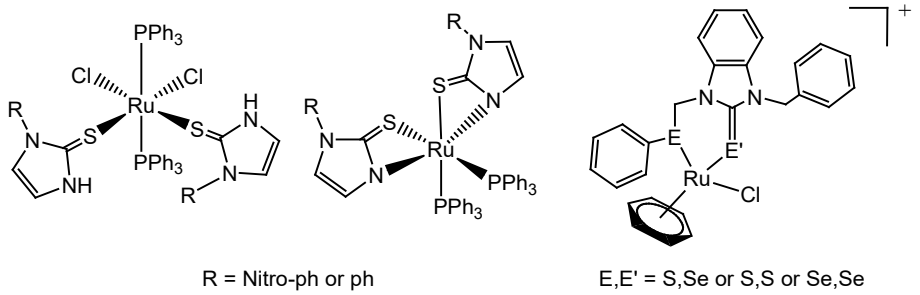

Figure 3.2. Reported Ru(II) complexes with imidazole-2-thione and selone ligands (R = alkyl or aryl; E = S or Se).[1,47]

In this work, we present the syntheses of a series of novel homoleptic and heteroleptic Ru(III) and Ru(II) thione and selone complexes with the formulae $[RuL_6]^{3+}$, $[RuL_6]^{2+}$, and RuL_4Cl_2 (L = MMI, dmit, and dmise), significantly expanding the repertoire of known ruthenium thione and selone complexes. We also examine hydrogen peroxide reactivity of the $[RuL_6]^{3+}$ complexes and the ability of $[Ru(MMI)_6]^{3+}$ to prevent iron-mediated DNA damage. Unlike previous complexes, these Ru(II) complexes allow comparison of the effects of multiple ruthenium oxidation states and thione or selone ligands on their properties and reactivity. In addition, our methods open the door to synthesize a wide variety of ruthenium thione and selone complexes to explore the applications of these complexes.

3.2 Results and Discussion

Synthesis of Ru(III) thione and selone complexes. Homoleptic $[RuL_6]Cl_3$ complexes were synthesized by treating $RuCl_3 \cdot 3H_2O$ with 6 equiv of MMI (**1a**), dmit (**2**), or dmise (**3**) in a 2:1 mixture of methanol/dichloromethane under argon (Scheme 3.1). Selone complex **3** forms after 3 h, notably faster than formation of thione complexes **1a** and **2** (5 h). All three complexes were synthesized in good yields (58-69%) and are stable to water and air as solids. In acetonitrile solutions, the compounds are stable in air and water for at least 12 h.

To determine whether $[Ru(MMI)_6]^{3+}$ could also be synthesized from a Ru(II) starting material, $[Ru(NCCH_3)_6][BF_4]_2$ was treated with 6 equiv MMI in a 2:1 mixture of methanol/dichloromethane, and heated to reflux for 4 h under argon, replacing all

acetonitrile ligands with MMI ligands (Scheme 3.1). The hot reaction mixture was then opened to air and allowed to oxidize (Scheme 3.1), and at the same time, 1 equiv of $NaNO_3$ was added to provide additional counterions for a Ru(III) species. The resulting $[Ru(MMI)_6][BF_4]_2[NO_3]$ complex (**1b**) is formed in a similar yield (65%) as the $[RuL_6]^{3+}$ complexes formed from $RuCl_3 \cdot 3H_2O$.

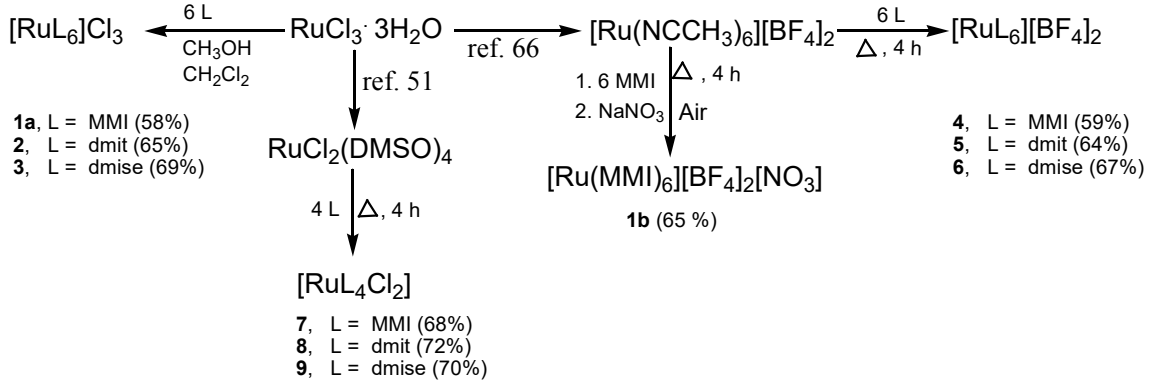

Scheme 3.1. Synthesis of Ru-thione and -selone complexes **1**-**9**. All reactions were carried out in a 2:1 ratio of acetonitrile to CH_2Cl_2.

Synthesis of Ru(II) thione and selone complexes. Ru(II) analogs of the $[RuL_6]^{3+}$ complexes were synthesized under argon by heating a solution of $[Ru(NCCH_3)_6][BF_4]_2$ in 2:1 methanol/dichloromethane to reflux with 6 equiv of thione or selone ligand to yield $[Ru(L)_6][BF_4]_2$, where L = MMI (**4**), dmit (**5**), and dmise (**6**). Yields of these Ru(II) complexes are similar to those of their Ru(III) analogs (59-67%; Scheme 1). Complexes **4**, **5**, and **6** are stable under inert atmosphere, both as solids and in organic solvents. Air or water exposure results in oxidative decomposition that occurs faster with the dmise complex **6** (~ 1 h) than for thione compounds **4** and **5** (~3 h).

To obtain heteroleptic Ru(II) solvato complexes with thione and selone ligands, $Ru(DMSO)_4Cl_2$[51] (DMSO = dimethylsulfoxide)was treated with 4 equiv of thione or selone

compound and heated to reflux for 4 h to yield RuL_4Cl_2 complexes, where L = MMI (**7**), dmit (**8**), and dmise (**9**) (Scheme 3.1). Air and water stability of compounds **7-9** are similar to that of complexes **4-6**. Similar to acetonitrile ligands in $[Ru(NCCH_3)_6]^{2+}$, DMSO is also a photolabile ligand, and $Ru(DMSO)_4Cl_2$ has been studied for its antitumor activity as a photosentizer for photodynamic therapy.[52] Thus, the DMSO ligands on these heteroleptic complexes provide additional sites for potential ligand exchange and photoreactivity.

MALDI mass spectrometry results (Figures 3.29-3.38) show the molecular ion with an associated chloride ion, $[Ru(MMI)_6]Cl]^{2+}$, for **1a**, but for **1b**, only $[Ru(MMI)_2(BF_4)(NO_3)]^+$ with two coordinated MMI ligands is observed. Similarly, mass spectrometry data for Ru(III) complexes **2** and **3** show species with a maximum of two thione or selone ligands coordinated: $[Ru(dmit)_2Cl_2]^+$ and $[Ru(dmise)_2Cl_2]^+$, respectively. For mass spectrometry data of Ru(II) ions **4-6**, a maximum of three or four of the six thione/selone ligands remained associated to afford ions with the formulae $[Ru(MMI)_4F]^+$, $[Ru(dmit)_4BF_4]^+$, and $[Ru(dmise)_3(BF_4)_2H]^+$, respectively. RuL_4Cl_2 complexes **7-9** also were subject to thione or selone ligand loss under mass spectrometry conditions, yielding $[RuCl_2(MMI)_3H]^+$, $[Ru(dmit)_2Cl_2H]^+$, and $[Ru(dmise)_2Cl_2H]^+$ ions, respectively. Accurate elemental analyses were obtained for all ten complexes, indicating that mass spectrometry may not be a reliable method to assess thione/selone coordination stoichiometry in these complexes.

Structural analysis of ruthenium - thione complexes. Single crystals of **1a**, **1b**, and **5** were grown by slow diffusion of diethyl ether into acetonitrile solutions of the complexes and characterized by X-ray structural analysis. All three complexes have distorted

octahedral geometry around the central ruthenium ion (S-Ru-S angles of 84.83(3)-95.17(3)º for **1a** and 86.25(11)-93.75(11)º for **5**) and are bound through the sulfur atoms of the six thione ligands (Figure 3.3 with bond distances and angles in Table 3.1; the structure of **1b** and bond lengths and angles are provided in Figure 3.9 and Table 3.5, respectively).

Ru-S bond lengths in **1a** range from 2.3930(7) to 2.4033(7) Å (and from 2.4010(6)-2.4155(7) Å in **1b**), slightly shorter in average than in **5** (2.403(3)-2.409(3) Å). The Ru-S bond lengths in **5** are similar to those for the reported Ru(II) complexes with two monodentate thione ligands, $RuL_2(PPh_3)_2Cl_2$ (Figure 3.2, left), where L = 1-(4-methyl-phenyl)-imidazole-2-thione (2.478(2)Å[47]), 1-(4-chlorophenyl)imidazole-2-thione (2.4087(15) Å[50]), or 1,3-dihydrobenzoimidazole-2-thione (2.435(3) Å[1]).

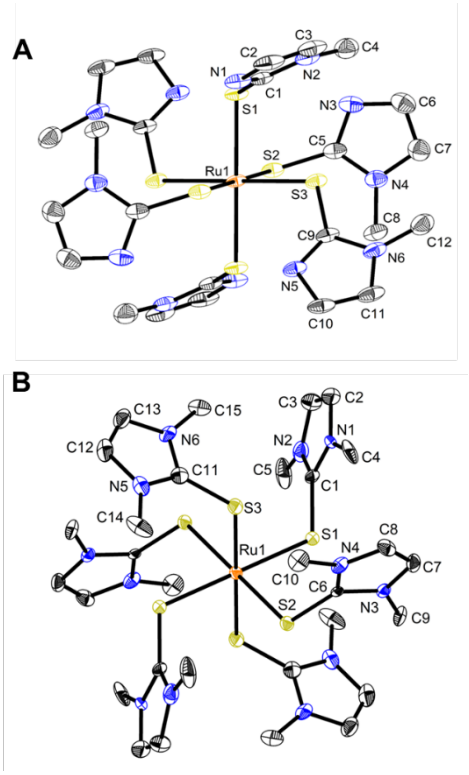

Figure 3.3. Crystal structure diagrams of A) $[Ru(MMI)_6]Cl_3$ (**1a**) and B) $[Ru(dmit)_6](BF_4)_2$ (**5**) with 50% probability density ellipsoids. Hydrogen atoms and counterions are omitted for clarity.

Table 3.1. Selected bond lengths (Å) and angles (°) for $[Ru(MMI)_6]Cl_3$ (**1a**) and $[Ru(dmit)_6](BF_4)_2$ (**5**) and unbound thione ligands.

	1a	**5**	**MMI[53]**	**dmit[54]**
Ru1—S1	2.4033(7)	2.411(3)		
Ru1—S2	2.4002(7)	2.409(3)		
Ru1—S3	2.3930(7)	2.403(3)		
S1—C1	1.726(3)	1.719(13)	1.685(2)	1.696(5)
S3—C9	1.717(3)	1.720(15)		
N1-C1	1.345(6)	1.328(16)	1.345(3)	1.349(4)
N2-C1	1.387(6)	1.379(17)	1.387(4)	1.392(6)
S3-Ru1-S3	180.0	180.0		
S3-Ru1-S2	95.17(3)	91.80(11)		
S3-Ru1-S2	84.83(3)	88.20(11)		
S3-Ru1-S1	86.55(2)	87.20(11)		
S2-Ru1-S1	90.47(2)	93.75(11)		
S3-Ru1-S1	93.45(2)	92.80(11)		
S2-Ru1-S1	89.53(2)	86.25(11)		
S1-Ru1-S1	180.0	180.0		

C=S bond lengths range from 1.717(3)-1.726(3) Å and 1.718(2)-1.725(2) Å in **1a** and **1b**, respectively, whereas in **5**, C=S bonds range from 1.719(12)-1.720(15) Å. In all three complexes, these bond distances are significantly longer than the C=S bonds in unbound methimazole (1.685(2) Å[53]) or dmit (1.696(5)Å[54]), respectively. Average N-C bond lengths (1.348(4)-1.387(4) Å) for the methimazole ligands in **1a** and **1b** are similar to those of N-C bonds in unbound methimazole (1.345(6) and 1.387(4) Å[53]). Likewise, N-C bond lengths for dmit complex **5** (1.328(16)-1.379(17) Å) are not significantly different from those in unbound dmit (1.349(4)-1.392(6) Å[54]). Lengthening of the C-S bonds upon Ru coordination is consistent with metal binding causing an increased contribution from the zwitterionic resonance structure of the thione ligand, a trend that is observed for the iron-thione complexes $Fe(dmit)_2Cl_2$ and $[Fe(dmit)_4][OTf]_2$.[26]

Infrared and NMR spectroscopy. All the synthesized ruthenium thione and selone complexes (**1a**, **1b**, and **2**-**9**) were characterized using infrared (IR) spectroscopy (Table 3.2 and Figures 3.18-3.27) to determine the bonding characteristics of the thione and selone ligands. Ru-MMI complexes **1a**, **1b**, **4**, and **7** have C=S stretching bands around 1151 cm^{-1}, comparable to that for unbound MMI (1150 cm^{-1}).[55] Similarly, Ru-coordinated dmise ligands in complexes **3**, **6**, and **9** have C=Se stretching bands from 1150-1152 cm^{-1}, little shifted compared to unbound dmise (1147 cm^{-1}).[56] Ru-bound dmit ligands in **2**, **5**, and **8** have C=S stretching bands ranging from 1171-1172 cm^{-1}, only slightly shifted to lower energy compared to unbound dmit (1181 cm^{-1}).[57-59] The lack of significant change between Ru-bound and unbound MMI and dmise ligands indicate that they are primarily σ- and π-donors without significant π-acceptor character. Dmit complexes **2**, **5**, and **8** show slight backbonding interactions, consistent with the longer C=S bonds observed in these

Table 3.2. C=S/C=Se IR stretches and ^{1}H NMR resonances (in D_2O).[a]

Compound	C=S/C=Se (cm^{-1})	^{1}H NMR shifts (δ)	
		CH_3	Olefinic C-H
MMI	1150	3.52	6.91, 6.98
Dmit	1181	3.48	6.95
Dmise	1147	3.61	7.16
$[Ru(MMI)_6]Cl_3$ (**1a**)	1151	–	–
$[Ru(MMI)_6][BF_4]_2[NO_3]$ (**1b**)	1151	–	–
$[Ru(dmit)_6]Cl_3$ (**2**)	1171	–	–
$[Ru(dmise)_6]Cl_3$ (**3**)	1150	–	–
$[Ru(MMI)_6][BF_4]_2$ (**4**)	1151	3.58	6.95, 7.03
$[Ru(dmit)_6][BF_4]_2$ (**5**)	1171	3.59	7.16
$[Ru(dmise)_6][BF_4]_2$ (**6**)	1152	3.53	6.98
$Ru(MMI)_4Cl_2$ (**7**)	1151	3.89	7.59, 7.71
$Ru(dmit)_4Cl_2$ (**8**)	1172	3.76	7.80
$Ru(dmise)_4Cl_2$ (**9**)	1151	3.72	7.75

[a] ^{1}H NMR spectra are not obtainable for Ru(III) complexes.

complexes compared to unbound dmit. Similar thione and selone bonding behavior was

observed for thione and selone complexes of Cu(I/II), Fe(II), and Zn(II).[23,26,60-61] No differences in ligand donor properties are observed with Ru oxidation state changes, since IR stretches of analogous Ru(III) and Ru(II) complexes are identical.

For the unbound ligands and the Ru(II) complexes (Table 3.2 and Figures 3.9-3.11), ^{1}H NMR spectra in D_2O were collected immediately after sample preparation; ^{1}H NMR spectra of complexes **1a**, **1b**, and **2-3** are not obtainable due to the paramagnetic properties of Ru(III). Upon metal coordination, the *N*-methyl group resonances for complexes **4-9** shift slightly downfield from the unbound ligands (Figure 3.12-3.17). ^{1}H NMR data show downfield shifts for the olefinic resonances of MMI in **4** (δ 6.95 and 7.03) and dmit in **5** (δ 7.16) compared to the resonances for unbound MMI (δ 6.91, 6.98), and dmit (δ 6.95). In contrast, ^{1}H NMR data show an upfield shift for the olefinic proton resonances of dmise in **6** (δ 6.98) compared to the resonances of unbound dmise (δ 7.16). This shifting of the olefinic proton resonances indicates that Ru(II) binding to MMI or dmit results in an increased contribution of the zwitterionic resonance structure (with increased negative charge on the sulfur atom and an aromatic imidazole ring) compared to the unbound thiones. This trend has been observed previously for iron-thione such as $Fe(dmit)_2Cl_2$ and $[Fe(dmit)_4][OTf]_2$ complexes.[23,26,59]

Similar, but more pronounced downfield shifts upon Ru(II) coordination are observed for the olefinic proton resonance shifts are observed for the *tetrakis* thione/selone complexes **7-9** (Table 3.2). Although it may seem that complexes with two Cl^- ligands would disfavor the thione resonance structure that places more negative charge on the S atoms, the greater electron affinity of Cl relative to S suggests that the Cl^- ligands stabilize

their negative charges better than thione S atoms. Therefore, while both the chloride and sulfur atoms are formally π-donating, the Ru-Cl bonds are more electron withdrawing overall than the Ru-S bonds and may favor the zwitterionic resonance structure of the thione ligands that places partial negative charges on the sulfur atoms.

In contrast, based on NMR shifts, Ru(II) binding to dmise in **6** disfavors this zwitterionic resonance structure compared to unbound dmise, a trend that has not been reported. The analogous dmit complex **5** shows slight Ru-thione backbonding by IR, corroborated by a downfield shift of δ 0.21 the olefinic protons compared to unbound dmit. The analogous MMI complex **4** shows little shift in the olefinic resonances (δ 0.04 and 0.05) compared to unbound MMI. In contrast, the olefinic resonances of **6** show an *upfield* shift of δ 0.18 compared to unbound dmise. RuL_4Cl_2 complexes **7**, **8**, and **9** show significant downfield shifts of the oelfinic protons (δ 0.68-0.73, 0.85, and 0.59, respectively) compared to the corresponding unbound ligands. This unusual effect observed for **6** may be a result of six electron-rich dmise ligands coordinating a single Ru(II) ion.

UV-vis kinetic studies with H_2O_2. To examine the potential antioxidant activity of the air-stable $[RuL_6]^{3+}$ complexes, UV-vis spectroscopy was used to determine their reactivity with hydrogen peroxide. The π- π^* transition bands for the Ru-bound thione or selone ligands in acetonitrile solutions of **1a**, **2**, and **3** are observed at 265, 272, and 275 nm, respectively (spectra for **1a** is shown in Figure 3.4, and spectra for **2** and **3** are shown in Figures 3.39-3.43). In addition to these UV bands, charge transfer bands are observed for complexes **1a** and **2** at 683 and 567 nm, respectively, but no charge transfer band appears in the visible region for complex **3**.

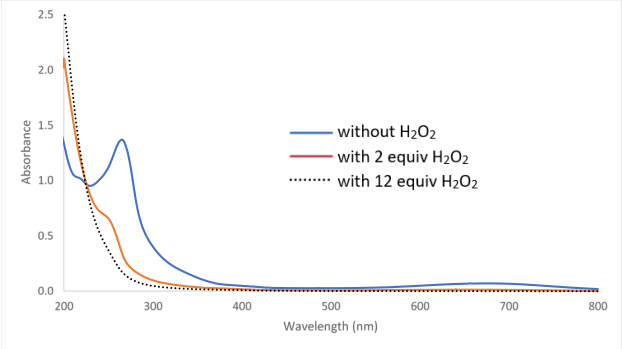

Figure 3.4. UV-vis spectra of $[Ru(MMI)_6]Cl_3$ (100 μM) in acetonitrile before and after addition of 2 and 12 equiv H_2O_2

When acetonitrile solutions of complexes **1a**, **2**, and **3** are treated with 2 or 12 equiv of H_2O_2, the highly colored Ru(III) solutions lightened significantly over time and brown precipitate formed. In the UV-vis spectra, hydrogen peroxide addition reduced the intensity of the π- π^* transition bands of the imidazole thione or selone ligands, and these bands were no longer visible after addition of 12 equiv (Figure 3.4 and Figures 3.44). Disappearance of this absorbance band occurred over different times for the different complexes: 1 h for MMI complex **1a** and dmise complex **3**, and 3 h for dmit complex **2**.

Kinetics of the reactivity of **1a**, **2**, and **3** with 2 and 12 equiv hydrogen peroxide were measured by observing the decrease in the π- π^* transition of the thione or selone

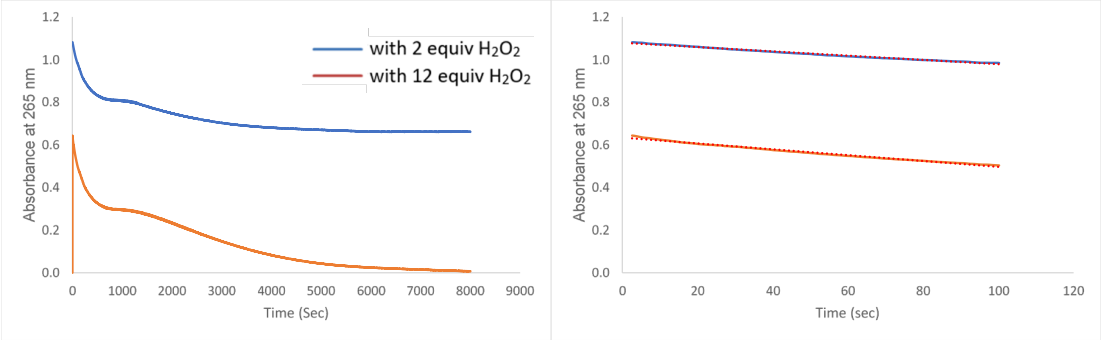

Figure 3.5. Kinetics of $[Ru(MMI)_6]Cl_3$ with A) 2 equiv and 12 equiv H_2O_2, (0-8000 s) and B) The best-fit line fit to the initial linear portion of the kinetic curves for 2 equiv and 12 equiv H_2O_2 (0-100 sec, $R^2 = 0.991$ and $R^2 = 0.990$, respectively).

ligand at λ_{max} values of 265, 272, and 275 nm, respectively. Initial rates were determined by the slope of the best-fit line fit to the initial linear portion of the kinetic curves (Figure 3.5 and Figures 3.43-3.44). For all three complexes, initial rates of reactivity with 2 and 12 equiv of H_2O_2 are very similar, indicating the reaction is independent of hydrogen peroxide concentration Table 3.3. The rate of H_2O_2 reactivity for MMI complex **1a** was the fastest, followed closely by dmise complex **2**, and the rate of H_2O_2 reactivity for dmit complex **2** was approximately 30 times slower than for **1a** or **3**.

Table 3.3. Initial rates for reaction of complexes **1a**, **2**, and **3** with H_2O_2.

Complex	**Initial rate × 10^{-3} (s^{-1})**	
	2 equiv H_2O_2	**12 equiv H_2O_2**
$[Ru(MMI)_6]Cl_3$ (**1a**)	1.0 ± 0.1	1.4 ± 0.1
$[Ru(dmit)_6]Cl_3$ (**2**)	0.05 ± 0.002	0.05 ± 0.002
$[Ru(dmise)_6]Cl_3$ (**3**)	1.7 ± 0.1	1.7 ± 0.2

To determine the products of hydrogen peroxide oxidations, solutions of **1a**, **2**, and **3** were combined with 12 equiv H_2O_2 and allowed to sit for 3 h before the solvent was removed *in vacuo* and the resulting solids were analyzed by MALDI mass spectrometry (Figures 3.38-3.43). The positive-ion MALDI mass spectrum of the product that was formed from treating $[Ru(MMI)_6]Cl_3$ with 12 equiv H_2O_2 shows formation of the methylimidazolium cation (m/z = 84.7) and $[RuCl_3H]^+$ (m/z = 209; Figure 3.38), while $[SO_2H]^-$ (m/z = 64.5), sulfite $[SO_3H]^-$ (m/z 80.9), and sulfate $[SO_4H]^-$ (m/z 96.3) were observed in the negative-ion MALDI mass spectrum of the same reaction (Figure 3.39). Similar H_2O_2 reaction products were observed for complexes **2** and **3** (Figures 3.40 and 43). Based on these observations, Ru-coordinated MMI and dmise much more efficiently scavenge H_2O_2 compared to Ru-bound dmit (Scheme 3.2).

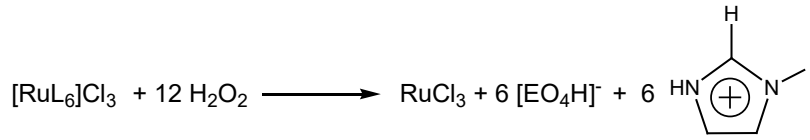

Scheme 3.2. Reactivity of $[RuL_6]Cl_3$ with H_2O_2; E = S, L= MMI or dmit; E = Se, L = dmise.

Reactivity of ruthenium-thione/selone complexes with reactive oxygen species (ROS) has not been examined, but oxidation of a Ru(II)-bound thiolate ligand in $[Ru(DPPBT)_3]^-$ (DPPBT = 2-(diphenylphosphino)benzene thiolate) to a Ru(III)-bound sulfinate ligand was reported upon O_2 exposure. Treating this Ru(III)-sulfinate species with hydroxide rapidly reduces it to a Ru(II)-sulfinate complex.[62] On the other hand, addition of selenious acid to carbon-supported catalysts (Ru/C) increases the catalytic activity by selenium prevention of RuO_2-film formation.[63] Therefore, selenium can react with ruthenium metal to form $RuSe_y$ or $RuSe_yO_x$ species (where $y < 2$, $x < 2$), thereby enhancing catalytic activity.[63] Uncoordinated thione and selone compounds have been widely investigated as antioxidants[26,65] and dmit and dmise sacrificially react with two equivalents of hydrogen peroxide to yield dimethylimidazolium and S/SeO_x species.[44] Ruthenium can bind up to six thione and selone ligands (**1a**, **2**, and **3**), potentially enhancing the antioxidant activity of imidazole thiones and selones.

DNA damage prevention studies. To determine whether the H_2O_2 reactivity of these Ru(III) complexes translates into prevention of biological oxidation, we examined the ability of $[Ru(MMI)_6]Cl_3$ (**3**) to prevent oxidative DNA damage. In this assay, plasmid DNA is treated with Fe(II)/H_2O_2 to generate DNA-damaging hydroxyl radical (Reaction 1.1) in the presence and absence of **3**, since this complex reacts with hydrogen peroxide the fastest. Addition of $[Ru(MMI)_6]Cl_3$ in the presence of H_2O_2 causes no DNA damage

(Figure 3.6, lane 3), but Fe(II)/H_2O_2 causes 86% DNA damage (lane 4). When DNA is treated with Fe(II)/H_2O_2 and increasing concentrations of **3** (0.1-1000 μM; lanes 5-13), DNA damage is significantly reduced at low micromolar concentrations, with over 90% DNA damage inhibited at 10 μM.

Since this Ru(III)-thione complex acts as an antioxidant, the graph of DNA damage inhibition vs. complex **3** concentration was fit to a sigmoidal dose-response curve, and the concentration at which **3** prevents 50% of the DNA damage (IC_{50} value) is 1.76 μM (Figure 3.7). This IC_{50} value for **3** is 3.28 fold lower than for prevention of Fe(II)/H_2O_2-mediated DNA damage by MMI alone (IC_{50} = 5.78 ± 0.07 μM[65]). Thus, Ru-MMI coordination

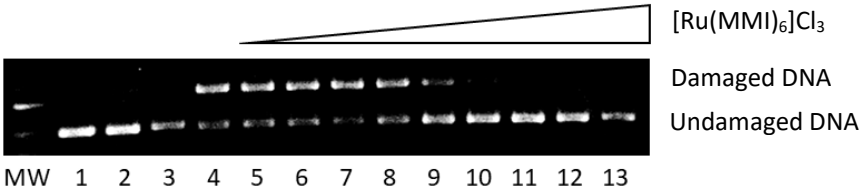

Figure 3.6. Gel electrophoresis image of iron-mediated DNA damage prevention by $[Ru(MMI)_6]Cl_3$. Lanes are MW: 1 kb molecular weight marker; lane 1: plasmid DNA (p); lane 2: p + H_2O_2 (50 μM); lane 3: p + 1000 μM $[Ru(MMI)_6]Cl_3$ + H_2O_2; lane 4: p + Fe^{2+} (2 μM) + H_2O_2; lanes 5-14: p + Fe^{2+} + H_2O_2 + 0.001, 0.01, 0.1, 1, 10, 50, 100, 500, and 1000 μM $[Ru(MMI)_6]Cl_3$, respectively.

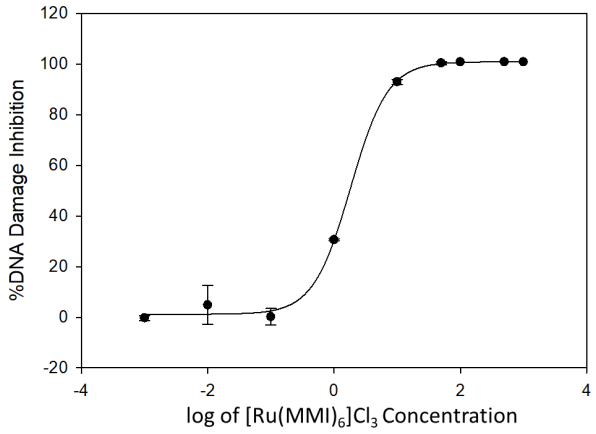

Figure 3.7 Graph of oxidative DNA damage prevention by $[Ru(MMI)_6]Cl_3$ showing the best-fit dose response curve with a calculated IC_{50} value of 1.76 ± 0.01 μM.

increases the efficacy of MMI as an antioxidant, most likely by increasing the local MMI concentration. As a result, the synthesized ruthenium thione and selone complexes not only exhibit interesting coordination chemistry, but also demonstrate that metal binding can directly enhance thione antioxidant activity.

3.3 Conclusions

In summary, ten novel homoleptic or heteroleptic Ru(II/III) thione and selone complexes were synthesized and fully characterized, representing the first ruthenium complexes with more than two thione or selone ligands. In addition, the $[RuL_6]^{3+}$ complexes **1a**, **2**, and **3** react to scavenge H_2O_2, and this scavenging ability likely contributes to the ability of $[Ru(MMI)_6]^{3+}$ (**3**) to prevent oxidative DNA damage more effectively than MMI alone. This work represents a substantial advance in understanding the coordination properties and reactivity of thione and selone complexes, and opens up new directions to explore metal-modulated antioxidant behavior.

3.4 Experimental methods

General methods. Synthesis of all complexes was performed under argon using standard air-sensitive Schlenk techniques except where indicated. Ruthenium(III) chloride hydrate (Oakwood) and methimazole (BDH) were used without purification. $RuCl_2(DMSO)_4$,[51] $[Ru(NCCH_3)_6][BF_4]_2$,[66] 1,3-dimethyl-2-imidazolethione (dmit)[39] and 1,3-dimethyl-2-imidazoleselone (dmise)[39] were synthesized as reported. Acetonitrile, dichloromethane and methanol were purified by distillation under an argon atmosphere, and anhydrous diethyl ether (BDH) was used without further purification.

^{1}H NMR spectra were recorded using a 300 MHz Bruker-AVANCE NMR spectrometer; ^{1}H NMR chemical shifts are reported in δ relative to tetramethylsilane (δ 0) and referenced to solvent. ^{1}H NMR spectra of ruthenium complexes **4-9** in D_2O (referenced to (δ 4.79[67]) are provided in Figures 3.12-3.17. IR spectra were obtained from Nujol mulls on KBr salt plates with a Magna 550 IR spectrometer (spectra for all complexes are provided in Figures 3.18-3.27). Vibrational data are described using the abbreviations: vs, very strong; s, strong; m, medium; w, weak; b, broad.

MALDI mass spectra were obtained using a Bruker Microflex MALDI-TOF mass spectrometer with *trans*-2-[3-(4-tert-butylphenyl)-2-methyl-2-propenyldiene] malonitrile ($m/z = 251$ for cation with H^+) as the matrix. Samples were spotted as acetonitrile solutions, and data were collected with laser intensities of 27-33%. All observed peak envelopes match theoretical calculations[68] or their ions within the accuracy of the callibration (± 1 *m*/*z*; Figures 3.28-3.37). UV-vis spectra were obtained using a Shimadzu UV-3101 PC spectrophotometer in quartz cuvettes with a 1 cm path length (spectra for complexes **1a**, **2**, and **3** are provided in Figures 3.4 and 3.44).

*Synthesis of [Ru(MMI)$_6$]Cl$_3$ (**1a**)*. Methimazole (MMI; 6 mmol, 684 mg) was dissolved in dichloromethane (15 mL) and added to a solution of $RuCl_3 \cdot 3H_2O$ (1 mmol, 261 mg) in methanol (30 mL). The reaction mixture was stirred for 4 h at room temperature. The solvent was removed *in vacuo*, and the resulting dark-blue powder was washed with diethyl ether (2 × 20 mL) and recrystallized at least twice by diethyl ether diffusion into an acetonitrile solution of the product. Yield: 556 mg, 58%. Crystals for X-ray analysis were grown from vapor diffusion of diethyl ether into a solution of **1a** in acetonitrile. IR (Nujol,

cm^{-1}): 3413 (b), 3109 (w), 2923 (b), 2816 (b), 2733 (w), 1643 (w), 1567 (s), 1455 (s), 1377 (s), 1316 (w), 1283 (m), 1151 (s), 1101 (m), 918 (w), 853(w), 724 (b,s) 677 (m), 500(w), 411 (w). Analysis of $C_{24}H_{36}Cl_3N_{12}RuS_6 \cdot 4HCl$: Calcd. (Exp.): C, 27.76 (28.00); H, 3.88 (3.86); N, 16.19 (15.89). MALDI-MS (*m/z*) = 409, $[Ru(MMI)_6]Cl]^{2+}$. UV-vis λ_{max} (CH_3CN): 265 nm.

*Synthesis of $[Ru(MMI)_6][BF_4]_2[NO_3]$ (**1b**).* Methimazole (6 mmol, 684 mg) dissolved in dichloromethane (15 mL) was added via cannula to a solution of $[Ru(NCCH_3)_6][BF_4]_2$ (1 mmol, 521 mg) in methanol (30 mL). Then the reaction mixture was heated to reflux with stirring for 4 h. The hot, pale blue solution was exposed to air and turned dark blue with stirring for 30 min $NaNO_3$ (1 mmol, 84 mg) was added to this solution with stirring in air for 1 h. The reaction mixture was filtered, then the solvent was removed *in vacuo*, and the resulting dark-blue powder was washed with diethyl ether (2 × 20 mL) and recrystallized in acetonitrile at -20 ºC for at least 6 h. The precipitate was filtered, and the filtrate was dried *in vacuo* to afford product. Yield: 626 mg, 65%. The resulting dark-blue powder was washed with diethyl ether (2 × 20 mL) and recrystallized at least twice by diethyl ether diffusion into an acetonitrile solution of the product. Crystals for X-ray analysis were grown from vapor diffusion of diethyl ether into a solution of **1b** in acetonitrile. IR (Nujol, cm^{-1}): 3410 (b), 3105 (w), 2920 (b), 2819 (b), 2736 (w), 1568 (s), 1462 (s), 1378 (s), 1317 (w), 1283 (m), 1151 (s), 1089 (m), 919 (w), 788(w), 724 (b,s), 677 (m), 500(w), 410 (w). Analysis of $C_{24}H_{36}\ B_2F_8N_{13}O_3RuS_6 \cdot 3CH_3OH \cdot H_2O$: Calcd. (Exp.): C, 28.54 (28.55); H, 4.44 (4.64); N, 16.03 (16.49). MALDI-MS (*m/z*) = 478 $[Ru(MMI)_2(BF_4)(NO_3)]^+$.

*Synthesis of [Ru(dmit)$_6$]Cl$_3$ (**2**).* Synthesis of **2** was carried out using the procedure described for **1a**, except that dmit (6 mmol, 769 mg) was used in place of methimazole. The resulting dark-purple solid was purified as described for **1a**. Yield: 635 mg, 65%. IR (Nujol, cm^{-1}): 3432 (b), 3177 (w) 3111 (s) 2922 (s), 2811 (s), 2716 (w), 1728 (w), 1563 (s), 1456 (s), 1378 (s), 1250 (w), 1171 (s), 1095 (s), 1046 (s), 1016 (w), 856 (w), 745 (s), 679 (s), 582 (w), 501 (w). Analysis of $C_{30}H_{48}Cl_3N_{12}RuS_6 \cdot 2H_2O$: Calcd. (Exp.): C, 35.58 (35.51); H, 5.18 (5.09); N, 16.60 (16.56). MALDI, (*m/z*) = 428, $[Ru(dmit)_2Cl_2]^+$. UV-vis λ_{max} (CH_3CN): 272 nm.

*Synthesis of [Ru(dmise)$_6$]Cl$_3$ (**3**).* Synthesis of **3** was carried out using the procedure described for **1a** except that dmise (6 mmol, 1051 mg) was added in place of methimazole. The resulting dark-brown powder was purified as described for **1a**. Yield: 868 mg, 69%. IR (Nujol, cm^{-1}): 3405 (b), 3099 (w), 2920 (s), 2801 (s), 2708 (w), 1568 (s), 1462 (s), 1378 (s), 1317 (s), 1283 (s), 1150 (s), 1089 (s), 919 (s), 788 (s), 724 (s), 677 (s), 489 (s). Analysis of $C_{30}H_{48}Cl_3N_{12}RuSe_6 \cdot 3CH_3CN \cdot 2HCl$): Calcd. (Exp.): 30.53 (30.36); H, 4.18(4.21); N, 15.00 (15.75). MALDI-MS (*m/z*) = 522, $[Ru(dmise)_2Cl_2]^+$. UV-vis λ_{max} (CH_3CN): 275 nm.

*Synthesis of [Ru(MMI)$_6$][BF$_4$]$_2$ (**4**).* To a solution of $[Ru(NCCH_3)_6][BF_4]_2$ (1 mmol, 521 mg) dissolved in methanol (30 mL), a solution of methimazole (MMI; 6 mmol, 684 mg) dissolved in dichloromethane (15 mL) was added via cannula. The reaction mixture was heated to reflux with stirring for 4 h, the reaction was cooled to room temperature, and the solvent was removed *in vacuo*. The resulting greenish powder was purified as described for **1b**. Yield: 566 mg, 59%. ^{1}H NMR (D_2O): δ 3.58 (3H), 6.95 (1H), and 7.03 (1H). IR (Nujol, cm^{-1}): 3429 (b), 3101 (w), 2925 (b), 2814 (b), 2737 (w), 1568 (s), 1460 (s), 1378

(s), 1282 (m), 1151 (s), 1084 (m), 918 (w), 852(w), 724 (b,s), 675 (m), 503(w), 412 (w). Analysis of ($C_{24}H_{36}B_2F_8N_{12}RuS_6 \cdot 4H_2O$) Calcd. (Exp.): C, 27.94 (27.93); H, 4.28 (4.05); N, 16.26 (15.56). MALDI-MS (*m*/*z*) = 577 $[Ru(MMI)_4F]^+$ and 778 $[Ru(MMI)_4(BF_4)(F)H]^+$.

*Synthesis of $[Ru(dmit)_6][BF_4]_2$ (**5**).* Synthesis of **5** was carried out using the procedure described for **4** except that dmit (6 mmol, 769.2 mg) was added in place of methimazole. The resulting blue powder was purified as described for **1b**. Yield: 668 mg, 64%. ^{1}H NMR (D_2O): δ 3.53 (3H) and δ 7.12 (2H). IR (Nujol, cm^{-1}): 3411 (b), 3181 (w), 3103 (w), 2920 (s), 2807 (s), 2710 (w), 1663 (w), 1564 (s), 1463 (s), 1378 (s), 1239 (s), 1171 (s), 1101 (w), 1057 (s,b), 749 (s), 731 (s), 663 (s), 594 (s), 517 (s). Analysis of $C_{30}H_{48}B_2F_8N_{12}RuS_6 \cdot 2CH_3CN$: Calcd. (Exp.): C, 36.27 (36.34); H, 4.83 (4.95); N, 17.42 (17.74). MALDI-MS (*m*/*z*) = 701, $[Ru(dmit)_4BF_4]^+$.

*Synthesis of $[Ru(dmise)_6][BF_4]_2$ (**6**).* Synthesis of **6** was carried out using the procedure described for **4** except that dmise (6 mmol, 1051 mg) was added in place of methimazole. The resulting brownish powder was purified as described for **1b**. Yield: 887, 67%. ^{1}H NMR (D_2O): δ 3.59 (3H) and δ 7.33 (2H). IR (Nujol, cm^{-1}): 3382 (b), 3107 (vw), 2932 (s,b), 2824 (s), 2713 (w), 1639 (s), 1491 (s), 1379 (s), 1233 (s), 1152 (m), 1082 (s), 914 (w), 809 (w), 738 (s), 729 (s), 662 (s), 622 (m), 492 (w). Analysis of $C_{30}H_{48}B_2F_8N_{12}RuS_6 \cdot 4CH_3CN$: Calcd. (Exp.): C, 30.62 (30.15); H, 4.06 (4.07); N, 15.03 (15.72). MALDI-MS (*m*/*z*) = 801, $[Ru(dmise)_3(BF_4)_2H]^+$.

*Synthesis of $Ru(MMI)_4Cl_2$ (**7**).* To a solution of $Ru(DMSO)_4Cl_2$ (484 mg, 1 mmol) in methanol (30 mL), a solution of methimazole (MMI; 4 mmol, 456 mg) in

dichloromethane (15 mL) was added via cannula. The mixture reaction was heated to reflux with stirring for 4 h and then cooled to room temperature. The solvent was removed *in vacuo*, and the resulting greenish powder was purified as described for **1b**. Yield: 427 mg, 68%. ^{1}H NMR (D_2O): δ 3.89 (3H), 7.59 (1H), and 7.71 (1H). IR (Nujol, cm^{-1}): 3427 (b), 3110 (w), 2923 (b), 2819 (b), 2728 (w), 1643 (w), 1567 (s), 1455 (s), 1377 (s), 1316 (w), 1283 (m), 1151 (s), 1100 (m), 918 (w), 852(w), 724 (b,s) 678 (m), 500(w), 409 (w). Analysis of $C_{16}H_{24}Cl_2N_8RuS_4 \cdot 2HCl$: Calcd. (Exp.): C, 27.39 (27.25); H, 3.74 (3.85); N, 15.96 (15.48). MALDI-MS (*m*/*z*) = 515, $[RuCl_2(MMI)_3H]^+$.

Synthesis of Ru(dmit)$_4$Cl$_2$ (**8**). Synthesis of **8** was carried out using the procedure described for **7** except that dmit (4 mmol, 513 mg) was added in place of methimazole. The resulting brown powder was purified as described for **1b**. Yield: 443 mg; 72%. ^{1}H NMR (D_2O): δ 3.76 (3H) and δ 7.80 (2H). IR (Nujol, cm^{-1}): 3414 (b), 3190 (w), 3101 (w), 2922 (s), 2809 (s), 2712 (w), 1728 (w), 1563 (s), 1463 (s), 1378 (s), 1249 (m), 1172 (s), 1095 (w), 1046 (s), 745 (s), 679 (s), 618 (s), 582 (s), 511 (w). Analysis of $C_{30}H_{48}B_2F_8N_{12}RuS_6 \cdot 2CH_3CN$): Calcd. (Exp.): C, 35.03 (34.39); H, 4.67 (4.70); N, 16.37 (16.78). MALDI-MS (*m*/*z*) = 393, $[Ru(dmit)_2Cl]^+$; 429, $[Ru(dmit)_2Cl_2H]^+$.

*Synthesis of Ru(dmise)$_4$Cl$_2$ (**9**)*. Synthesis of **9** was carried out using the procedure described for **7** except that dmise (6 mmol, 1051 mg) was added in place of methimazole. The resulting brown powder was purified as described for **1b**. Yield: 610 mg, 70%. ^{1}H NMR (D_2O): δ 3.59 (3H) and δ 7.33 (2H). IR (Nujol, cm^{-1}): 3409 (b), 3091 (vw), 2916 (s,b), 2804 (s), 2716 (w), 1646 (w), 1562 (s), 1461 (s), 1378 (s), 1240 (s), 1151 (s), 1092 (s), 915 (w), 804 (w), 738 (s), 723 (s), 662 (s), 617 (m), 470 (w). Analysis of

$C_{30}H_{48}B_2F_8N_{12}RuS_6 \cdot 4CH_3CN$: Calcd. (Exp.): C, 28.20 (28.62); H, 4.36 (4.41); N, 11.97 (12.15). MALDI-MS (m/z) = 523, $[Ru(dmise)_2Cl_2H]^+$.

X-ray crystallography. Complexes **1a**, **1b**, and **5** were characterized by X-ray structural analysis. Single crystals of **1a**, **1b**, and **5** were grown via slow diffusion of diethyl ether into acetonitrile solutions. Diffraction data were collected using a Bruker D8 Venture with an incoatec microfocus source (Mo Kα, λ = 0.71073 Å) and a Photon 100 CMOS detector. Data were processed and corrected for absorption using the Apex 3 software suite, and the structures were subsequently solved and refined by least squares techniques on F^2 using the SHELXTL suite. In **1a**, four molecules of H_2O (likely from humid ambient atmosphere) per formula unit were found to occupy void space between the ruthenium complex and chloride anions, and these solvent molecules were included in the refinement model. In the case of **1b**, 1.5 molecules of acetonitrile were present as a solvate in the crystal structure, and these were included in the structure refinement. X-ray structural analysis data of complexes **1** and **5** are shown in Table 3.4, and data for **1b** are shown in Table 3.6.

*Reactivity of $[Ru(MMI)_6]Cl_3$ (**1a**) with H_2O_2.* In air, $[Ru(MMI)_6]Cl_3$ (8.9 mg, 0.1 mmol) was dissolved in acetonitrile (10 mL) and treated with 2 or 12 equiv of H_2O_2 (15 and 90 μL, respectively, of a 9.77 M solution in water). Immediately upon addition of H_2O_2, the color of the reaction mixture started to turn from dark blue to pale brown, and a dark brown precipitate formed. After stirring for 1 h, the reaction mixture was dried *in*

vacuo. MALDI-MS (positive ionization, *m/z*): 84 $[C_4H_6N_2]^+$, 209 $[RuCl_3H]^+$; (negative ionization; *m/z*) = 97 $[SO_4H]^-$, 80.9 $[SO_3H]^-$, 65 $[SO_2H]^-$.

Table 3.4. Crystallographic data for complexes **1** and **5**.

	1a $[Ru(MMI)_6]Cl_3 \cdot 4H_2O$	**5** $[Ru(dmit)_6](BF_4)_2$
Empirical formula	$C_{24}H_{44}Cl_3N_{12}O_4RuS_6$	$C_{30}H_{48}B_2F_8N_{12}RuS_6$
Formula weight (g/mol)	964.49	1043.85
Temperature (K)	100	147(2)
Crystal system	Triclinic	monoclinic
Space group	*P*-1	*C*2/*c*
Unit cell dimensions (Å,°)	*a* = 9.4451(8) *b* = 10.0437(8) *c* = 11.1320(10)	a = 15.952(3) b = 15.238(3) c = 20.460(4)
volume ($Å^3$)	1022.37(15)	4972.8(16)
Z, calcd density (g/cm^3)	1.567	1.394 g/cm^3
absorption coefficient (mm^{-1})	0.933	0.633
F(000)	495	2136
crystal size (mm)	0.053 × 0.089 × 0.141	0.057 × 0.062 × 0.109 mm
T_{max}, T_{min}	1.0000 and 0.9417	1.0000 and 0.8253
Θ range for data (°)	2.17 to -27.16	3.21 to 25.25
Reflns collected/unique/obs.	54423	24939
Data/restraints/parameters	4531 /12/249	4202 / 64 / 323
Goodness-of-fit on F^2	1.077	1.061
R1, wR^2 ($I \geq 2\sigma(I)$)	0.0368, 0.0931	0.1187, 0.2743
R1, wR^2 (all data)	0.0430, 0.0972	0.1621, 0.2975
Largest diff. peak, hole ($e/Å^3$)	1.529, -0.841	1.096 and -0.849

*Reactivity of [Ru(dmit)$_6$]Cl$_3$ (**2**) with H$_2$O$_2$*. Oxidation studies of $[Ru(dmit)_6]Cl_3$ were carried out as for $[Ru(MMI)_6]Cl_3$ oxidation studies, except that $[Ru(dmit)_6]Cl_3$ (9.7 mg, 0.1 mmol) was added in place of $[Ru(MMI)_6]Cl_3$. After 50 min, the reaction mixture started to turn from dark purple to pale brown, and a dark brown precipitate formed. After stirring for 4 h, the reaction mixture was dried *in vacuo*. MALDI-MS (positive ionization; *m/z*): 97 $[C_5H_8N_2]^+$, 209 $[RuCl_3H]^+$, (negative ionization; *m/z*): 97 $[SO_4H]^-$, 81 $[SO_3H]^-$, 65 $[SO_2H]^-$.

*Reactivity of [Ru(dmise)$_6$]Cl$_3$ (**3**) with H_2O_2.* Oxidation studies of [Ru(dmse)$_6$]Cl$_3$ were carried out as for [Ru(MMI)$_6$]Cl$_3$ oxidation studies, except that [Ru(dmise)$_6$]Cl$_3$ (12.57 mg, 0.1 mmol) was added in place of [Ru(MMI)$_6$]Cl$_3$. Immediately after H_2O_2 addition, the reaction mixture started to turn from dark brown to colorless, and a dark brown precipitate formed. After stirring for 1 h, the reaction mixture was dried *in vacuo*. MALDI-MS (positive ionization; *m/z*) = 97 $[C_5H_8N_2]^+$, 209 $[RuCl_3H]^+$, (negative ionization; *m/z*) = 144, $[SeO_4H]^-$; 111, $[SeO_2H]^-$.

UV-vis kinetics studies with H_2O_2. In air, acetonitile solutions of **1a**, **2**, and **3** (100 μM) were prepared, treated with 2 or 12 equiv of H_2O_2 (15 and 90 μL, respectively, of a 30% solution (9.77 M) in water), and quickly inverted to mix. Kinetic spectra were measured immediately after H_2O_2 addition at a λ_{max} of 265 nm for [Ru(MMI)$_6$]Cl$_3$ (8000 s), 272 nm for [Ru(dmit)$_6$]Cl$_3$ (12000 s), and 275 nm for [Ru(dmise)$_6$]Cl$_3$ (8000 s). For all three samples, a final spectrum was acquired at the conclusion of the kinetics studies.

Plasmid transfection, amplification, and purification. Plasmid DNA (pBSSK; 3 μL, 1 pmol) was purified from DH1 *E. coli* competent cells using Zyppy^{TM} Plasmid Miniprep Kit (400 count, Zymo Research). Tris-EDTA buffer (pH 8.01) was used to elute the plasmid from the spin columns. Plasmid DNA was dialyzed against 130 mM NaCl for 24 h at 4°C to ensure all Tris-EDTA buffer and metal contaminates were removed. Plasmid concentration was determined by UV-vis spectroscopy at a wavelength of 260 nm. Organic and protein contents were also determined using UV-vis spectroscopy from ratios of $A_{250}/A_{260} \leq 0.95$ and $A_{260}/A_{280} \geq 1.8$ respectively. Purity was determined through digestion of plasmid with Sac1 and Kpn1 in NEB buffer with bovine serum albumin was conducted

at 37°C for 90 min. Comparison to an undigested plasmid sample and a 1 kb molecular-weight marker was conducted by gel electrophoresis.

Plasmid DNA damage inhibition assays. Gel electrophoresis samples were prepared in deionized H_2O, MES buffer (10 mM, pH 6), NaCl (130 mM), 100% ethanol (10 mM), $FeSO_4$ (2 μM) and indicated concentrations of $[Ru(MMI)_6]Cl_3$ in water were combined in a microcentrifuge tube and allowed to stand for 5 min at room temperature. Plasmid (pBSSK; 0.1 pmol in 130 mmol NaCl solution) was then added to the reaction mixture and allowed to stand for 5 min at room temperature. Hydrogen peroxide (50 μM) was added to the indicated lanes and allowed to react at room temperature for 30 min, then EDTA (50 μM) was added to quench the reaction and loading dye (2 μL) was added. All given concentrations are final concentrations in a 12 μL volume. Samples were loaded into a 1% agarose gel in TAE running buffer; and damaged and undamaged plasmid DNA was separated by electrophoresis (140 V for 30 min). Gels were then stained using ethidium bromide and washed with diH_2O before being imaged under UV light. The amounts of nicked (damaged) and circular (undamaged) DNA were quantified using UViProMW (Jencons Scientific Inc.). The intensity of the circular plasmid band was multiplied by 1.24, due to the different binding abilities of ethidium bromide to supercoiled and nicked plasmid DNA.[69-70] Intensities of the nicked and supercoiled bands were normalized for each lane so that % nicked + % supercoiled = 100%. All percentages were corrected for residual nicked DNA prior to calculation. Results were obtained in triplicate for all experiments, and standard deviations are represented as error bars. Statistical significance was determined by calculating p values at 95% confidence ($p < 0.05$ indicates significance) as

described by Perkowski, *et al*.[71]

Calculation of percent DNA damage inhibition and IC_{50} value determination. The formula 1-[%N-%B]*100 was used to calculate percent DNA damage inhibition; %N = percent of nicked DNA in lanes 5-13, and %B = the percent of nicked DNA in the Fe^{2+}/H_2O_2 control lanes. Percentages were corrected for residual nicked DNA (lane 2) prior to calculations. Results were obtained from an average of three trials, with indicated standard deviations. A plot of percent inhibition of DNA damage versus log concentration of $[Ru(MMI)_6]Cl_3$ was fit to a variable-slope sigmoidal dose-response curve using SigmaPlot, version 11 (Systat Software, Inc.). IC_{50} value errors were calculated from error propagation of the gel electrophoresis measurements. DNA damage prevention studies were performed by Andrea Gaertner in the Department of Chemistry at Clemson University.

3.5 Supplemental Material

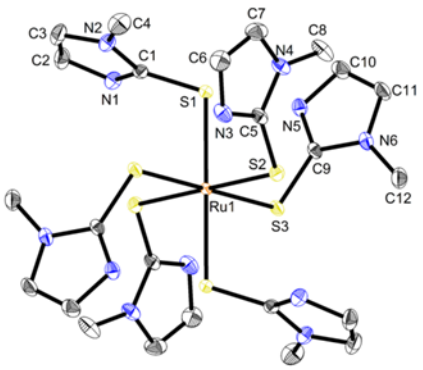

Figure 3.8. Crystal structure of the ruthenium complex in $[Ru(MMI)_6](BF_4)_2(NO_3)\cdot 1.5(C_2H_3N)$ (**1b**) with 50% probability density ellipsoids; hydrogen atoms, counterions, and solvent molecules omitted for clarity.

Table 3.5. Selected interatomic distances (Å) and angles (°) for $[Ru(MMI)_6](BF_4)_2(NO_3)\cdot 1.5(C_2H_3N)$ (**1b**).

	1b
Ru1-S1	2.4142(6)
Ru1-S2	2.4155(6)
Ru1-S3	2.4010(6)
S1-C1	1.719(2)
S3-C9	1.725(2)
S3-Ru1-S3	180.0
S3-Ru1-S2	92.91(2)
S3-Ru1-S2	87.09(2)
S3-Ru1-S1	83.54(2)
S2-Ru1-S1	94.19(2)
S3-Ru1-S1	96.46(2)
S2-Ru1-S1	85.81(2)
S1-Ru1-S1	180.0

Table 3.6. Crystallographic data for $[Ru(MMI)_6](BF_4)_2(NO_3)\cdot 1.5(C_2H_3N)$ (**1b**).

	1b
Empirical formula	$C_{27}H_{40.50}B_2F_8N_{14.50}O_3RuS_6$
Formula weight (g/mol)	1083.29
Ttemperature (K)	100
Crystal system	Triclinic
Space group	*P*-1
Unit cell dimensions (Å,º)	*a* = 10.6424(9) *b* = 13.0583(13) *c* = 17.1260(16)
Volume ($Å^3$)	1022.37(15)
Z, calcd density (g/cm^3)	2
Absorption coefficient (mm^{-1})	0.721
F(000)	1100
Crystal size (mm)	0.021 × 0.076 × 0.167
T_{max}, T_{min}	1.0000, 0.9612
Θ range for data (º)	2.03-26.00
Reflections collected/unique/observed	104786
Data/restraints/parameters	8681/3/579
Goodness-of-fit on F^2	1.173
R1, wR^2 ($I \geq 2\sigma(I)$)	0.0278, 0.0732
R1, wR^2 (all data)	0.0351, 0.0854
Largest diff. peak, hole ($e/Å^3$)	1.055, -0.584

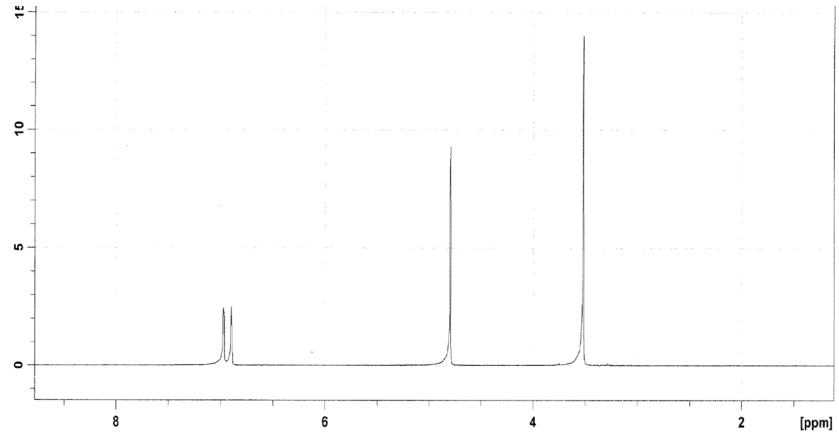

Figure 3.9. ^{1}H NMR spectrum of unbound methimazole (MMI) in D_2O (δ 4.79).

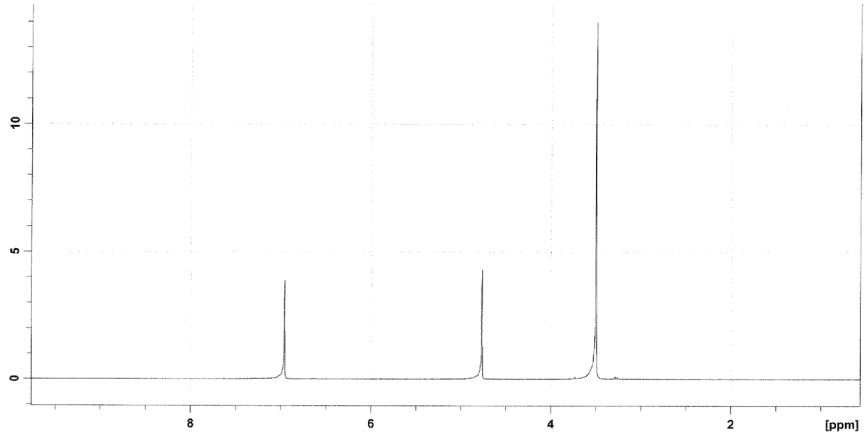

Figure 3.10. ^{1}H NMR spectrum of unbound *N*,*N*'-dimethylimidazole-2-thione (dmit) in D_2O (δ 4.79).

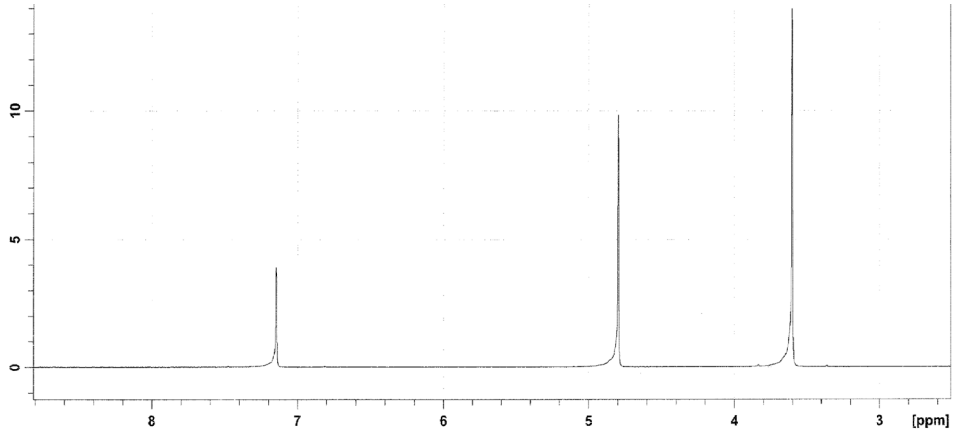

Figure 3.11. ^{1}H NMR spectrum of unbound *N*,*N*'-dimethylimidazole-2-selone (dmise) in D_2O (δ 4.79).

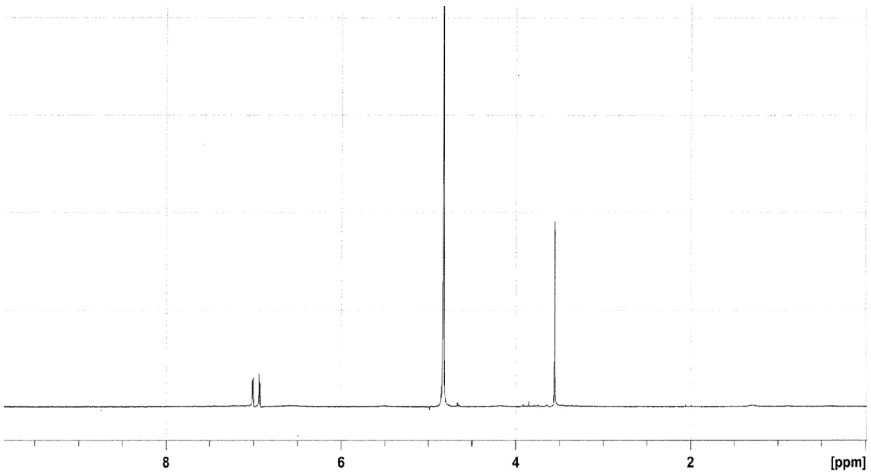

Figure 3.12. ^{1}H NMR spectrum of $[Ru(MMI)_6][BF_4]_2$ (**4**) in D_2O (δ 4.79).

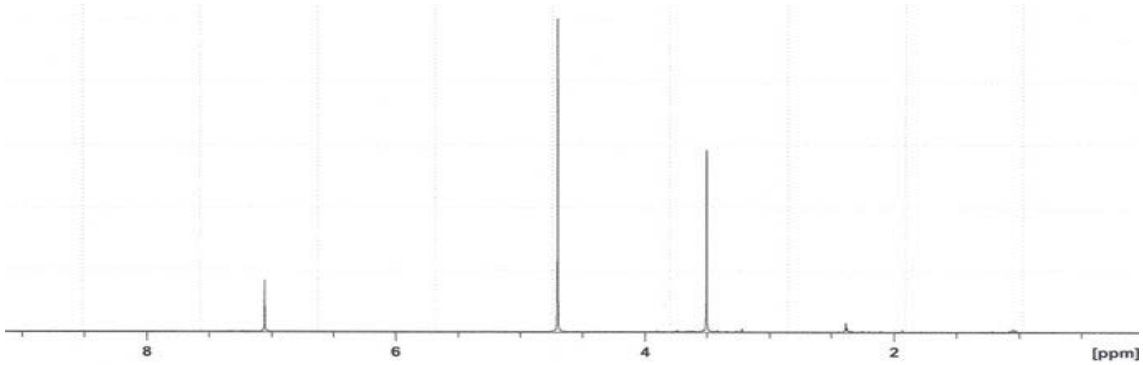

Figure 3.13. ^{1}H NMR spectrum of $[Ru(dmit)_6][BF_4]_2$ (**5**) in D_2O (δ 4.79).

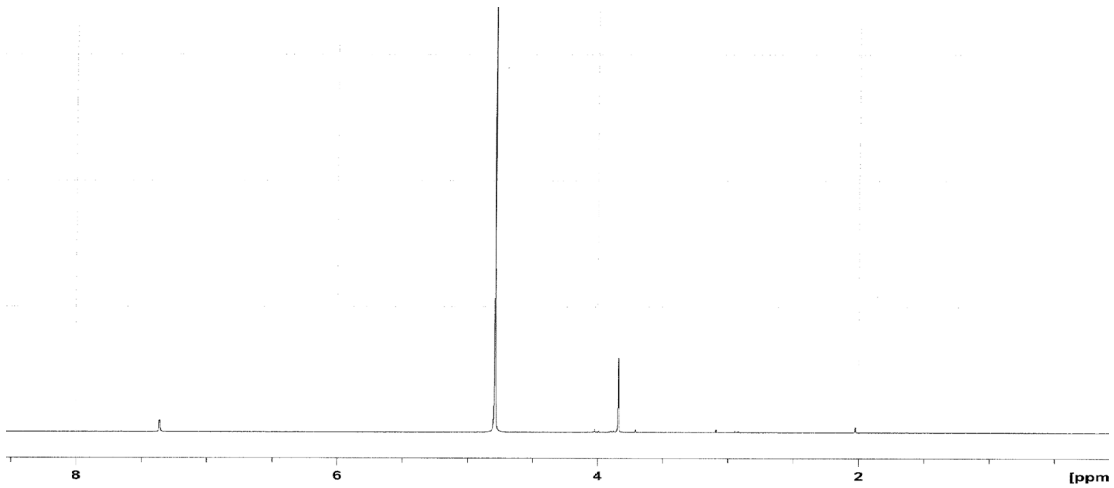

Figure 3.14. ^{1}H NMR spectrum of $[Ru(dmise)_6][BF_4]_2$ (**6**) in D_2O (δ 4.79).

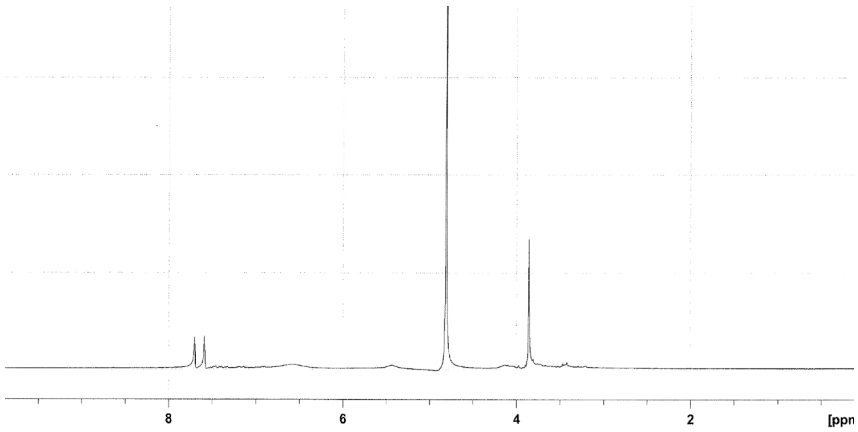

Figure 3.15. ^{1}H NMR spectrum of $Ru(MMI)_4Cl_2$ (**7**) in D_2O (δ 4.79).

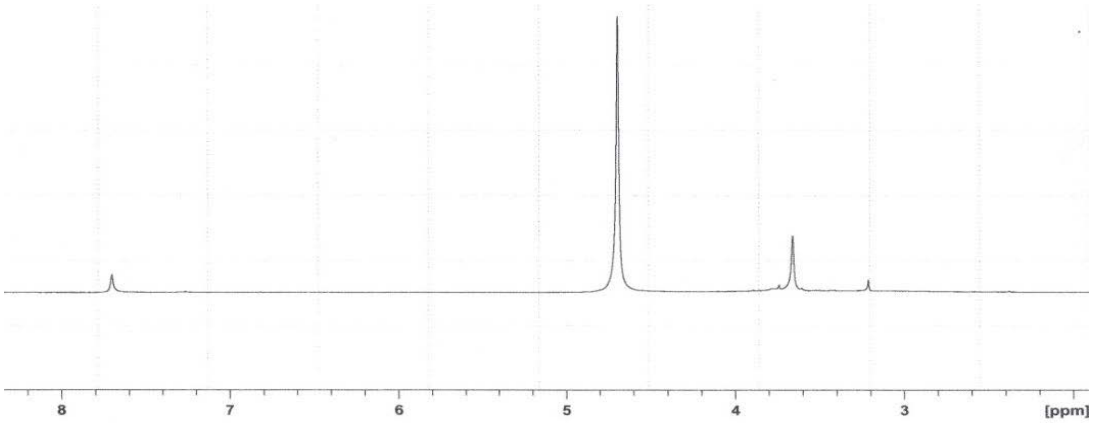

Figure 3.16. ^{1}H NMR spectrum of Ru $Cl_2(dmit)_4$ **(8)** in D_2O (δ 4.79).

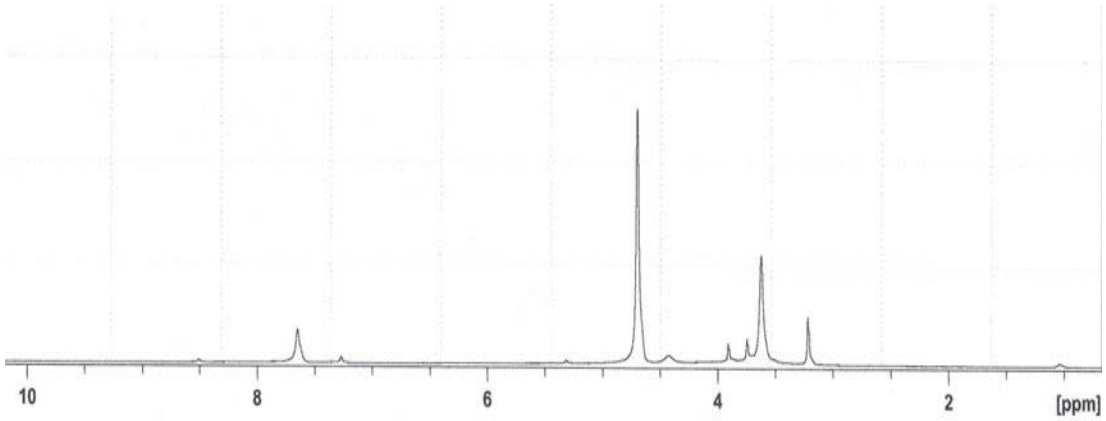

Figure 3.17. ^{1}H NMR spectrum of $RuCl_2(dmise)_4$ (**9**) in D_2O (δ 4.79).

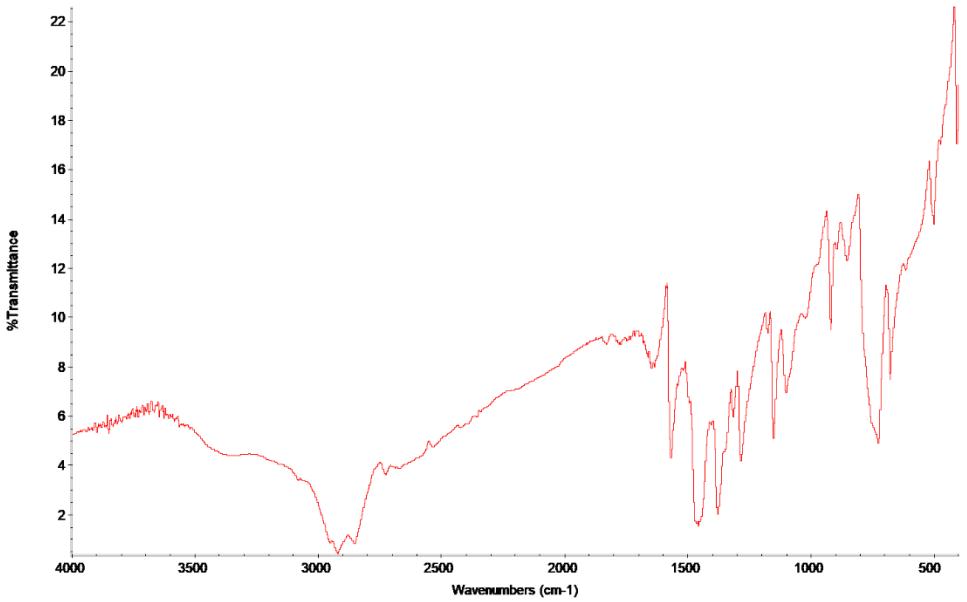

Figure 3.18. Transmittance IR spectrum of $[Ru(MMI)_6]Cl_3$ (**1a**) acquired as a Nujol mull.

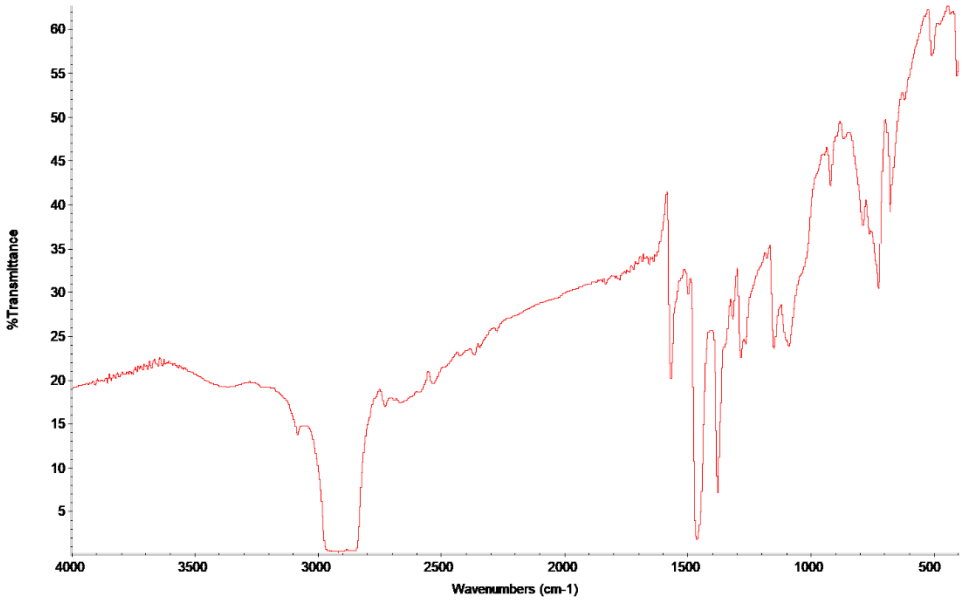

Figure 3.19. Transmittance IR spectrum of $[Ru(MMI)_6][BF_4]_2$ $[NO_3]$ (**1b**) acquired as a Nujol mull.

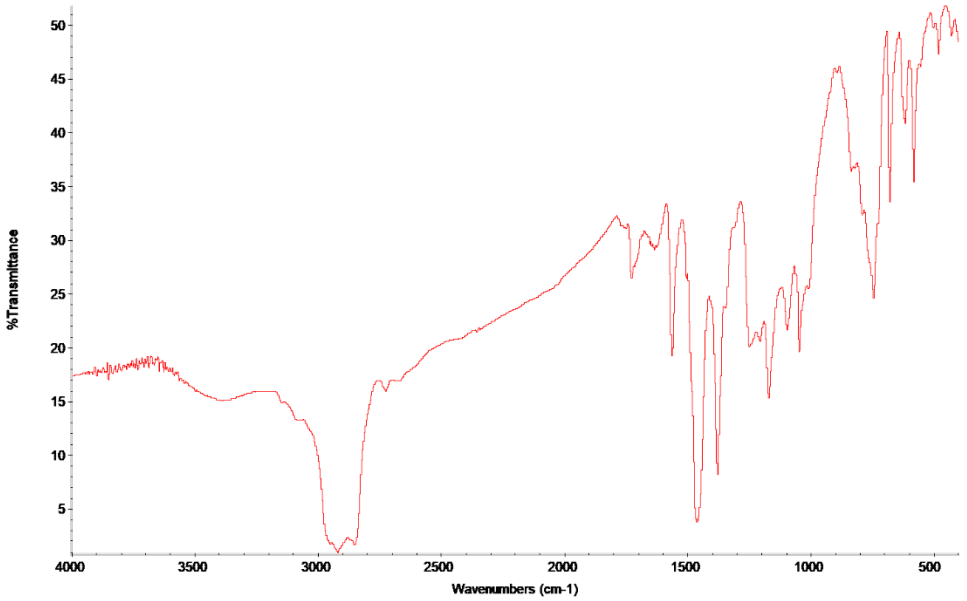

Figure 3.20. Transmittance IR spectrum of $[Ru(dmit)_6]Cl_3$ (**2**) acquired as a Nujol mull.

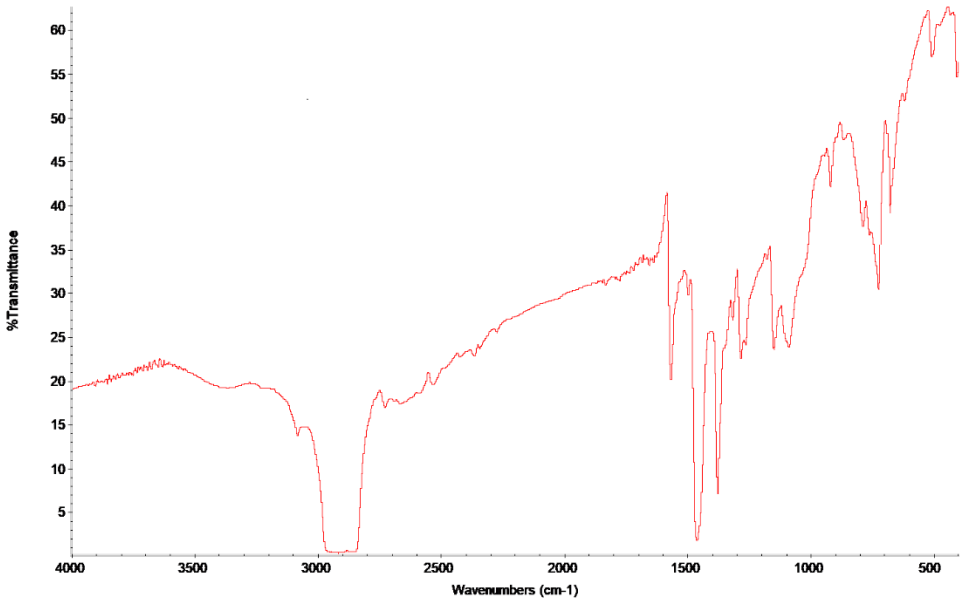

Figure 3.21. Transmittance IR spectrum of $[Ru(dmise)_6]Cl_3$ (**3**) acquired as a Nujol mull.

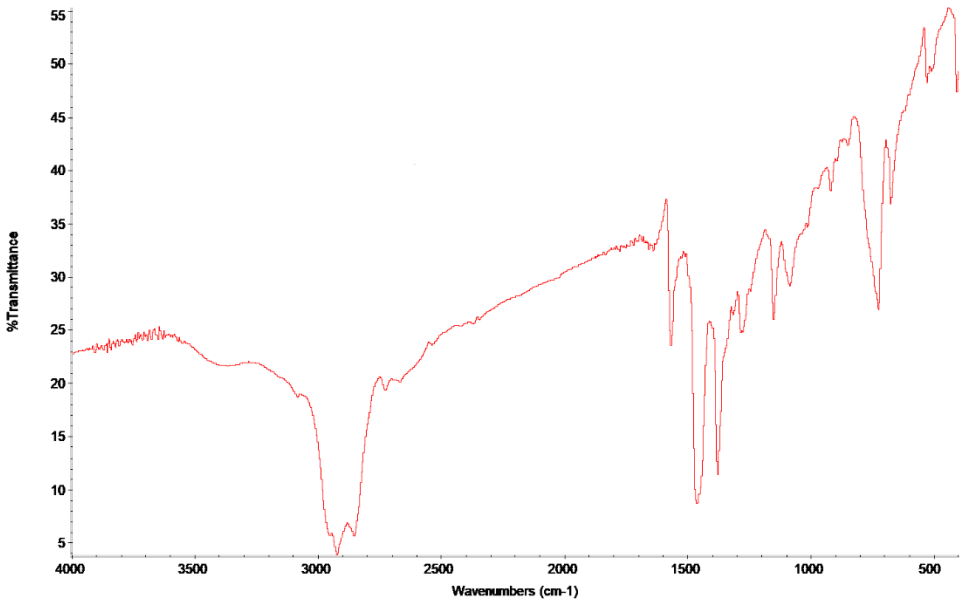

Figure 3.22. Transmittance IR spectrum of $[Ru(MMI)_6][BF_4]_2$ (**4**) acquired as a Nujol mull.

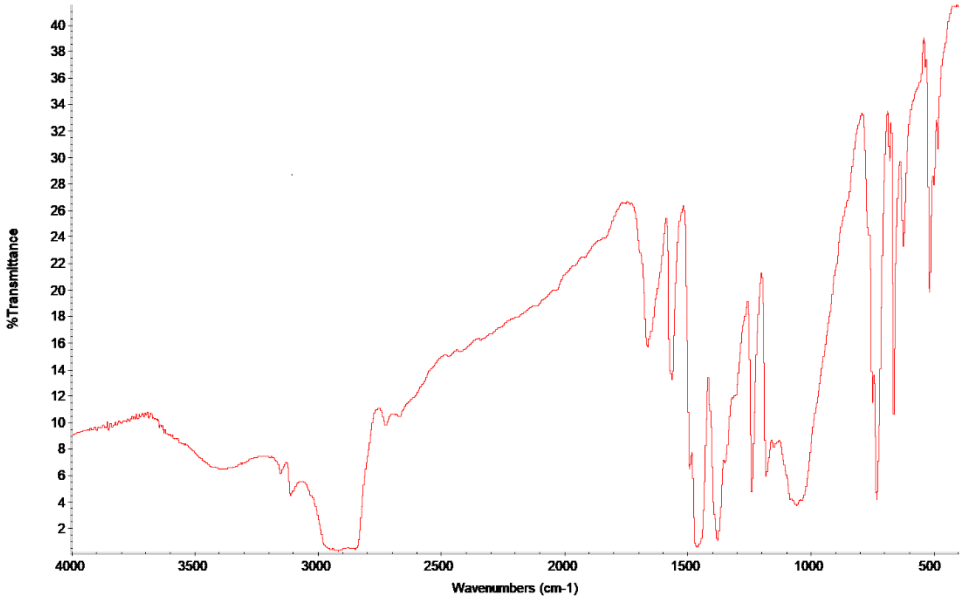

Figure 3.23. Transmittance IR spectrum of $[Ru(dmit)_6][BF_4]_2$ (**5**) acquired as a Nujol mull.

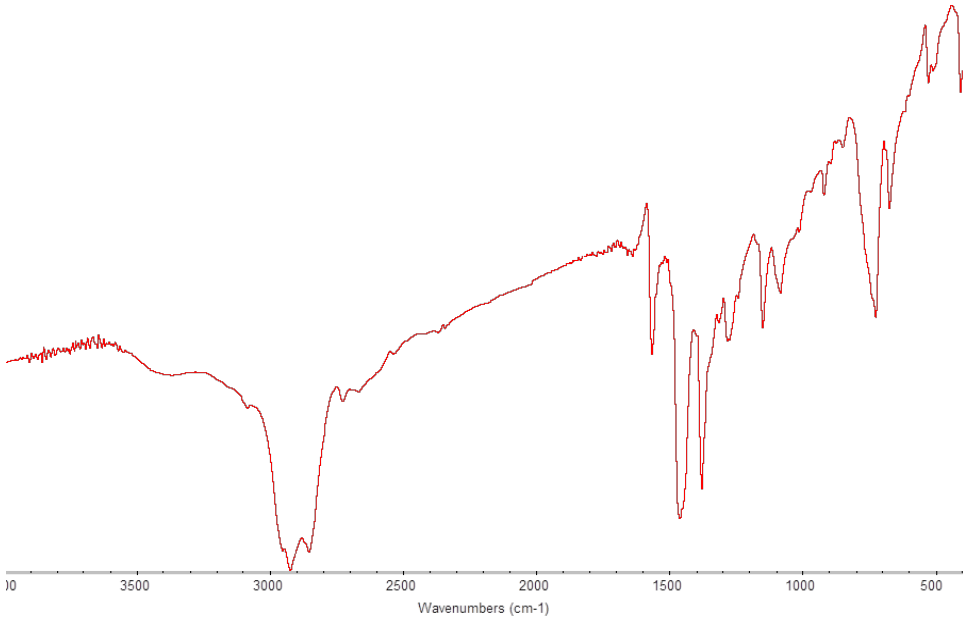

Figure 3.24. Transmittance IR spectrum of $[Ru(dmise)_6][BF_4]_2$ (**6**) acquired as a Nujol mull.

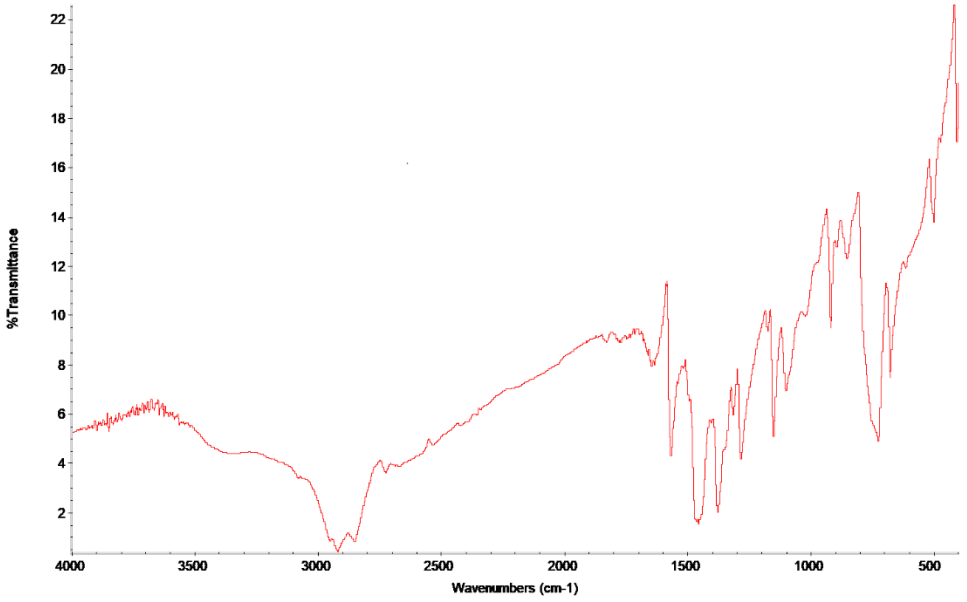

Figure 3.25. Transmittance IR spectrum of $RuCl_2(MMI)_4$ (**7**) acquired as a Nujol mull.

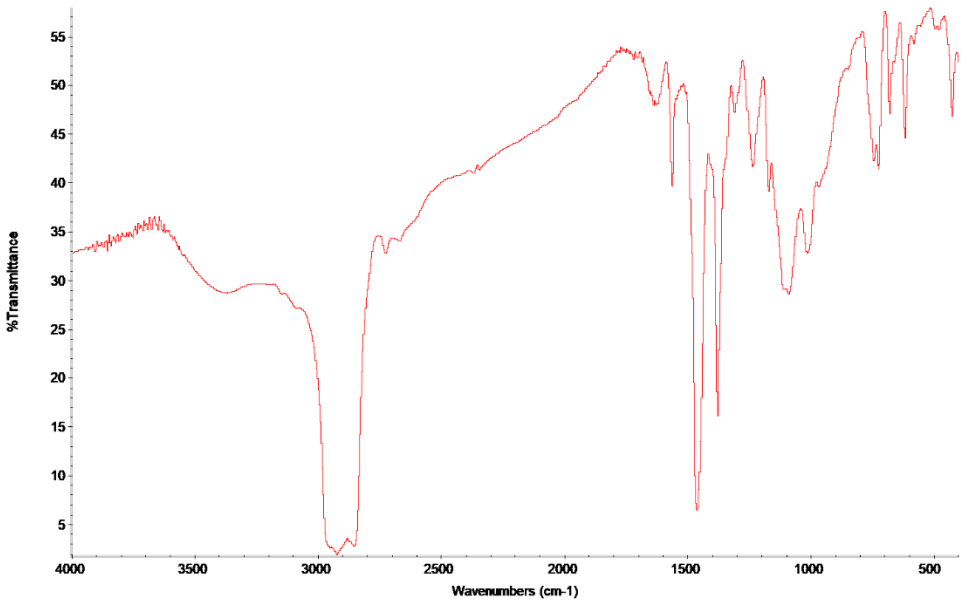

Figure 3.26. Transmittance IR spectrum of $RuCl_2(dmit)_4$ (**8**) acquired as a Nujol mull.

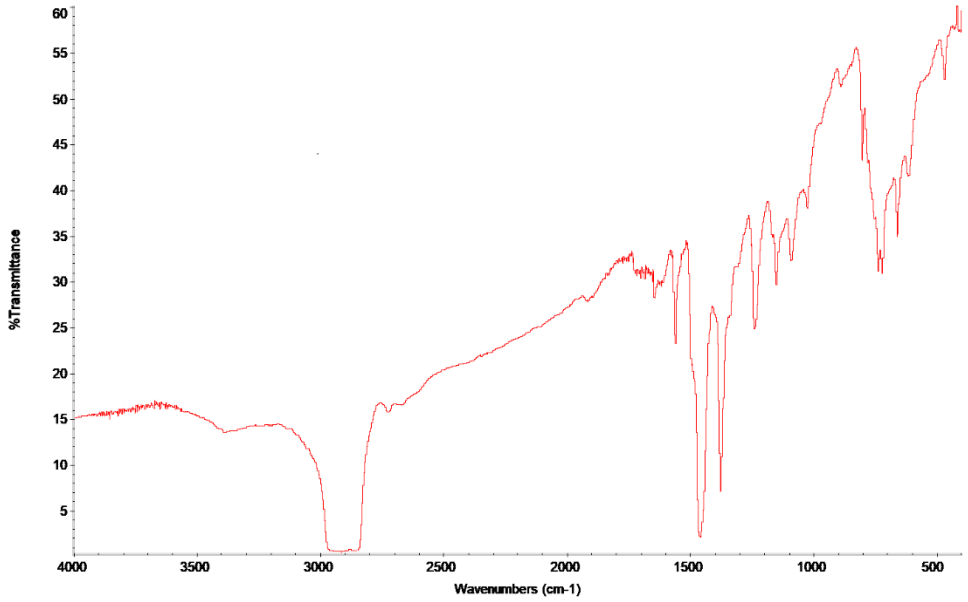

Figure 3.27. Transmittance IR spectrum $RuCl_2(dmise)_4$ (**9**) acquired as a Nujol mull.

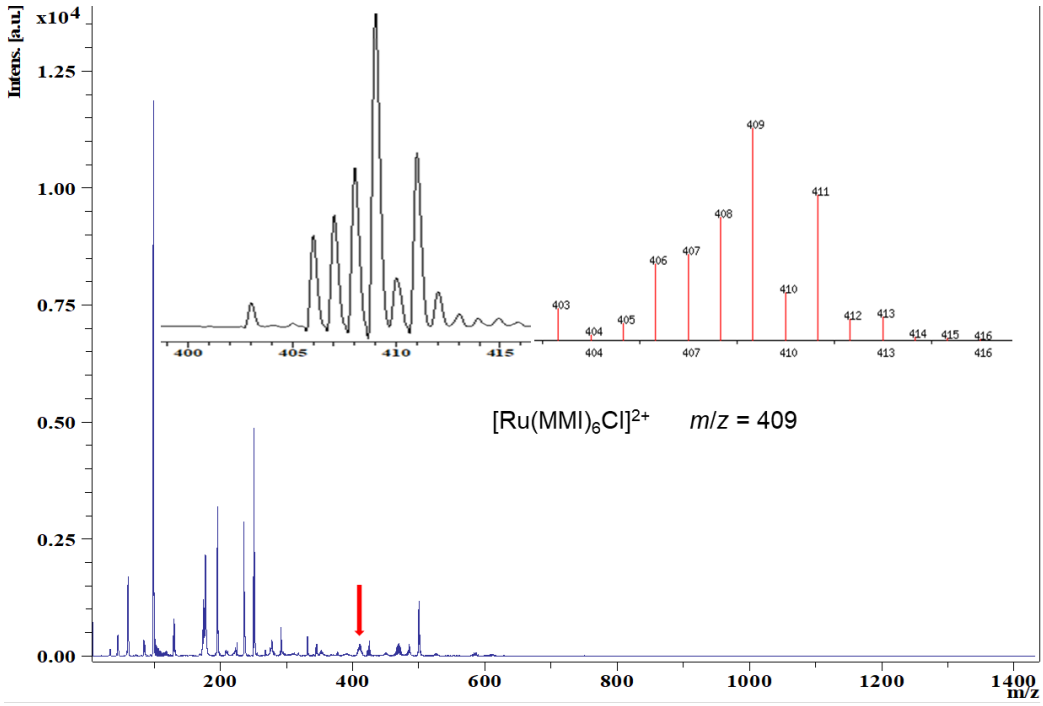

Figure 3.28. MALDI mass spectrum with insets of experimental (left) and simulated (right) envelope intensities for $[Ru(MMI)_6]Cl_3$ (**1a**).

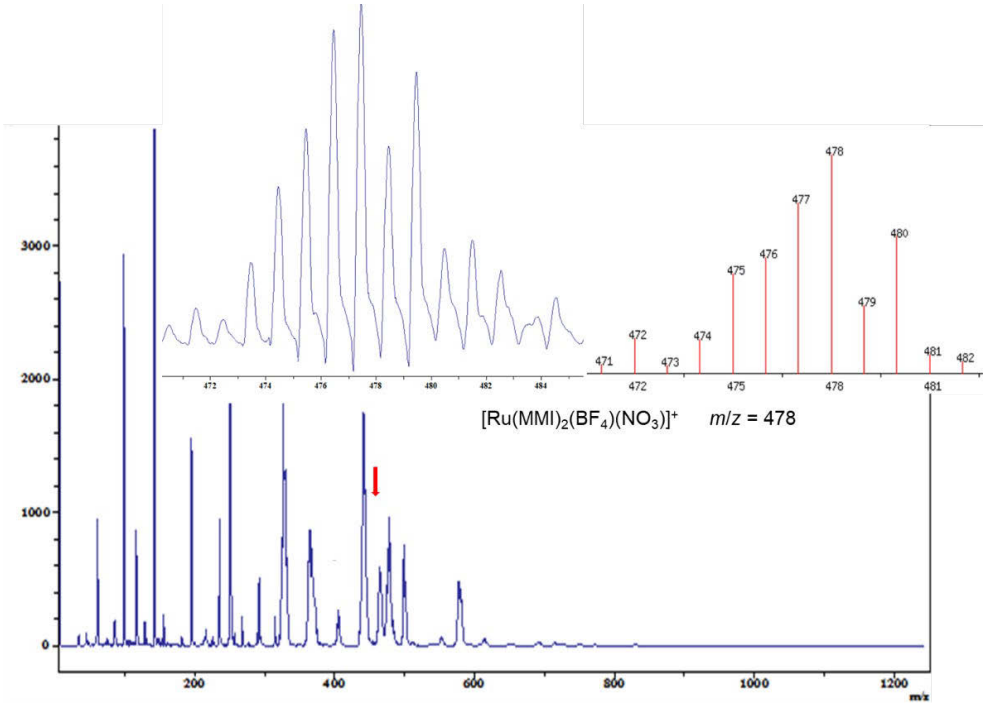

Figure 3.29. MALDI mass spectrum with insets of experimental (left) and simulated (right) envelope intensities for $[Ru(MMI)_6](BF_4)_2(NO_3)$ (**1b**).

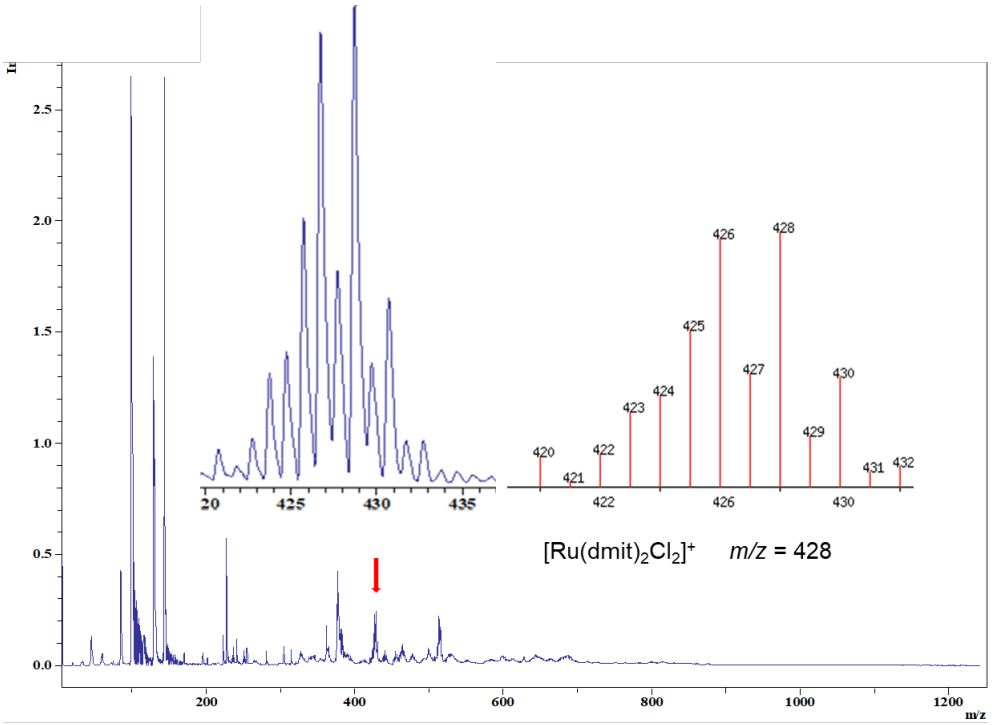

Figure 3.30. MALDI mass spectrum with insets of experimental (left) and simulated (right) envelope intensities for $[Ru(dmit)_6]Cl_3$ (**2**).

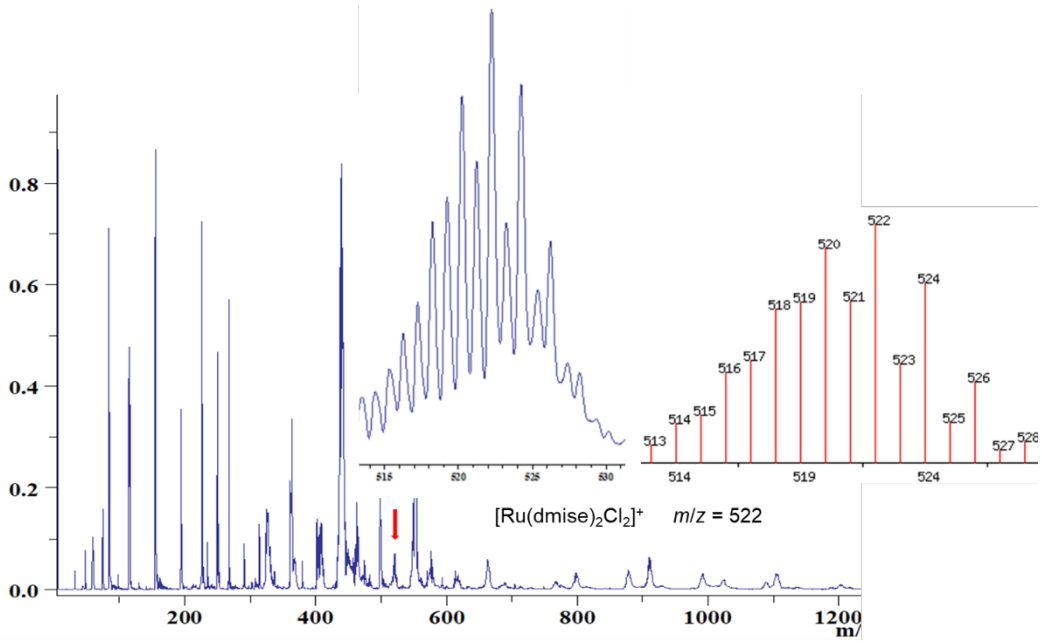

Figure 3.31. MALDI mass spectrum with insets of experimental (left) and simulated (right) envelope intensities for $[Ru(dmise)_6]Cl_3$ (**3**).

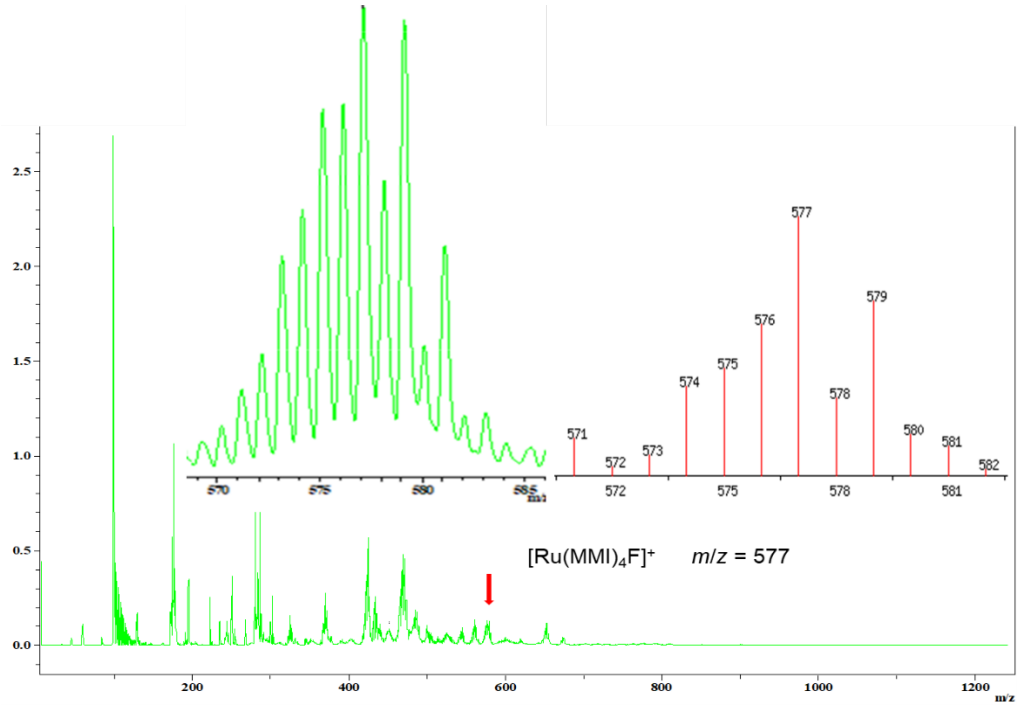

Figure 3.32. MALDI mass spectrum with insets of experimental (left) and simulated (right) envelope intensities for $[Ru(MMI)_6][BF_4]_2$ (**4**).

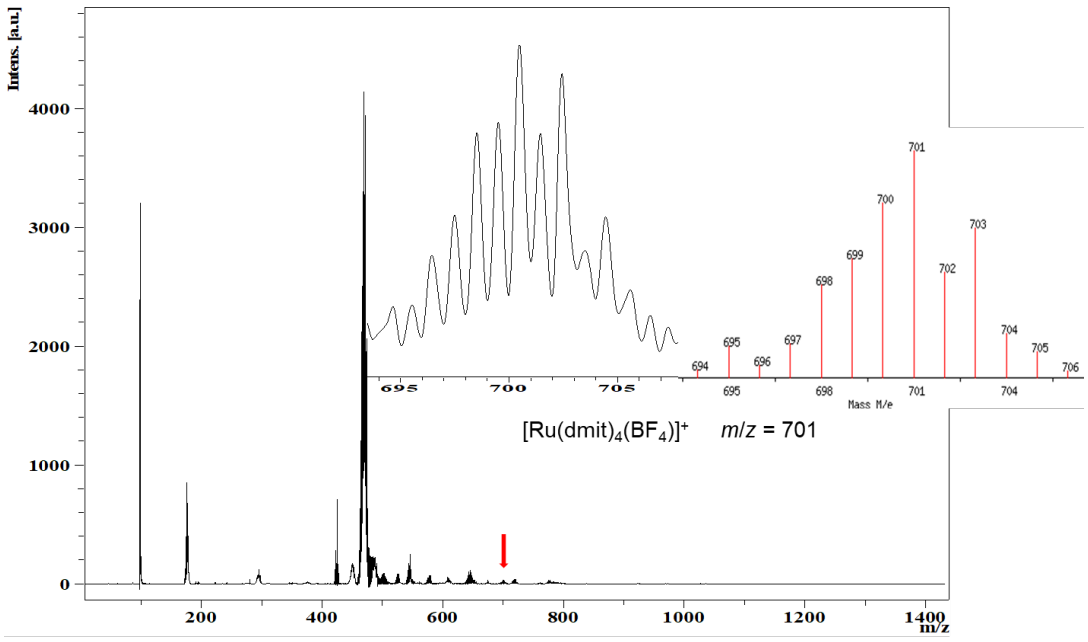

Figure 3.33. MALDI mass spectrum with insets of experimental (left) and simulated (right) envelope intensities for $[Ru(dmit)_6][BF_4]_2$ (**5**).

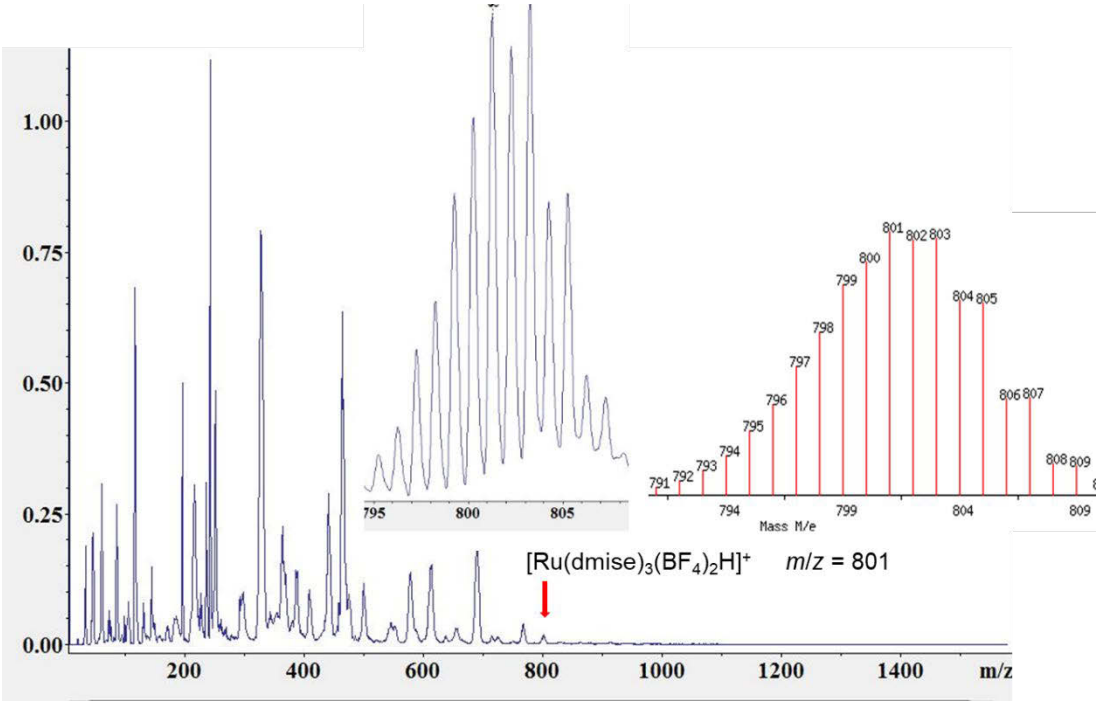

Figure 3.34. MALDI mass spectrum with insets of experimental (left) and simulated (right) envelope intensities for $[Ru(dmise)_6][BF_4]_2$ (**6**).

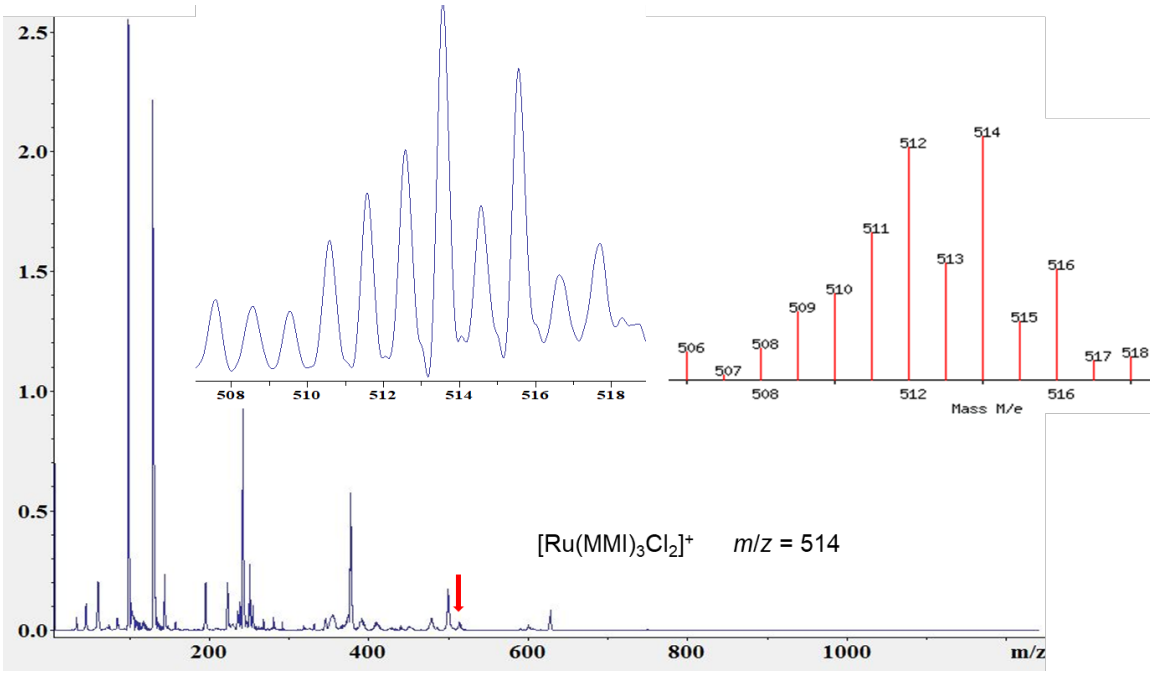

Figure 3.35. MALDI mass spectrum with insets of experimental (left) and simulated (right) envelope intensities for $RuCl_2(MMI)_4$ (**7**).

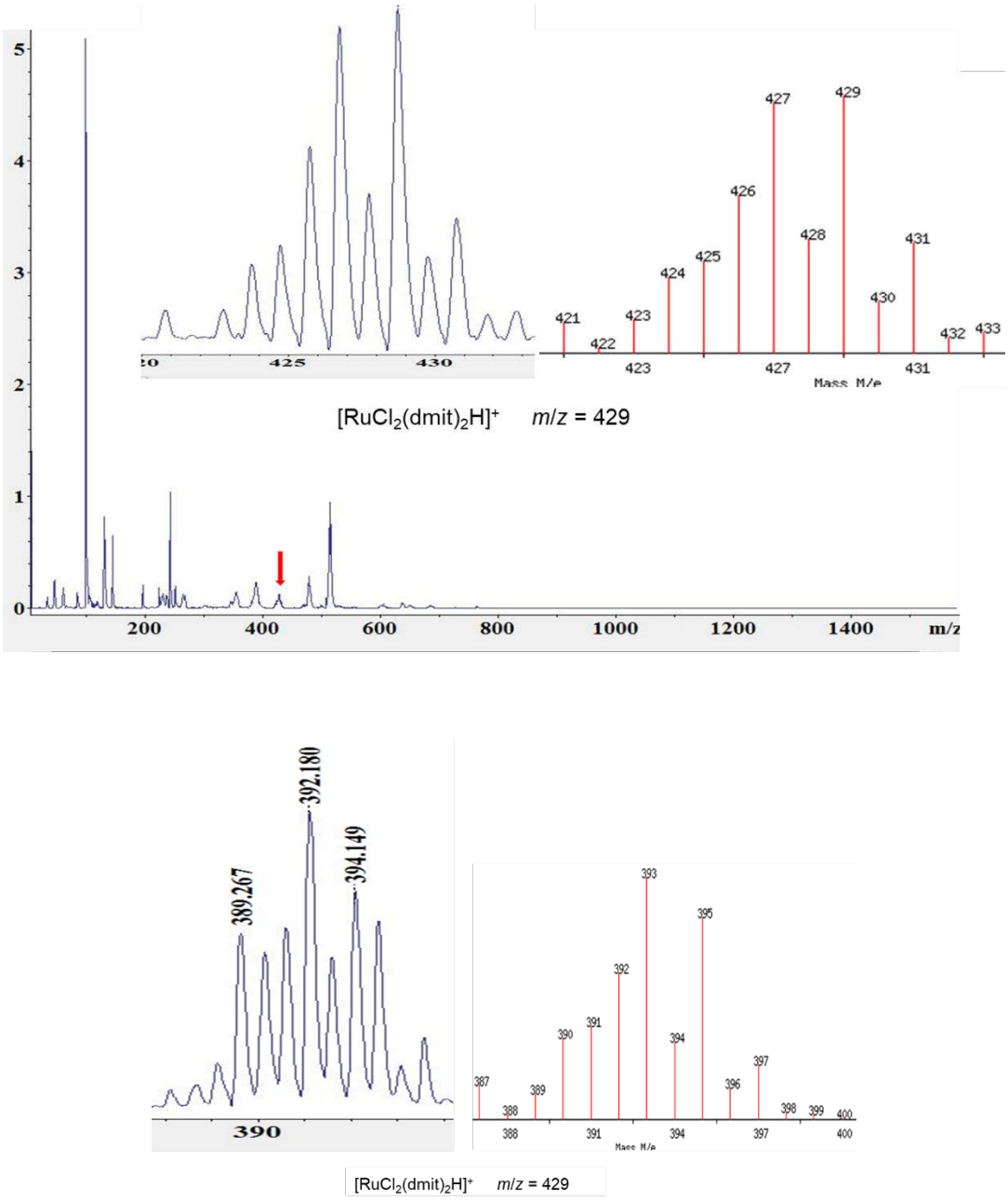

Figure 3.36. MALDI mass spectrum with insets of experimental (left) and simulated (right) envelope intensities for $Ru(dmit)_4Cl_2$ (**8**).

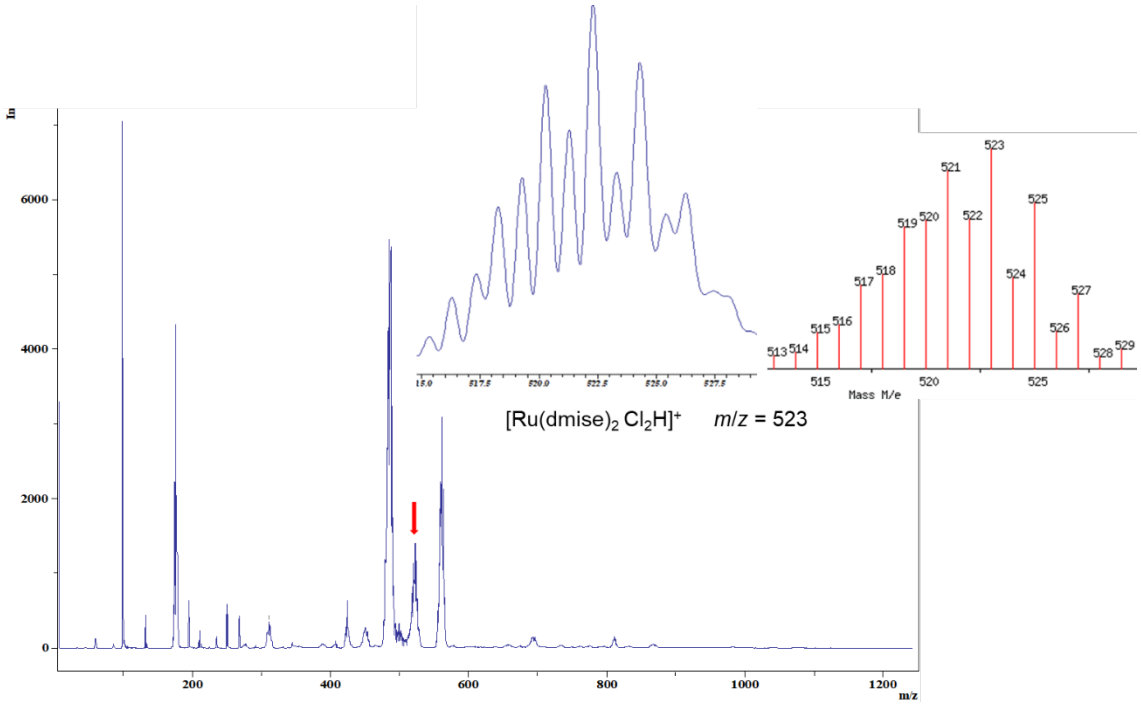

Figure 3.37. MALDI mass spectrum with insets of experimental (left) and simulated (right) envelope intensities for Ru (dmise)$_4$Cl$_2$ (**9**).

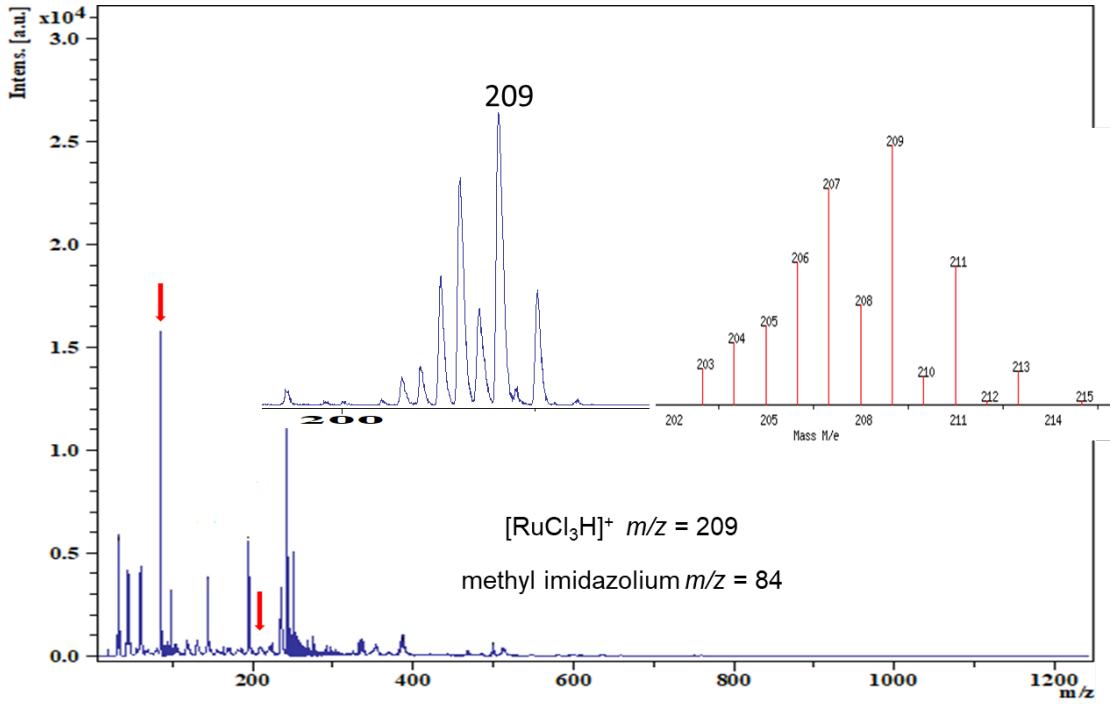

Figure 3.38. Positive-ion MALDI mass spectrum with insets of experimental (left) and simulated (right) envelope intensities for [Ru(MMI)$_6$]Cl$_3$ (**1a**) after H_2O_2 addition.

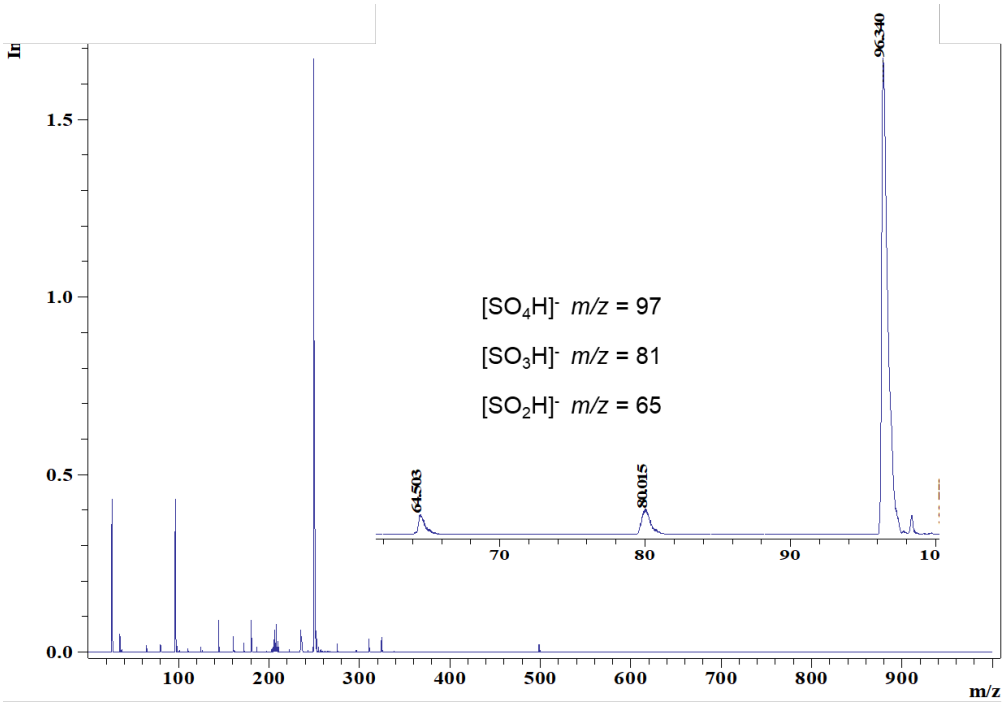

Figure 3.39. Negative-ion MALDI mass spectrum with insets of experimental envelope intensities for $[Ru(MMI)_6]Cl_3$ (**1a**) after H_2O_2 addition.

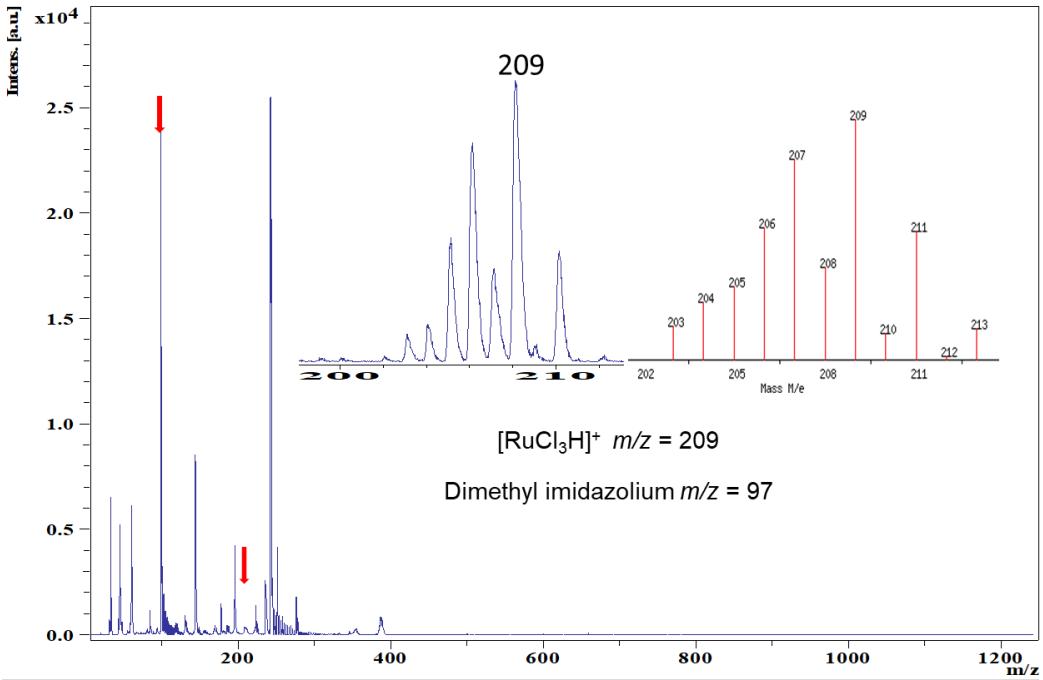

Figure 3.40. Positive-ion MALDI mass spectrum with insets of experimental (left) and simulated (right) envelope intensities for $[Ru(dmit)_6]Cl_3$ (**2**) after H_2O_2 addition.

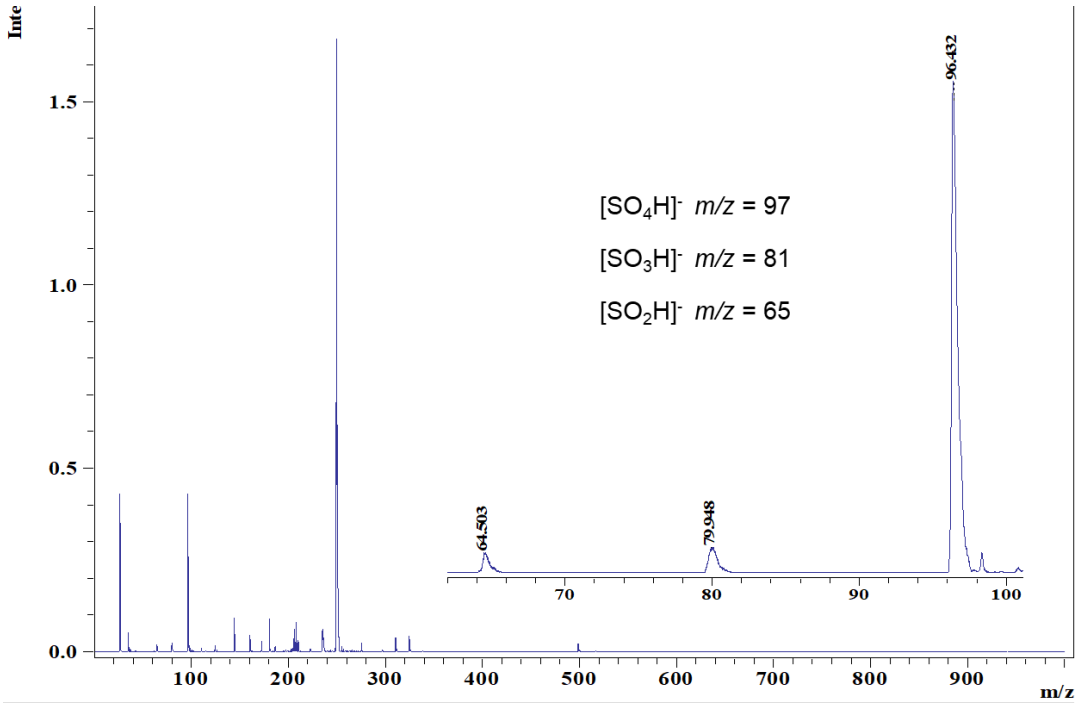

Figure 3.41. Negative-ion MALDI mass spectrum with insets of experimental envelope intensities for $[Ru(dmit)_6]Cl_3$ (**2**) after H_2O_2 addition.

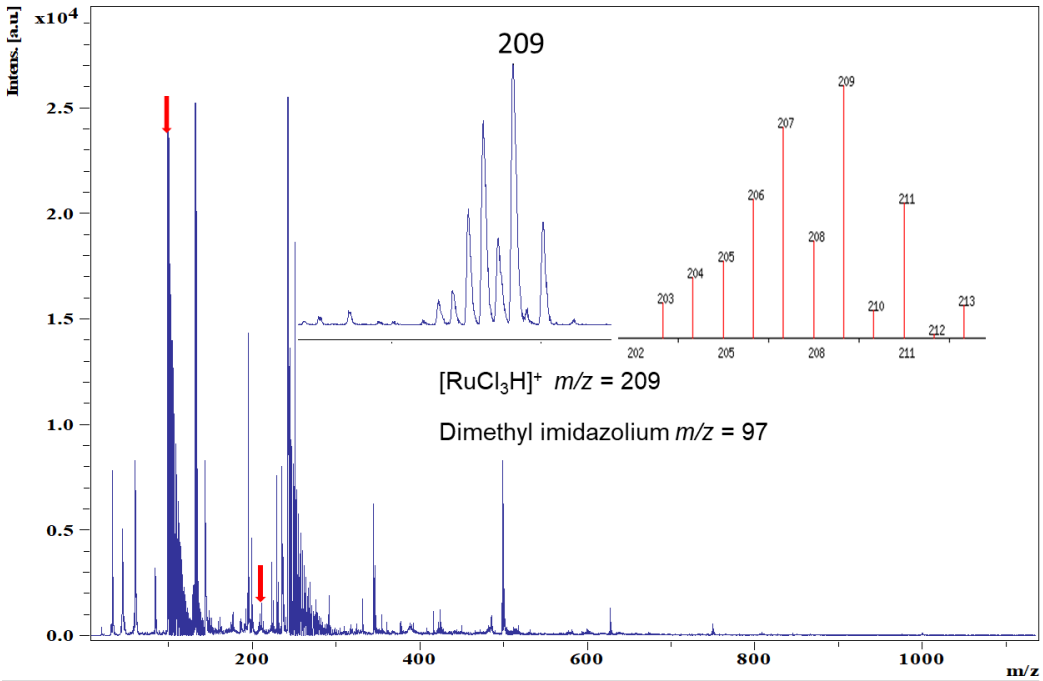

Figure 3.42. Positive-ion MALDI mass spectrum with insets of experimental (left) and simulated (right) envelope intensities for $[Ru(dmise)_6]Cl_3$ (**3**) after H_2O_2 addition.

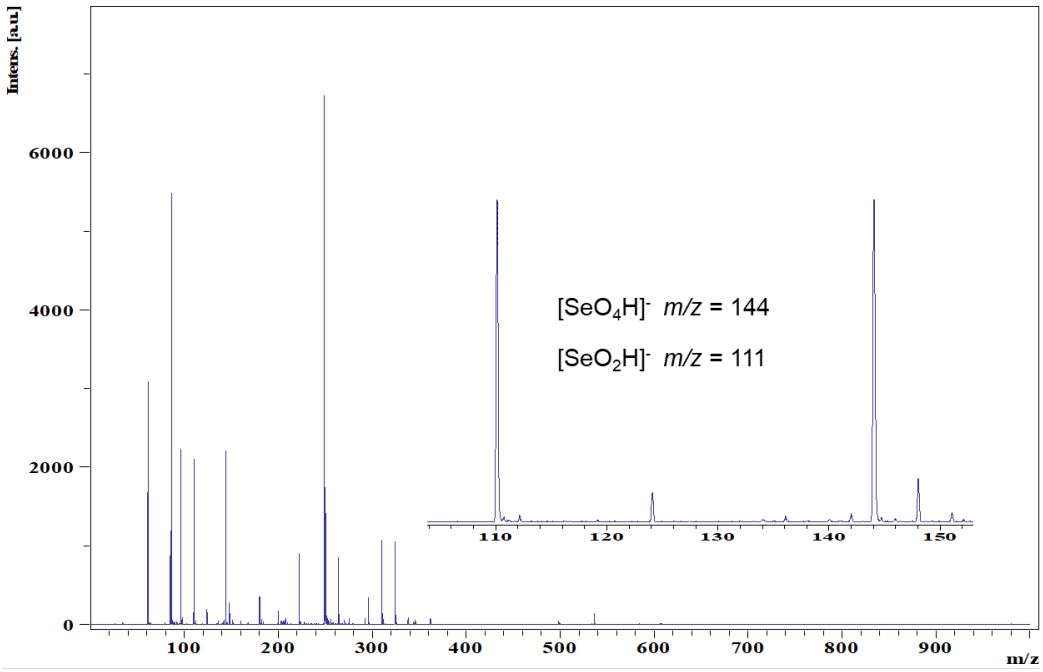

Figure 3.43. Negative-ion MALDI mass spectrum with insets of experimental envelope intensities for $[Ru(dmise)_6]Cl_3$ (**3**) after H_2O_2 addition.

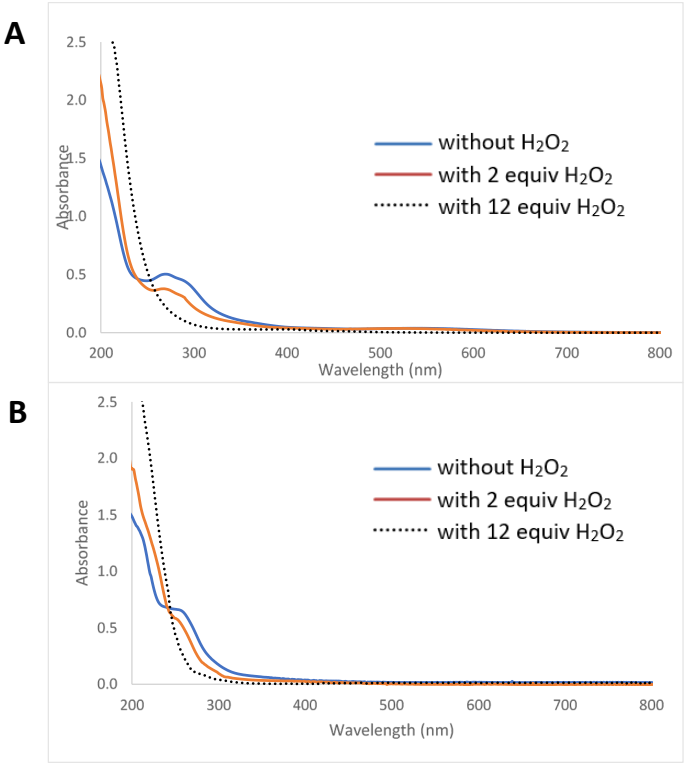

Figure 3.44. UV-vis spectra of A) $[Ru(dmit)_6]Cl_3$ and B) $[Ru(dmise)_6]Cl_3$ (100 µM) in acetonitrile before and after addition of 2 and 12equiv H_2O_2.

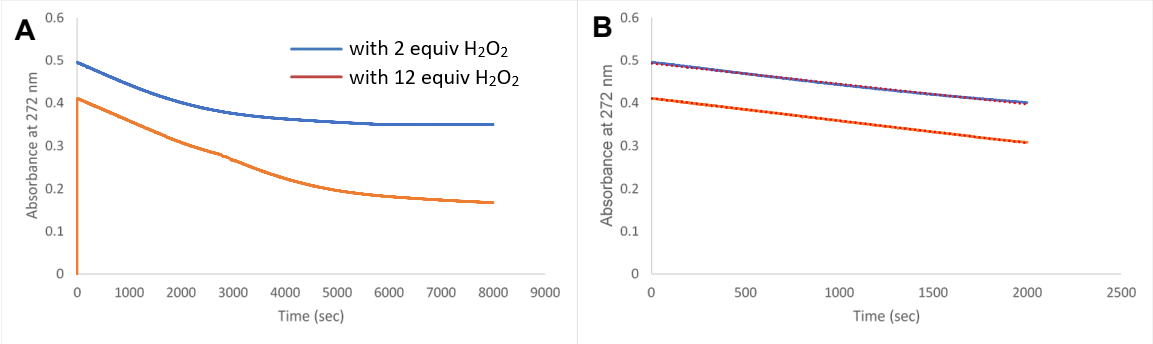

Figure 3.45. Kinetics curves for $[Ru(dmit)_6]Cl_3$ upon treatment with A) 2 equiv and 12 equiv H_2O_2, (0-8000 s) and B) the best-fit line fit to the initial linear portion of the kinetic curves with 2 equiv and 12 equiv H_2O_2 (0-2000 s; $R^2 = 0.996$ and 0.999, respectively).

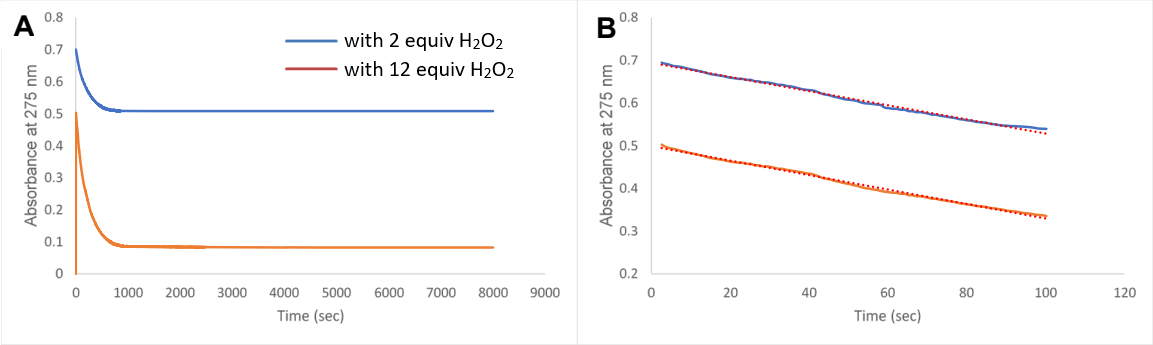

Figure 3.46. Kinetics curves for $[Ru(dmise)_6]Cl_3$ upon treatment with A) 2 equiv and 12 equiv H_2O_2, (0-8000 s) and B) the best-fit line fit to the initial linear portion of the kinetic curves with 2 equiv and 12 equiv H_2O_2 (0-100 s; $R^2 = 0.994$ and 0.995, respectively).

Table 3.7. Gel electrophoresis results for DNA damage prevention assays with $[Ru(MMI)_6]Cl_3$ (**1**).[a]

Gel lane	[**1**] (μM)	% Supercoiled	% Nicked	% Damage Inhibition	*p* Value
1: plasmid DNA (p)	0	99.93 ± 0.12	0.07	-	-
2: p + H_2O_2 (50 μM)	0	99.31 ± 1.20	0.69	-	-
3: p + $[Ru(MMI)_6]Cl_3$ (**1**) + H_2O_2	1000	98.91 ± 1.39	1.09	-	-
4: p + Fe^{II} (2 μM) + H_2O_2	0	13.62 ± 4.33	86.38	-	-
5: p + Fe^{II} + H_2O_2 + **1**	0.001	12.70 ± 1.00	87.30	-0.30 ± 1.01	0.658
6:	0.01	17.06 ± 7.73	82.94	4.79 ± 7.72	0.395
7:	0.1	13.05 ± 3.26	86.95	0.16 ± 3.25	0.940
8:	1	39.31 ± 0.35	60.69	30.57 ± 0.35	>0.001
9:	10	93.18 ± 0.99	6.82	92.89 ± 1.00	>0.001
10:	50	99.61 ± 0.58	0.39	100.34 ±0.61	>0.001
11:	100	100.00 ± 0	0.00	100.80 ± 0	>0.001
12:	500	100.00 ± 0	0.00	100.80 ± 0	>0.001
13:	1000	100.00 ± 0	0.00	100.80 ± 0	>0.001

[a]Data are reported as the average of three trials with calculated standard deviations shown.

3.6 References

(1) Sharma, A. K.; Joshi, H.; Sharma, K. N.; Gupta, P. L.; Singh, A. K. *Organometallics* **2014**, *33*, 3629–3639.

(2) Santos, K.; Dinelli, L. R.; Bogado, A. L.; Ramos, L. A.; Cavalheiro, É. T.; Ellena, J.; Castellano, E. E.; Batista, A. A. *Inorg. Chim. Acta* **2015**, *429*, 237–242.

(3) Sampath, K.; Sathiyaraj, S.; Jayabalakrishnan, C. *Spectrochim. Acta A Mol. Biomol. Spectr.* **2013**, *105*, 582–592.

(4) Scintilla, S.; Brustolin, L.; Gambalunga, A.; Chiara, F.; Trevisan, A.; Nardon, C.; Fregona, D. *J. Inorg. Biochem.* **2016**, *165*, 159–169.

(5) Zhang, Q.-F.; Cheung, F. K. M.; Wong, W.-Y.; Williams, I. D.; Leung, W.-H. *Organometallics* **2001**, *20*, 3777–3781.

(6) Corrêa, R. S.; da Silva, M. M.; Graminha, A. E.; Meira, C. S.; Santos, J. A. F. dos; Moreira, D. R. M.; Soares, M. B. P.; Von Poelhsitz, G.; Castellano, E. E.; Bloch, C.; Cominettih, M. R.; Batistaa, A. A. *J. Inorg. Biochem.* **2016**, *156*, 153–163.

(7) Hayat, F.; Zia-ur-Rehman; Khan, M. H. *J. Coord. Chem.* **2017**, *70*, 279–295.

(8) Devagi, G.; Dallemer, F.; Kalaivani, P.; Prabhakaran, R. *J. Organomet. Chem.* **2018**, *854*, 1–14.

(9) Deng, Z.; Yu, L.; Cao, W.; Zheng, W.; Chen, T. *Chem. Commun.* **2015**, *51*, 2637–2640.

(10) Appelt, P.; Fagundes, F. D.; Facchin, G.; Gabriela Kramer, M.; Back, D. F.; Cunha, M. A. A.; Sandrino, B.; Wohnrath, K.; de Araujo, M. P. *Inorg. Chim. Acta*

2015, *436*, 152–158.

(11) Dragutan, I.; Dragutan, V.; Demonceau, A. *Molecules* **2015**, *20*, 17244–17274.

(12) Li, F.; Collins, J. G.; Keene, F. R. *Chem. Soc. Rev.* **2015**, *44*, 2529–2542.

(13) Allardyce, C. S.; Dyson, P. J. *Platinum Met. Rev.* **2001**, *45*, 62–69.

(14) Valko, M.; Izakovic, M.; Mazur, M.; Rhodes, C. J.; Telser, J. *Mol. Cell. Biochem.* **2004**, *266*, 37-56.

(15) Valko, M.; Leibfritz, D.; Moncol, J.; Cronin, M. T.; Mazur, M.; Telser, J. *Int. J. Biochem. Cell Biol.* **2007**, *39*, 44-84.

(16) Valko, M.; Morris, H.; Cronin, M. T. *Curr. Med. Chem.* **2005**, *12*, 1161-1208.

(17) Valko, M.; Morris, H.; Mazur, M.; Rapta, P.; Bilton, R. F. *Biochim. Biophys. Acta* **2001**, *1527*, 161-166.

(18) Valko, M.; Rhodes, C. J.; Moncol, J.; Izakovic, M.; Mazur, M. *Chem. Biol. Interact.* **2006**, *160*, 1-40.

(19) Dragutan, I.; Dragutan, V.; Demonceau, A. *Molecules* **2015**, *20*, 17244–17274.

(20) Battin, E. E.; Zimmerman, M. T.; Ramoutar, R. R.; Quarles, C. E.; Brumaghim, J. L. *Metallomics* **2010**, *3*, 503-512.

(21) Battin, E. E.; Perron, N. R.; Brumaghim, J. L. *Inorg. Chem.* **2006**, *45*, 499-501.

(22) Battin, E. E.; Zimmerman, M. T.; Ramoutar, R. R.; Quarles, C. E.; Brumaghim, J. L. *Metallomics* **2011**, *3*, 503–512.

(23) Kimani, M. M.; Bayse, C. A.; Brumaghim, J. L. *Dalton Trans.* **2011**, *40*, 3711–3723.

(24) Kimani, M. M.; Bayse, C. A.; Stadelman, B. S.; Brumaghim, J. L. *Inorg. Chem.*

2013, *52*, 11685–11687.

(25) Stadelman, B. S.; Kimani, M. M.; Bayse, C. A.; McMillen, C. D.; Brumaghim, J. L. *Dalton Trans.* **2016**, *45*, 4697–4711.

(26) Stadelman, B. Ph. D. dissertation, Clemson University, Clemson, SC **2016**.

(27) Seifried, H. E. *J. Nutr. Biochem.* **2007**, *18*, 168-171.

(28) Brewer, A. C.; Mustafi, S. B.; Murray, T. V.; Rajasekaran, N. S.; Benjamin, I. J. *Antioxid. Redox Signaly* **2012**, *18*, 1114-1127.

(29) Epand, R. M.; Epand, R. F.; Wong, S. C. *J. Clin. Chem. Clin. Biochem.* **1988**, *26*, 623-626.

(30) Akanmu, D.; Cecchini, R.; Arouma, O.; Halliwell, B. *Arch. Biochem. Biophys.* **1991**, *288*, 10-16.

(31) Aruoma, O. I.; Whiteman, M.; England, T. G.; Halliwell, B. *Biochem. Biophys. Res. Commun.* **1997**, *231*, 389-391.

(32) Aruoma, O. I.; Spencer, J. P.; Mahmood, N. *Food Chem. Toxicol.* **1999**, *37*, 1043-1053.

(33) Yamashita, Y., M. Yamashita, *J. Biol. Chem.* **2010**, *285*, 18134-18138.

(34) Banerjee, M.; Karri, R.; Rawat, K. S.; Muthuvel, K.; Pathak, B.; Roy, G. *Angew. Chem. Int. Ed.* **2015**, *54*, 9323–9327.

(35) Rahaman, S. A.; Roy, B.; Mandal, S.; Bandyopadhyay, S. *Inorg. Chem.* **2016**, *55*, 1069–1075.

(36) Banerjee, M.; Karri, R.; Chalana, A.; Das, R.; Rai, R. K.; Rawat, K. S.; Pathak, B.; Roy, G. *Chem. Eur. J.* **2017**, *23*, 5696–5707.

(37) Karri, R.; Banerjee, M.; Chalana, A.; Jha, K. K.; Roy, G. *Inorg. Chem.* **2017**, *56*, 12102–12115.

(38) Roy, G.; Das, D.; Mugesh, G. *Inorg. Chim. Acta* **2007**, *360*, 303–316.

(39) Roy, G.; Mugesh, G. *Bioinorg. Chem. Appl.* **2006**, *23214, 1-9.*

(40) Reich, H. J.; Hondal, R. J. *ACS Chem. Biol.* **2016**, *11*, 821–841.

(41) Savjani, J. K.; Gajjar, A. K. *Pak. J. Biol. Sci.* **2011**, *14*, 1076–1089.

(42) Kimani, M. M.; Brumaghim, J. L., VanDerveer; D. *Inorg. Chem.* **2010**, *49*, 9200-9211.

(43) Kimani, M. M.; VanDerveer; D., Brumaghim, J. L. *Acta. Crystallogr.* **2011**, *C67*, 208- 210.

(44) Kimani, M. M.; Wang, H. C., Brumaghim, J. L. *Dalton Trans.* **2012**, *41*, 5248-5259.

(45) Roy G., Mugesh, G. *Chem. Biodivers.* **2008**, *5*, 414-439.

(46) Ferreira A. C., Carvalho Cardoso L. de, Rosenthal D., Carvalho D. P. de. *Eur. J. Biochem.* **2003**, *270*, 2363-2368.

(47) Qin, Y.; Ma, Q.; Jia, A.-Q.; Chen, Q.; Zhang, Q.-F. *J. Coord. Chem.* **2013**, *66*, 1405–1415.

(48) Bailey, P. J.; Bell, N. L.; Nichol, G. S. *Dalton Trans.* **2013**, *42*, 11281–11294.

(49) Foreman, M. R. S.-J.; Ma, C.; Hill, A. F.; Otten, N. E.; Sharma, M.; Tshabang, N.; Ward, J. S. *Dalton Trans.* **2017**, *46*, 14957–14972.

(50) Zhu, H.; Ma, Q.; Jia, A.-Q.; Chen, Q.; Leung, W.-H.; Zhang, Q.-F. *Inorg. Chim. Acta* **2013**, *405*, 427–436.

(51) Evans, I. P.; Spencer, A.; Wilkinson, G. *J. Chem. Soc., Dalton Trans.* **1973**, *2*, 204–209.

(52) Brindell, M.; Kuliś, E.; Elmroth, S. K. C.; Urbańska, K.; Stochel, G. *J. Med. Chem.* **2005**, *48*, 7298–7304.

(53) Raper, E. S.; Creighton, J. R.; Oughtred, R. E.; Nowell, I. W. *Acta Crystallogr.* **1983**, *B39*, 355-360.

(54) Ansell, G. B. *J. Chem. Soc., Perkin Trans. 2* **1972**, 841-843.

(55) Biswas, N.; Thomas, S.; Sarkar, A.; Mukherjee, T.; Kapoor, S. *J. Phys. Chem. C.* **2009**, *113*, 7091-7100.

(56) Landry, V. K.; Minoura, M.; Pang, K.; Buccella, D.; Kelly, B. V.; Parkin, G. *J. Am. Chem. Soc.* **2006**, *128*, 12490-12497.

(57) Williams, D. J.; Ly, T. A.; Mudge, J. W.; Vanderveer, D.; Jones, R. L. *Inorg. Chim. Acta* **1994**, *218*, 133-138.

(58) Kimani, M. M.; Bayse, C. A.; Brumaghim, J. L. *Dalton Trans.* **2011**, *40*, 3711–3723.

(59) Kimani, M. M.; Brumaghim, J. L.; VanDerveer, D. *Inorg. Chem.* **2010**, *49*, 9200-9211.

(60) Jia, W.; Huang, Y.; Lin, Y.; Wang, G.; Jin, G. *Eur. J. Inorg. Chem.* **2008**, 4063-4073.

(61) Aggarwal, V.; Kumar, V. R.; Singh, U. P. *J. Chem. Crystallogr.* **2011**, *41*, 121-126.

(62) Grapperhaus, C. A.; Poturovic, S.; Mashuta, M. S. O. *Inorg. Chem.* **2005**, *44*, 8185–8187.

(63) Schulenburg, H.; Hilgendorff, M.; Dorbandt, I.; Radnik, J.; Bogdanoff, P.; Fiechter, S.; Bron, M.; Tributsch, H. *J. Power Sources* **2006**, *155*, 47–51.

(64) Kimani, M. M.; Brumaghim, J. L.; VanDerveer, D. *Inorg. Chem.* **2010**, *49*, 9200–9211.

(65) Zimmerman, M. Ph. D. Dissertation, Clemson University, Clemson, SC, **2014**.

(66) Abbas, M. A.; McMillen, C. D.; Brumaghim, J. L. *Inorg. Chim. Acta* **2017**, *468*, 308–315.

(67) Gottlieb, H. E.; Kotlyar, V.; Nudelman, A. *J. Org. Chem.* **1997**, *62*, 7512-7515.

(68) https://www.sisweb.com/mstools/isotope.htm (accessed March 23, 2019

(69) Hertzberg, R. P.; Dervan, P. B. *J. Am. Chem. Soc.* **1982**, *104*, 313–315.

(70) Lloyd, R. S.; Haidle, C. W.; Robberson, D. L. *Biochemistry* **1978**, *17*, 1890–1896.

(71) Perkowski, D. A.; Perkowski, M. Data and probability connections; Connections in mathematics courses for teachers; Pearson Prentice Hall; London: Pearson Education Ltd: Upper Saddle River, N.J., 2007.

CHAPTER FOUR

SYNTHESIS OF NOVEL RUTHENIUM NITROSYL THIONE AND SELONE COMPLEXES USING A NITRATE SALT

4.1. Introduction

Nitric oxide (NO) is a vital molecule in living systems due to its multiple biological functions,[1-4] including control of sleep and body temperature,[5-6] regulation of blood pressure,[6-7] cardiovascular control, neurotransmission,[7-10] modulation of the immune and endocrine response, and induction of apoptosis.[11-12] Biological NO is generated by nitric oxide synthase (NOS), an enzyme that converts L-arginine to L-citrulline and NO.[13] The short lifetime and instability of NO makes the study of its physiological roles difficult;[1] therefore, many studies have used transition metal complexation as a way to obtain stable nitrosyl compounds.[14-15] In addition, NO delivery by metal-nitrosyl complexes can release NO to biological targets directly while avoiding effects on untargeted cells, and ruthenium-nitrosyl complexes have been synthesized for this purpose.[16]

Ruthenium complexes have high affinity for NO, solubility in water, accessibility of different oxidation states under physiological conditions, thermodynamic stability, low toxicity, and photolability; therefore, ruthenium nitrosyl complexes are some of the most investigated compounds for biological NO delivery.[1,17-23] For example, the nitrosyl ligand in the complex *trans*-$[(Ru(NH_3)_4L(NO)]^{3+}$ (L = pyridine, 4-methyl-pyridine) can be released in aqueous solution upon UV irradiation (300-370 nm) to form *trans*-$[(Ru(NH_3)_4L(H_2O)]^{3+}$.[23]

In addition to NO delivery agents, ruthenium complexes have been synthesized as

biological NO scavengers.[18,24-27] NO scavenging can control nitric oxide bioavailability and modulate homeostatic vascular function that is regulated by NO release.[28] The nitrosyl complex [Ru(NO)(dha-tsc)Cl(H_2O)] (dhs-tsc = *N*-dehydroacetic acid-thiosemicarbazide) was examined for its antibacterial properties as a potential treatment for urinary tract infections.[29]

In addition to nitrosyl complexes of ruthenium, complexes with thione and selone ligands are also of interest as models for the reactivity of biological thiones and selones such as ergothioneine,[30-37] selenoneine,[38] and methimazole.[39-40] In recent years, thione ruthenium complexes have attracted attention due to their potential antimicrobial and antitumor applications.[41-44] Despite a variety of potential applications, however, synthesis of metal-nitrosyl complexes can be difficult, requiring toxic NO gas or unstable nitrosyl salts to add this ligand.

In this work, we report the synthesis and characterization of Ru(II)-nitrosyl complexes with *N*,*N'*-dimethylimdiazole -thione (dmit) or *N*,*N'*-dimethylimdiazole -selone (dmise) ligands from $RuCl_3 \cdot xH_2O$ and silver nitrate as a simple and convenient nitrosyl source. This synthetic procedure avoids complicated syntheses of nitrosyl complexes with low yields and the use of toxic or unstable reagents for NO addition. This method will greatly facilitate synthesis of ruthenium-nitrosyl complexes, a class of widely studied, potentially bioactive compounds.

4.2. Results and Discussion

Synthesis of Ru(II)-nitrosyl complexes. Novel Ru(II)-nitrosyl complexes with

thione or selone ligands were synthesized using a two-step process. In the first step, a solution of $RuCl_3 \cdot xH_2O$ in acetonitrile was treated with $AgNO_3$ (2 equiv) under argon, and the reaction mixture was heated to reflux for 4 h (Scheme 4.1). During this time, the dark reaction mixture became pale, indicating Ru(III) reduction to Ru(II). After filtration of the AgCl precipitate, an acetonitrile solution of dmit or dmise (4 equiv) was added to the filtrate. The reaction mixture was then heated to reflux for 4 h and cooled before adding $NaBF_4$ (2 equiv) and heating the reaction mixture to reflux for an additional 8 h. After purification, $[Ru(NO)(dmit)_4Cl][BF_4]_2$ (**1**) and $[Ru(NO)(dmise)_4Cl][BF_4]_2$ (**2**) were obtained in good yield as brown and purple solids, respectively (Scheme 4.1). Both Ru-nitrosyl complexes are soluble in and stable to water and air as solids and stable in solution for at least 24 h.

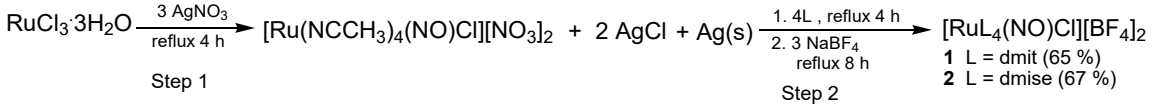

Scheme 4.1. Method for forming Ru(II) complexes **1** and **2** in acetonitrile.

The identities of complexes **1** and **2** are supported by mass spectrometry data that show $[Ru(NO)(dmit)_3(BF_4)_2]^+$ (*m/z* = 690) and $[Ru(NO)(dmit)_4Cl(BF_4)]^+$ (*m/z* = 766) ions for **1**, and $[Ru(NO)(dmise)_2(BF_4)_2]^+$ (*m/z* = 655) and $[Ru(NO)(dmise)_2Cl(BF_4)_2H]^+$ (*m/z* = 692) ions for **2** (Figures 4.3-4.4). The product formed prior to dmit or dmise addition, was also characterized by mass spectrometry as the Ru(II)-NO complex $[Ru(NO)(NCCH_3)_4Cl(NO_3)]^+$ (*m/z* = 392; Figure 4.5), indicating that Ru(III) reduction and NO formation occur in step 1. A small amount of silver mirror formed on the bottom of the reaction flask, indicating Ag^+ reduction to Ag^0, and the Ag^+/Ag^0 redox potential (0.80 V)

and Ru^{3+}/Ru^{2+} redox potential (0.25 V)[45] support electrochemical reduction of Ru^{3+} to Ru^{2+} and Ag^{+} to Ag^{0} by electrons released from thermal decomposition of NO_3 to NO and O_2.[46-47] No Ru-NO product is observed as a product of the step 1 reaction unless the reaction mixture is heated. Thus, step 2 replaces the labile acetonitrile ligands with thione and selone ligands and exchanges the counterions. Interestingly, products **1** and **2** also form in very low yields when $NaNO_3$ is used in place of $AgNO_3$, so it is likely the presence of Ag^{+} facilitates this reaction. To the best of our knowledge, this is the first report of Ru-NO complexes synthesized using a nitrate salt, although NO has been reported as a thermal decomposition product of metal nitrates.[47] The use of a nitrate salt in place of typical NO addition reagents greatly simplifies generation of Ru-NO complexes.

Structural analysis of Ru(II)-nitrosyl complexes. Complexes **1** and **2** were characterized by X-ray structural analysis from single crystals grown by slow diffusion of diethyl ether into acetonitrile solutions of the complexes. Both complexes crystalize in space group $P2_1/c$, although they are not isomorphous. Ru(II) centers in **1** and **2** adopt distorted octahedral geometry, with S1-Ru1-S2 bond angles of 89.38(4) and 90.62(4)º in **1** and Se1-Ru1-Se2 bond angles of 89.690(16)-90.311(16) in **2** (Figure 4.1 and Tables 4.1, 4.5, and 4.6). The four dmit/dmise ligands in the equatorial plane are coordinated through the S/Se atoms, with the nitrosyl and chloride ligands *trans* to each other in the axial positions to complete the coordination sphere. In both complexes, the NO and Cl ligands are disordered with one another over both of the axial positions, as often occurs in such complexes. The Ru-S bond lengths in **1** are 2.426(10) and 2.4349(10) Å, similar to Ru-S bond lengths of other Ru(II)-thione complexes are such as in $[RuCl(L^1)_2CO(PPh_3)_2]$ (L^1 =

1-(4-methyl-phenyl)-imidazole-2-thione) 2.478(2) Å,[48] and $[Ru(L^2)_2(PPh_3)_2Cl_2]$ (L^2 = 1-(4-chlorophenyl)imidazole-2-thione) 2.4087(16) Å .[49] For **2**, the Ru-Se bonds lengths are slightly longer (2.5422(5) and 2.5452(5) Å), similar to Ru-Se bond lengths in $[(\eta^6\text{-}C_6H_6)Ru(L^3)Cl][PF_6]$($L^3$ = 1-benzyl-3-phenylselenylmethyl-1,3-dihydrobenzoimidazole-2-selone) (2.5431(10) and 2.5434(9) Å.[50]

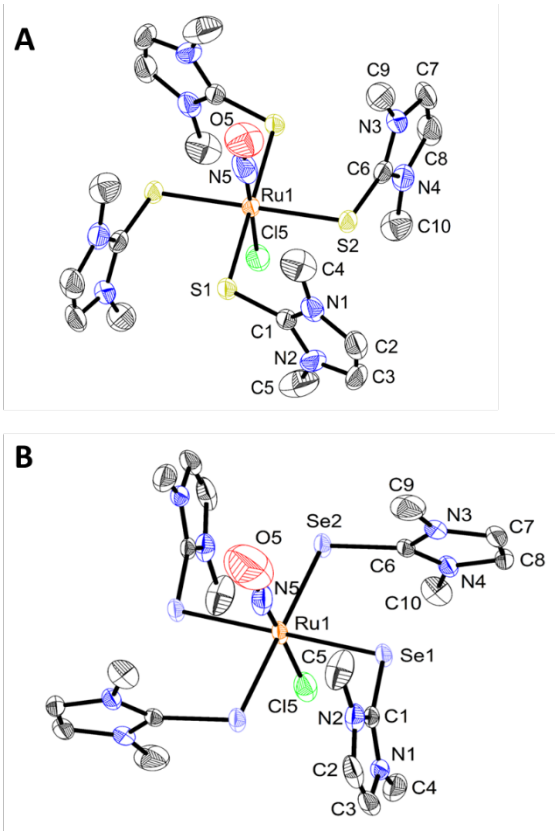

Figure 4.1. Crystal structure diagrams of A) $[Ru(NO)(dmit)_4Cl](BF_4)_2$ (**1**) and B) $Ru(NO)(dmise)_4Cl](BF_4)_2$ (**2**) showing 50% ellipsoids; hydrogen atoms and counterions are omitted for clarity.

The C-S bond lengths in **1** are 1.714(4) and 1.718(4) Å, longer than in unbound dmit (1.696 Å[51]), this elongation is due to increased contribution from the zwitterionic resonance structure upon metal binding, a trend that has been observed previously.[52-54] The range of

N-C bond lengths of 1.343(6)-1.377(6) in the dmit ligands in **1** is not significantly different from the N-C bond lengths in unbound dmit (1.349(6) Å[51]). Similarly, the C-Se bond lengths in **2** are 1.865(5) and 1.868(4) Å, and also slightly longer than those for unbound dmise 1.843(4) Å.[55] Similarly, the C-N bond lengths for the dmise ligands in **2** are not significantly different from those of unbound dmise (1.334(7) and 1.343(6) Å, respectively).[55]

Table 4.1. Selected bond lengths (Å) and angles (deg) for $[Ru(NO)(dmit)_4Cl](BF_4)_2$ (**1**) and $[Ru(NO)(dmise)_4Cl](BF_4)_2$ (**2**).

	1	**2**
Ru1-N5	1.69(2)	1.679(13)
Ru1-E1	2.4259(10)	2.5422(5)
Ru1-E2	2.4349(10)	2.5452(5)
E1-C1	1.714(4)	1.865(5)
N-O	1.31(2)	1.23(18)
N5-Ru1-E1	89.1(11)	90.4(8)
N5-Ru1-E1	90.9(11)	89.7(8)
E1-Ru1-E1	180.00(6)	180.0
Cl5-Ru1-E2	90.7(2)	93.06(14)
O-N-Ru	174(3)	169(3)

In both complexes, the coordinated NO ligand is nearly linear, with Ru-N-O angles of 174(3) and 169(3)º for **1** and **2**, respectively. This indicates a formal NO^+ ligand, consistent with the range of Ru-N-O angles (164-178º) for reported Ru-NO complexes with linear binding modes.[58-59,61,64] The N-O bond length in **1** (1.31(2) Å) is longer than that of **2** (1.234(18) Å; Table 4.5), indicating the possibility of greater Ru(II)-NO backbonding in dmit complex **1**. For both complexes, the N-O bond length is longer than the N-O bond lengths for reported Ru(II)-nitrosyl complexes (1.14-1.25 Å),[14-15,56-69] and the Ru-N distances in **1** and **2** (1.69 (2) and 1.679(13) Å, respectively) are slightly shorter than those in reported nitrosyl ruthenium complexes (1.72-1.79 Å).[14-15,55-69] These effects may be due

to the NO/Cl disorder present in the structures. These complexes represent, to our knowledge, the first reported Ru-nitrosyl compounds with imidazole -thione or -selone.

Infrared and NMR spectroscopy. IR spectra of $[Ru(NO)(dmit)_4Cl][BF_4]_2$ (**1**) and $[Ru(NO)(dmise)_4Cl][BF_4]_2$ (**2**) show NO stretching bands of the nitrosyl ligands at 1827 and 1810 cm^{-1}, respectively (Table 4.2; Figures 4.6, 4.7, and 4.10). The presence of these bands in the 1700-1920 cm^{-1} range are diagnostic of a formally NO^+ ligand bound to Ru(II),[70] consistent with linear NO binding as observed in the structures of **1** and **2**.[63,70] Relative to unbound NO (1870 cm^{-1} [71]), bands at 1829 and 1810 cm^{-1} for **1** and **2**, respectively, indicating that the Ru-bound NO ligand is less reactive than free NO. The range for NO^+ stretching bands in $[Ru(NO)(R\text{-}Phtpy)Cl_2]^+$ (R-Phtpy = 4′-position of terpyridine ligands) and $[Ru(NO)(NH_3)_3Cl_2]Cl$ is 1880-1930 cm^{-1},[59,64] higher than observed for **1** and **2**, likely indicating that dmit and dmise binding decreases the NO stretching frequency relative to nitrogen donor ligands.

Table 4.2. Selected IR stretches and NMR resonances (in D_2O) for compounds **1** and **2**.

	IR (cm^{-1})		^1H NMR shifts (δ)	
Compound	S/Se=C	N≡O	CH_3	C-H
Dmit	1181[71]	-	3.48	6.95
Dmise	1147[72]	-	3.61	7.16
$[Ru(NO)(dmit)_4Cl][BF_4]_2$ (**1**)	1171	1827	3.61	7.17
$[Ru(NO)(dmise)_4Cl][BF_4]_2$ (**2**)	1151	1810	3.61	6.72

The C=S stretching band for **1** is observed at 1171 cm^{-1}, slightly shifted to lower energy compared to unbound dmit (1181 cm^{-1};[72] Table 4.2). In contrast, the C=Se stretch for **2** is observed at 1151 cm^{-1}, not significantly shifted compared to unbound dmise (1147 cm^{-1} [73]). These IR results suggest the primarily σ- and π-donor interactions of Ru(II)-coordinated dmit and dmise ligands, with dmise having somewhat more donor character

than dmit. Similar shifts in C=S/C=Se bond stretches have been observed for Cu(I),[75-76] Ni(II),[77] Co(III),[77-78] Fe(II),[50] and Zn(II)[50] complexes of dmit and dmise.

^{1}H NMR spectra for **1** and **2** (Table 4.2 and Figures 4.3-4.5) show a downfield shift for the methyl proton resonance in dmit complex **1** (δ 3.61) compared to unbound dmit (δ 3.48), but show no shift for the methyl resonances in dmise complex **2** (δ 3.61) relative to unbound dimse. This downfield shift for the methyl proton resonance of **1** is consistent with increasing the contribution of the aromatic resonance structure that increases the negative charge on the sulfur atom of the thione.[51] The stronger donor character of Ru(II)-coordinated dmise compared to dmit is also observed in a downfield shift for the olefinic protons (δ 7.17) in **1** compared to unbound dmit (δ 6.95), whereas the olefinic resonances for dmise complex **2** (δ 6.72) shift upfield relative to unbound dmise (δ 7.16). These opposite NMR shifts for the olefinic protons indicate less contribution of the zwitterionic resonance structure for dmise ligands in **2** relative to dmit ligands in **1**, consistent with IR results.

To further investigate the identity of the product formed prior to dmit or dmise addition (Scheme 4.1), the reaction mixture was filtered after step 1 to remove the AgCl precipitate, and the solvent was removed *in vacuo* to yield a brown powder. As mentioned previously, analysis of this sample by mass spectrometry indicates the presence of $[Ru(NO)(NCCH_3)_4Cl(NO_3)]^+$. Consistent with formation of this Ru(II)-nitrosyl species, nitrile stretches are observed at 2300 and 2331 cm^{-1} in the IR spectrum of the reaction mixture, consistent with Ru-bound acetonitrile ligands (Figure 4.10).[79] Additionally, a sharp NO stretching band is observed at 1894 cm^{-1}, consistent with the species identified

by mass spectrometry. This NO stretch is 67 and 84 cm^{-1} higher than the NO stretches in **1** and **2**, respectively, likely due to the increased electron donation of dmit and dmise relative to acetonitrile ligands. In contrast, N-O stretching bands for coordinated nitrate ligands in $[Ag(H_2BzPh)(NO_3)]$ (H_2BzPh = 2-benzoylpyridine benzoylhydrazone) are observed at 1384 cm^{-1},[80] much lower frequency than bands for coordinated NO. These results further support the formation of NO directly from $AgNO_3$ treatment of $RuCl_3 \cdot xH_2O$, prior to dmit or dmise addition. Crystallization attempts of this Ru(II) nitrosyl-containing product have thus far proven unsuccessful.

Electrochemical analysis. Understanding the electronic distribution in transition metal-nitrosyl bonds is complex,[82-84] and Ru-NO complexes have been synthesized and their electrochemical properties examined for this purpose.[82-84] In the cyclic voltammograms (CV) of $[Ru(NO)(dmit)_4Cl][BF_4]_2$ (**1**) $[Ru(NO)(dmise)_4Cl][BF_4]_2$ (**2**), dmit and dmise ligand-based redox waves dominate, with (Ep_c) and oxidation (Ep_a) waves for Ru-bound dmit in **1** observed at 0.36 and 1.06 V, respectively (Figure 4.2 and Table 4.3). These waves are 0.50 and 0.58 V higher, respectively, than analogous waves observed for unbound dmit. For Ru-bound dmise in **2**, Ep_c and Ep_a waves are seen at 0.31 and 0.85 V,respectively, 0.46 and 0.48 V higher than for unbound dmise.[51] Thus, Ru coordination shifts the ligand-based potentials to higher potential, indicating that both ligand oxidation and reduction are more spontaneous. This effect is slightly more pronounced for dmit complex **1** compared to dmise complex **2**, and similar trends are observed Fe(II)-thione complexes $Fe(dmit)_2Cl_2$, $[Fe(dmit)_2(CH_3CN)_2][BF_4]_2$, and $[Fe(dmit)_4][OTf]_2$.[50]

In the CV for dmise complex **2**, smaller waves at high potentials are consistent with a reversible Ru(III/II) couple ($E_{1/2}$ = 1.03 V; Table 4.3), which is typically observed in the range of 0.18 to 1.67 V.[87] Ru(IV/III) reduction potentials for $[Ru^{III}Cl_3(CH_3CN)L_1]\cdot L_1\cdot 3H_2O$, ($L_1$ = 2-(2'-pyridyl)benzimidazole) are in the range 1.05 to 1.16 V,[88] consistent with this assignment. Similar Ru(IV/III) waves are not clearly observed in the CV for **1**, perhaps due to overlap with the strong ligand-based waves.

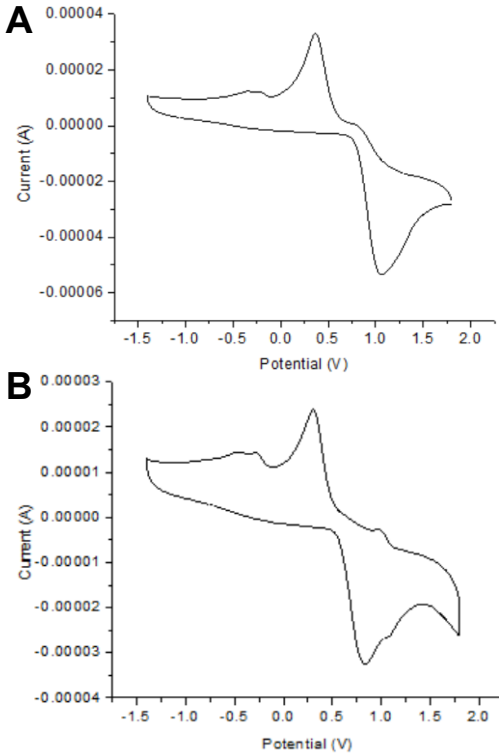

Figure 4.2. A) Cyclic voltammogram (CV) for A) $[Ru(dmit)_4Cl(NO)][BF_4]_2$ (**1**), B) CV for $[Ru(dmise)_4Cl(NO)][BF_4]_2$ (**2**). Samples were prepared with 0.1 mM complex in acetonitrile with tetra-*n*-butyl ammonium phosphate (0.1 M) as the supporting electrolyte.

For both complexes **1** and **2**, two additional reduction waves are observed at -0.33 and -0.24 V for **1** and -0.46 and -0.29 V for **2** (Figure 4.10), likely corresponding to Ru(III/II) and NO reductions. Typical Ru(III/II) cathodic waves occur in the range 1.5 to −0.4 V[88] whereas NO-based cathodic waves occur in the -0.10 to -0.40 V range for

$[Ru(NO)(bpy)_2L]^{2+}$ (L = Cl^-, N_3^-, NO_2^-) and $[Ru(NO)(bpy)_2L]^{3+}$ (L = NH_3, $NCCH_3$, and pyridine) complexes,[70] at significantly lower potentials than the corresponding Ru(III/II) waves for these complexes. These comparisons suggest that the cathodic waves at -0.33 and -0.46 for **1** and **2**, respectively, are due to NO-based reduction waves, whereas the cathodic waves at -0.24 and -0.29 V are due to Ru(III/II) reduction for **1** and **2**, respectively. If this is the case, the presence of Ru-bound dmit ligands in **1** does not significantly shift NO-based reduction potentials compared to the similar $[Ru(NO)(bpy)_2Cl]^{2+}$ complex (NO reduction at -0.36 V),[70] but analogous dmise coordination in **2** makes NO reduction less favorable. Corresponding Ru(II/III oxidation waves are not clearly observed, although additional differential pulse voltammogram experiments may help to identify these oxidation waves, as well as Ru(IV/III) waves for complex **1**. The results of these electrochemical studies, combined with the IR and NMR characterization data indicate that dmit binding differs from dmise binding in these Ru(II)-nitrosyl complexes, and that dmise binding makes the nitrosyl ligand more nucleophilic.

Table 4.3. Electrochemical data for thione and selone ligands and ruthenium complexes **1** and **2** vs. NHE.

Ligand or Complex	Ligand-based Potentials (V)		$Ru^{IV/III}$-based Potentials (V)			
	Ep_c	Ep_a	Ep_c	Ep_a	ΔE	$E_{1/2}$
dmit	-0.14	0.59	-	-	-	-
dmise	-0.15	0.37	-	-	-	-
$[Ru(NO)(dmit)_4Cl]^{2+}$ (**1**)	0.36	1.06	-	-	-	-
$[Ru(NO)(dmise)_4Cl]^{2+}$ (**2**)	0.31	0.85	0.97	1.08	0.11	1.03

4.3. Conclusions

Overall, this work reports the synthesis and characterization of two novel Ru(II)-nitrosyl complexes with thione and selone ligands. Their synthesis is notable because the

nitrosyl ligand is derived from a metal nitrate salt, a much easier method than using typical NO-addition reagents. This method allows a simple entry point into Ru-NO chemistry, and further investigations will determine whether this reaction method can be extended to form NO complexes with other *d*-block metal ions. This work greatly facilitates synthesis of Ru-nitrosyl complexes and may contribute to enhancing and developing their applications.

4.4. **Experimental methods**

General methods. Synthesis of all complexes was performed under argon using standard air-sensitive Schlenk techniques except where indicated. Ru(III) chloride hydrate (Oakwood), silver nitrate (BDH) , and sodium nitrate (BDH) were used without purification. 1,3-Dimethyl-2(3H)-imidazolethione (dimt) and 1,3-dimethyl-2(3H)-imidazoleselone(dimse) were synthesized as reported by Roy *et al*.[40] Acetonitrile was purified by distillation under an argon atmosphere, and anhydrous diethyl ether (BDH) was used without further purification.

^{1}H NMR spectra were recorded using a 300 MHz Bruker-AVANCE NMR spectrometer; ^{1}H NMR chemical shifts are reported in δ relative to tetramethylsilane (δ 0) and referenced to solvent (^{1}H NMR spectra of **1** and **2** in D_2O are shown in Figures 4.2-4.3). IR spectra were obtained from Nujol mulls on KBr salt plates with a Magna 550 IR spectrometer (Figures 4.4-4.6). Vibrational data are described using the abbreviations: vs, very strong; s, strong; m, medium; w, weak; b, broad. MALDI mass spectra were obtained using a Bruker Microflex MALDI-TOF mass spectrometer with *trans*-2-[3-(4-tert-butylphenyl)-2-methyl-2-propenyldiene] malonitrile (*m*/*z* 251.3 for cation with H^+) as the

matrix. All observed peak envelopes match theoretical calculations[89] for their ions (Figures 4.7-4.9).

*Synthesis of [Ru(NO)(dmit)$_4$Cl][BF$_4$]$_2$ (**1**).* $RuCl_3 \cdot 3H_2O$ (261 mg, 1 mmol) was dissolved in acetonitrile and $AgNO_3$ (3 mmol, 510 mg) was added to the solution. The reaction mixture was stirred and heated to reflux for 4 h under argon, then filtered to remove the AgCl precipitate. Dmit (4 mmol, 513 mg) dissolved in dichloromethane (15 mL) was added to the filtrate, and the reaction mixture was stirred and heated to reflux for an additional 4 h. Upon cooling, $NaBF_4$ (3 mmol, 330 mg) was added to the reaction mixture, and it was again stirred and heated to reflux for 8 h, during which time a white precipitate formed. The reaction mixture was cooled and filtered to remove the precipitate, and the solvent was removed *in vacuo*. The resulting brown powder was washed with diethyl ether (2 × 20 mL) and dissolved in acetonitrile (25 mL). The resulting mixture was filtered and recrystallized by vapor diffusion of diethyl ether into the acetonitrile solution at room temperature. After 6-12 h, crystals of $[Ru(NCCH_3)_6][BF_4]_2$ were filtered, and the resulting filtrate was again crystallized from vapor diffusion of diethyl ether to afford **1** as a brown, microcrystalline solid. Yield: 554 mg, 65%. Crystals for X-ray analysis were grown from vapor diffusion of diethyl ether into a solution of **1** in acetonitrile. IR (Nujol, cm^{-1}): 3404 (b), 3148 (w), 2926 (s), 2856 (s), 2727 (w), 1827 (w), 1662 (m), 1562 (m), 1460 (s), 1378 (s), 1304 (w), 1172 (s), 1083 (s), 1044 (w), 851 (w), 723 (s)), 647 (w), 520 (w). Analysis of $C_{20}H_{32}ClB_2F_8N_9RuS_4 \cdot 2CH_3CN \cdot 3H_2O$, Calcd. (Exp.): C, 28.58 (28.82); H, 4.56 (4.63); N, 15.21 (14.82). MALDI-MS *m/z* = 690, $[Ru(NO)(dmit)_3(BF_4)_2]^+$ and 766, $[Ru(NO)(dmit)_4Cl(BF_4)]^+$. Complex **1** was synthesized also using the same procedure as

described above except that $NaNO_3$ (3 mmol, 245 mg) was added in place of $AgNO_3$, yield 7%.

*Synthesis of $[Ru(NO)(dmit)_4Cl][BF_4]_2$ (**2**).* Synthesis of **2** was carried out using the same procedure as described for **1** except that dmise (4 mmol, 700 mg) was added in place of dmit. The resulting purple powder was purified as described for **1**, affording product **2** as a purple, microcrystalline solid. Crystals for X-ray analysis were grown from vapor diffusion of diethyl ether into a solution of **2**in acetonitrile. Yield: 697 mg, 67 %. IR (Nujol, cm^{-1}): 3399 (b), 3174 (w) 2925 (s), 2831 (s), 2728 (w), 1810 (w), 1661 (w), 1566 (m), 1456 (s), 1379 (s), 1238 (w), 1151 (s), 1077 (s), 1042 (s), 966 (m), 851 (w), 723 (s), 651 (w), 519(w), 468 (w). Analysis of $C_{20}H_{32}ClB_2F_8N_9RuSe_4 \cdot CH_3CN$): Calcd. (Exp.): C, 24.39 (24.87); H, 3.23 (3.23); N, 12.93 (12.90). MALDI-MS *m/z* = 655, $[Ru(NO)(dmise)_2(BF_4)_2]^+$ and 692, $[Ru(NO)(dmise)_2Cl(BF_4)_2H]^+$. Complex **2** was synthesized also using the same procedure as described above except that $NaNO_3$ (3 mmol, 245 mg) was added in place of $AgNO_3$, yield 10%.

Electrochemistry. Cyclic voltammogram and differential pulse voltammetry (DPV) measurements for complexes **1** and **2** were obtained using a CH Electrochemical Analyzer (CH Instruments, Inc.) with a glassy carbon working electrode, Ag/AgCl reference electrode, and a Pt counter-electrode in a compartment cell. Tetra-*n*-butyl ammonium phosphate (0.1 M) was used as the supporting electrolyte in acetonitrile (distilled under argon and stored over 4 Å molecular sieves) with a 0.1 mM concentration for complexes **1** and **2**. Samples were deaerated for 10 minutes by vigorous nitrogen purge. CV studies were conducted at a scan rate of 100 mV/s. All measured redox potentials were adjusted to

NHE (0.198 V[83]) from Ag/AgCl, and referenced to the ferrocenium/ferrocene couple (0.400 V vs. NHE[84]).

X-ray crystallography. Complexes **1** and **2** were characterized by X-ray structural analysis. Single crystals of **1** and **2** were grown via slow diffusion of diethyl ether into acetonitrile solutions. Diffraction data were collected using a Bruker D8 Venture diffractometer with a Mo Kα (λ = 0.71073 Å) microfocus source and a Photon 100 CMOS detector. Data were collected by phi and omega scans, and processed and corrected for absorption using the Apex 3 software suite. The structures were solved and refined by full-matrix least squares techniques on F^2 using the SHELXTL software suite. Crystallographic data for complexes **1** and **2** is shown in Table 5.

Table 4.4. Crystallographic data for $[RuCl(NO)(dmit)_4](BF_4)_2$ (**1**) and $[RuCl(NO)(dmise)_4](BF_4)_2$ (**2**).

	1	**2**
Empirical formula	$C_{20}H_{32}B_2ClF_8N_9ORuS_4$	$C_{20}H_{32}B_2ClF_8N_9ORuSe_4$
Formula weight (g/mol)	852.92	1040.52 g/mol
Temperature (K)	140(2) K	140(2) K
Crystal system	monoclinic	monoclinic
Space group	$P2_1/c$	$P2_1/c$
Unit cell dimensions (Å,°)	a = 8.3673(6)Å b = 19.5553(12) Å c = 10.5028(7) Å β = 98.257(2) °	a = 10.6266(5) Å b = 10.3586(5) Å c = 16.1181(8) Å β = 95.229(2) °
Volume (Å^3)	1700.7(2)	1766.84(15)
Z, calcd density (g/cm^3)	2	2
Absorption coefficient (mm^{-1})	0.862	4.714
F(000)	860	1004
Crystal size (mm)	0.038 × 0.087 × 0.301	0.032 × 0.187 × 0.214
T_{max}, T_{min}	0.9680 and 0.7810	1.0000 and 0.7553
Θ range for data	2.67 to 25.50°	2.75 to 26.43°
Reflns collected/unique/obs.	41562	34262
Data/restraints/parameters	3160 / 36 / 256	3622 / 19 / 237
Goodness-of-fit on F^2	1.262	1.062
R1, wR^2 ($I \geq 2\sigma(I)$)	R1 = 0.0517, wR^2 = 0.0974	R1 = 0.0421, wR^2 = 0.1030
R1, wR^2 (all data)	R1 = 0.0604, wR^2 = 0.1001	R1 = 0.0581, wR^2 = 0.1123
Largest diff. peak, hole (e/Å^3)	0.427 and -0.842	0.787 and -0.766

4.5 Supplemental Material

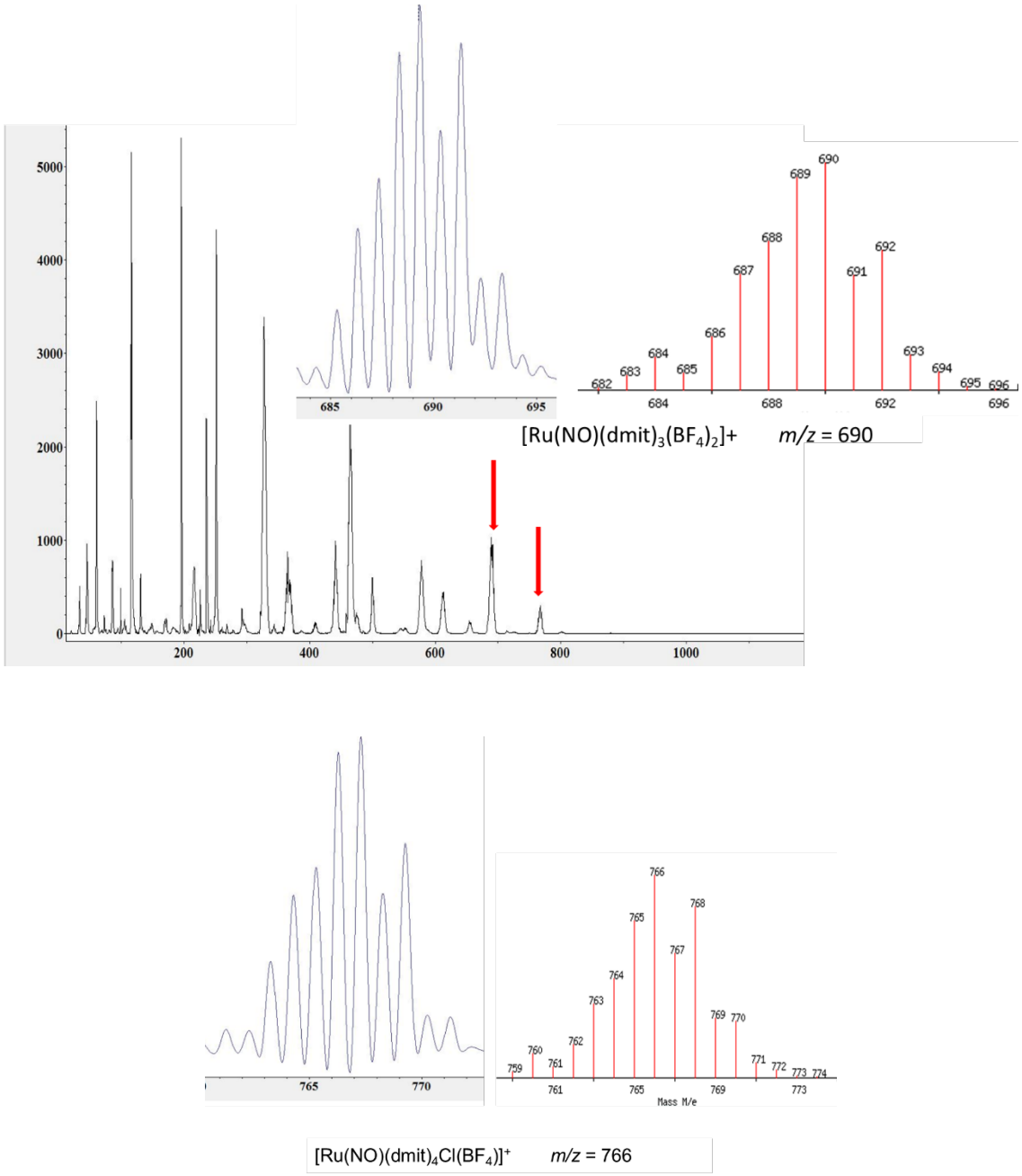

Figure 4.3. MALDI mass spectrum with insets of experimental (left) and simulated (right) envelope intensities for $[Ru(NO)(dmit)_4Cl][BF_4]_2$ (**1**).

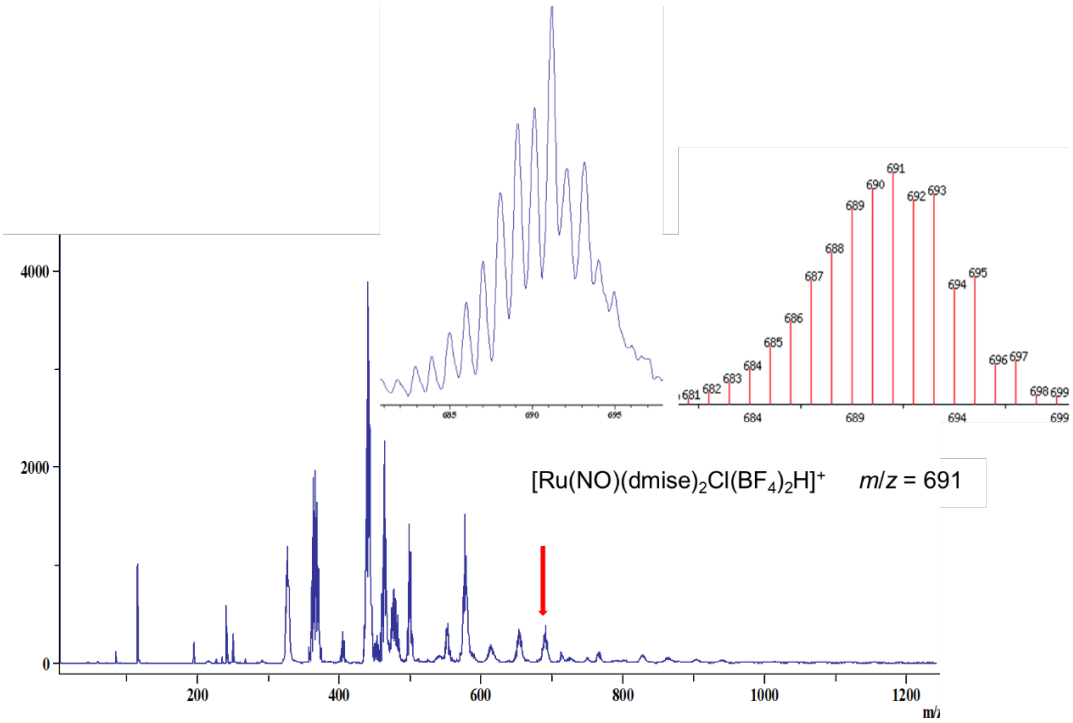

Figure 4.4. MALDI mass spectrum with insets of experimental (left) and simulated (right) envelope intensities for $[Ru(NO)(dmise)_4Cl][BF_4]_2$ (**2**).

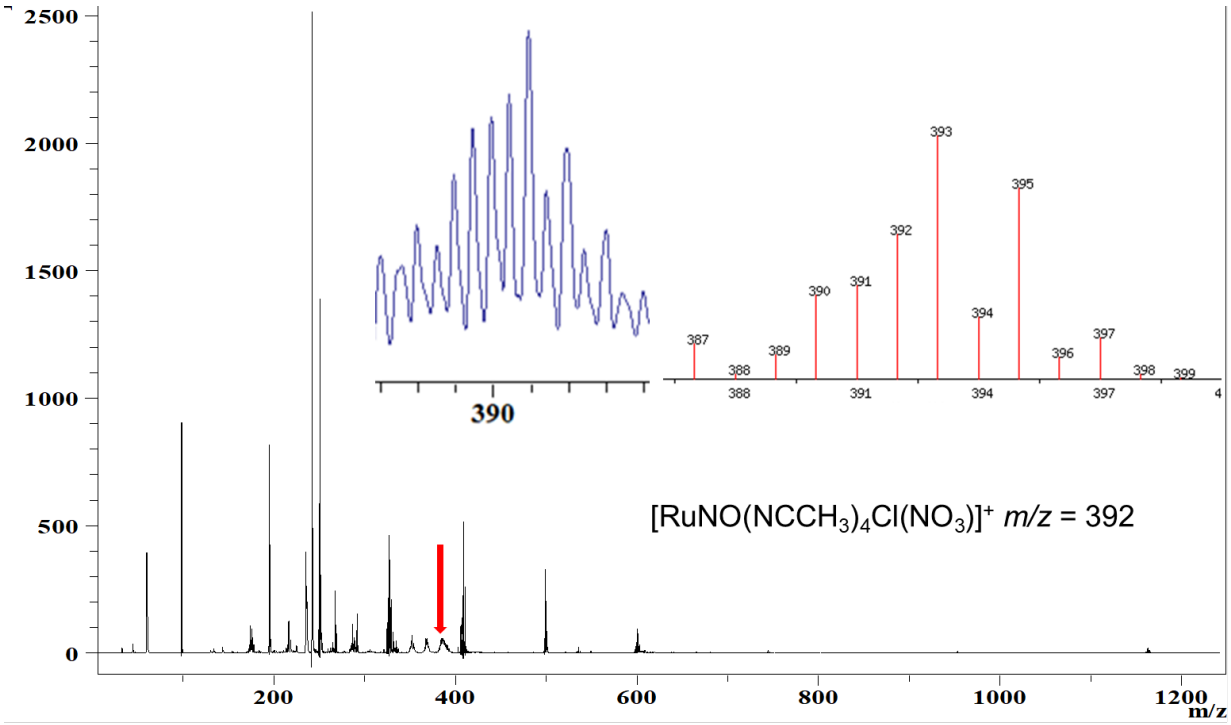

Figure 4.5. MALDI mass spectrum with insets of experimental (left) and simulated (right) envelope intensities for the reaction mixture prior to addition of dmit or dmise.

Table 4.5. Selected interatomic distances and angles for $[Ru(NO)(dmit)_4Cl][BF_4]_2$ (**1**).

Bond lengths (Å)				**Bond angles (°)**			
Ru1-N5	1.69(2)	Ru1-Cl5	2.263(6)	N5-Ru1-S1	89.1(11)	Cl5-Ru1-S1	90.1(2)
Ru1-S1	2.4259(10)	Ru1-S1	2.4260(10)	N5-Ru1-S1	90.9(11)	Cl5-Ru1-S1	89.9(2)
Ru1-S2	2.4349(10)	Ru1-S2	2.4350(10)	S1-Ru1-S1	180.00(6)	N5-Ru1-S2	90.4(11)
S1-C1	1.714(4)	S2-C6	1.718(4)	Cl5-Ru1-S2	90.7(2)	S1-Ru1-S2	89.38(4)
N5-O5	1.31(2)	N1-C1	1.344(6)	S1-Ru1-S2	90.62(4)	N5-Ru1-S2	89.6(11)
N1-C2	1.384(7)	N1-C4	1.454(7)	Cl5-Ru1-S2	89.3(2)	S1-Ru1-S2	90.62(4)
N2-C1	1.341(6)	N2-C3	1.392(7)	S1-Ru1-S2	89.38(4)	S2-Ru1-S2	180.0
N2-C5	1.446(8)	N3-C6	1.343(6)	C1-S1-Ru1	108.56(14)	C6-S2-Ru1	106.40(15)
N3-C7	1.377(7)	N3-C9	1.455(7)	O5-N5-Ru1	174.(3)	C1-N1-C2	108.5(5)
N4-C6	1.351(6)	N4-C8	1.377(6)	C1-N1-C4	125.6(4)	C2-N1-C4	125.9(5)
N4-C10	1.450(7)	C2-C3	1.307(9)	C1-N2-C3	108.3(5)	C1-N2-C5	124.8(5)
C2-H2	0.95	C3-H3	0.95	C3-N2-C5	126.9(5)	C6-N3-C7	108.9(5)
C4-H4A	0.98	C4-H4B	0.98	C6-N3-C9	125.3(4)	C7-N3-C9	125.7(5)

Table 4.6. Selected interatomic distances (Å) and angles (°) for $[Ru(NO)(dmise)_4Cl][BF_4]_2$ (**2**).

Bond lengths (Å)				**Bond angles (°)**			
Ru1-N5	1.679(13)	Ru1-Cl5	2.437(11)	N5-Ru1-Se1	90.4(8)	Cl5-Ru1-Se1	88.31(14)
Ru1-Se1	2.5422(5)	Ru1-Se1	2.5422(5)	N5-Ru1-Se1	89.7(8)	Cl5-Ru1-Se1	91.69(14)
Ru1-Se2	2.5452(5)	Ru1-Se2	2.5453(5)	Se1-Ru1-Se1	180.0	N5-Ru1-Se2	90.8(8)
Se1-C1	1.865(5)	Se2-C6	1.868(4)	Cl5-Ru1-Se2	93.06(14)	Se1-Ru1-Se2	89.689(16)
N5-O5	1.234(18)	N1-C1	1.350(7)	Se1-Ru1-Se2	90.311(16)	N5-Ru1-Se2	89.2(8)
N1-C3	1.364(8)	N1-C4	1.444(9)	Cl5-Ru1-Se2	86.94(14)	Se1-Ru1-Se2	90.310(16)
N2-C1	1.350(7)	N2-C2	1.386(8)	Se1-Ru1-Se2	89.690(16)	Se2-Ru1-Se2	180.0
N2-C5	1.460(10)	N3-C6	1.362(7)	C1-Se1-Ru1	104.83(13)	C6-Se2-Ru1	105.65(13)
N3-C7	1.365(7)	N3-C9	1.463(8)	O5-N5-Ru1	169.(3)	C1-N1-C3	109.4(6)
N4-C6	1.333(6)	N4-C8	1.371(6)	C1-N1-C4	125.5(5)	C3-N1-C4	125.1(6)
N4-C10	1.455(7)	C2-C3	1.337(11)				

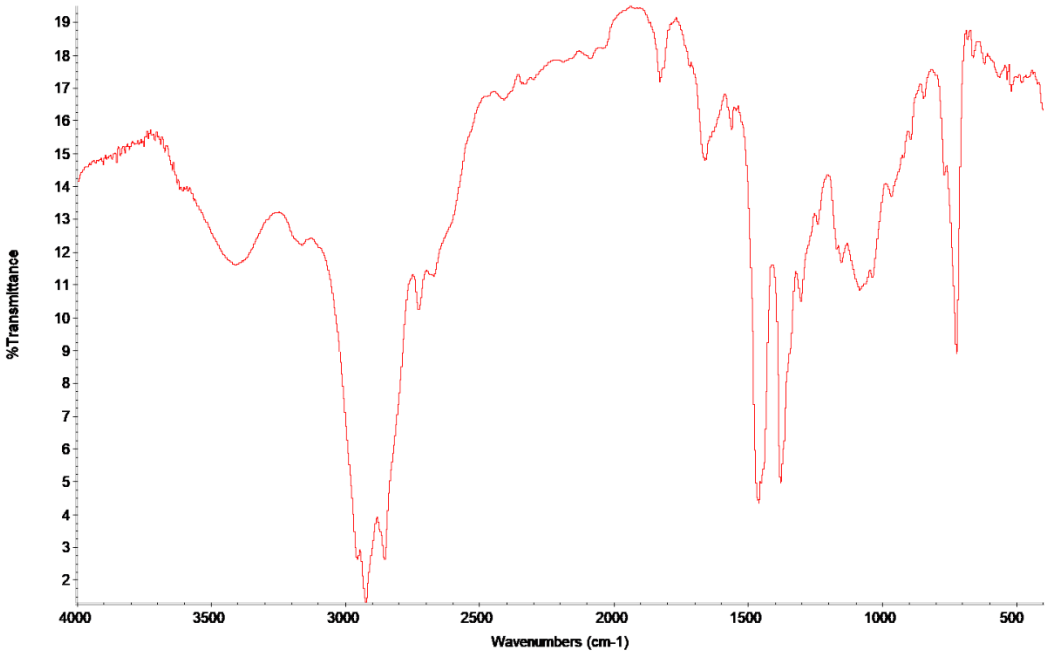

Figure 4.6. Transmittance IR spectrum of $[Ru(NO)(dmit)_4Cl][BF_4]_2$ (**1**) acquired as a Nujol mull.

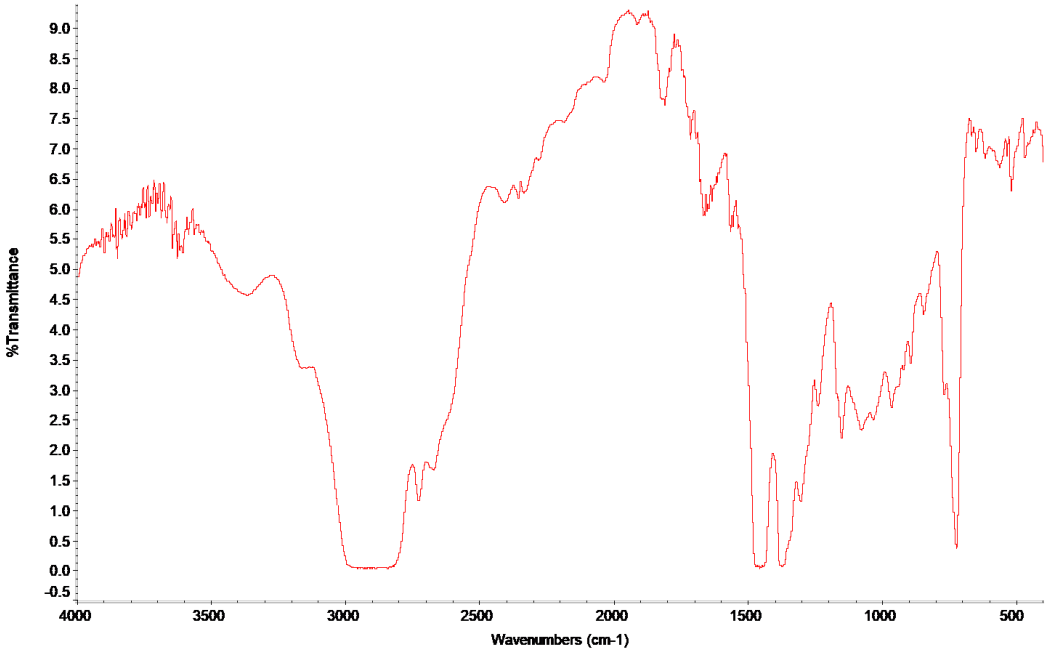

Figure 4.7. Transmittance IR spectrum of $[Ru (NO)(dmise)_4Cl][BF_4]_2$ (**2**) acquired as a Nujol mull.

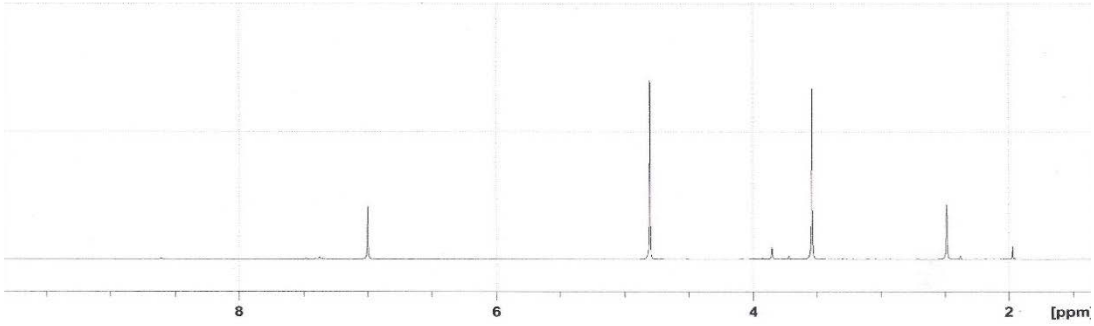

Figure 4.8. ^{1}H NMR spectrum of $[Ru(NO)(dmit)_4Cl][BF_4]_2$ (**1**) in D_2O (δ 4.79).

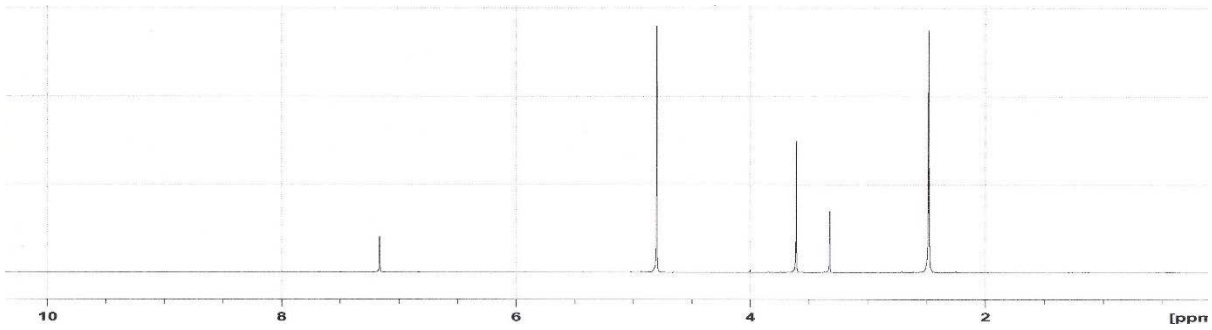

Figure 4.9. ^{1}H NMR spectrum of $[Ru(NO)(dmise)_4Cl][BF_4]_2$ (**2**) in D_2O (δ 4.79).

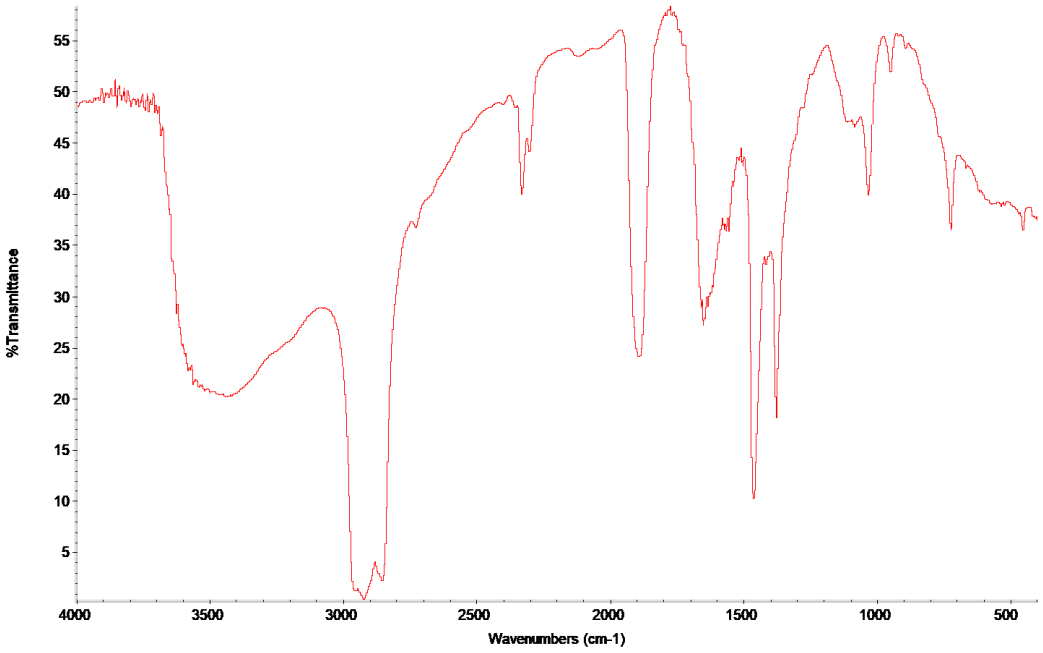

Figure 4.10. IR spectrum of reaction mixture prior to dmit or dmise addition acquired as a Nujol mull.

4.6. References

(1) Rodrigues, G. L. S.; Rocha, W. R. *J. Phys. Chem. B* **2016**, *120*, 11821–11833.

(2) Ignarro, L. J.; Buga, G. M.; Wood, K. S.; Byrnes, R. E.; Chaudhuri, G. *Proc. Natl. Acad. Sci. U. S. A.* **1987**, *84*, 9265−9269.

(3) Palmer, R. M. J.; Ashton, D. S.; Moncada, S. Vascular *Nature* **1988**, *333*, 664−666.

(4) Ignarro, L. J. *Pharm. Res.***1989**, *6*, 651−659.

(5) Guix, F. X.; Uribesalgo, I.; Coma, M.; Muñoz, F. J. *Prog. Neurobiol.* **2005**, *76*, 126-152.

(6) Monti, J. M.; Jantos, H. *Life Sci.* **2004**, *75*, 2027–2034.

(7) Ignarro; L.J. *FASEB J.* **1989**, *3*, 31–36.

(8) Silva-Santos, J. E.; Assreuy, J. *J. Pharmacol. Exp. Ther.* **1999**, *290*, 380-387.

(9) Bredt, D.S.; Hwang, P.M.; Snyder, S.H. *Nature* **1990**, *347*, 768–770.

(10) Manukhina, E. B.; Smirin, B. V.; Malyshev, I. Y.; Stoclet, J.-C.; Muller, B.; Solodkov, A. P.; Shebeko, V. I.; Vanin, A. F. *Biol. Bull. Russ. Acad. Sci.* **2002**, *29*, 477–486.

(11) Cullota, E.; Koshland, D. E. *Science* **1992**, *258*, 1862−1865.

(12) Tfouni, E.; Truzzi, D. R.; Tavares, A.; Gomes, A. J.; Figueiredo, L. E.; Franco, D. W. *Nitric Oxide* **2012**, *26*, 38−53.

(13) Palmer; R.M., Ashton; D.S., Moncada; S. *Nature* **1988**, *333*, 664–666.

(14) Tfouni, E.; Krieger, M.; McGarvey, B. R.; Franco, D. W. *Coord. Chem. Rev*. **2003**, *236*, 57−69.

(15) Sauaia, M. G.; de Lima, R. G.; Tedesco, A. C.; Da Silva, R. S. *Inorg. Chem*. **2005**,

44, 9946−9951.

(16) Bukhanko, V.; Lacroix, P. G.; Sasaki, I.; Tassé, M.; Mallet-Ladeira, S.; Voitenko, Z.; Malfant, I. *Inorg. Chim. Acta* 2018, 482, 195–205.

(17) Tfouni, E.; Doro, F. G.; Gomes, A. J.; Silva, R. S. d.; Metzker, G.; Benini, P. G. Z.; Franco, D. W. *Coord. Chem. Rev.* **2010**, *254*, 355–371.

(18) Tfouni, E.; Ferreira, K. Q.; Doro, F. G.; da Silva, R. S., da Rocha, Z.N. *Coord. Chem. Rev.* **2005**, *249*, 405–418.

(19) Tfouni, E; Krieger, M.; McGarvey, B. R.; Franco, D. W. *Coord. Chem. Rev.* **2003**, *236*, 57–69.

(20) Fry, N. L.; Heilman, B. J.; Mascharak, P. K. *Inorg. Chem.* **2011**, *50*, 317–324.

(21) Silva, F. O.; Candido, M. C.; Holanda, A. K.; Diogenes, I.C.; Sousa, E. H.; Lopes, L. G. *J. Inorg. Biochem.***2011**, *105*, 624–629.

(22) Bordini, J.; Hughes, D. L.; Motta Neto, J. D.; da Cunha, C. J. *Inorg. Chem.* **2002**, *41*, 5410–5416.

(23) Carlos, R. M.; Ferro, A. A.; Silva, H. A. S.; Gomes, M. G.; Borges, S. S. S.; Ford, P. C.; Tfouni, E.; Franco, D. W. *Inorg. Chim. Acta* **2004**, *357*, 1381−1388.

(24) Cameron, B. R.; Darkes, M. C.; Yee, H.; Olsen, M.; Fricker, S. P.; Skerlj, R. T.; Bridger, G. J.; Davies, N. A.; Wilson, M. T.; Rose, D. J.; Zubieta, J. *Inorg. Chem.* **2003***, 42*, 1868−1876.

(25) Marcondes, F. G.; Ferro, A. A.; Souza-Torsoni, A.; Sumitani, M.; Clarke, M. J.; Franco, D. W.; Tfouni, E.; Krieger, M. H. *Life Sci.* **2002**, *70*, 2735–2752.

(26) Hutchings, S. R.; Song, D.; Fricker, S. P.; Pang, C. C. *Euro. J. of Pharmacology*

2005, *528,*132–136.

(27) Mosi, R.; Seguin, B.; Cameron, B., Amankwa, L.; Darkes, M. C.; Fricker, S.P., *Biochem. Biophys. Res. Commun.* **2002**, *292*, 519–529.

(28) Azarov, I.; Huang, K. T.; Basu, S.; Gladwin, M. T.; Hogg, N.; Kim-Shapiro, D. B. *J. Biol. Chem.* **2005**, *280*, 39024–39032.

(29) Mohammad Mir, J.; Jain, N.; Jaget, P. S.; Khan, W.; Vishwakarma, P. K.; Rajak, D. K.; Malik, B. A.; Maurya, R. C. *J. King Saud Univ. - Sci.* **2019**, *31*, 89–100.

(30) Franzoni, F.; Colognato, R.; Galetta, F.; Laurenza, I.; Barsotti, M.; Di Stefano, R.; Bocchetti, R.; Regoli, F.; Carpi, A.; Balbarini, A.; Migliore, L.; Santoro, G. *Biomed. Biopharmcother.* **2006**, *60*, 453-457.

(31) Short, R. D. J.; Baskin, S. I. In *Oxidants, Antioxidants and Free Radicals*; Baskin, S. I., Salem, H., Eds.; Taylor&Friends: Washington, D.C., 1997, pp 203-206.

(32) Aruoma, O. I.; Spencer, J. P. E.; Mahmood, N. *Food Chem. Toxicol.* **1999**, *37*, 1043-1053.

(33) Deiana, M.; Rosa, A.; Casu, V.; Piga, R.; Assunta, D. M.; Aruoma, O. I. *Clin. Nutr.* **2004**, *23*, 183-193.

(34) Jang, J.-H.; Aruoma, O. I.; Jen, L.-S.; Chung, H. Y.; Surh, Y.-J. *Free Radic. Biol. Med.* **2004**, *36*, 288-299.

(35) Colognato, R.; Laurenza, I.; Fontana, I.; Coppede, F.; Siciliano, G.; Coecke, S.; Aruoma, O. I.; Benzi, L.; Migliore, L. *Clin. Nutr.* **2006**, *25*, 135-145.

(36) Markova, N. G.; Karaman-Jurukovska, N.; Dong, K. K.; Damaghi, N.; Smiles, K. A.; Yarosh, D. B. *Free Radic. Biol. Med.* **2009**, *46*, 1168-1176.

(37) Paul, B. D.; Snyder, S. H. *Cell Death Different.* **2010**, *17*, 1134-1140.

(38) Yamashita, Y.; Yamashita, M. *J. Biol. Chem.* **2010**, *285*, 18134-18138.

(39) Roy, G.; Das, D.; Mugesh, G. *Inorg. Chim. Acta* **2007**, *360*, 303–316.

(40) Roy, G.; Mugesh, G. *Bioinorg. Chem. Appl.* **2006**, *23214, 1-9.*

(41) Corrêa, R. S.; da Silva, M. M.; Graminha, A. E.; Meira, C. S.; Santos, J. A. F. dos; Moreira, D. R. M.; Soares, M. B. P.; Von Poelhsitz, G.; Castellano, E. E.; Bloch, C.; et al. *J. Inorg. Biochem.* **2016**, *156*, 153–163.

(42) Scintilla, S.; Brustolin, L.; Gambalunga, A.; Chiara, F.; Trevisan, A.; Nardon, C.; Fregona, D. *J. Inorg. Biochem.* **2016**, *165*, 159–169.

(43) Sampath, K.; Sathiyaraj, S.; Jayabalakrishnan, C. *Mol. Biomol. Spectroscopy* **2013**, *105*, 582–592.

(44) Appelt, P.; Fagundes, F. D.; Facchin, G.; Gabriela Kramer, M.; Back, D. F.; Cunha, M. A. A.; Sandrino, B.; Wohnrath, K.; de Araujo, M. P. *Inorg. Chim. Acta* **2015**, *436*, 152–158.

(45) Lever, A. B. P. *Inorg. Chem.* **1990**, *29*, 1271–1285. Vanýsek, Petr (2012). "Electrochemical Series". In Haynes, William M. (ed.). *Handbook of Chemistry and Physics: 93rd Edition*. Chemical Rubber Company. pp. 5–80.

(46) Johnston, H. S.; Cantrell, C. A.; Calvert, J. G. *J. Geophy. Res. Atmo.* **1986**, *91*, 5159–5172.

(47) Małecka, B.; Łącz, A.; Drożdż, E.; Małecki, A.. *J. Therm. Anal. Calorim.* **2015**, *119*, 1053–1061.

(48) Zhu, H.; Ma, Q.; Jia, A.-Q.; Chen, Q.; Leung, W.-H.; Zhang, Q.-F. *Inorg. Chim.*

Acta **2013**, *405*, 427–436.

(49) Qin, Y.; Ma, Q.; Jia, A.-Q.; Chen, Q.; Zhang, Q.-F. *J. Coord. Chem.* ***2013***, *66*, 1405–1415.

(50) Sharma, A. K.; Joshi, H.; Sharma, K. N.; Gupta, P. L.; Singh, A. K. *Organometallics* **2014**, *33*, 3629–3639.

(51) Raper, E. S.; Creighton, J. R.; Oughtred, R. E.; Nowell, I. W. *Acta Crystallogr.* **1983**, *B39*, 355-360.

(52) Stadelman, B. Ph. D. Clemson University, Clemson, SC, **2016**.

(53) Silvestri, A.; Ruisi, G.; Girasolo, M. A. *J. Inorg. Biochem.* **2002**, *92*, 171-176.

(54) Kimani, M. M.; Brumaghim, J. L.; VanDerveer, D. *Inorg. Chem.* **2010**, *49*, 9200-9211.

(55) Williams, D. J.; Fawcett-Brown, M. R.; Raye, R. R.; VanDerveer, D.; Pang, Y. T.; Jones, R. L. *Heteroat. Chem.* **1993**, *4*, 409-414.

(56) Szacilowski, K.; Macyk, W.; Drzewiecka-Maruszek, A.; Brindel,M.; Stochel, G. *Chem. Rev.* **2005**, *105*, 2647−2694.

(57) Rose, M. J.; Mascharak, P. K. *Coord. Chem. Rev.* **2008**, *252*, 2093−2114.

(58) Caramori, G. F.; Ortolan, A. O.; Parreira, R. L. T.; da Silva, E. H. R. *J. Organomet. Chem.* **2015**, *799-800*, 54–60.

(59) Amabilino, S.; Tasse, M.; Lacroix, P. G.; Mallet-Ladeira, S.; Pimienta, V.; Akl, J.; Sasaki, I.; Malfant, I. *New J. Chem.* **2017**, *41*, 7371–7383.

(60) Enriquez-Cabrera, A.; Lacroix, P. G.; Sasaki, I.; Mallet-Ladeira, S.; Farfán, N.; Barba-Barba, R. M.; Ramos-Ortiz, G.; Malfant, I. *Eur. J. Inorg. Chem.* **2018**, *2018*,

531–543.

(61) Freitag, L.; González, L. *Inorg. Chem.* **2014**, *53*, 6415–6426.

(62) Barbosa, G. A.; da Silva, J. P.; Appelt, P.; Fuganti, O.; Murakami, F. S.; de Araujo, M. P. *Inorg. Chem. Commun.* **2018**, *90*, 108–111.

(63) Kumar, A.; Pandey, R.; Gupta, R. K.; Ghosh, K.; Pandey, D. S. *Polyhedron* **2013**, *52*, 837–843.

(64) Vorobyev, V.; Emelyanov, V. A.; Plusnina, O. A.; Makarov, E. M.; Baidina, I. A.; Smolentsev, A. I.; Tkachev, S. V.; Asanova, T. I. *Eur. J. Inorg. Chem.* **2017**, *2017* (5), 971–978.

(65) Caramori, G. F.; Frenking, G. *Organometallics* **2007**, *26*, 5815–5825.

(66) Roose, M.; Sasaki, I.; Bukhanko, V.; Mallet-Ladeira, S.; Barba-Barba, R. M.; Ramos-Ortiz, G.; Enriquez-Cabrera, A.; Farfán, N.; Lacroix, P. G.; Malfant, I. *Polyhedron* **2018**, *151*, 100–111.

(67) Andriani, K. F.; Caramori, G. F.; Doro, F. G.; Parreira, R. L. T. R. *Dalton Trans.* **2014**, *43*, 8792–8804.

(68) Kumar, R.; Yadav, A.; Ratnam, A.; Kumar, S.; Bala, M.; Sur, D.; Narang, S.; Singh, U. P.; Mandal, P. K.; Ghosh, K. *Eur. J. Inorg. Chem.* **2017**, *2017*, 5334–5343.

(69) Caramori, G. F. and Frenking G. *Croat. Chem. Acta*. **2009**, *82*, 219-232.

(70) Callahan, R. W.; Meyer, T. J. *Inorg. Chem.* **1977**, *16*, 574–581.

(71) Lewandowska, H. Spectroscopic Characterization of Nitrosyl Complexes. In *Nitrosyl Complexes in Inorganic Chemistry, Biochemistry and Medicine I*; Mingos, D. M. P., Ed.; Structure and Bonding; Springer Berlin Heidelberg: Berlin,

Heidelberg, 2014; pp 115–165

(72) Williams, D. J.; Ly, T. A.; Mudge, J. W.; VanDerveer, D.; Jones, R. L. *Inorg. Chim. Acta* **1994**, *218*, 133-138.

(73) Landry, V. K.; Minoura, M.; Pang, K.; Buccella, D.; Kelly, B. V.; Parkin, G. *J. Am. Chem. Soc.* **2006**, *128*, 12490-12497.

(74) Kimani, M. M.; Bayse, C. A.; Brumaghim, J. L. *Dalton Trans.* **2011**, *40*, 3711-3723.

(75) Kimani, M. M.; Brumaghim, J. L.; VanDerveer, D. *Inorg. Chem.* **2010**, *49*, 9200-9211.

(76) Kimani M. M.; Wang, H. C.; Brumaghim, J. L. *Dalton Trans.* **2012**, *41*, 5248-5259.

(77) Jia W.; Huang, Y.; Lin, Y.; Wang, G.; Jin, G. *Eur. J. Inorg. Chem.* **2008**, 4063-4073.

(78) Aggarwal, V.; Kumar, V. R.; Singh, U. P. *J. Chem. Crystallogr.* **2011**, *41*, 121-126.

(79) Abbas, M. A.; McMillen, C. D.; Brumaghim, J. L. *Inorg. Chim. Acta* **2017**, *468*, 308–315.

(80) Santos, A. F.; Ferreira, I. P.; Pinheiro, C. B.; Santos, V. G.; Lopes, M. T. P.; Teixeira, L. R.; Rocha, W. R.; Rodrigues, G. L. S.; Beraldo, H. *ACS Omega* **2018**, *3*, 7027–7035.

(81) Addison, C. C.; Gatehouse, B. M. *J. Chem. Soc.* **1960**, 613–616.

(82) Callahan, R. W.; Brown, G. M.; Meyer, T. J. *J. Am. Chem. Soc.* **1975**, *97*, 894–895.

(83) Callahan, R. W.; Meyer, T. J. *Inorg. Chem.* **1977**, *16*, 574–581.

(84) Swain, P.; Mallika, C.; Jagadeeswara Rao, C.; Mudali, K.; Natarajan, R. *J. Appl. Electrochem.* **2015**, *45*, 209–216.

(85) Koepp, H. M.; Wendt, H.; Strehlow, H. Z. *Electrochem.* **1960**, *64*, 483-491.

(86) Connelly, N. G.; Geirger, W. E. R. *Chem. Rev.* **1996**, *96*, 877-910.

(87) Lever, A. B. P. E *Inorg. Chem.* **1990**, *29*, 1271–1285.

(88) Jabłońska-Wawrzycka, A.; Rogala, P.; Michałkiewicz, S.; Hodorowicz, M.; Barszcz, B. *Dalton Trans.* **2013**, *42*, 6092-6101.

(89) Adaptas Solutions. Scientific Instrument Services: Isotope Distribution Calculator and Mass Spec Plotter. https://www.sisweb.com/mstools/isotope.htm (accessed March 23, 2019).